THE UNIVERSITY *of* EDINBURGH

FRP-to-Concrete Bond Behaviour under High Strain Rates

Thesis submitted in fulfilment of the requirements for the degree of Doctor of Philosophy
By

Xiaoqin Li

Supervisors: Dr Jian-Fei Chen
Professor Yong Lu

The University of Edinburgh

April 2012

Declaration

This thesis, entitled “FRP-to-Concrete Bond Behaviour under High Strain Rates”, is submitted to The University of Edinburgh for the Degree of Doctor of Philosophy.

The research, on which this thesis is based, was carried out between October 2007 and September 2011 under the supervision of Dr Jian-Fei Chen and Professor Yong Lu. It is solely the work of the author except where otherwise acknowledged in the text. Where other sources were used, full references are given. It has not formed the basis of a submission for any other degree except that the test data in Chapter 7, which had been submitted as part of MEng theses by Andrew Sheil and Rory O’Sullivan.

The following publications are based on this thesis:

Li, X.Q., Yang, Z.J., Chen, J.F. and Lu, Y. (2011), "Loading rate effect on FRP-to-concrete bond behaviour", International Conference on Civil Engineering, Advanced Materials Research, Vols.250 (2011):3571-3576.

Li, X.Q., Chen, J.F. and Lu, Y. (2010), "Meso-scale modelling of FRP-to-concrete bond behaviour using LSDYNA", Proceedings of the 5th International Conference on FRP Composites in Civil Engineering, September 27-29, Beijing, China: 494-498.

Li, X.Q., Chen, J.F. and Lu, Y. (2010), "On mode-I fracture modelling of concrete in LS-DYNA explicit", Proceedings (CD-ROM) of the 13th International Conference on Structural Faults + Repair, June 15-17, Edinburgh, UK.

Xiaoqin Li

April 2012

Abstract

Fibre reinforced polymer (FRP) composites have been used for strengthening concrete structures since early 1990s. More recently, FRP has been used for retrofitting concrete structures for high energy events such as impact and blast. Debonding at the FRP-to-concrete interface is one of the predominant failure modes for both static and dynamic loading. Although extensive research has been conducted on the static bond behaviour, the bond-slip mechanics under high strain rates is not well understood yet. This thesis is mainly concerned with the FRP-to-concrete bond behaviour under dynamic loading.

Because debonding mostly occurs in the concrete adjacent to the FRP, the behaviour of concrete is of crucial importance for the FRP-to-concrete bond behaviour. The early emphasis of this thesis is thus on the meso-scale concrete modelling of concrete with appropriate consideration of static and dynamic properties. Issues related to FE modelling of tensile and compressive localization of concrete are first investiagetd in detail under static condition using the K&C concrete damage model in LS-DYNA. It is discovered for the first time that dilation of concrete plays an important role in the FRP-to-concrete bond behaviour. This has led to the development of a model relating the shear dilation factor to the concrete strength based on the modelling of a large number of static FRP-to-concrete shear tests, forming the basis for dynamic modelling.

Concrete dynamic increasing factor (DIF) has been a subject of extensive investigation and debate for many years, but it is for the first time discovered in this

study that mesh objectivity cannot be achieved in meso-scale modelling of concrete under high strain rate deformation. This has led to the development of a mesh and strain rate dependent concrete tension DIF model. This DIF model shall have wide applications in meso-scale modelling of concrete, not limited to the topic in this thesis.

Based on a detailed numerical investigation of the FRP-to-concrete bond shear test under different loading rates, taking on the above issues into careful consideration, a slip rate dependent FRP-to-concrete dynamic bond-slip model is finally proposed for the first time. The FE predictions deploring this proposed bond-slip model are compaed with test results of a set of FRP-to-concrete bonded specimens under impact loading, and a FRP plated slab under blast loading, validating the model.

Acknowledgement

I am deeply grateful to my supervisors, Dr Jian-fei Chen and Professor Yong Lu, for their encouragement, generous support and enlightening guidance in carrying out this research and in producing this thesis.

I would like to thank Dr Tim Stratford, Dr Zhi-Jun Zhong and Professor Ian May for their expert guidance and support in conducting the experiments. I am also very grateful for the assistance and cooperation from Andrew Sheil, Rory O'Sullivan, Lei Mao and Zhen-huan Song.

I would like to thank Dr Zhen-Jun Yang for his advice and review of Chapters 3 and 4 in this thesis.

I would also like thank the friends, and my colleagues in the University of Edinburgh for their help and support.

I would like to express my special thanks to my family for their love, care and support during the last 4 years. I am much indebted to them.

Finally, funding provided to the author by British Engineering and Physical Sciences Research Council (EPSRC) and Royal Dutch Shell plc UK Ltd through the Dorothy Hodgkin Postgraduate Award is greatly acknowledged.

Contents

List of figures

List of tables

Nomenclature

The definition of the symbols in the thesis

f_c'	The unconfined cylinder compressive strength of the concrete
f_t	The tensile strength of the concrete
ρ	The density
G_f^I	The Mode I fracture energy
w_c	The crack band width of the concrete
d_a	The maximum aggregate size of the concrete
h_c	The element characteristic length
E_t	The tangential strain-softening modulus based on a linear softening assumption
E_c	The Young's modulus of concrete
σ	The stress
ε	The strain
$\dot{\varepsilon}$	The strain rate
$\dot{\varepsilon}_s$	The reference static strain rate
$\Delta\sigma$	The effective deviatoric stress
p	The pressure
λ	The modified effective plastic strain of K&C concrete damage model
SDF	The scaled damage factor of K&C concrete damage model
l_w	The localized width of K&C concrete damage model
G_c	The compressive fracture energy
α	The dilation angle
φ	The friction angle
ω	An input parameter of K&C concrete damage model representing the ratio of associated plastic flow to Prandtl-Reuss plastic flow
b_c	The width of concrete prism
E_P	The elastic Young's modulus of the FRP plate
t_p	The thickness of the FRP plate

b_p	The FRP plate width
L_e	The effective bond length
L	The real bond length
β_w	The width ratio effect factor
β_L	The length effect factor
P_u	The ultimate load at the FRP end
τ	The bond stress
$\tau_{\max}$	The peak value of the bond stress
s_0	The slip correspond to $\tau_{\max}$
s_f	The final slip of the bond-slip curves
G_f^{II}	The Mode II fracture energy (the area under bond-slip curves)
$\dot{s}$	The slip rate
α_{DIF}	The DIF for bond-slip relationship at slip rate $\dot{s}$
m_e	The first mode mass of the pin-end beam
m_b	The beam mass
W	The explosive charge
R	The stand-off distance from explosive charge to the target
Z	The characteristic scaled distance

Chapter 1 Introduction

1.1 Background

Fibre-reinforced polymer (FRP) is a composite material made of a polymer matrix reinforced with fibres. The fibres are usually glass, carbon, or aramid, while the polymer is usually an epoxy, vinylester or polyester thermosetting plastic. According to the type of fibres, FRP composites are generally classified as carbon fibre reinforced polymer (CFRP), glass fibre reinforced polymer (GFRP), and aramid fibre reinforced polymer (AFRP) (Teng et al. 2002).

FRP has been used worldwide for strengthening RC structures since 1990s and more recently being developed as an effective way of retrofitting concrete structures for high energy events such as impact (Bhatti et al. 2011) and blast (Buchana and Chen 2007). Figure 1-1 shows an example of how FRP retrofitted structure resisted blast load. CFRP retrofitted wall remained standing, whearas the un-retrofitted wall was practically reduced to debris (Ehsani and Peña 2009). Debonding at the FRP-to-concrete interface is one of the predominant failure modes under both static (Chen and Teng 2001) and dynamic conditions (Buchana and Chen 2007). Comprehensive research has been conducted for the static bond-slip relationship (Chen and Teng

2001; Lu et al. 2004; Lu et al. 2005) but the bond mechanics under high strain rates is not well understood. Debonding mostly occurs in the concrete adjacent to FRP unless the adhesive layer is very weak or proper surface treatment is not followed, so the concrete is of crucial importance for FRP-to-concrete bond behaviour.

(A)Test specimens ready for blast test. Un-retrofitted(left) and CFRP retrofitted(right)

(B)Test specimens after the blast test.

Figure 1-1 Blast protection provided to masonry walls by CFRP strengthening; 200 pounds (90.72 *kg*) of equivalent TNT placed at a height of 3 feet (0.91*m*) and a distance of 30 feet (9.14*m*) away from the walls (Ehsani and Peña 2009).

1.2 Aim of research

This thesis is chiefly concerned with the meso-scale modelling of FRP-to-concrete bond behaviour under both static and dynamic conditions using the local concrete damage model. A dynamic bond-slip model is then developed and applied in FRP strengthened concrete structures under impact and blast loading.

A particular focus of the research is the concrete dynamic property and its application because of its crucial importance for FRP-to-concrete bond. The thesis is also relevant for other meso-scale modelling of concrete such as concrete-to-steel bond.

1.3 Methodology

Impact or explosive tests are expensive to conduct with high facility and instrumentation costs. Also experimental research requires a comprehensive prediction and design plan before testing. However there is a lack of design guidelines of FRP retrofitted concrete structures for high energy events, so the finite element (FE) method is chosen as the principle method for this research. To study the FRP-to-concrete bond behaviour under high strain rates, explicit analysis in LSDYNA is used due to its advantages in modelling high energy events. The K&C (Karagozian & Case) concrete damage model (Malvar et al. 1997), the #72 material in LSDYNA developed by Karagozian & Case consulting engineering firm, is chosen due to its capability of reproducing the concrete behaviour under various stress conditions covering a number of important factors that are pertinent to the dynamic behaviours of concrete (Tu and Lu 2009). A slip rate dependent dynamic bond-slip model is derived based on the numerical predictions. Each step of the modelling is compared with test results for validation. A set of impact tests on FRP-to-concrete bond was conducted and the accuracy of the dynamic bond-slip model is

validated with the impact test results. On the basis of the research presented in this thesis, further empirical and numerical research is proposed.

1.4 Review of thesis contents

Chapter 2 reviews relevant literature including FRP strengthened concrete structures, FRP-to-concrete bond behaviour and concrete. A review of FRP retrofitting types is presented and relevant studies on FRP strengthened concrete structure in high strain rate events including impact and blast are assessed. Existing research on FRP-to-concrete bond-slip is reviewed and their limitations are discussed. Because debonding almost always occurs in the concrete, the knowledge of concrete and concrete modelling is reviewed in detail for both static and dynamic conditions. The chosen K&C concrete model in LSDYNA is also reviewed in detail.

Mesh sensitivity associated with material softening is a major issue in finite element (FE) modelling of concrete. A number of issues in meso-scale modelling of concrete are first investigated in Chapter 3 including loading schemes and the localization of concrete in both tension and compression under static condition.

Based on an extensive numerical investigation, an empirical model for the shear dilation factor is proposed in Chapter 4. It has been demonstrated that the model can satisfactorily simulate the debonding behaviour, in terms of the load-carrying capacity, the local bond-slip behaviour and mesh objectivity. These investigations led to the accurate modelling of the static FRP-to-concrete pull-off test.

The dynamic increasing factor (DIF) of concrete has been a subject of extensive investigation and debate for many years. It is now generally accepted that the compressive DIF is attributable to the dynamic structural effect (i.e. it is not a material property), whereas for concrete under tension the DIF is deemed to be governed by the material behaviour. Chapter 5 presents a numerical study on the uniaxial tension DIF, with a particular focus on how the DIF, irrespective of its cause, should be included in an appropriate manner in the FE modelling with a local concrete model. The present study has revealed that the FE predictions are both mesh and strain rate dependent if the normal concrete DIF under tension is included due to numerical strain localization. This leads to the development of a mesh-objective and strain rate independent DIF model for concrete under tension.

These models are then used to model the FRP-to-concrete bond behaviour in Chapter 6. A slip rate dependent dynamic bond-slip model is proposed based on numerical experiments with the pull-off test under different slip rates. A Mode II DIF versus slip rate relationship is first developed for different concrete strengths based on Mode II energy. Then the slip rate dependent DIF is then added to one of the best existing static bond-slip models (Lu et al. 2005) forming the dynamic bond-slip model.

To investigate the bond behaviour under high strain rate rather than static test, FRP-to-concrete bond impact test specimens were designed and tested under 3 different drop heights. The test results are presented in Chapter 7 which show that the FRP-to-

concrete bond strength does increase under impact loading, even though the bond is damaged to some extent due to the impact wave travelling through the interface.

The concrete DIF model in Chapter 5 and the dynamic bond-slip model in Chapter 6 are used to model both the impact test specimens in Chapter 8 and a concrete slab under blast loading in Chapter 9. The numerical results are shown to be in close agreement with the test results, validating the proposed models.

1.5 References

Buchana, P.A. and Chen, J.F. (2007), "Blast resistance of FRP composites and polymer strengthened concrete and masonry structures – A state-of-the-art review", *Composites Part B: Engineering*, 38(5-6):509-522.

Bhatti, A.Q., Kishi, N. and Tan, K.H. (2011), "Impact resistant behaviour of RC slab strengthened with FRP sheet", *Materials and Structures/Materiaux et Constructions,* 1:1-10.

Chen, J.F. and Teng, J.G. (2001), "Anchorage strength models for FRP and steel plates bonded to concrete", *Journal of Structural Engineering, ASCE*, 127(7):784–791.

Ehsani, M. and Peña, C (2009), "Blast loading retrofit of un-reinforced masonry walls with carbon fiber reinforced polymer (CFRP) fabrics, *Structure Magazine*, April: 16-20.

Lu, X.Z., Ye, L.P., Teng, J.G. and Jiang, J.J. (2004), "Mesco-scale finite element model for FRP sheets/plates bonded to concrete", *Engineering structures*, 27: 564-575.

Lu, X.Z., Teng, J.G., Ye, L.P. and Jiang, J.J. (2005), "Bond–slip models for FRP sheets/plates bonded to concrete", *Engineering Structures*, 27:920–937.

Malvar, L.J., Crawford, J.E., Wesevich, J.W. and Simons, D. (1997), "A plasticity concrete material model for DYNA3D", *International Journal of Impact Engineering*, 19(9-10): 847-873.

Teng, J.G., Chen J.F., Smith, S.T. and Lam, L. (2002), FRP Strengthened RC Structures, John Wiley &Sons Ltd.

Tu, Z.G. and Lu, Y. (2009), "Evaluation of typical concrete material models used in hydrocodes for high dynamic response simulations", *International Journal of Impact Engineering*, 36(1):132-146.

Chapter 2 Literature review

2.1 Introduction

This chapter reviews the relevant background literature research on fibre-reinforced polymer (FRP) strengthened concrete structures, FRP-to-concrete bond behaviour and concrete constitutive models.

A review of FRP retrofitting methods is presented in Section 2.2, and relevant studies on FRP strengthened concrete structure in high strain rate events are assessed in Section 2.3. Existing research on FRP-to-concrete bond-slip is reviewed and the limitation of these studies is discussed in Section 2.4. Because the debonding of FRP plate from concrete mostly happens in the concrete unless the adhesive is very weak or proper surface treatment has not been followed, the knowledge of concrete and its modelling is reviewed for basic static and advanced dynamic states. The chosen K&C local concrete model in LSDYNA is detailed in Section 2.5.

2.2 FRP strengthening methods

2.2.1 FRP composites

FRP is an advanced material and most of the development in its application in structural retrofitting has taken place in the last two decades. It has been found to be very effective way of replacing steel plate bonding. The main advantage of FRP is its high strength to weight ratio and high corrosion resistance. FRP plates can be 2 to 10 times stronger than steel plates, while their density is just about 20% of that of steel.

FRP composites are formed by embedding continuous fibres in a resin matrix. The resin matrix binds the fibre together. Based on different types of fibres, carbon, glass and aramid fibres, the FRP can be generally divided into carbon fibre reinforced polymer (CFRP), glass fibre reinforced polymer (GFRP), and aramid fibre reinforced polymer (AFRP) respectively (Teng et al. 2002).

The wide variety of strength and stiffness for different types of FRP are listed in Table 2-1 indicating CFRP composites have superior properties to GFRP and AFRP composites, but CFRP composites are more expensive than the latter. Most of the FRP materials have the similar stress-strain behaviour: linear elastic up to final brittle rupture when subject to tension.

Table 2-1 Typical mechanical properties of CFRP, GFRP and AFRP composites (Head 1996)

FRP types	Fibre weight ratio (%)	Density (kg/m^3)	Young's modulus (GPa)	Tensile strength (MPa)
CFRP	65-75	1600-1900	120-250	1200-2250
GFRP	50-80	1600-2000	20-55	400-1800
AFRP	60-70	1050-1250	40-125	1000-1800

2.2.2 Flexure strengthening of concrete beams

Flexural strengthening of RC beams using FRP is generally by bonding an FRP plate to the soffit of the beam shown in Figure 2-1.

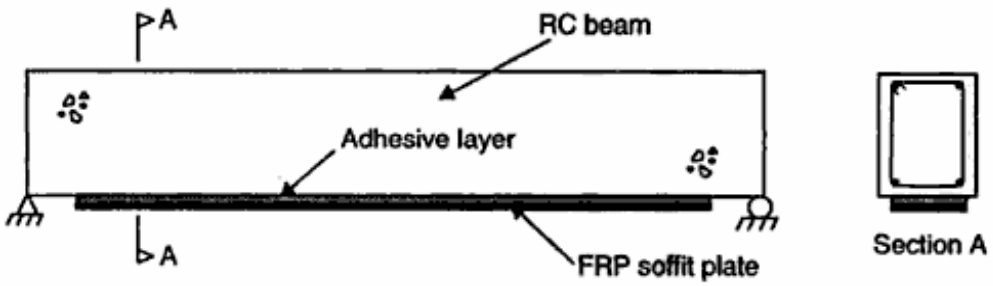

Figure 2-1 FRP flexure strengthening of RC beam (Teng et al. 2002)

Before strengthening, the surface of the RC beam must be prepared by removing the weak surface layer of the concrete and exposing the concrete aggregate to improve the bond with FRP (Teng et al. 2002). Strong adhesives are available for FRP plate bonding, and their strength generally exceeds that of concrete so failure in the adhesive is rare. But if adhesive layer is very weak or proper surface treatment has not been followed, the failure may happen in the adhesive layer.

The failure modes of the FRP flexure strengthened RC beams include FRP rupture, crushing of compressive concrete, shear failure, concrete cover separation, plate-end interfacial debonding, intermediate flexural crack-induced interfacial debonding and intermediate flexural shear crack-induced interfacial debonding (Teng et al. 2002).

2.2.3 Shear strengthening of RC beams

Shear strengthening methods for preventing shear failure of beams with FRP includes: bonding FRP to the sides of a beam only, bonding FRP U jackets to both the sides and the tension side of the beam, and wrapping FRP around the whole cross-section of a beam presented in Figure 2-2.

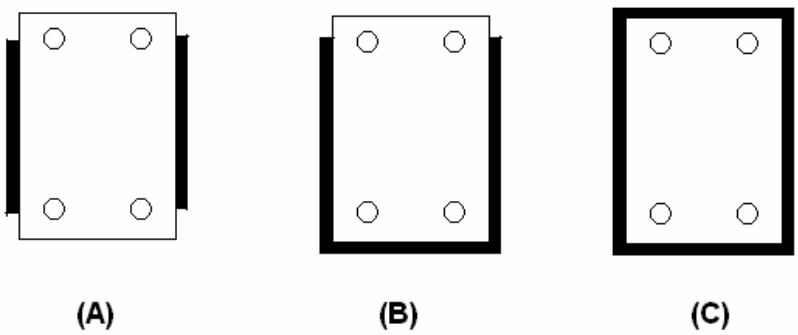

Figure 2-2 Shear strengthening schemes: (A) Side strengthening; (B) U jacketing; (C) wrapping

The failure modes of the FRP shear strengthened RC beams can be generally divided into 3 types: RC beam shear failure with FRP rupture, shear failure without FRP rupture, shear failure due to FRP debonding (Teng et al. 2002).

2.2.4 Flexure strengthening of slabs

The basic procedure of flexure strengthening of slabs using FRP is to bond FRP plate to the tension face of the slab which is similar to the strengthening method of RC beam. Intermediate crack-induced debonding and plate-end interfacial debonding are normally observed (Teng et al. 2002).

Compression face retrofitting is also normally used for slab strengthening for increasing the ductility of the section as plating the compression face reduces

compressive force in the concrete. Debonding of compression face occurs through either plated end debonding or interface shear (Oehlers et al. 2008)

2.2.5 Strengthening of columns

FRP wrapping is the most commonly used technique for column strengthening and the typical FRP wrapping methods for RC column are presented in Figure 2-3.

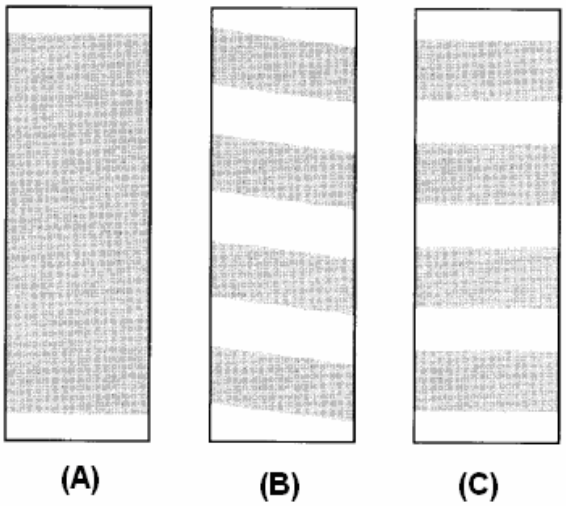

Figure 2-3 FRP wrapping methods for RC columns: (a) full wrapping using FRP sheets; (b) partial wrapping using FRP straps in a continuous spiral; (c) partial wrapping using FRP straps in discrete rings (Teng et al. 2002).

When an FRP-confined column is subject to axial compression, the concrete expands laterally and its expansion is confined by the FRP. The concrete strength is increased due to the confinement. FRP is subject to tension in the hoop direction. FRP rupture failure occurs when the hoop tensile strength is reached. FRP rupture failure mode has been reported for the majority of existing test on FRP-confined columns (Teng et al. 2002).

2.3 FRP strengthened concrete structures in high strain rate events

FRP strengthening for RC structures has been used world wide since the early 1990s and more recently being developed as an effective way of retrofitting concrete structures for high energy events. The analytical and empirical review of this area is given as follows:

2.3.1 Analytical research on FRP strengthened structure under high strain rates

Several guidelines are available for the FRP retrofitting of RC structures for monotonic and seismic loading (Mosallam and Teng 2003; Teng et al. 2003; Oehlers and Seracino 2004; Oehlers et al. 2008; Teng et al. 2006). However, no advice is provided from these guidelines for retrofitting RC structures against high energy events, i.e. blast and impact, due to the complexity of the problem where too many variables exist and experiments alone do not lead to effective design methods.

The main characteristics of impulsive loads induced by blast or impact are a high loading rate and a very short period of application that results in high material strain rates. Current design guidelines for structural response analysis under high energy events such as TM5 (1990) and ASCE (1997), still use single–degree-of-freedom (SDOF) systems to perform dynamic analysis. These guidelines are for general structures but no advice is provided for retrofitted RC structures against impulsive

load. Wu et al. (2009b) formulates a layered model that allows for both FRP strengthening and the consideration of strain rate effects on the blast resistant capacity of flexural structural members. It is incorporated into a SDOF model for dynamic analyses. However, the SDOF model is only sufficient for analyzing the peak response of the structure under non-oscillatory loads. An in-depth understanding of the structural behaviour under high energy events is required.

Although the finite element (FE) method based on continuum mechanics approaches can be used to analyze large scale structural response to blast, it is still rarely used in design because of its perceived complexity and expense due to the numerous difficulties and challenges involved in modelling bond between FRP and concrete (Wu et al. 2009b).

Perfect bond has been normally assumed in FE modelling (Nam et al. 2010; Schmidt and Cheng 2009). But the application of the perfect bond is conditional that debonding occurs in the concrete layer, so the concrete dynamic properties are properly captured and the FE mesh should be close to or smaller than the normal debonding depth, which is approximately 2-5mm (Lu et al. 2004). For computational cost consideration, perfect bond modelling is normally suitable for the analysis of FRP-to-concrete bonded test joints, not for structural elements such as beams, columns or slabs, when the element size requirement is in meso-scale. A bond-slip model is used for solving these problems so that a layer of interface element describing the FRP-to-concrete bond mechanics can be employed and macro-scale elements could be used in FE modelling. For modelling large scale structures

strengthened with FRP under high strain rates, there is a lack of comprehensive dynamic bond slip model to properly capture the FRP-to-concrete bond behaviour under high strain rates.

A dynamic bond-slip model to capture the FRP-to-concrete bond behaviour under high strain rates is investigated in the thesis. Before doing experimental and numerical research on FRP-to-concrete bond behaviour under high strain rates, the existing empirical research on FRP strengthened structures under blast and impact load is reviewed below.

2.3.2 Empirical research on FRP strengthened structure under high strain rates

2.3.2.1 FRP strengthened concrete structure under blast

Buchan and Chen (2007) presents a comprehensive review of FRP strengthened concrete and masonry structure in blast events, which is classified with different RC or masonry structure types and different strengthening methods as well as choice of retrofitting materials. Buchan and Chen (2007) have indicated FRP and polymer retrofitting can significantly increase the blast resistance of a structure, by increasing the structural strength and ductility plus reducing fragmentation.

Razaqpur et al. (2007) did experiments on two-way concrete slabs strengthened with GFRP under blast load. Eight 1000x1000x70*mm* slabs were made of 40 *MPa* concrete and reinforced with top and bottom steel meshes. Four slabs were retrofitted with adhesively bonded 500*mm* wide GFRP laminate strips on both faces, one in

each direction parallel to the panel edges. The panels were subjected to blast loads generated by the detonation of either 22.4kg (scaled distance 1.137 $m/kg^{1/3}$) or 33.4kg (scaled distance 0.995 $m/kg^{1/3}$) ANFO explosive charge located at a 3m standoff. Razaqpur et al. (2009) did another series of experiments with the same concrete panels and same explosive charge/stand-off distance as Razaqpur et al. (2007). The only difference was the strengthening material was CFRP. It was found that in the cases 22.4 kg ANFO the retrofitted panel performed better than the companion un-retrofitted panel. The post-blast static strength of both the GFRP and CFRP retrofitted slab was approximately 75% higher than that of the companion un-retrofitted slabs. However, some of the retrofitted panels completely disintegrated while none of the un-retrofitted panels suffered such catastrophic damage, and some of the retro fitted panels perform better than un-retrofitted for the cases of 33.4 kg ANFO. It can be discovered that when it is close-in blast, i.e. scaled distance smaller close or smaller than 1 $m/kg^{1/3}$, minor changes in material properties, test set-up and the surrounding environment could produce significantly different responses. So the test repeatability is poor in such cases. Even for the cases of 22.4 kg ANFO, the repeatability regarding the measured blast pressures, impulses and slab deformation is not good. Assessing the blast response and resistance of reinforced concrete elements by using actual explosives is a complex task, and it needs to be carefully justified before doing tests.

Ha et al. (2011) also did experiments on two-way concrete slabs strengthened with a new retrofit composite material proposed by combining highly stiff and strong CFRP

with highly ductile Polyurea (PU) on the compression side of the slabs. Nine 1000x1000x150mm RC panel specimens retrofitted with CFRP, PU, or hybrid composite sheets were blast tested. The blast load was generated by detonating a 15.88kg ANFO explosive charge at 1.5m standoff distance (scaled distance 0.596 $m/kg^{1/3}$). In the case of the retrofitted specimens, CFRP had spalling and serious damage at the centre and the edge of the specimen. In case of the Polyurea specimen, it shows more spalling and cracks compared with CFRP specimen. Hybrid CFRP/Polyurea specimens showed small damage on the top surface, but larger damage was developed on the side surface compared to other specimens due to the better retrofitting effect of hybrid CFRP/Polyurea. The tests in Ha et al. (2011) were still close-in blast, and the scaled distance is even smaller than the 33.4kg ANFO in Razaqpur et al. (2007) and Razaqpur et al. (2009). All the compressive side only retrofitted specimens performs better than the un-retroffited ones in Ha et al. (2011), but some of the tensile and compressive sides retrofitted slab completely failed under the blast load while none of the control slabs experienced complete failure under similar load in Razaqpur et al. (2007) and Razaqpur et al. (2009), indicating the blast resistance of structures that are loaded in the impulse realm can be effectively increased by increasing their ductility rather than their strength.

Wu et al. (2009a) did a series of blast testing of ultra-high performance fibre and FRP-retrofitted one-way concrete slabs with normal reinforced concrete (NRC) slabs tested as control specimens. 2000x1000x100mm concrete slabs with CFRP retrofitted on the compressive side of the slabs were tested under different explosive charges and stand-off distances. Testing indicated that CFRP and polymer retrofitting can

significantly reduce the mid-span deflection of the specimens. Wu et al. (2009b) also did analytical investigation on FRP strengthened concrete slabs under impact load with a layered capacity analysis indicating the element layer division through the specimen thickness should be sufficient so that it allows for varying strain rates at different levels of the cross-section has been developed for calculating the dynamic capacity of FRP plated RC members.

2.3.2.2 FRP strengthened concrete structures under impact

White et al. (2001) presented experiments investigation aiming effects of strain rate on the behaviour of 3*m* long, 150*mm* wide and 300*mm* high RC beams strengthened with CFRP laminates on the tensile face of the specimens. The stroke rates ranged from 0.0167*mm/s* (slow rate of loading) to 36*mm/s* (fast rate of loading). This induced a strain rate in the CFRP of 2.96 $\mu\varepsilon/s$ (slow rate) to 6,930 $\mu\varepsilon/s$ (fast rate). It was observed that strengthening with CFRP increases the flexural capacity and stiffness but reduced the energy absorption and ductility. However ductility and the mode of failure were not directly affected by the change in loading rate. The magnitude of these changes is dependent on the amount of CFRP reinforcement, steel reinforcement, and the mode of failure.

Tang and Saadatmanesh (2005) did both analytical and experimental studies of FRP-strengthened concrete beams under impact loading. 27 concrete beams with 203x95*mm* cross section and two different spans, 1.98 and 2.9*m*, were tested to investigate the behaviour of beams strengthened with FRP laminates on the tensile face of the specimen under impact loading. The test results revealed that bonding

composite laminates to concrete beams could significantly improve the performance of this type of structure to resist impact loading while reducing the number of cracks, crack widths, and the maximum deflection. The residual stiffness of the strengthened beam after first impact was two to three times that of an un-retrofitted beam, and the maximum deflection decreased by 30 to 40%.

Bhatti et al. (2011) used falling 300*kg* steel striker to investigate the impact resistance of RC slabs strengthened with AFRP sheets and CFRP sheets to the back of the slab. A total of 12 RC slabs with 1650x1650x150*mm* geometry were used for these experiments. The results indicated the impact resistance of the RC slabs can be improved by attaching a strengthen FRP sheet to the back surface and the load bearing mechanism of RC slabs depends on the loading type and strengthening volume of the FRP sheet, and also the impact response behaviour of an RC slab is greatly affected by the loading history.

Khalighi and Banthia (2011) tested concrete specimens with Sprayed FRP under impact loading. A novel 550× 150×150*mm* notched specimen was developed and a 75*mm* wide strip of Sprayed FRP was applied to strengthen the specimen. Results showed that sand blasting is the most effective surface preparation method resulting in the highest bond strength values. Their results indicate that the FRP–concrete bond is highly strain sensitive, and in general the bond strength increases and the fracture energy decreases under higher rates of strain. Untreated specimens are shown to be more strain-rate sensitive than the surface treated ones.

2.3.3 Summary

According to the literature review, strengthening with FRP is an effective way of increasing the flexural capacity and stiffness to resist high strain rate events of concrete structures including impact and blast. Experimental observations also indicate that the rate sensitivity is very important. SDOF analysis is not sufficient enough for understanding the FRP strengthened structure response under impulsive loads, and FE modelling is a good way of carrying out further investigation. The dynamic bond behaviour between FRP and concrete is of crucial importance for numerical application. However there is a lack of comprehensive dynamic bond slip model to properly capture the FRP-to-concrete bond behaviour under high strain rates, and this is the main issue of current study. The existing research on FRP-to-concrete bond slip behaviour is reviewed in the next section.

2.4 FRP-Concrete bond slip behaviour

2.4.1 Bond-slip behavior

Extensive experiments have demonstrated that concrete structures strengthened with externally bonded FRP are susceptible to failure by FRP debonding, through a variety of mechanisms (Smith and Teng 2002) and thus the bond of FRP laminates to concrete has been the subject of numerous experimental tests and theoretical models, of which Chen and Teng (2001) gave a comprehensive review. The bond behaviour

of an FRP laminate bonded to a concrete element (e.g. concrete beam and etc.) across an existing crack is similar to that in a simple shear test on FRP to concrete bonded joints, where the FRP plates are pulled presented in Figure 2-4 .

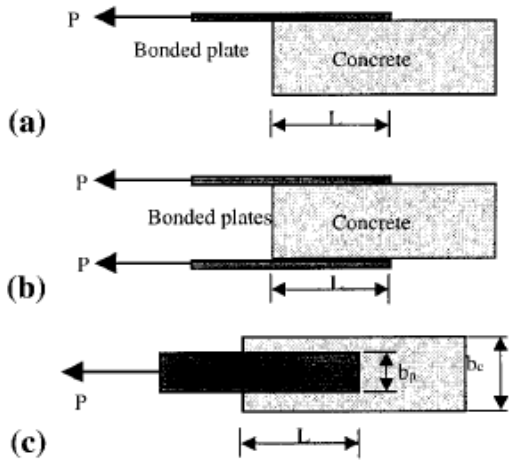

Figure 2-4 Single and Double Shear Tests: (a) Single Shear Test; (b) Double Shear Test; (c) Plan (Chen and Teng. 2001)

Various pull-out tests under static load with low loading and strain rates have been done both experimentally and numerically for obtaining bond-slip models. Both Chen and Teng (2001) and Yuan et al. (2004) indicated that the main parameters governing the local bond-slip behaviour in pull tests are the concrete strength, the bond length, the FRP axial stiffness, the FRP plate to concrete width ratio, the adhesive strength and the effective bond length L_e in mm (Equation (2-1)), beyond which an extension of the bond length cannot increase the ultimate load (Chen and Teng 2001).

$$L_e = \sqrt{\frac{E_p t_p}{\sqrt{f_c'}}} \qquad (2\text{-}1)$$

where E_p is the Young's modulus of the FRP plate in MPa ; t_p is the thickness of FRP plate in ; f_c' is the unconfined cylinder compressive strength of the concrete in MPa .

If the width of the bonded plate is smaller than that of the concrete member, the force transfer from the plate to the concrete leads to a non-uniform stress distribution across the width of the concrete member. A smaller FRP plate width b_p compared to concrete prism width b_c may result in a higher shear stress in the adhesive at failure, attributed to the contribution from the concrete outside the bond area. Chen and Teng (2001) proposed the ultimate bond strength was linear to β_w according to the test data according to the test data (Equation (2-2)).

$$\beta_w = \sqrt{\frac{2 - b_p / b_c}{1 + b_p / b_c}} \tag{2-2}$$

The ultimate load of the pull-off test is presented in Equation (2-3) and the length effect factor β_L related to the real bond length L and effective bond length is presented in Equation (2-4) (Chen and Teng 2001).

$$P_u = 0.427 \beta_w \beta_L \sqrt{f_c'} b_p L_e \tag{2-3}$$

$$\beta_L = \begin{cases} 1 & if \quad L \geq L_e \\ \sin \dfrac{\pi L}{L_e} & if \quad L < L_e \end{cases} \tag{2-4}$$

2.4.2 Static bond-slip models

For prediction of the FRP-concrete bond behavior under various loading conditions as well as the whole structure response, a bond-slip model, that is the bond stress versus slip relationship, is needed to describe the bond behavior between the FRP and concrete.

Lu et al. (2005) gave a comprehensive test database and comparison of the existing bond strength models and indicating only Neubauer and Rostasy (1997) and Chen and Teng (2001) before their work considered all the factors including concrete strength, FRP plate stiffness, effective bond length, and width ratio before his work. Chen and Teng (2001) did not propose a bond-slip relationship which could be directly introduced in to numerical application but had already been a very good prediction for bond strength and ultimate loads compared to large mount of experiment results. Chen and Teng (2001) had set the basis for the static bond-slip model proposed by Lu et al. (2005). The author produced the predictions of the bond strength models and the data of 118 test specimens listed in Lu et al. (2005) in Figure 2-5 and the standard deviation Δ to the desired value(test results) is presented in Table 2-2.

The standard deviation Δ in statistics is used here to justify which existing static bond-slip model should be used here as the basis of the dynamic bond-slip model.

$$\Delta = \sqrt{\frac{\sum_{i=1}^{n}(x-\bar{x})^2}{n}} \tag{2-5}$$

Δ is the standard deviation, of which the unit is the same as the sample x in the equation. $\bar{x}$ is the expected value or the average value. For the current application, x is the normalized ultimate load, which is equal to the analytical ultimated load calculated from the existing bond slip model according to Equation (2-6) divided by the ultimate load from the test measurement. $\bar{x}$ is set as 1(expected value). Because the standar4d deviation is calculated from the normalized values, the unit of Δ is, 1.

$$\tau_{\max} = \frac{P_u^2}{E_p t_p b_p^2 s_f} \tag{2-6}$$

where $\tau_{\max}$ is the peak value of the bond stress; P_u is the ultimate load at the FRP end from the load slip curves; E_P is the elastic Young's modulus of the FRP plate; t_p is the thickness of the FRP plate; b_p is the FRP plate width; s_f is the final slip of the bond-slip curves.

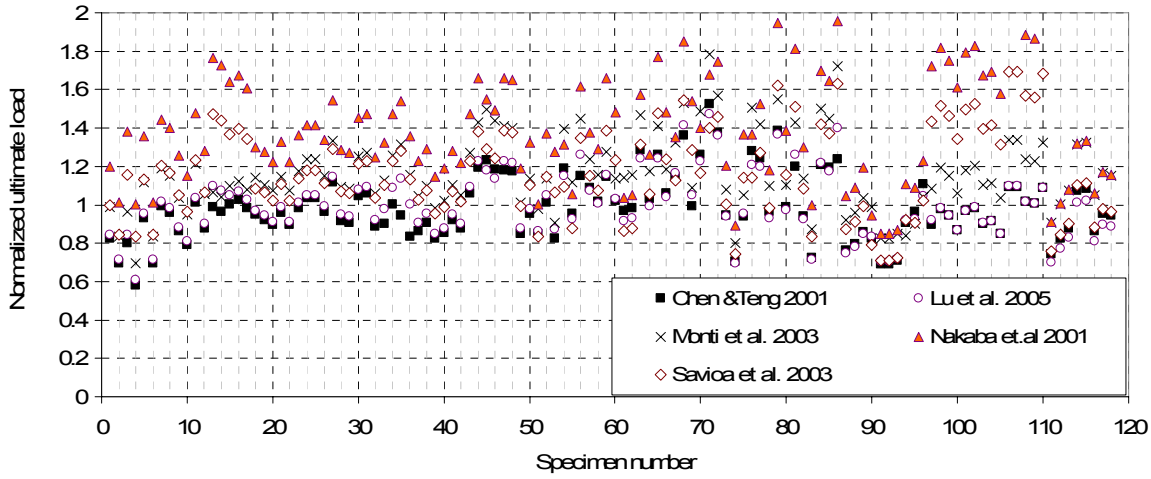

Figure 2-5 Normalized ultimate load predictions from bond strength models compared with test data

Table 2-2 Standard deviations for bond strength models in Figure 2-5

Models	Standard deviation Δ
Chen and Teng (2001)	0.165527335
Lu et al. (2005)	0.165061377
Monti et al. (2003)	0.255940034
Nakaba et al. (2001)	0.485593974
Savioa et al. (2003)	0.286571942

It can be seen that the Chen and Teng's (2001) model produced agreement with experimental results. The static bond-slip curves from Lu et al. (2005) give a similar standard deviation to Chen and Teng (2001). It is better than other bond-slip models.

Lu et al. (2004) indicated there were two approaches to the simulation of debonding in FRP-strengthened RC structures using a nonlinear FE model. One approach is to employ a layer of interface elements between the FRP and the concrete, in which

debonding is simulated as failure of the interface elements. This method is based upon an existing bond-slip model. In the second approach, the use of interface elements is avoided; instead, debonding is directly simulated by modelling the cracking and failure of concrete elements at a few millimetres distance from the adhesive layer. The bond-slip model is avoided. Indeed, the second approach has the capability of predicting the bond-slip relationship for use in a model following the first approach (Lu et al. 2004). From the FE results of the shear tests, the bond-slip curve of a point along the interface can be obtained by plotting the smoothed bond stress value at that point versus the slip of the point, and this was the way Lu et al. (2004) and Lu et al. (2005) have proposed the static bond-slip model presented in Equations (2-7) to (2-14).

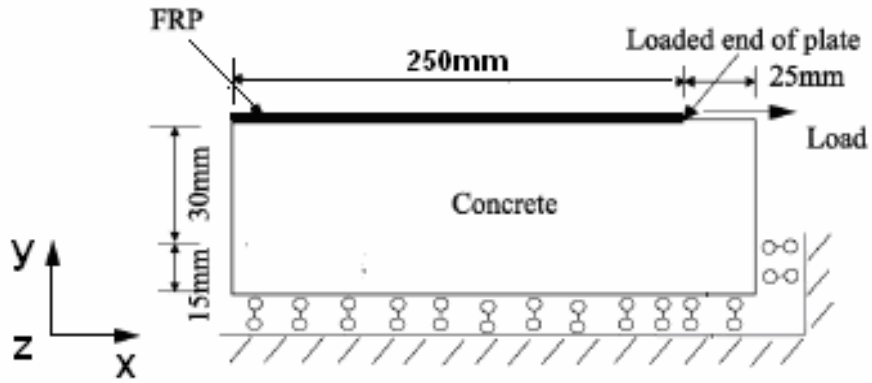

Figure 2-6 Pull-off test FE model geometry (Lu et al. 2004)

$$\tau_{\max\_s} = 1.5\beta_w f_t \quad (2\text{-}7)$$

$$s_{0s} = 0.0195\tau_{\max\_s} f_t \quad (2\text{-}8)$$

$$G_{fs}^{II} = 0.308\beta_w^2\sqrt{f_t} \quad (2\text{-}9)$$

$$s_{fs} = 2G_{fs}^{II} / \tau_{\max\_s} \quad (2\text{-}10)$$

$$f_t = 0.53\sqrt{f_c'} \tag{2-11}$$

$$\tau = \tau_{\max\_s} \frac{s}{s_{0s}} \text{ if } s \le s_{0s} \tag{2-12}$$

$$\tau = \tau_{\max\_s} \frac{s_{fs} - s}{s_{fs} - s_{0s}} \text{ if } s_{0s} < s \le s_{fs} \tag{2-13}$$

$$\tau = 0 \text{ if } s > s_{fs} \tag{2-14}$$

where $\tau_{\max\_s}$ is the maximum value of the static bond stress and s_{0s} is the corresponding slip; s_{fs} is the slip at failure where bond stress τ drops to zero; f_t is the concrete tensile strength; f_c' is the concrete cylinder unconfined compressive strength; G_{fs}^{II} is the fracture energy equal to the area under the bond-slip curve.

2.4.3 Dynamic bond-slip model

Compared to the vast amount of investigation on bond slip models under static load, little work has been done for bond behaviour under blast loads. It has also been observed that debonding on the FRP-concrete interface is one of the predominant failure modes under dynamic loadings. However, most of previous studies were either experimental (Tarapada and Debabrata 2006) with limited analytical investigation (De Lorenzis and La Tegola 2005), or macro-scale numerical simulations focused on the global structural behaviour (Crawford et al. 2001). Little attention has been paid to the critical FRP-concrete interfacial bond behaviour under dynamic loadings. The dynamic bond behaviour could be very different from that

under static or quasi-static loadings because of the effects of higher strain rate, concrete deterioration due to the incident or reflected stress wave propagation before debonding mechanics, and fracture mechanics under impulsive load. Accurate quantification of these effects by experiments is very demanding both economically and technically, especially for high loading rate scenarios such as impact and blast, where advanced finite element (FE) simulations can play a viable role.

De Lorenzis and La Tegola (2005) analysed the bond behaviour for high energy invents. They developed an analytical solution for the bond-slip model under impulsive loading, which expresses the impulsive to static maximum stress ratio $\tau_{\max} / \tau_{\max\_s}$ as a function of the ratio of the total duration of the impulse propagation time in the total FRP bond length to the one in the effective bond length t_a / t_e. It was assumed that the bond length was significantly larger than the effective bond length. The analysis was restricted to the linear region only of the bond-slip law without considering softening, nonlinearity, and it was analyzed in a static framework due to the assumption that the effect of inertia forces was neglected. The analytical solution achieved by De Lorenzis and La Tegola (2005) is greatly restricted by these simplified assumptions.

The bond behaviour of an FRP laminate bonded to a concrete element across an existing crack is similar to that in a simple shear test on FRP-to-concrete bonded joints, where the FRP is pulled (De Lorenzis and La Tegola 2005), so it is possible to develop a bond-slip model under different slip rates using the pull-off test by properly modelling the concrete with dynamic effects. Concrete modelling is the

main aspect of modelling debonding of FRP from concrete prism as the debonding mostly happens in a thin layer of concrete adjacent to the FRP (Lu et al. 2004). Therefore, in the following section, the review on concrete and concrete models is presented.

2.5 Concrete and concrete constitutive models

2.5.1 Crack band theory

Concrete is a quasi-brittle material. In classical fracture mechanics, three distinctive cracking modes are defined, namely, a) Mode I: opening mode, b) Mode II: shearing mode, and c) Mode III: out of plane shear mode. As far as concrete is concerned, Mode I is the only clear type of crack propagation mode. CEB-FIP (1993) recommended a standard for describing the concrete Mode I cracking as a material property, which is related to the concrete strength and aggregate size (CEB-FIP 1993). Mode II and III are complex failure modes, which can hardly be realized in an experiment. There is no pure shear test in real world; even the failure modes in the popular four-point shear beam and double-edge notched concrete specimens are more or less mixed modes. The experimental results reported in the literature thus far have not been very promising, and it seems that in Mode II fracture experiments the cracks still tend to nucleate and propagate in Mode I (Van Mier 1997). It is also not clear as to whether there exists an independent measure of shear mode fracture energy.

The fracture energy, G_f^I, is defined as the energy consumed in the formation and opening of all micro-cracks per unit area of plane (Bazant and Oh 1983). The concept of damage is usually associated with a zone of certain characteristic width, w_c, which is generally taken as three times the maximum aggregate size (Bazant and Oh 1983):

$$w_c \approx 3d_a \tag{2-15}$$

where w_c is the crack-band width with physical meaning, d_a is the maximum aggregate size.

In CEB-FIP (1993), the concrete Mode-I fracture energy G_f^I (in *N/mm*) is considered as a material constant, and is related to the concrete unconfined compressive strength $f_c^{'}$ (in *MPa*) and maximum aggregate size, as:

$$G_f^I = \alpha \left(\frac{f_c^{'}}{10} \right)^{0.7} \tag{2-16}$$

where α is a coefficient related to the maximum aggregate size, e.g. for a maximum aggregate size of 16mm, α =0.3.

2.5.2 Local and non-local concrete models

Physically, not only G_f^I, f_t (tensile strength), but also w_c are independent material parameters that can differ from concrete to concrete (Bazant and Oh 1983). However

in FE modelling with a local concrete material model, the crack band width is dominated by the element characteristic length h_c instead of the physical w_c, and this is because in an FE model the tensile failure would normally localize in a single element.

Bazant and Oh (1983) discussed in detail the FE modelling cases with element size larger than w_c. The tangential strain-softening modulus E_t based on a linear softening assumption is expressed as a function of the element characteristic length to ensure that the fracture energy in each element resembles a material constant:

$$E_t = (\frac{1}{E_c} - \frac{2G_f^I}{f_t^2 h_c})^{-1} \tag{2-17}$$

where E_c is the Young's modulus and f_t is the tensile strength of the concrete. An upper limit of the element size exists, as (Bazant and Oh 1983):

$$h_c < \frac{2G_f^I E_c}{f_t^2} \tag{2-18}$$

The limiting case $h_c = 2G_f^I E_c / f_t^2$ corresponds to $E_t^{-1} = 0$ or $E_t \to -\infty$, which amount to a sudden (vertical) stress drop.

According to Kwak and Filippou (1990), when the element size is smaller than three times the maximum aggregate size, the crack strain can be treated as uniform in the element when the smeared crack model is used. Hence, to maintain a given fracture energy it requires:

$$\int \sigma d\varepsilon = \frac{G_f^I}{h_c} \tag{2-19}$$

where h_c is the element characteristic length, $\int \sigma d\varepsilon$ stands for the area under the stress strain curve for the concrete under uniaxial tension.

The only way to maintain the physical meaning of when the element size is smaller than the physical crack band width is to introduce a non-local continuum scheme (Pijaudier-Cabot and Bazant 1987) into the concrete model, as illustrated in Figure 2-7. With a non-local concrete model the FE characteristic length can span a number of elements; however, this type of algorithm is computationally very expensive. Therefore, use of a local material model is still the first choice in the FE modelling.

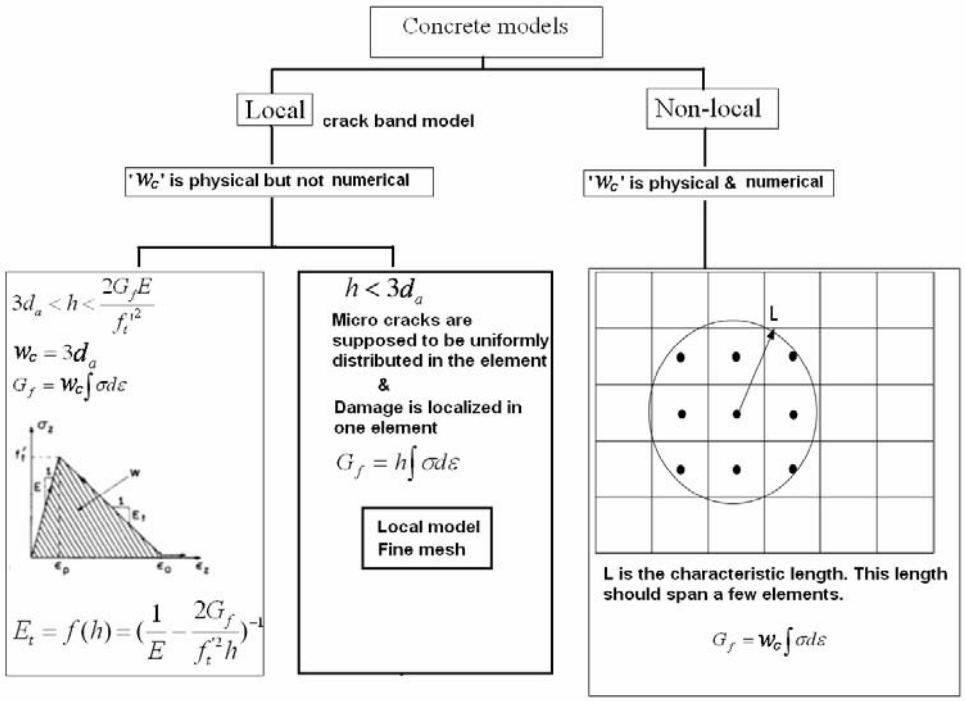

Figure 2-7 Local and non-local concrete models

The difference between local and non-local is the damage of the local concrete model tends to happen in every single element but with non-local continuum schemes the numerical damage localization does not happen in single element but several elements depending on the crack band width defined when the loading/strain rate is lower, e.g. static state. It seems the non-local concrete model is a better choice because the crack band width is a concrete material property which corresponds to approximately three times the maximum aggregate size Bazant and Oh (1983) and it is better to model concrete fracture in such a crack band accordingly. However it is obtained from the static test and with dynamic/impulsive load the crack band width may be changed, and according to the best knowledge of the author, there is no such a systemic conclusion on this based on plenty of experimental investigations. Furthermore, even for the static modelling, the real cracking of the concrete tends to be 2-5 *mm* width for some tests, e.g. the debonding tests (Lu et al. 2004). That is already smaller than the regular aggregate sizes, e.g. 8*mm*. For the local failure in such a small width, some of the macro material properties such as crack band equal to three times the maximum aggregate size has little meaning here either for modelling or physics. Aggregate may give some effect but it may mostly come from the mortar. Therefore even for static state, it is still unknown that which non-local crack band width should be used in such cases. Another reason why non-local model is not widely used is the heavy computation. When the users capture the debonding failure of the bond behaviour, the mesh should be at least one order smaller than the physical cracking width. The FE modelling process would be an endless process with non-local crack band width set as only 5 times the current element sizes according to

the static numerical attempting. If the user set the non-local characteristic length more than 10 times the element size, the memory size requirement according to current normal computation effort would not be sufficient according to the current numerical model. Due to the low computational cost with a sufficient reliability of the results (Scotta et al. 2001) local concrete models are still the main option in FE modelling because it is an economical method compared to non-local. Therefore the meso-scale numerical investigation based on local concrete model with crack band theory for both static and dynamic states is significant in FE.

2.5.3 Dynamic increasing factor (DIF)

For reinforced concrete structures subjected to rapid loading, e.g., impact and blast, high strain rates in a range of 1 to 10^3 s^{-1} will typically occur. At such high strain rates, the apparent strength of concrete can increase significantly (Malvar and Crawford 1998) as compared to its quasi-static counterpart. According to experimental observations, the dynamic increase factor (DIF), i.e. the ratio of the dynamic to static strength, is a function of strain rate (Malvar and Crawford 1998).

The CEB-FIP (1993) DIF curve for concrete in compression is expressed as:

$$DIF = f_c / f_{cs} = \left(\frac{\dot{\varepsilon}}{\dot{\varepsilon}_S} \right)^{1.026\alpha_S} \quad \text{for } \dot{\varepsilon} \le 30 s^{-1} \tag{2-20}$$

$$DIF = f_c / f_{cs} = \gamma_S \left(\frac{\dot{\varepsilon}}{\dot{\varepsilon}_S} \right)^{1/3} \quad \text{for } \dot{\varepsilon} > 30 s^{-1} \tag{2-21}$$

where $\dot{\varepsilon}$ is the strain rate (ranging from 30×10^{-6} to $300\,s^{-1}$), $\dot{\varepsilon}_S$=$30\times10^{-6}\ s^{-1}$ is the reference static strain rate, f_c is the dynamic compressive strength at $\dot{\varepsilon}$, f_{cs} is the static compressive strength at $\dot{\varepsilon}_S$, and

$$\log\gamma_s = 6.456\alpha_s - 2 \tag{2-22}$$

$$\alpha_s = 1/(5+9f_{cs}/f_{co}) \tag{2-23}$$

$$f_{co} = 10MPa = 1450\ psi \tag{2-24}$$

For concrete in tension and within a strain rate in the range of 10^{-6} to $160\,s^{-1}$, a Modified CEB-FIP curve as proposed by Malvar and Crawford (1998) is often adopted for its improved accuracy compared with the original CEB-FIP (1993) curve:

$$DIF = f_t / f_{ts} = \left(\frac{\dot{\varepsilon}}{\dot{\varepsilon}_S}\right)^{\delta} \text{ for } \dot{\varepsilon} \le 1s^{-1} \tag{2-25}$$

$$DIF = f_t / f_{ts} = \beta\left(\frac{\dot{\varepsilon}}{\dot{\varepsilon}_S}\right)^{1/3} \text{ for } \dot{\varepsilon} > 1s^{-1} \tag{2-26}$$

where f_t=dynamic tensile strength at $\dot{\varepsilon}$, f_{ts}=static tensile strength at $\dot{\varepsilon}_s=10^{-6}\ s^{-1}$ and

$$\log\beta = 6\delta - 2 \tag{2-27}$$

$$\delta = 1/(1+8f_{cs}/f_{co}) \tag{2-28}$$

$$f_{co} = 10MPa = 1450\ psi \tag{2-29}$$

However, the mechanisms governing the experimentally observed DIF remain to be a subject of much debate. The key issue is centralised about whether or not the DIF should be treated as an inherent material property, despite that in the widely-used CEB code (1993) the DIF has been introduced as a material property. It tends to be generally accepted that under "uniaxial" compression, the DIF is rather a dynamic structural effect than a material property. Several recent studies have demonstrated that the inertia-induced radial confinement makes a large contribution to the dynamic compressive strength enhancement (Li and Meng 2003; Lu et al. 2010; Zhang et al. 2009). When a high compression stress pulse is imposed to the specimen, the specimen tends to expand in the hoop direction, resulting in a radial inertia force which is equivalent to a confining stress, and subsequently increasing the axial strength of the concrete. As such, it is argued that the concrete DIF in compression should not be imposed at the material constitutive model level, i.e., it should be disabled or simply set as unity for material models that incorporate DIF for compression in a refined finite element analysis.

On the other hand, when concrete is under tension, the radial inertia force would change direction; and moreover, the effect of lateral (inertia) stress on the axial tensile strength is very different from that of confining stress on the axial compression. As a matter of fact, the concrete tensile failure is much more localized than that under compression. Furthermore, experimental observations have indicated that the DIF for tension can be considerably larger than for compression at a comparable strain rate. For example, for the class of 30-*MPa* concrete (static compressive strength $f_c' = 30\,MPa$), when the strain rate is $100\,s^{-1}$, the (apparent)

DIF is 8.0 and 2.3 for tension and compression, respectively. Such a difference is hardly explicable by the effect of inertia force theory. Some numerical studies, using the discrete element modelling (Hentz et al. 2004) or the finite element (FE) modelling (Lu and Li 2011), with comparison to dynamic tensile tests (direct, splitting or spalling), suggested that the DIF of the tensile strength observed in dynamic tensile tests could be a genuine material effect. Consequently, it is deemed to be rational to include the DIF for the dynamic tensile strength in the material descriptions in an analysis where tension plays a dominant role.

2.5.4 K&C concrete damage model

The finite element package LS-DYNA Explicit (LS-DYNA 2007) was employed in this study due to its capability in modelling high energy events such as blast and impact loadings. The concrete material was modelled by an enhanced version (material #72_Rel3 in LS-DYNA v971) of the K&C concrete damage model (Malvar et al. 1997). The model is regarded as one of the most comprehensive damage plasticity models for concrete-like materials in transient analysis codes including DIF (Tu and Lu 2009).

The model uses three independent strength surfaces, namely, an initial yield surface, a maximum failure surface and a residual surface with consideration of three stress invariants, I_1, J_2 and J_3. The compressive meridians of the three surfaces are defined independently as (Malvar et al. 1997).

$$\Delta\sigma_y = a_{0y} + \frac{p}{a_{1y} + a_{2y}} \text{ (initial yield failure surface)} \quad (2\text{-}30)$$

$$\Delta\sigma_m = a_0 + \frac{p}{a_1 + a_2} \text{ (maximum failure surface)} \quad (2\text{-}31)$$

$$\Delta\sigma_r = \frac{p}{a_{1f} + a_{2f}} \text{ (residual failure surface)} \quad (2\text{-}32)$$

where these functions of $\Delta\sigma_y$, $\Delta\sigma_m$ and $\Delta\sigma_r$ related to p are the three failure surfaces for the effective deviatoric stress ($\Delta\sigma = \sqrt{3J_2}$); and $p = I_1/3$ is the pressure. The coefficients $a_{0y}, a_{1y}, a_{2y}, a_0, a_1, a_2, a_{0f}, a_{1f}$ and a_{2f} can be determined from experiments (Malvar et al. 1997). During an analysis, the current failure surface is interpolated from the maximum failure surface and either the yield or the residual failure surface as:

$$\Delta\sigma = \eta\Delta\sigma_m + (1-\eta)\Delta\sigma_y \text{ when } \lambda \le \lambda_m \quad (2\text{-}33)$$

$$\Delta\sigma = \eta\Delta\sigma_m + (1-\eta)\Delta\sigma_r \text{ when } \lambda > \lambda_m \quad (2\text{-}34)$$

The damage accumulation is governed by a function $\eta(\lambda)$, which is defined as a series of (λ, η) pairs in the concrete model. This function increases from 0 at λ=0, to 1 at $\lambda = \lambda_m$, and then decreases to 0 as λ further increases. Here λ is the modified effective plastic strain (Malvar and Simons 1996; Malvar et al. 1997):

$$\lambda = \int_0^{\overline{\varepsilon^p}} \frac{d\overline{\varepsilon^p}}{r_f(1+p/r_f f_t)^{b_1}} \qquad for \qquad p \geq 0 \tag{2-35}$$

$$\lambda = \int_0^{\overline{\varepsilon^p}} \frac{d\overline{\varepsilon^p}}{r_f(1+p/r_f f_t)^{b_2}} \qquad for \qquad p < 0 \tag{2-36}$$

where $d\overline{\varepsilon^p} = \sqrt{(2/3)d\varepsilon_{ij}^p d\varepsilon_{ij}^p}$ is the effective plastic strain increment, f_t the quasi-static concrete tensile strength, r_f the rate enhancement factor from an unconfined uniaxial compression test, b_1 and b_2 the parameters controlling the softening part of the stress strain curves.

A scaled damage factor (SDF) is defined to measure the damage:

$$SDF = \frac{2\lambda}{\lambda + \lambda_m} \tag{2-37}$$

where λ_m is the value of λ at the maximum failure surface (η=1). λ is a positive non-decreasing variable: 0< SDF <1 means no damage, $SDF \geq 1$ damage with material softening, and SDF =2 full damage.

The above K&C model requires only the unconfined compressive strength $f_c^{'}$ to be specified with all other material parameters derivable.

2.6 Conclusions

FRP strengthening is an effective way of increasing the flexural capacity and stiffness to resist high strain rate events of concrete structures, i.e. impact and blast. The static bond-slip model should not be sufficient enough, and the rate sensitivity needs to be considered.

Based on the review of existing research on bond-slip model between FRP and concrete, there is a lack of an advanced dynamic bond-slip model. Because debonding mostly occurs in the concrete layer unless the adhesive is rather weak, for deriving dynamic bond-slip models from numerical analyses, the concrete modelling is of crucial importance.

Based on a detailed review on concrete and concrete models, the local concrete model K&C together with dynamic effects consideration in ANSYS-LSDYNA is chosen as the basis of the numerical investigation of the dynamic bond-slip model in this thesis.

2.7 Reference

Bazant, Z. P., and Oh, B. H. (1983), "Crack band theory for fracture of concrete", *Materials and Structures (RILEM, Paris)*, 16: 155–177.

Bhatti, A.Q., Kishi, N. and Tan, K.H. (2011), “Impact resistant behaviour of RC slab strengthened with FRP sheet”, *Materials and Structures*, 1-10.

Buchana, P.A. and Chen, J.F. (2007), “Blast resistance of FRP composites and polymer strengthened concrete and masonry structures – A state-of-the-art review”, *Composites Part B: Engineering*, 38(5-6):509-522.

CEB-FIP (1993), Model Code 90, Lausanne.

Chen, J.F. and Teng, J.G. (2001), “Anchorage strength models for FRP and steel plates bonded to concrete”, *Journal of Structural Engineering*, 27(7):784-791.

Crawford, J. E., Malvar, L. J., Morrill, K. B. and Ferritto, J. M. (2001), "Composite Retrofits to Increase the Blast Resistance of Reinforced Concrete Buildings", Proceedings of the 10th International Symposium on Interaction of the Effects of Munitions with Structures, San Diego, CA, May.

De Lorenzis, L. and La Tegola, A. (2005), "Bond of FRP laminates to concrete under impulse loading: a simple model", Proc. International Symposium on Bond Behaviour of FRP in Structures (BBFS 2005), Hong Kong, China: 503-508.

Ha, J.H., Yi, N.H., Choi, J.K. and Kim, J.H.J. (2011), “Experimental study on hybrid CFRP-PU strengthening effect on RC panels under blast loading”, *Composite Structures*, 93:2070–2082.

Head, P.R. (1996), “Advanced composites in civil engineering- a critical overview at the high interest, low usage stage of development”, Advanced Composite Materials in Bridges and Structures, Proceedings of the Second International Conference, Quebec, Canada, edited by M.M.EI-Badry, pp.3-15, Canadian Society for Civil Engineering, Montreal, Canada.

Hentz S., Donze, F.V. and Daudeville, L. (2004), “Discrete element modelling of concrete submitted to dynamic loading at high strain rates”, *Computer structure,* 82: 2509-2524.

Kwak, H.G. & Filippou, F.C. (1990), Finite element analysis of reinforced concrete structures under monotonic load. Research report of Department of Civil Engineering, U. C. Berkeley, No. UCB/SEMM-90/14.

Khalighi, Y. and Banthia, N. (2011), "A study of FRP-concrete bond under impact", *Applied Mechanics and Materials*, 82:630-635.

Li, Q.M. and Meng, H. (2003), "About the Dynamic strength enhancement of concrete like materials in a split Hopkinson pressure bar test", *Int J Solids Struct*. , 40: 343-360.

Lu, X. Z., Teng, J. G., Ye, L. P. and Jiang, J. J. (2005), "Bond–slip models for FRP sheets/plates bonded to concrete", *Engineering Structures*, 27:920–937.

Lu, X. Z., Ye, L. P., Teng, J. G. and Jiang, J. J. (2004), "Mesco-scale finite element model for FRP sheets/plates bonded to concrete", *Engineering structures*, 27:564-575.

Lu, Y., Song, Z. and Tu, Z. (2010), "Analysis of dynamic response of concrete using a mesoscale model incorporating 3D effects", *Int J Protective Structures*, 1(2):197-217.

Lu, Y.B. and Li, Q.M. (2011), "About the dynamic uniaxial tensile strength of concrete-like material", *International journal of impact engineering*, 38: 171-180.

Malvar, L.J. and Crawford, J.E. (1998), "Dynamic increasing factors for concrete", Twenty-Eight DDESB Seminar, Orlando, August.

Malvar, L. J., Crawford, J. E. and Morrill, K. B. (2000), "K&C Concrete material model release3—automated generation of material model input", K&C documents, August.

Malvar, L. J., Crawford, J. E., Wesevich, J. W. and Simons, D. (1997), "A plasticity concrete material model for DYNA3D*", International Journal of Impact Engineering*, 19(9-10): 847-873.

Malvar, L. J. and Simons, D. (1996), "Concrete material modelling in explicit computations", Workshop on Recent Advances in Computational Structural Dynamics and High Performance Computing, USAE Waterways Experiment Station, April 24-26.

Monti, M., Renzelli, M. and Luciani, P. (2003), "FRP adhesion in un-cracked andcracked concrete zones", In: Proc. of 6th international symposium on FRP reinforcement for concrete structures. Singapore: World Scientific Publications:183–92.

Mosallam, A. and Teng, J.G. (2003), "Special issue on FRP composites in civil engineering", *Journal of Reinforced Plastics and Composites*, 22(13): 1145–1147.

Nam, J. M., Kim, H. J., Kim, S. B., Yi, N. H. and Kim, J. H. J. (2010), "Numerical evaluation of the retrofit effectiveness for GFRP retrofitted concrete slab subjected to blast pressure", *Composite Structures*, 92:1212–1222.

Nakaba, K., Toshiyuki, K., Tomoki, F. and Hiroyuki, Y. (2001), "Bond behaviour between fibre-reinforced polymer laminates and concrete", *ACI Structural Journal*, 98(3):359–67.

Neubauer, U. and Rostasy, F.S. (1997), "Design aspects of concrete structures strengthened with externally bonded CFRP plates", In: Proc. of 7th international conference on structural faults and repair, vol. 2. Edinburgh (Scotland): ECS Publications: 109–18.

Oehlers, D.J. and Seracino, R. (2004), Design of FRP and Steel Plated RC Structures: Retrofitting Beams and Slabs for Strength, Stiffness and Ductility, Elsevier, UK.

Oehlers, D.J., Seracino, R. and Smith, S. (2008), *Design Guideline for RC Structures Retrofitted with FRP and Metal Plates: Beams and Slabs*, Standards Australia HB 305. Publishers SAI Global Limited. ISBN 07337 78313.

Pijaudier-Cabot, G. and Bazant, Z.P. (1987), "Nonlocal Damage Theory", *Journal of Engineering Mechanics*, *ASCE*, 13(10):1512-1533.

Razaqpur, A.G., Tolba, A. and Contestabile, E. (2007), "Blast loading response of reinforced concrete panels reinforced with externally bonded GFRP laminates", *Composites: Part B 38*: 535–546.

Razaqpur, A.G., Contestabile, E. and Tolba, A. (2009), "Experimental study of the strength and deformations of carbon fibre reinforced polymer (CFRP) retrofitted reinforced concrete slabs under blast load", *Canadian Journal of Civil Engineering*, 36(8):1366-1377.

Savioa, M., Farracuti, B. and Mazzotti, D. (2003), "Non-linear bond–slip law for FRP-concrete interface", In: Proc. of 6th international symposium on FRP reinforcement for concrete structures. Singapore: World Scientific Publications: 163–72.

Scotta, R., Vitaliania, R., Saettab, A., Oñate, E. and Hanganuc, A. (2001), "A scalar damage model with a shear retention factor for the analysis of reinforced concrete structures: theory and validation", *Computers & Structures*, 79(7): 737-755.

Tang, T.P. and Saadatmanesh, H (2005), "Analytical and experimental studies of fiber-reinforced polymer-strengthened concrete beams under impact loading", *Structural Journal*, 102(1): 139-149.

Tarapada, R. and Debabrata, C. (2006), "Delamination in hybrid FRP laminates under low velocity impact", *Journal of Reinforced Plastics and Composites*, 25(18):1939-56.

Teng, J.G., Chen J.F., Smith, S.T. and Lam, L. (2002), FRP Strengthened RC Structures, John Wiley &Sons Ltd.

Teng, J.G., Smith, S.T., Yao, J. and Chen, J.F. (2003), "Intermediate crack-induced debonding in RC beams and slabs", *Construction and Building Materials*, 17(6–7): 447–462.

Teng, J.G., De Lorenzis, L., Wang, B., Li, R., Wong, T.N. and Lam, L. (2006), "Debonding failures of RIC beams strengthened with near surface mounted CFRP strips", *Journal of Composites for Constructions, ASCE*, 10(2):92–105.

Van Mier, J. G. M. (1997), Fracture Processes of Concrete: Assessment of Material Parameters for Fracture Models, CRC Press, Inc.

White, T., Soudki, K. and Erki, M. A. (2001), "Response of RC beams strengthened with CFRP laminates and subjected to a high rate of loading," *Journal of Composites for Construction*, ASCE, 5(3):153-162.

Wu, C., Oehlers, D.J., Rebentrost, M., Leach, J. and Whittaker, A.S. (2009a), "Blast testing of ultra-high performance fibre and FRP-retrofitted concrete slabs", *Engineering Structures*, 31(3): 2060-2069.

Wu, C., Oehlers, D.J and Day, I. (2009b), "Layered blast capacity analysis of FRP retrofitted RC member", *Advances in Structural Engineering*, 12(3): 435-49.

Yuan, H., Teng, J.G., Seracino, R., Wu, Z.S. and Yao, J. (2004), "Full-range behavior of FRP-to-concrete bonded joints", *Engineering Structures*, 26(5): 553-564.

Zhang, M., Wu, H.J., Li, Q.M. and Huang, F.L. (2009), "Further investigation on the dynamic compressive strength enhancement of concrete-like materials based on split Hopkinson pressure bar tests. Part I: Experiments", *International Journal of Impact Engineering*, 36:1327-1334.

Chapter 3 Issues of meso-scale modelling of concrete

3.1 Introduction

The mesh sensitivity associated with material softening is a key issue in finite element (FE) modelling of concrete behaviour. There are two different ways of modelling for smeared crack band approach in FE, i.e., local and non-local continuum damage schemes (Li et al. 2010a). The difference is that the damage in the local concrete model tends to happen in every single element but in the non-local continuums schemes the damage occurs in several elements depending on the crack band width defined when the loading/strain rate is lower, e.g. static state. It seems the non-local concrete model is a better choice because the crack band width is a material property which corresponds to approximately three times the maximum aggregate size Bazant and Oh (1983). However it is obtained from the static test and with dynamic/impulsive load the crack band width may be changed. To the best knowledge of the author, there is no systematic conclusion on this based on sufficient experiment investigations. Furthermore, even for the static modelling, the real crack width in concrete tends to be 2-5*mm* for some tests, e.g. the FRP-concrete debonding tests (Lu et al. 2004). That is already smaller than the regular aggregate sizes, e.g.

8*mm*. For the local failure in such a small width, some of the macro material properties such as crack band width equal to three times the maximum aggregate size has little meaning. Aggregates may have some effect but it may mostly come from the mortar. Therefore even for static state, it is still unknown that which non-local crack band width should be used in such cases. Another reason why the non-local model is not widely used is the high computation cost. To capture the debonding failure of the FRP-to-concrete bonded joints, the mesh should be at least one order smaller than the physical cracking width. The FE modelling process would be very time-consuming with non-local crack band width set as only 5 time the current element sizes according to the static numerical attempts. Due to the low computational cost with sufficient reliability of the results (Scotta et al. 2001), the local concrete model is still the main option in FE. Therefore the meso-scale numerical investigation based on the local concrete model with the crack band theory for both static and dynamic states has great significance in FE.

Concrete is an important material in civil engineering and defence construction. Because the material has very complicated non-linear behaviour, it is difficult to be fully described for general stress conditions by a simple constitutive model. In particular, when concrete is subjected to extreme loadings such as blast and impact, the modelling of concrete can be further complicated due to rate effects, overloading and large deformations (Tu and Lu 2009). The K&C concrete damage model was first developed for DYNA3D (Malvar et al. 1997) and now is available in LS-DYNA as #Mat_72. From various numerical modelling compared with tests (Bao and Li 2010; Magallanes et al. 2010; Sangi and May 2009; Tanapornraweekit et al. 2010),

the simulation results with K&C concrete show reasonable agreement when compared with the tests and for the overall kinematics response of the concrete structures with macro-scale element sizes. The K&C concrete damage model is well known as its automatic generation ability based on the unconfined compressive strength $f_c^{'}$ (Malvar et al. 2000). This concrete model can give good estimation of the structure behaviour compared with the test results with its automatic generation (Schwer and Malvar 2005). The default localization width, crack band, in this model is 1*inch* (25.4*mm*) (Malvar et al. 2000), which corresponds to 3/8*inch* maximum aggregate size. For modelling large structure with element sizes larger than the default localization width 25.4*mm*, this model will correct the fracture energy automatically for every single element, hence the crack band width here has its real physical meaning.

For element sizes below the localization width (or the default 1*inch*), the fracture energy can also be a constant with changing the localization width to the element characteristic length (Malvar et al. 2000; Tu and Lu 2009). This makes this local concrete model be capable of modelling the concrete behaviour in meso-scale level with small element sizes. However there is a lack of detailed discussion on the meso-scale fracture modelling based on the current local concrete model. The work conducted by Tu and Lu (2009) has mentioned the importance of the softening parameter definition of K&C concrete damage model when it is used as a local concrete model. It was referred to the automatic generation document of the model (Malvar et al. 2000) in that paper. However both of the two pieces of work just briefly mentioned the Mode I fracture energy was of great importance on the fracture

mechanics. Malvar et al. (2000) mainly focus on the model characteristic based on the real crack band width as this concrete model they defined is mainly used for macro-scale modelling at that time. Tu and Lu (2009) mentioned the localization width for the concrete model should be set as the characteristic length of the element; however they did not give detailed discussion on how the concrete model works with the localization in tension and compression when used with element sizes extremely smaller than the default crack band width of this model 25.4*mm* (1*inch*). The current chapter focuses on the meso-scale investigation of the concrete model, which is an attempt of discussing how to use the local concrete model in concrete fracture behaviour modelling in detail, starting from the uniaxial tension followed by uniaxial compression. The localization in tension might be simple as it is generally accepted to be simplified as the localization happening in every single element (Tu and Lu 2009), especially when the state is static. But the compressive localization is much more complicated. When the Mode I fracture energy was given as a material property in CEB-FIP (1993), the compressive material property was still described as a macro stress strain curve. The concrete compressive fracture energy and compressive localization in FE modelling is discussed in detail in this chapter. Any stress state of the concrete material can be simplified as the combination of the tensile and compressive states, and the author tried to explore issues on modelling with local concrete model both in tension and compression at meso-scale level so that the modelling of concrete fracture can be properly captured. This chapter will start from the static state discussion without the rate effects investigation first as it is the concrete model basis. The rate effect aspects will be discussed as well.

3.2 Concrete Mode I fracture modelling

3.2.1 Tensile localization

Modelling of fracture and cracking in concrete structures has received tremendous attention since 1960s because of the low tensile strength of concrete. However, much of the research has been limited to static or quasi-static loading, and under relatively simple stress conditions. Modelling of fracture and tension-dominated problems in a general finite element environment, so as to facilitate the analysis under complex stress conditions and dynamic loading, remains to be a less-cultivated area. The study reported in the current chapter is part of the thesis research programme aiming at a reliable simulation of fracture and its effect on the global as well as local responses in concrete structures using the finite element method. To enable the incorporation of dynamic loading, the simulation model is developed using a transient dynamic analysis code, namely LS-DYNA Explicit (LSDYNA 2007). A series of investigations have been conducted on typical fracture scenarios to evaluate the model performance and calibrate the parameter settings. Mode-I fracture is one of the scenarios being considered, which is detailed in Section 2.5.1.

The K&C concrete damage model with its automated generation ability is normally used for modelling large scale structures with macro scale element sizes under impulsive load, i.e. blast or impact, and by default the localized width of damage is set equal to three times the maximum aggregate diameter (LSDYNA 2007). The default value of the localized width is 1 *inch* (25.4*mm*), which corresponds

approximately to a maximum aggregate size of 3/8 *inch* (Malvar et al. 2000). The failure of a RC structure under impulsive load is normally compression-dominated, because in such a structure the steel reinforcement would undertake most of the tensile forces even if damage occurs in concrete due to tension or shear.

According to Kwak and Filippou (1990), when the element size is smaller than three times the maximum aggregate size, the crack strain can be treated as uniform in the element when the smeared crack model is used. Hence, to maintain a given fracture energy it requires:

$$\int \sigma d\varepsilon = \frac{G_f^I}{h_c} \tag{3-1}$$

where h_c is the element characteristic length, $\int \sigma d\varepsilon$ stands for the area under the stress strain curve for the concrete under uniaxial tension.

The K&C concrete damage model in LSDYNA is a smeared crack band model. The material localization width l_w in this concrete model represents the concrete crack band width w_c. According to the above discussion, when the element size is smaller than three times the maximum aggregate size, the localized width should be set equal to the element characteristic length, i.e. $l_w = h_c$. For a first-order solid element with a single integration point, the element characteristic length is represented by the cubic root of the element volume $\sqrt[3]{V}$ (LSDYNA 1998).

The fracture energy calibration of the K&C model has been made on the basis of the CEB-FIP model code (Malvar et al. 1997; Malvar et al. 2000). For example, for f_c' =45*MPa* and a 100*mm* cubic element, a fracture energy of G_f=100*N/m* was obtained for b_2=1.35. This is approximately the CEB-FIP (1993) recommended value for a C47 concrete grade and 16-*mm* aggregate size. The effect of varying the compressive strength on the fracture energy with the automated generation procedure has been improved as evidenced in the example C20 and C80 concrete in Malvar et al. (2000). Both the upper and lower bound values tested properly represent the data recommended by CEB-FIP (1993). However, the K&C concrete damage model does not allow a direct input for G_f^I. The fracture energy is indirectly controlled by the uniaxial tensile stress strain curve in an element. As such, if the fracture energy is found to be unsatisfactory following the automated generation of the material parameters, adjustment may be made on the b_2 value, which governs the softening part under uniaxial tension.

3.2.2 FE modelling of notched beam test

To examine the performance of the above framework in modelling mode-I crack propagation in concrete, a three-point bending test on a notched beam is investigated. Figure 3-1 shows the beam geometry of the test done by Peterson (1981). The concrete had a Young's modulus of 30 *GPa* and a Poisson's ratio of υ=0.18. The thickness of the concrete beam was 50 *mm*. The fracture energy was 137 N/m. The area under the load-displacement curve is equal to the fracture energy of the concrete times the mid-section area above the notch. In the numerical simulation, the input

unconfined compressive strength is $f_c^{'}$ =40 *MPa* which automatically generated concrete Young's modulus of 30 *GPa* following CEB-FIP (1993) relationship $E_c = 18.275(f_c^{'}/10)^{1/3}$ where both $f_c^{'}$ is in *MPa* and E_c is in *GPa* .

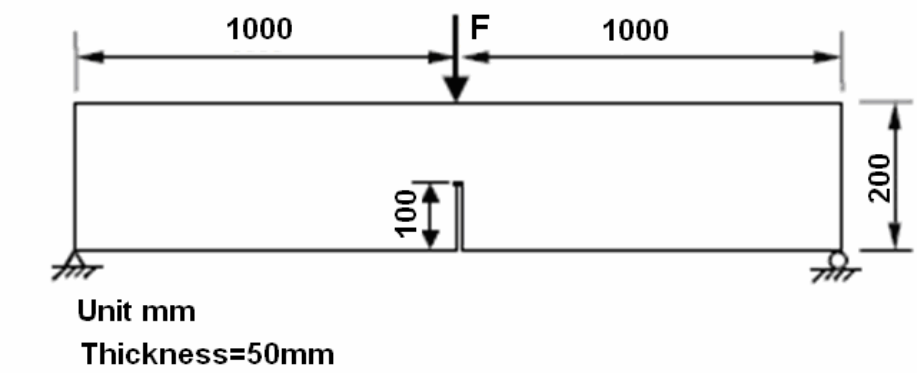

Figure 3-1 Three-point notched-beam test (Mode I) (Unit of dimensions: *mm*)

The dynamic effect becomes negligible when the total loading time is greater or equal to 10*T*, where *T* is the natural period of the whole structure (Chen et al. 2009), and this has been improved in the current model (Li et al. 2010a). A smooth velocity loading is advantageous considering that the initial displacement, velocity and acceleration are all equal to zero.

A mesh convergence study was conducted first. To be consistent, the overall boundary and geometry conditions were kept the same, including the notch width, for different meshes, see Figure 3-2. The notch width is kept at 10*mm* for the 10-*mm*, 5-*mm*, 2-*mm* and 1-*mm* mesh size models, except for the coarse mesh model with a 25-*mm* grid, where the notch width was set as 25*mm*.

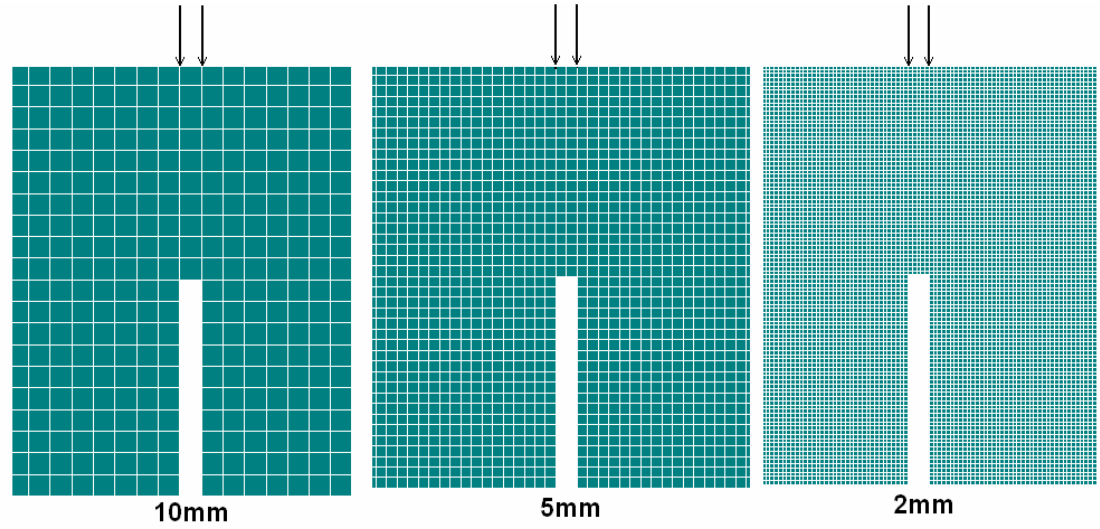

Figure 3-2 Local meshes for 3-point notched-beam test

The beam was modelled as a plane stress problem. Because the K&C concrete damage model is implemented in LS-DYNA only for solid elements, a thin-plate configuration was employed, with a single layer of elements in the out-of-plane direction. To avoid the out-of-plane movement, the model was constrained on one face of the nodes in the direction normal to the plane. In view of the future extension of the model to dynamic analysis, a single-point integration solid element was chosen. This, however, necessitates control over the so-called hourglass deformation.

Hourglass deformations are orthogonal to the directions in which strain calculations are performed. Work done by the hourglass resistance is thus neglected in the energy equation, leading to the loss of energy (LSDYNA 1998). If zig-zag mesh deformation is seen, hourglass can be a serious problem in the FE model leading to inaccurate results in terms of both stiffness and load carrying capacity.

An alternative option is to use the full integration scheme. However, severe shear locking can occur for the first order eight node hexahedron solid element. When the full integration scheme was trialled in modelling the pull-off test, it led to unrealistically stiff behaviour and automatic termination. Therefore, the one point integration scheme was adopted for the concrete elements. The full integration scheme was adopted for the FRP elements as they did not result in the shear locking phenomenon.

The effect of hourglass deformation (HD) may be controlled in LSDYNA by a user defined hourglass coefficient, which has a default value of 0.1. A large hourglass coefficient usually corresponds to large hourglass resisting forces. In an FE model with re-diced one integration point elements, the ratio of the hourglass energy to the internal energy of the structure should be smaller than 5% (LSDYNA 1998). Otherwise the results are unreliable. In the present analysis the hourglass control is introduced and it is deemed to be satisfied when the ratio between the total hourglass energy and the total internal energy is smaller than 5%.

3.2.3 Fracture energy and mesh objectivity

As discussed before, in an FE analysis with a local concrete material model, the localized width l_w should be set as the element characteristic length h_c. In this way, the fracture energy in the FE analysis, i.e., the area under the stress strain curve in a single element multiplied by the element characteristic length is expected to preserve the target concrete fracture energy. On the contrary, if a fixed crack band width

(somewhat "physical") is used as the localized width in the FE model, while the actual localization confines within an element characteristic length, the achieved fracture energy in the FE model then would inevitably become mesh-dependent.

Figure 3-3 shows the computed load versus mid-span deflection relationships for the five models using five different meshes but a constant localization width equal to the default value of $25.4mm$. The results from the five models with the localization width equal to the mesh grid size are given in Figure 3-4.

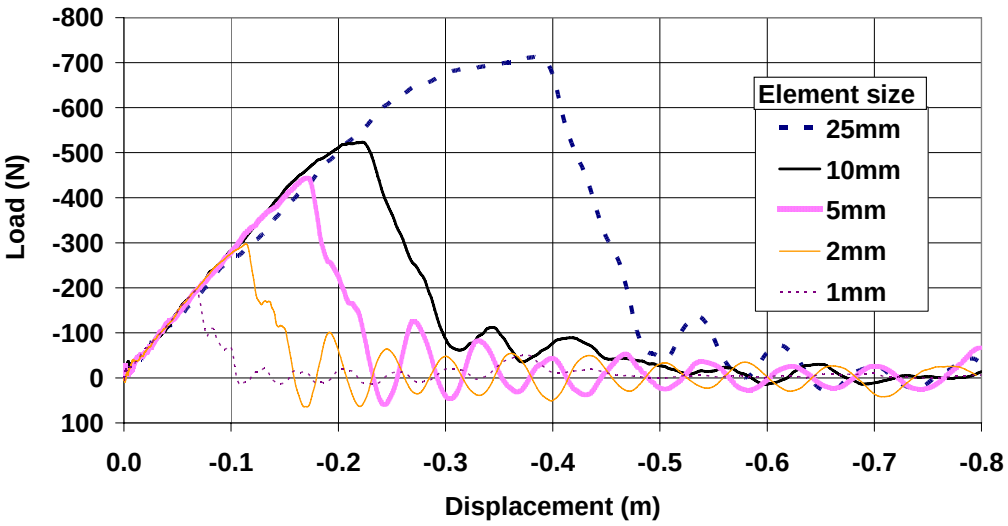

Figure 3-3 Notched beam load-displacement curves with default localization width $l_w = 25.4mm$

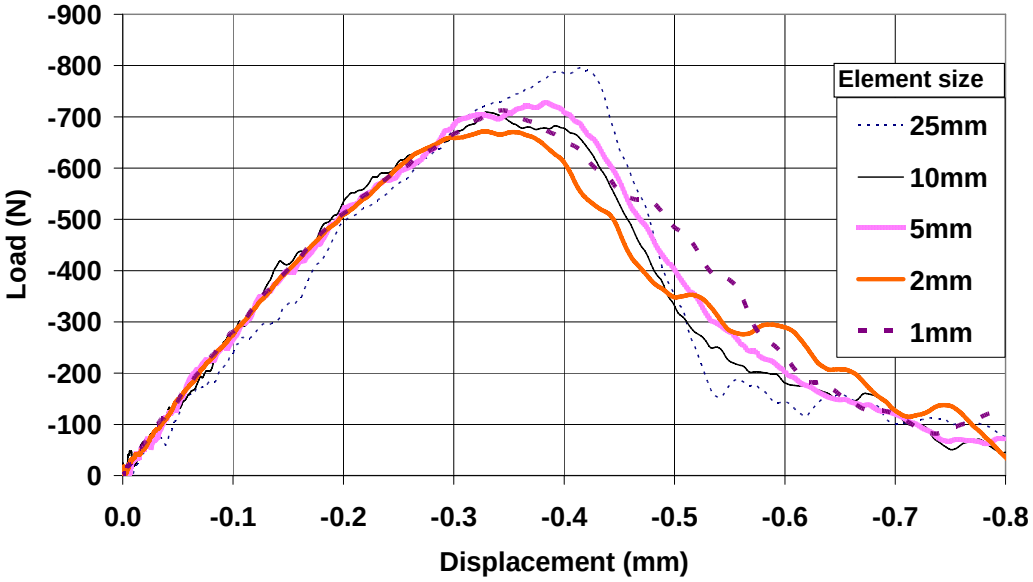

Figure 3-4 Notched beam load-displacement curves with $l_w = h_c$

From Figure 3-3 and Figure 3-4, it can be found that the results were strongly mesh dependent when a constant crack band width was used as the localized width; but they become almost mesh-independent when the localized width was set equal to the element characteristic length. This observation echoes what was mentioned in Malvar et al. (1997), that unless the softening is governed by an appropriate localization limiter or characteristic length, the results from a local damage model like K&C are inevitably mesh-dependent; and by forcing the area under the stress-strain curve to be G_f^I / h_c, such mesh dependency is eliminated.

With the constant localized width equal to 25.4*mm*, the notched beam behaves increasingly brittle with decreasing the element size. This is because the damage in the FE model is actually concentrated in a single column of elements above the notch, the width of which is equal to the varying element width rather than the presumed localization width of 25.4*mm*. Consequently, the actual fracture energy (per unit

crack length) in the FE model will be equal to $(G_f^I / l_w) \times h_c = G_f^I \times h_c / 25.4$, which decreases proportionately with the decrease of the element size below 25.4*mm*. This in turn influences the global load-deflection behaviour of the notched beam in a similar manner as the global response is dominated by the crack above the notch in such a specimen.

The above analysis clearly indicates that the global behaviour of a tension-fracture dominated problem can not be predicted reliably if a constant crack band width is adopted as a concrete material constant in FE modelling when the element characteristic length is smaller than the crack band width. For such problems, by setting $l_w = h_c$, i.e., letting the localized width equal the element characteristic length, the global load-displacement behaviour can be predicted in a mesh-independent manner.

3.2.4 Control of G_f^I and uniaxial tensile softening behavior

The results presented above were produced from models with the concrete material parameters being automatically generated for the 40-*MPa* concrete with a Young's modulus of 30 *GPa* . In such a model, the mode-I fracture energy is tied to the material parameter being generated. However, if one is not satisfied with the fracture energy thus obtained, modification may be achieved by adjusting the b_2 parameter, as it controls the softening part of the uniaxial stress strain curve in the concrete damage model. For example, when b_2 is changed from the default 1.35 (for 40-*MPa*

concrete) to -0.45, the mode-I fracture energy is increased from about 100 to 137 *N/m*, which is deemed to be more suitable for this class of concrete according to CEB-FIP (1993).

3.2.5 Strain localization in the FE model of a notched beam

In the present simulation using the concrete damage material model, the distribution of damage may be presented with a contour plot of the damage index *SDF*, defined in Equation (2-37). To identify fracture from such a plot, however, it is necessary to establish a correlation between the *SDF* index and the position in the softening branch of the tensile stress-strain curve.

Figure 3-5 depicts the stress-strain curve as obtained from a single-element model subjected to uniaxial tension, with loading and unloading at different stages. From the graph, it can be found that the unloading slope is parallel to each other and nearly equal to the elastic loading slope, indicating that the model does not account for the stiffness degradation (this issue is beyond the scope of the present discussion). As such, the consumed fracture energy at any particular response level, for instance the shaded area under the stress strain curve, can be directly calculated from the total strain energy according to the strain value. The strain value in turn is related to the *SDF*. Thus, a correlation between *SDF* and the consumed fracture energy is obtained.

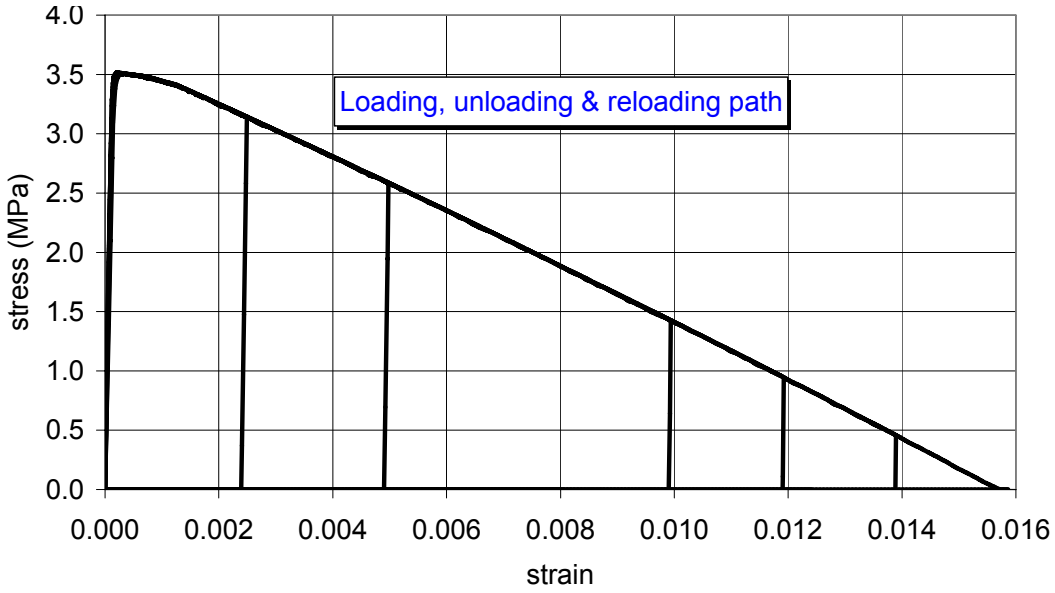

Figure 3-5 Stress-strain curve from a single element tension model, with loading and unloading (element size = 5*mm*)

Figure 3-6 shows the normalized mode-I fracture energy dissipation vs. *SDF* curve as obtained from the single element tension loading and unloading model. The normalized energy dissipation is the ratio between the energy dissipated at a particular strain level and the total Mode-I fracture energy. It becomes immediately clear that the energy dissipation in an element becomes significant only when the *SDF* is close to 2.0; in fact, even when *SDF*=1.95, the energy dissipated is still less than 50% of the total fracture energy in an element.

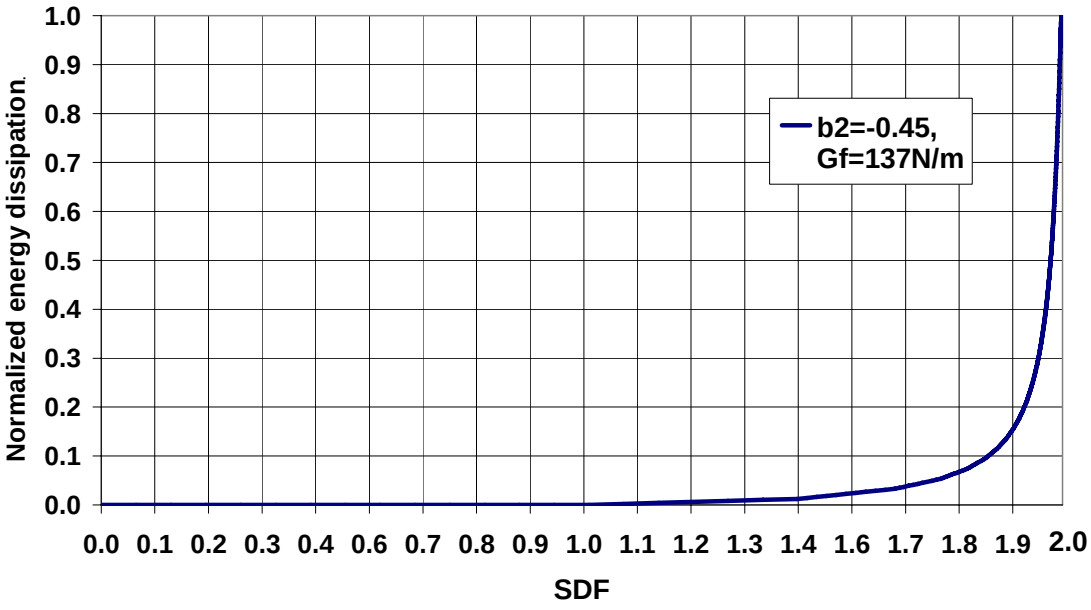

Figure 3-6 Normalized Mode-I fracture energy dissipation vs. *SDF* curve

Figure 3-7 shows the *SDF* contours for the 2-*mm* mesh size model when the displacement at the mid-notch reaches 0.8*mm*. Based on the correlation between *SDF* and the fracture described above, three different scales of *SDF* are used in plotting the *SDF* contours, with the last one ranging in 1.97~2.0, which may be considered as representing the actual crack. It can be found that, although damage occurs in a large area above the notch, total failure is concentrated primarily along a single column of elements. This explains the mesh objectivity in Figure 3-4, where $l_w = h_c$ is adopted in all models. It is worth noting, however, that when the localization width is set equal to the element characteristic length, the mesh objectivity is attainable only if cracking is indeed concentrated within one column of elements in the FE analysis. The localization of cracking is the basic character by which the crack band model would work.

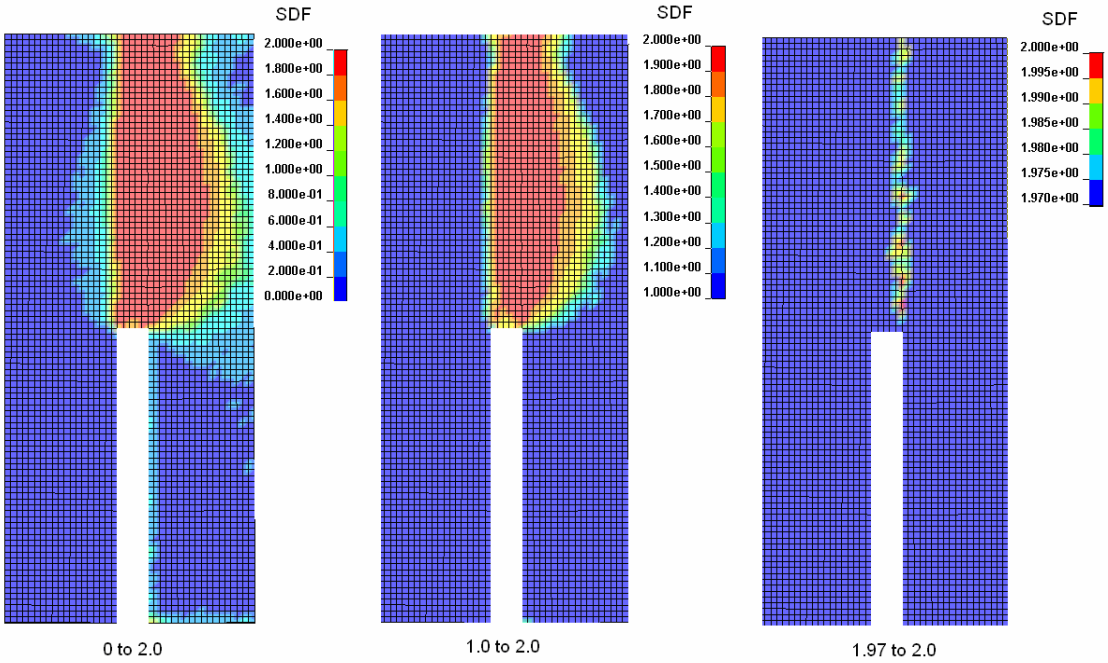

Figure 3-7 Damage contours for 2-*mm* mesh size model with different scales of *SDF* (Central deflection = 0.8*mm*)

3.2.6 Effect of notch width

The effect of notch width was investigated with the 2-*mm* mesh size model. The same material parameters were adopted as the experiment done by Peterson (1981), namely a Young's modulus equal to 30*GPa*, and fracture energy of 137*N/m*. For the K&C model, 40-*MPa* concrete was chosen so that the automatically generated Young's modulus is equal to 30*GPa*. The b_2 parameter is adjusted to -0.45, so that the resulting Mode-I fracture energy is 137*N/m*, as desired. Figure 3-8 depicts the results for different notch widths.

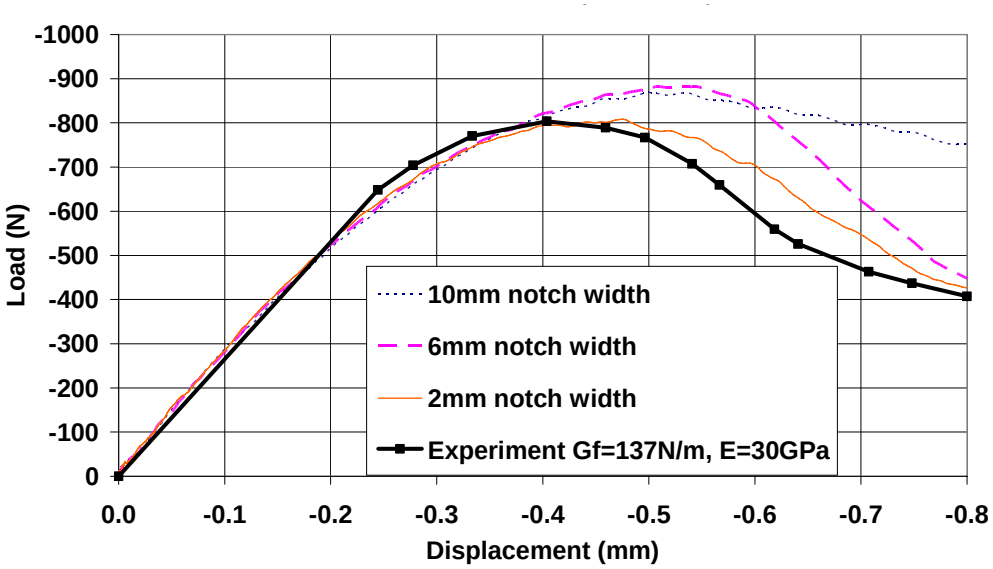

Figure 3-8 Load-displacement curves for different notch widths

Normally in the test, it is better to keep the notch width as smaller as possible, normally 1 to 3*mm*. From Figure 3-8, it can be observed that the load-displacement curve approaches to the experimental curve as the notch width is reduced. The best result among the three scenarios is that when the notch width is equal to 2*mm*, which just fits in one element width in the 2-*mm* mesh model. Therefore, for the subsequent analysis, a notch of one element wide is chosen.

3.2.7 Comparison of FE predictions with notched-beam test

Further modelling analyses for the same notched-beam but assuming different values of the fracture energy were also carried out. The results are compared with the experimental data, as well as numerical results obtained by some other researchers using the FEM (Peterson 1981) and the BEM (Saleh and Aliabadi 1995), in Figure 3-9. It can be found that the current FE model gives a good match to the experimental results.

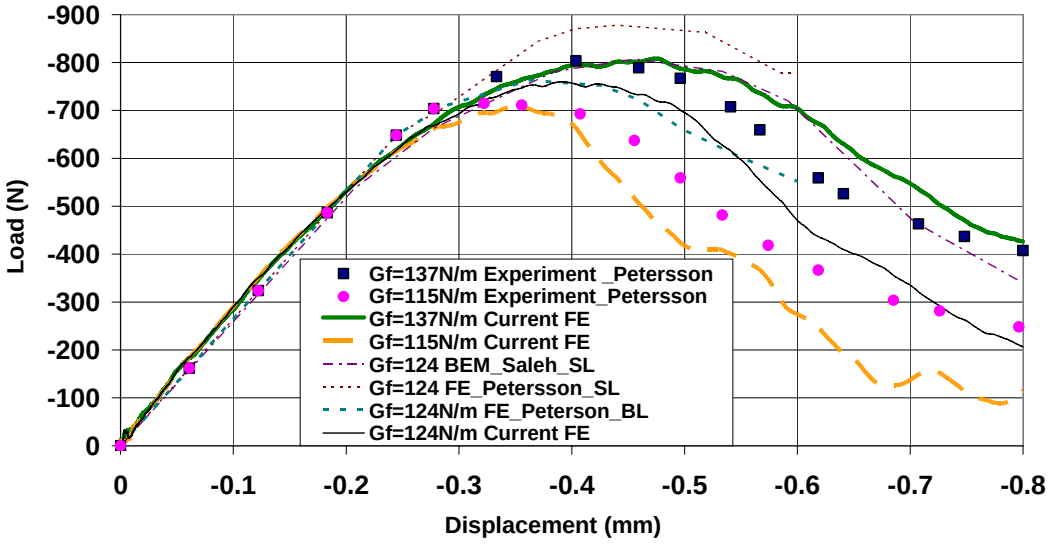

Figure 3-9 Comparison of load-displacement curves

3.3 Concrete compression modelling

3.3.1 Compressive localization

In the last few years, researchers have started to realize that localization also occurs for concrete loaded in compression. Compressive localization means that the descending branch of the stress-strain curve becomes specimen size dependent, and the stress-strain curve can therefore not be regarded as a pure material property (Markeset and Hillerborg 1995). However for practical reasons and due to lack of sufficient experimental data, the strain concentrations from compressive localization are generally smeared, and the macro-scale compressive stress strain relationship has been described by equations (2.1-18) to (2.1-21) in CEB-FIP(1993) as the concrete uniaxial compressive material property. These equations are only for a length of the

concrete prism subjected to compression of approximately 200 mm with a square cross-section 100x100 mm^2. Meanwhile, the descending branch of the stress-strain relation in compression is influenced by the length of the member subjected to compression (CEB-FIP 1993). The size effects for the softening part of the compressive stress strain relationship are presented in Figure 2.1.3 in CEB-FIP (1993). All of these presented in CEB-FIP were based on the research Van Mier. (1984).

Compressive localization was highlighted in Van Mier (1984). A few studies on compressive localization were carried out, but the localization fracture zones under compressive stress have not been determined accurately (Nakamura and Higai 1999). Compressive failure is more complex than tensile failure, as it is always accompanied by lateral deformations. The lateral deformations have to do with longitudinal distributed splitting cracks, which form and expand during the failure process (Markeset and Hillerborg 1995). It is generally accepted that tensile failure usually takes place in a relatively narrow localized zone about three times the maximum aggregate size approximately. However, according to the experimental work in Nakamura and Higai (1999), compression failure occurs within a larger (larger than tensile localized zone), but still a limited damaged zone. The empirical results indicate that the compressive fracture length is influenced by the concrete strength, maximum aggregate size, the aggregate grading and the distance between the aggregate. The relationship between compressive fracture zone l_p and $f_c^{'}$ was expressed in Equation (3-2) by Nakamura and Higa (1995).

$$l_P = \frac{1300}{\sqrt{f_c^{'}}} \tag{3-2}$$

Here the units of $f_c^{'}$ and l_P are *MPa* and *mm* respectively. Their research also indicates that the value of the compressive fracture energy G_c is influenced obviously by the aggregate grading. However, when the aggregate grading is constant, G_c can be assumed as a material constant (Nakamura and Higa 1995).

$$G_c = 8.8\sqrt{f_c^{'}} \tag{3-3}$$

$$\text{Or} \quad G_c = 250 G_f^I \tag{3-4}$$

Here the unit of $f_c^{'}$ is *MPa* and the unit for energy is *N/mm*.

The compressive fracture energy $G_c = 250 G_f^I$ is the energy dissipated in the compressive fracture zone $l_P = \frac{1300}{\sqrt{f_c^{'}}}$ (Nakamura and Higa 1995), and the maximum aggregate grading for the particular relationship was $20\,mm$. It is normally larger than the tensile crack band width equal to $60\,mm$ approximately. However, in macro scale static FE modelling with local concrete model, it is generally accepted that the compressive localization width is equal to tensile localization width and the compressive fracture energy G_c is about 100 times the Mode I fracture energy G_f^I (Ozbolt and Reinhardt 2002). The process of compression in FE is similar to tensile state, concrete compressive fracture energy is a material constant with the value

of $100G_f^I$, and is smeared in the crack band which is equal to the single element characteristic length in local model.

$$G_c = h_c \int \sigma_c \, d\varepsilon_c \tag{3-5}$$

$$G_c = 100 G_f^I \tag{3-6}$$

The compressive stress strain curve for local concrete model should be mesh-dependent too. The validity of introducing G_c into FE modelling, but not using constant stress strain relationship directly from CEB-FIP(1993) for local concrete compressive material definition, is discussed below.

3.3.2 FE model

A 100x100x200 mm^3 concrete prism was chosen for uniaxial compressive test (CEB-FIP 1993; Van Mier 1984). The equations (2.1-18) to (2.1-21) in CEB-FIP (1993) give the general macroscopic compressive stress strain curve of concrete with 100x100x200 mm^3 geometry.

The aim of the work in this section is to capture the compressive localization failure mode in meso-scale FE modelling for numerical exploration of compressive localization. The real failure mode of the concrete specimen for uniaxial compressive tests strongly depends on the boundary conditions. It concerns with the mount of friction at the up and bottom supports of the uniaxial compressive test. For example, for two ends frictionless boundary conditions, the failure is splitting at the middle

centre of the concrete specimen. To achieve the expected splitting failure mode, the mesh should be very fine at the centre for mesh convergence which will require a huge mount of computation effort. However, under the boundary condition with one end frictionless and another end fixed, the failure mode is shear failure with a shear band, and expected failure mode can be achieved with large element sizes. Van Mier (1984) also indicated a very important observation that the difference in fracture mode of a specimen does not seem to influence the macroscopic stress strain curve in the tests. Two types of boundary conditions, one end effectively fixed and the other end effectively pinned and two ends fixed, were adopted.

To reduce computation efforts, the numerical specimen is simplified as a plane stress problem and 50*mm*, 10*mm*, 5*mm* and 2*mm* mesh sizes are chosen. The concrete strength in uniaxial compressive test is 43*MPa*. The displacement control is used and 0.3*mm* vertical displacement is applied within 1.5 seconds, which is over 10 times the first mode natural period from the eigenvalue analysis.

3.3.3 FE results with constant uniaxial compressive stress strain curve

The first attempt was to use constant uniaxial stress strain curves as concrete material properties for different mesh sizes. For K&C concrete damage model, it can be achieved by setting the localized width equal to the default value 25.4*mm* when the element size is smaller than it. The local stress strain curve from single element uniaxial compressive test is presented in Figure 3-10. 50*mm* element was also used in this model and it can be discovered that when the element size is larger than the default localized width 25.4*mm*, the crack band corresponds to 3/8*inch* maximum

aggregate size. The K&C concrete model will automatically convert the energy. This default setting does benefit to the normal macro scale modelling, because it can ensure the energy self-adapting with different element sizes used in one model for macro-scale modelling. Figure 3-11 is the global engineering uniaxial compressive stress strain curve obtained from the numerical models of which Figure 3-10 is the material property input.

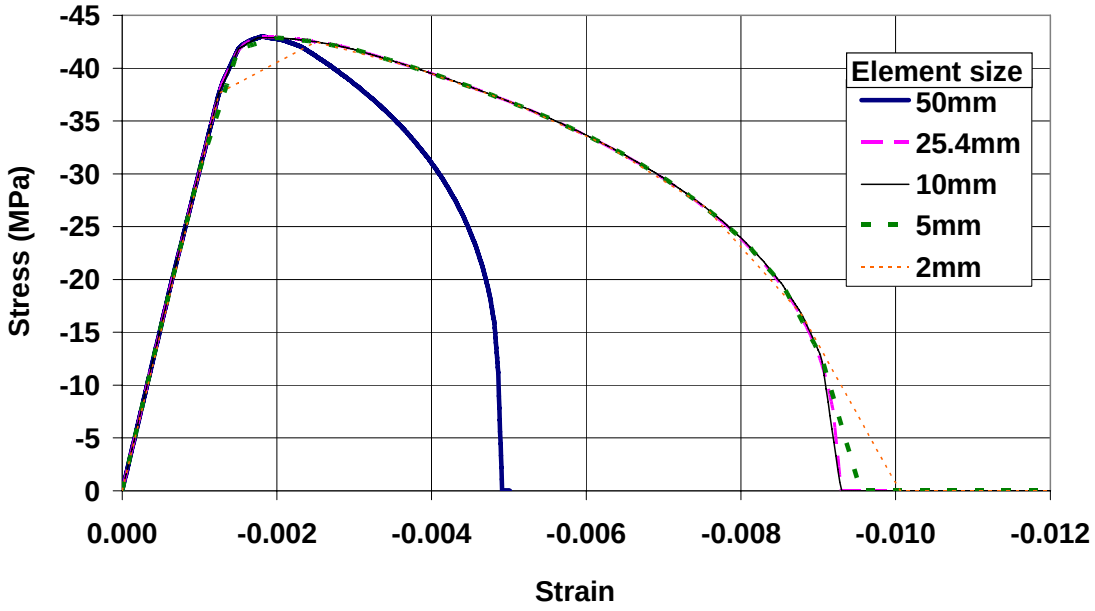

Figure 3-10 Uniaxial compressive local stress strain curves input for single element ($l_w = 25.4mm$)

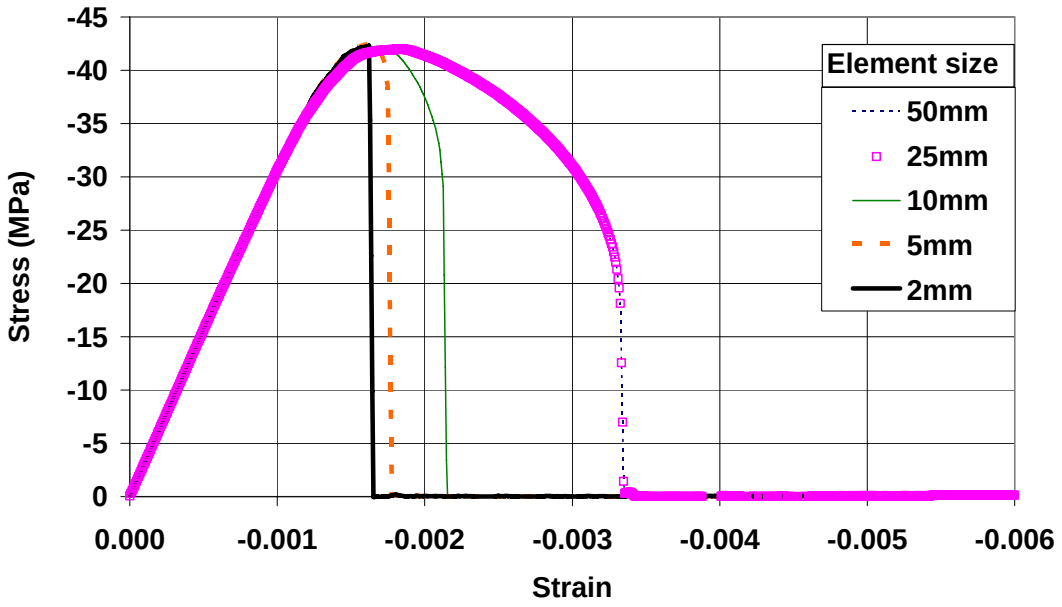

Figure 3-11 Global engineering uniaxial compressive stress strain curves output from the numerical test specimens ($l_w = 25.4mm$)

From Figure 3-11, it can be discovered that the specimens behave much more brittle with mesh refinement. There is no compressive stress strain softening observed with $5mm$ and $2mm$ element size model. Crushing failure occurs as soon as the strength reaches the concrete compressive strength. Mesh convergence can not be achieved with setting constant uniaxial compressive stress strain curves as the local material properties for different mesh size models, because element failure in the compression test is compression dominated and constant compression stress strain curve for smaller element size means smaller displacement is needed for achieving failure, which is the evidence of existing compressive localization.

3.3.4 FE results with constant compressive fracture energy

It has been improved that mesh convergence can not be achieved with considering stress strain relationship as the local material property input in FE model and the compressive localization in FE modelling really exists. It is compatible to considering the compressive localization the same as the tensile state. Another attempt with keeping compressive stress displacement curve constant similar to tensile localization modelling by insuring the compressive fracture energy G_c as the material property instead of constant uniaxial stress strain curve for different mesh size in FE modelling is presented in the current section.

With localized width equal to the element characteristic length, the local uniaxial compressive stress strain curves input are mesh dependent showed in Figure 3-12 but the compressive fracture energy G_c is a constant as the material property, which is equal to the element characteristic length times the area under the softening part of the stress strain curve. Figure 3-13 is the global engineering uniaxial compressive stress strain curve obtained from the test specimens. The global uniaxial compressive stress strain curve from CEB-FIP (1993) is also plotted in Figure 3-13. Figure 3-14 is the damage patterns for different mesh size models.

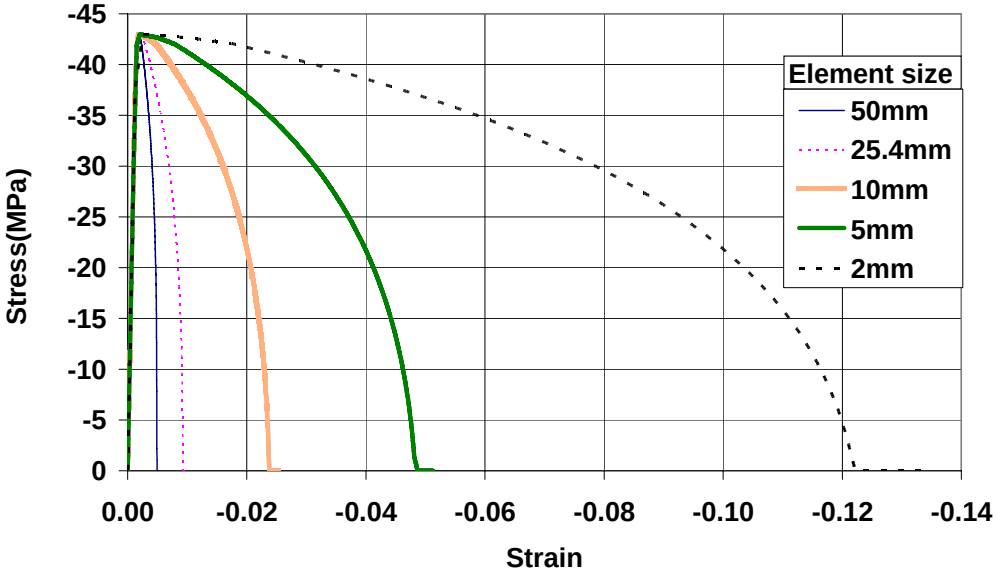

Figure 3-12 Uniaxial compressive local stress strain curves input for single element ($l_w = h_c, G_c = 100G_f^I$)

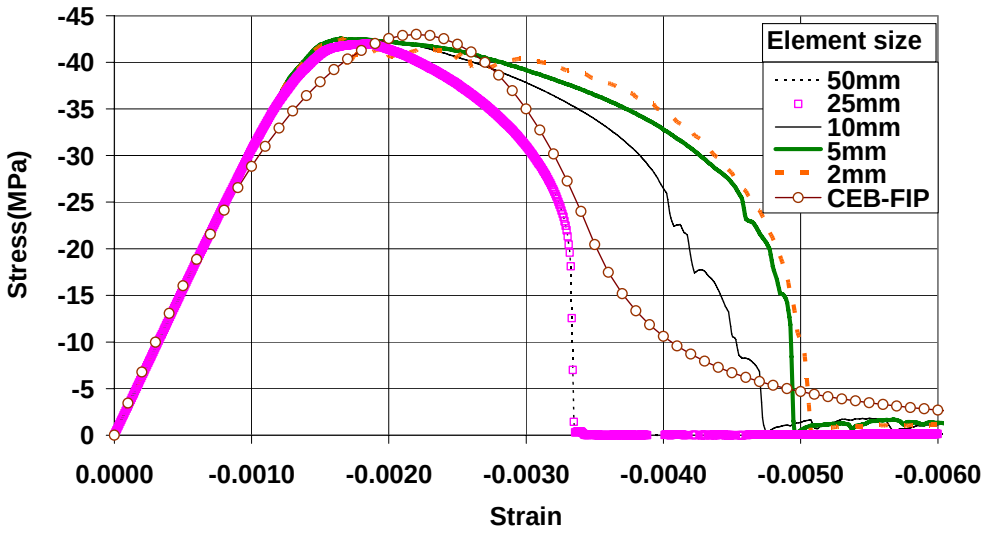

Figure 3-13 Macroscopic engineering uniaxial compressive stress strain curves output from the test specimens ($l_w = h_c, G_c = 100G_f^I$)

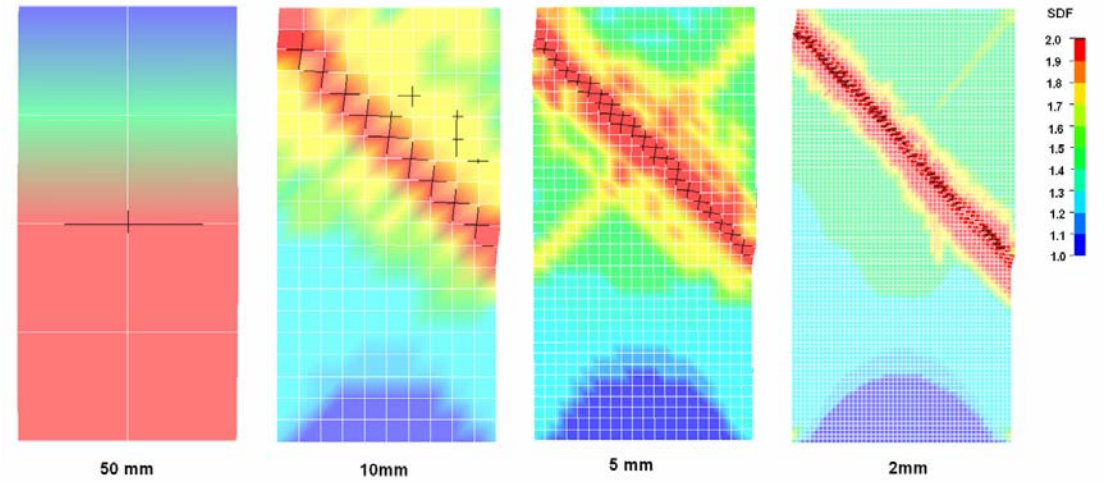

Figure 3-14 Damage patterns of different mesh size specimens with constant compressive fracture energy (mesh dependent stress strain curve) input as the material property

It can be discovered in Figure 3-13 that when the element size is larger than the default localized width l_w, 25.4mm. The macroscopic engineering stress strain curve obtained gives nice match to the standard. The damage contour in Figure 3-14 shows that with such element sizes, e.g. 50mm, the localized shear band can not be observed and the damage is smeared in the whole specimen. This indicates that the K&C concrete damage mode can well predict the concrete behaviour in macro scale modelling.

Localized shear band for one end friction less and one end fixed boundary conditions is observed with mesh refinement. The compressive stress strain softening is perceived in Figure 3-13 with constant compressive fracture energy and mesh dependent compressive stress strain curves as the local material property. Though the global engineering stress strain curve obtained meso-scale meshing was with stress

strain softening ductility enhancement for 5*mm* and 2*mm* mesh sizes in Figure 3-13, mesh convergence has still been achieved for the two mesh sizes.

The reason for the enhancement of the ductility in Figure 3-13 for the model with meso-scale element sizes is compressive localization case dependency. The most important difference between tensile and compressive localization is: once the localization occurs in tension, it is concentrated in a particular layer of localized elements and the elements beside the localization ones can contribute little energy to the failure; however, for compressive localization, the elements beside the localization zone still contribute energy to the whole failure process even the main failure elements are strongly damaged. Therefore, the ductility enhancement is observed for the softening part of the output engineering stress strain curve in Figure 3-13 with small element sizes. This indicates when the compressive localization does not exactly happens in single elements, numerical setting with "$l_w = h_c$ and $G_c = 100G_f^I$ " will overestimate the global response of the structure. But according to the mesh objectivity of the results from 5*mm* and 2*mm* mesh size models in Figure 3-13, it can be summarised the localization still converges to a value $n \cdot h_c$, where n is a constant for the current boundary condition and h_c is the current element characteristic length.

Nevertheless, with the consideration of numerical compressive localization width, $n \cdot h_c$, compressive fracture energy for every single element should be some value related to the element size for numerical local material property definition

when considering the localization still happens in every single element and $l_w = h_c$.

That is "$l_w = n \cdot h_c$"or "$G_c = \frac{100 G_f^I}{n}$" in numerical application.

As the experimental results reported in the literature thus far have not been very promising, and it seems that in Mode II fracture and compressive experiments the cracks still tend to nucleate and propagate in Mode I, it is suggested to keep $l_w = h_c$, and use "$G_c = \frac{100 G_f^I}{n}$" to describe the compressive localization case dependency in FE modelling local concrete model.

Because the difference in fracture mode of a specimen due to different boundary conditions does not seem to influence the macroscopic stress strain curve in the tests (Van Mier 1984), the value of "n" should be case dependent so that the numerical global engineering stress strain curve output matches the CEB-FIP(1993) stress strain curve for the particular concrete strength. The case dependence of "n" is presented in Figure 3-15 and Figure 3-16.

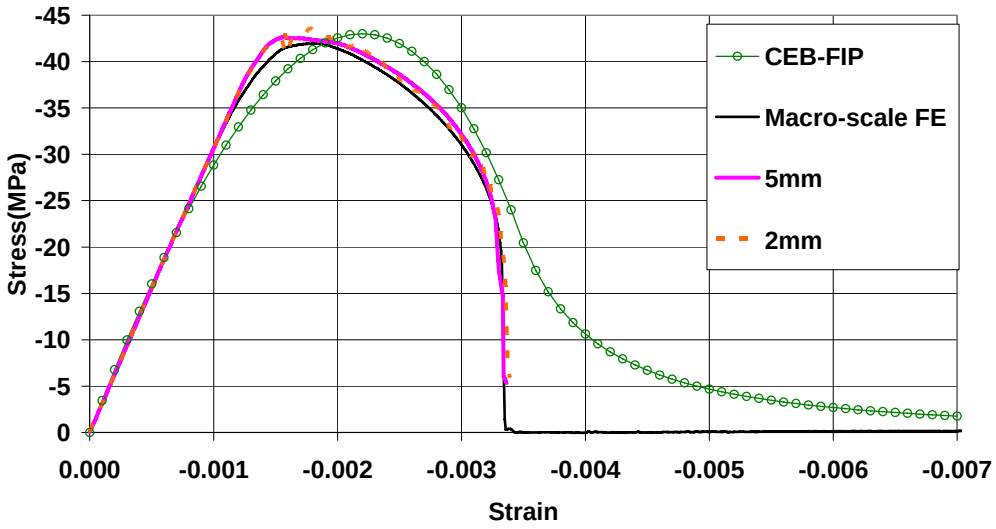

Figure 3-15 Macroscopic uniaxial compressive stress strain curves from the test specimens: one end fixed & one end frictionless ($l_w = h_c$, n=1.6, $G_c = 60G_f^I$)

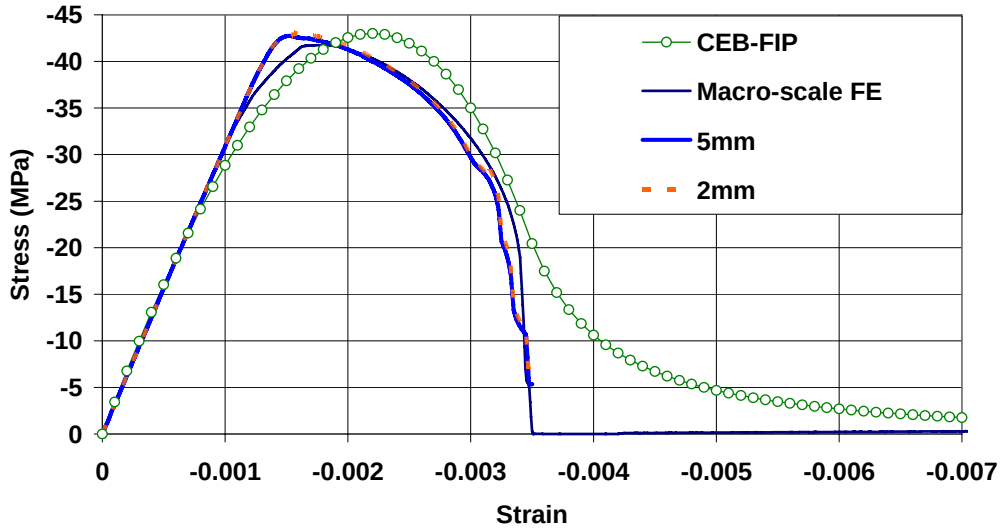

Figure 3-16 Macroscopic uniaxial compressive stress strain curves from the test specimens: two ends fixed ($l_w = h_c$, n=2.3, $G_c = 43G_f^I$)

For uniaxial compressive test with one end fixed and one end frictionless, with localized width equal to the element characteristic length for meso-scale modelling, $l_w = h_c$, "$G_c = 60G_f^I$"is found to give a nice match to the CEB-FIP(1993) compressive softening curve, which approximately corresponds to "n" equal to 1.6.

For uniaxial compressive test with two ends fixed, "$G_c = 43G_f^I$"is found to give a nice match to the CEB-FIP compressive softening curve, which approximately corresponds to "n" equal to 2.3.

For the two cases of uniaxial compressive test above compressive localization case dependency affects a lot, because the failure mode is compressive dominated. However, for general fracture modelling, i.e. notched beam test (Peterson 1981) or FRP pull-off test (Lu et al. 2004), tensile localization is still superior. In such cases, the compressive fracture energy G_c is about 100 times the Mode I fracture energy G_f^I with localization happening in every single element, say $l_w = h_c$ (Ozbolt and Reinhardt 2002).

3.4 Impact modelling of a concrete beam

Based on the static tensile and compressive investigation before, an impact test was modelled to see how the concrete model works in the high energy events. A three point bend concrete prism is simplified as 2D plane stress problem. The impact test was done by Du et al. (1992). The geometry is shown in Figure 3-17.

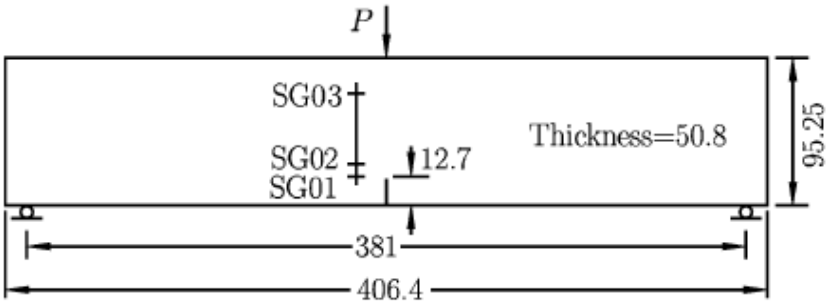

Figure 3-17 Impact test of a concrete beam (unit: *mm*) (Su et al. 2010)

The impact load history obtained from the test was input as the loading condition as in (Su et al. 2010a; Su et al. 2010b). The support condition is simply supported where one side of the support is constrained in both horizontal and vertical direction and another side is only restricted in vertical direction but can be moved in horizontal direction, although in normal impact tests the support are ideally to be pin-ended where both of supports are not allowed horizontal movement. The reason the author use simply supported boundary condition is the initial stiffness $k = 1 \times 10^5$ *MPa.mm*. From the eigenvalue analysis of the FE model, for simply supported beam the first model natural frequency is $\overline{\omega} = 4.8 \times 10^3$ *rad/s*, but it is 7.4×10^3 *rad/s* for pin-ended support conditions. The mass m of the beam is approximately 4.6 kg ($\rho = 2.5 \times 10^{-6}\, kg/mm^3$) between the two supports. According to $\overline{\omega} = \sqrt{\frac{k}{m}}$, only the simply supported boundary condition can satisfy the initial stiffness.

The impact load history obtained from the test (Figure 3-18) was input as the loading condition instead of modelling the striker drop for simplification.

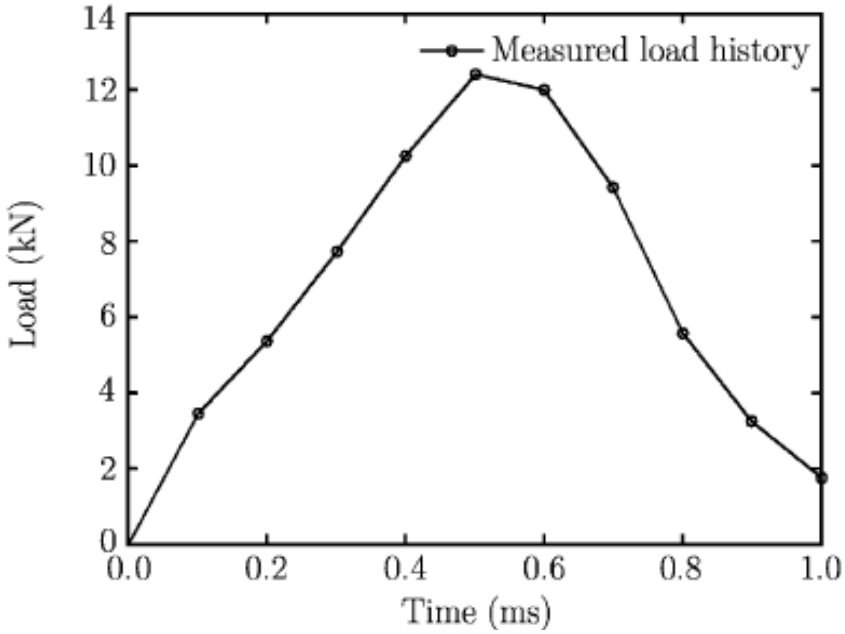

Figure 3-18 Input load history (Su et al. 2010)

Three strain gauges were located at the three points which showed in Figure 3-17 above. "SG" stands for strain gauge. The distance from the middle notch to the three strain gauges in horizontal direction is 0.5*inch*, 12.7*mm*. The distance from the centre of the SG01 to the bottom of the beam is 12.7*mm*. It is 25.4*mm* (1*inch*) and 76.2*mm* (3*inches*) for SG02 and SG03 respectively.

The concrete properties input are concrete unconfined compressive strength $f_c^{'}$=53 *MPa* to insure the concrete young's modulus $E = 34480 MPa$. The Poisson's ratio $v = 0.2$ and the density of the concrete is $\rho = 2.5 \times 10^{-6} kg/mm^3$. The b_2 is set as -0.15 to insure the Mode I fracture energy $G_f^I = 152$ *N/m*. Figure 3-19 is the load displacement curve comparison and Figure 3-20 is the strain time history comparison.

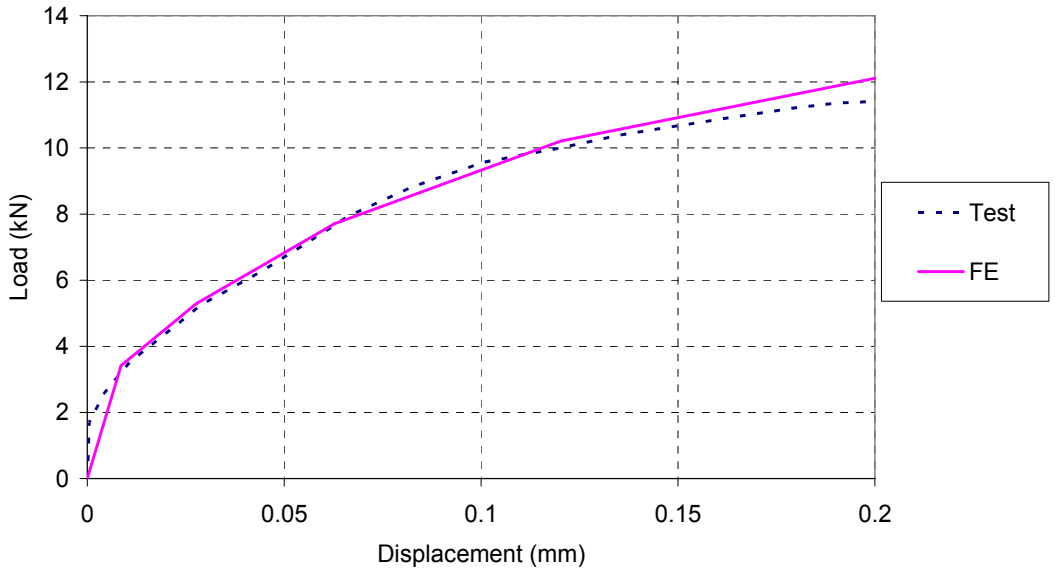

Figure 3-19 Load displacement curve comparison

It can be discovered that the strain reading from the FE for SG03 is quite close to the experiment result. But for SG01 and SG02, the readings are all lower than the tests. That is because the strain rate effects of the concrete properties have not been included to the current FE model. For the same concrete strength the strain rate effects are much more sensitive in tension than compression, where the dynamic increasing factor for tension is always much higher than compression when the strain rate is the same (Malvar and Crawford 1998). In the current case, SG01 and SG02 are located the place where the dominate stress state is tension due to bending. However SG03 is located at the place where the domain is compression.

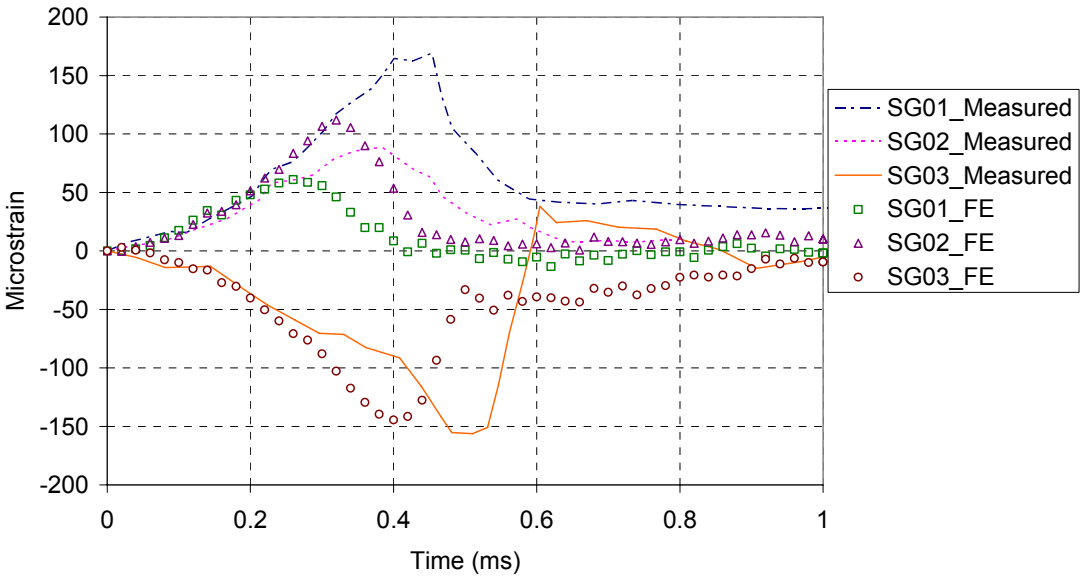

Figure 3-20 the strain time history comparison

3.5 Conclusions

Modelling of fracture in concrete is an important topic, and this is particularly so when a finite element analysis with a local material damage model is employed. Mesh-objectivity cannot be achieved without an appropriate consideration of the localization in the finite element model and its relationship to the fracture energy. For mesoscopic modelling where the element size is smaller than the standard concrete aggregate size, the localized width (or crack band) should be set as the element characteristic length. For tension-dominated problems the localization generally takes place in a single element width both in tension and compression. The results reported in this chapter prove that the uniaxial tension and compression stress strain curve in a single element is mesh dependent, but the overall behaviour becomes essentially mesh-independent due to keeping the tension and compression

fracture energy as constants. An evaluation of the relationship between the commonly used damage indices, such as the *SDF* employed in LS-DYNA, and the consumed fracture energy enables a clear identification of the actual fracture zone from the damage contour plots.

3.6 References

Bazant, Z.P. and Oh, B.H. (1983), "Crack band theory for fracture of concrete", *Materials and Structures (RILEM, Paris)*, 16: 155–177.

CEB-FIP (1993), Model Code 90. Lausanne.

Chen, G.M., Teng, J.G. and Chen, J.F. (2009), "Finite element simulation of IC debonding in FRP-plated RC beams: a dynamic approach", The 9th International Symposium on Fibre Reinforced Polymer for Concrete Structures (FRPRCS9), July, Sydney, Australia: 13-15.

Du, J., Yon, J.H., Hawkins, N.M., Arakawa, K. and Kobayashi, A. S. (1992), "Fracture process zone for concrete for dynamic loading", *ACI Materials Journal*, 89: 252-258.

Kwak, H.G. and Filippou, F.C. (1990), Finite element analysis of reinforced concrete structures under monotonic load. Research report of Department of Civil Engineering, U. C. Berkeley, No. UCB/SEMM-90/14.

Li, X.Q., Chen, J.F. and Lu, Y. (2010a), "On mode-I fracture modelling of concrete in LS-DYNA explicit", Proceedings (CD-ROM) of the 13th International Conference on Structural Faults + Repair, Edinburgh, UK.

Li, X.Q., Chen, J.F. and Lu, Y. (2010b), "Meso-scale modelling of FRP-to-concrete bond behaviour using LSDYNA", Proceedings of the 5th International Conference on FRP Composites in Civil Engineering, Beijing: 494-498.

Lu, X.Z., Ye, L.P., Teng, J.G. and Jiang, J.J. (2004), "Mesco-scale finite element model for FRP sheets/plates bonded to concrete", *Engineering structures*, 27:564-575.

LSDYNA (1998), Theory Manual Version 971, Livermore Software Technology Corporation.

LSDYNA (2007), Keyword User's Manual Version 971, Livermore Software Technology Corporation.

Malvar, L.J., and Crawford, J.E. (1998), "Dynamic increasing factors for concrete", Twenty-Eighth DDESB Seminar, Orlando, FL, August.

Malvar, L.J., Crawford, J.E. and Morrill, K.B. (2000), "K&C Concrete material model release3—automated generation of material model input", K&C documents, August.

Malvar, L.J., Crawford, J.E., Wesevich, J.W. and Simons, D. (1997), "A plasticity concrete material model for DYNA3D", *International Journal of Impact Engineering*, 19(9-10): 847-873.

Malvar, L.J. and Simons, D. (1996), "Concrete material modelling in explicit computations", Workshop on Recent Advances in Computational Structural Dynamics and High Performance Computing, USAE Waterways Experiment Station, April 24-26.

Markeset, G. and Hillerborg, A. (1995), "Softening of Concrete in Compression Localization and size effects", *Cement and Concrete Research*, 25(4): 702-708.

Nakamura, H. and Higai, T. (1999), "Compressive fracture energy and fracture zone length of concrete", *Nippon Konkurito Kogaku Kyokai Ronbunshu*, 51(E):259-272.

Ozbolt, J. and Reinhardt, H.W. (2002), "Numerical study of mixed-mode fracture in concrete", *International Journal of Fracture*, 118: 145–161.

Peterson, P.E. (1981), "Crack growth and development of fracture zone in plain concrete and similar materials", Report TVBM-1006, Lund Institute of Technology, Lund, Sweden.

Saleh, A.L. and Aliabadi, M.H. (1995), "Crack growth analysis concrete using boundary element method", *Engineering Fracture Mechanics*, 51:533–545.

Scotta, R., Vitaliania, R., Saettab, A., Oñate, E. and Hanganuc, A. (2001), "A scalar damage model with a shear retention factor for the analysis of reinforced concrete structures: theory and validation", *Computers & Structures*, 79 (7): 737-755.

Schwer, L.E. and Malvar, L.J. (2005), "Simplified concrete modelling with *mat_concrete_damage_rel3", JRI LS-Dyna User Week, Nagoya, Japan.

Su, X.T., Yang, Z.J. and Liu, G.H. (2010a), "Finite element modelling of complex 3D static and dynamic crack propagation by embedding cohesive elements in ABAQUS", *Acta Mechanica slida Sinica*, 23(3): 271-282.

Su, X.T., Yang, Z.J. and Liu, G.H. (2010b), "Monte Carlo simulation of complex cohesive fracture in random heterogeneous quasi-brittle materials: a 3D study", *International Journal of Solids and Structures*, 47(7):2336-2345.

Tu, Z.G. and Lu, Y. (2009), "Evaluation of typical concrete material models used in hydrocodes for high dynamic response simulations", *International Journal of Impact Engineering*, 36(1):132-146.

Ueda,T., Sato,Y. and Asano,Y. (1999), "Experimental study on bond strength of continuous carbon fiber sheet", Proceedings of 4th int. sym. on fiber reinforced polymer reinforcement for reinforced concrete structure: 407–416.

Van Mier, J. G.M. (1984), Strain-softening of Concrete under Multiaxial Loading Conditions, PhD Thesis, Eindhoven University of Technology.

Van Mier, J. G.M. (1997), Fracture Processes of Concrete: Assessment of Material Parameters for Fracture Models, CRC Press, Inc.

Chapter 4 Modelling of static pull-off test

4.1 Introduction

Studies for FRP retrofitted concrete structure against impact (Bhatti et al. 2011; Boyd et al. 2008), blast (Buchan and Chen 2007; Crawford et al. 1997; Heffernan et al. 2011; Wu et al. 2009) and earthquake (Niroomandi et al. 2010; Pantelides and Gergely 2007; Teng et al. 2007) have confirmed that FRP retrofitting was effective in increasing the structural resistance against these dynamic loadings as well as preventing fragmentation-induced damage to people and properties. It has also been observed that, as for static loading cases, debonding on the FRP-concrete interface is one of the predominant failure modes under dynamic loadings. However, most of these studies were either experimental (Tarapada and Debabrata 2006) with limited analytical investigation (De Lorenzis and La Tegola 2005), or macro-scale numerical simulations focused on the global structural behaviour (Crawford et al. 2001). Little attention has been paid to the critical FRP-to-concrete interfacial bond behaviour under dynamic loadings. The dynamic bond behaviour could be very different from that under static or quasi-static loadings because of the effects of higher strain rates, concrete deterioration due to the incident or reflected stress wave propagation before debonding mechanics, and fracture mechanics under impulsive load. Accurate quantification of these effects by experiments is very demanding both economically

and technically, especially for high loading rate scenarios such as impact and blast, where advanced finite element (FE) simulations can play a viable role.

There have been many static finite element studies on concrete structures strengthened by FRP composites (Chen et al. 2011; Chen and Teng 2001; Kim and Vecchio 2008; Lu et al. 2004; Teng et al. 2002; Yang et al. 2003). Because most debonding failures occur in a thin layer of concrete adjacent to the FRP rather than in the adhesive layer at the FRP-to-adhesive or adhesive-to-concrete interfaces, modelling fracture and damage in concrete is crucial.

In FE analysis, there are mainly two models for concrete cracking: the smeared crack model based on continuum mechanics (Bazant and Oh 1983) and the discrete crack model explicitly modelling discontinuity (Yang et al. 2003). Although the latter is capable of modelling individual macro-cracks, the need of re-meshing or embedding cohesive elements(Su et al. 2010; Yang et al. 2009) makes it cumbersome to model a large number of meso-scale distributed cracks during debonding in FRP-strengthened concrete structures. The smeared crack model is more suitable for such cases because it does not require re-meshing and can make use of concrete stress-strain curves that are readily available for static and dynamic loadings. This model has indeed been adopted in most of existing studies (Chen and Tao 2010; Lu et al. 2004) to investigate the meso-scale debonding behaviour of FRP-to-concrete joints. However, all these studies considered static or quasi-static loadings only.

There exist two classes of smeared crack models, local and non-local (Li et al. 2010b). Concrete damage is calculated in each element independently in the former,

whereas in the latter damage calculation in an element takes into account the stiffness degradation in its surrounding elements, depending on the crack band width and the element size. The crack band width, often approximated as three times the maximum aggregate size under static loading (Bazant and Oh 1983), may be regarded as a material property. However, no consensus on its value has been reached for dynamic loadings due to the lack of reliable experimental data. In FRP-bonded concrete structures under static loading, debonding usually happens in 2-5*mm* depth of the concrete adjacent to the FRP (Lu et al. 2004). This depth is smaller than the aggregate sizes 10-40*mm* in normal strength concrete, and much smaller than the assumed crack band width, making the non-local models unsuitable for modelling the FRP-concrete debonding behaviour.

This study develops a finite element model based on the K&C local damage concrete model in LS-DYNA (LSDYNA 2007; Malvar et al. 2000; Malvar et al. 1997; Malvar and Simons 1996) for accurate prediction of debonding behaviour of the FRP-to-concrete bonded joint. The model was first validated by a large number of specimens under static pull-off tests. It was then applied to simulate similar tests under high strain rate loadings.

4.2 Static pull-off test modelling

4.2.1 The FE model

In various debonding failure modes, the stress state of the interface is similar to that in a pull-off test in which a plate is bonded to a concrete prism and is subject to tension (Lu et al. 2004) presented in Figure 4-1.

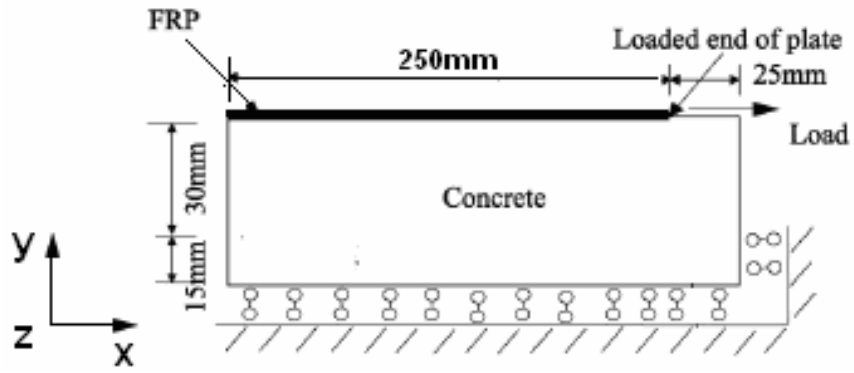

Figure 4-1 Pull-off test FE model geometry

The FRP-to-concrete pull-off test specimen S-CFS-400-25 reported in (Wu et al. 2001) was used as the reference case in this study. The specimen consisted of a 275×100×100*mm* (length × width × depth) concrete prism bonded with a 0.22*mm* thick and 40*mm* wide FRP sheet with a bond length of 250*mm*. The concrete had a cylindrical compressive strength of 57.6*MPa*. The FRP had a modulus of elasticity of 230*GPa*.

The same geometry and boundary conditions as Lu et al.'s (2004) FE model were adopted (Figure 4-1). The test was modelled as a 2D plane stress problem but the predicted results including loads, stresses, strains and slips were corrected according to Chen and Teng's (2001) width effect factor to consider the 3D effects.

There are generally two approaches to modelling debonding in FRP-strengthened RC structures: one approach is to employ a layer of interface elements between the FRP and the concrete, in which debonding is simulated as failure of the interface elements, when an existing bond-slip model is available; another approach is that the use of interface elements is avoided, and debonding is directly simulated by modelling thecracking and failure of concrete elements adjacent to the adhesive layer. Compared to the first modelling approach, an existing bond-slip model is not necessary here. Furthermore, the second approach has the capability of predicting the bond–slip relationship for use in a model following the first approach (Lu et al. 2004). The aim of the current chapter is to find a static modelling base for further dynamic bond-slip mechanics investigation. The concrete dynamic properties will be involved after properly modelling the static pull-off test. Therefore, the second approach is adopted and the concrete modelling is of crucial importance.

The K&C concrete model employed in this study requires a 3D setting. Therefore, in the present model both the FRP plate and the concrete were modelled using the eight node hexahedron 3D solid elements. To simulate a 2D problem the width direction of the test specimen (z direction in Figure 4-1) was represented by a single element of unit thickness. The model thus consists of a single layer of elements. All nodes on one face (at z=0) of this layer of elements were restrained for displacement in z direction to simulate the plane stress condition.

The FRP was modelled as an isotropic linear elastic material with a thickness t_p=1mm and Young's modulus E_p = 50.6GPa so that its axial rigidity $E_p t_p$ remains

the same as in the test. Because debonding of FRP in the pull-off test usually occurs at a small distance beneath the adhesive-concrete interface in the concrete, the FRP was assumed to be perfectly bonded to the concrete prism in the current study. The specimen was loaded with a time dependent displacement at the loaded end in the FE model.

It should be noted that the K&C concrete damage model is a smeared crack band model with a default localisation width l_w=25.4mm which is presumably applicable when the characteristic length of the element is larger than 25.4mm. However, if the default l_w is adopted and the element size is small, for example, less than 25.4mm for the first-order cubic elements, no mesh objectivity of results can be achieved. To rectify this, l_w should be set equal to the element characteristic length h_c, so that the Mode I fracture energy G_f^I remains a material constant in each element. In other words, the following equation should hold when the uniaxial tensile stress strain curve is input as the tensile constitutive law for concrete

$$\int \sigma d\varepsilon = \frac{G_f^I}{h_c} \tag{4-1}$$

There is a parameter b_2 in K&C concrete damage model (Equation (2-36)) which governs the softening branch of the concrete uniaxial tension. Its default value is 1.35 based on laboratory material characterization of 45.6MPa concrete, which is used as the "standard concrete" in many numerical simulations (Schwer and Malvar 2005) However, this default value may not produce the correct fracture energy G_f^I when

the concrete strength is different so the b_2 value may need to be adjusted accordingly. Generally, a reduction in b_2 increases G_f^I. In the reference pull-off test, G_f^I was found to be $102N/m$ according to CEB-FIP (1993). To produce this value, b_2 was set to 0.45. Here b_1 is set as 1.6 so that the compressive fracture energy is approximately 100 times the tensile fracture energy for tensile dominated pull-off test modelling due of which the localization happens in every single element.

4.2.2 FE calibration factor according to Chen and Teng's model

As mentioned before, the model was simplified as a plane stress problem, where the widths of the FRP b_p and concrete b_c are the same. However in the test, the actual width of FRP plate b_p and concrete prism b_c in the test is $40mm$ and $100mm$, respectively. The width effect factor β_w must be considered for dealing with the numerical output data including stress and strain. It is calculated according to Chen and Teng (2001):

$$\beta_w = \sqrt{\frac{2 - b_p / b_c}{1 + b_p / b_{ct}}} \tag{4-2}$$

4.2.3 Static modeling results

As a basis of introducing following dynamic aspects discussion into the pull-off test modelling, the explicit method was chosen for the current static modelling instead of implicit method. When explicit solvers are used to model static and quasi-static

problems, the loading time should be long enough to avoid the dynamic effect, but not too long for computational efficiency. The largest possible time step Δt_{cr} without causing numerical instability is usually the time for the P-wave to travel through the smallest element in the model. The dynamic effect becomes negligible when the total loading time is greater or equal to $10T$, where T is the natural period of the whole structure (Chen et al. 2009). A smooth velocity loading is advantageous considering that the initial displacement, velocity and acceleration are all equal to zero. A maximum displacement of 1.6*mm* was applied for the reference test specimen. More details can be found in (Li et al. 2010a).

Figure 4-2 shows the computed load-slip responses with three mesh sizes. It can be seen that the loading capacity increased with a reduction of the mesh size in general but the difference was already very small between those from the 1*mm* and 0.5*mm* meshes. The peak load 14.5*kN* predicted from the 0.5*mm* mesh was closer to the test result 14.1*kN* than the FE prediction 13.8*kN* in Lu et al. (2004), and theoretical prediction 11.4*kN* in Chen and Teng (2001). The model can thus simulate the static FRP-to-concrete bond behaviour in terms of the load-carrying capacity with reasonable accuracy and mesh objectivity.

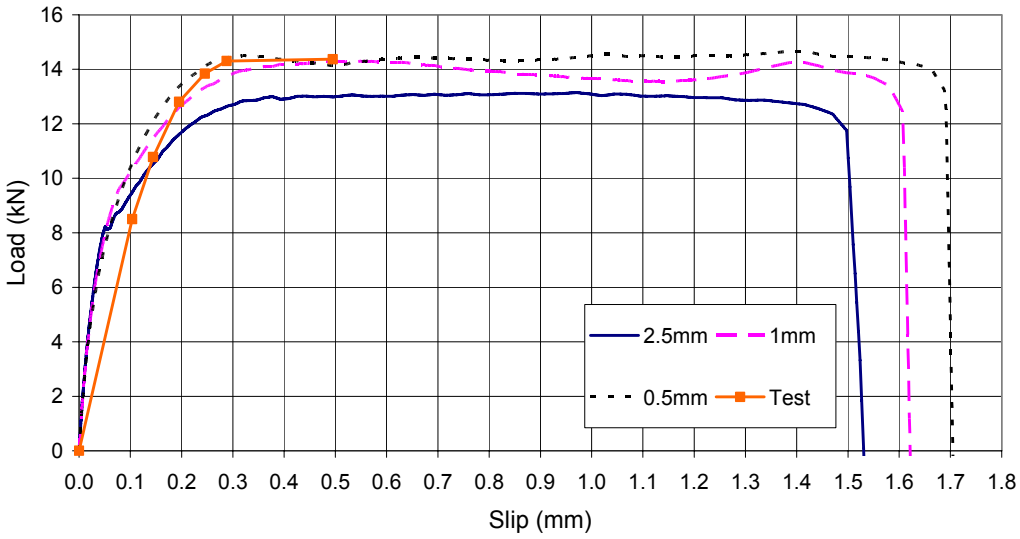

Figure 4-2 Pull-off test load-slip curves: mesh convergence study

The numerical modelling successfully reproduced the debonding failure which occurred in the test, as described by damage contours at different loading stages shown in Figure 4-3.

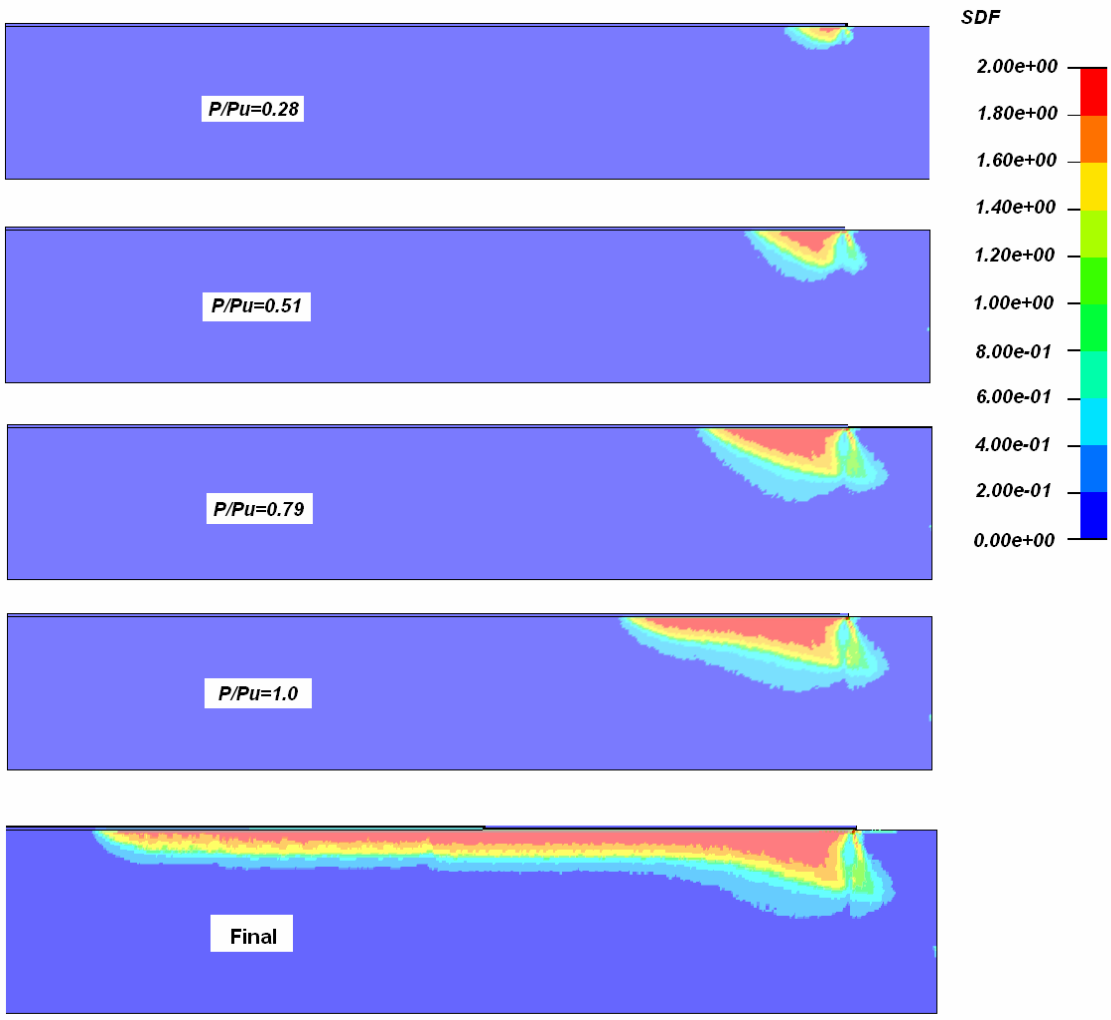

Figure 4-3 Damage contour

The FE results from the 0.5*mm* mesh were further analysed here in terms of the FRP strain distribution and the bond-slip relationship. Figure 4-4 shows that the FRP strain distributions at different loading levels were in close agreement with the test data of Wu et al. (2001) and the FE predictions of Lu et al. (2004). Note that the load was normalised in Figure 4-4 by their respective ultimate load P_u from the three studies.

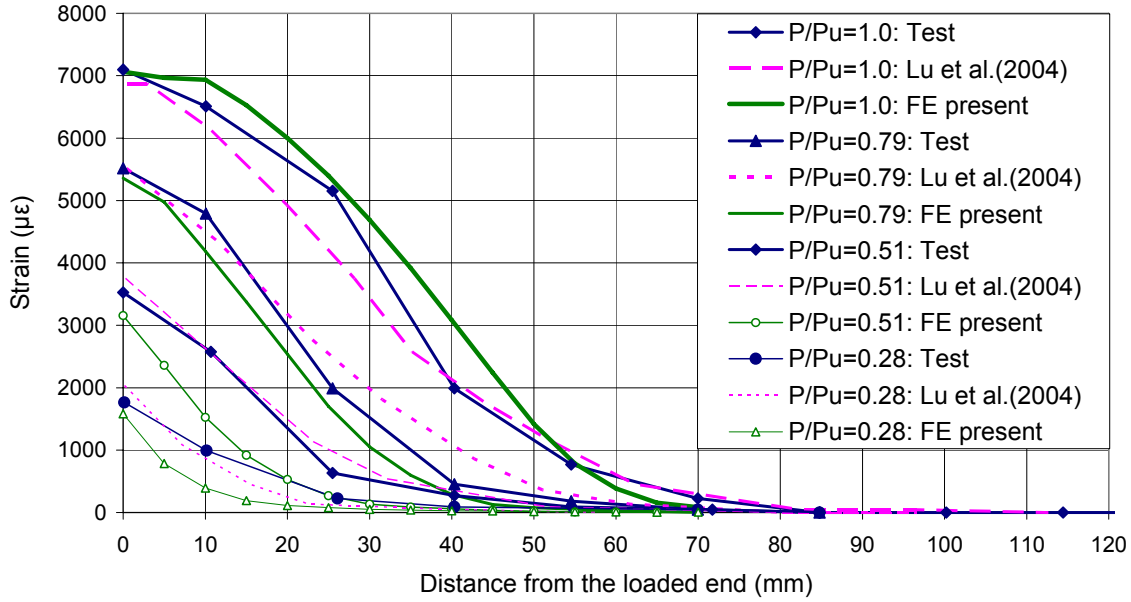

Figure 4-4 FRP strain distribution

Figure 4-5 shows the local bond-slip relationship obtained at 19.5*mm* from the loaded end via the following equation:

$$\tau = \frac{\Delta\sigma_f}{\Delta x} t_p \qquad (4\text{-}3)$$

in which τ is the local bond stress, $\Delta\sigma_f$ the difference of axial stress between two adjacent FRP elements, Δx the length of the FRP element, and t_p the thickness of the FRP plate.

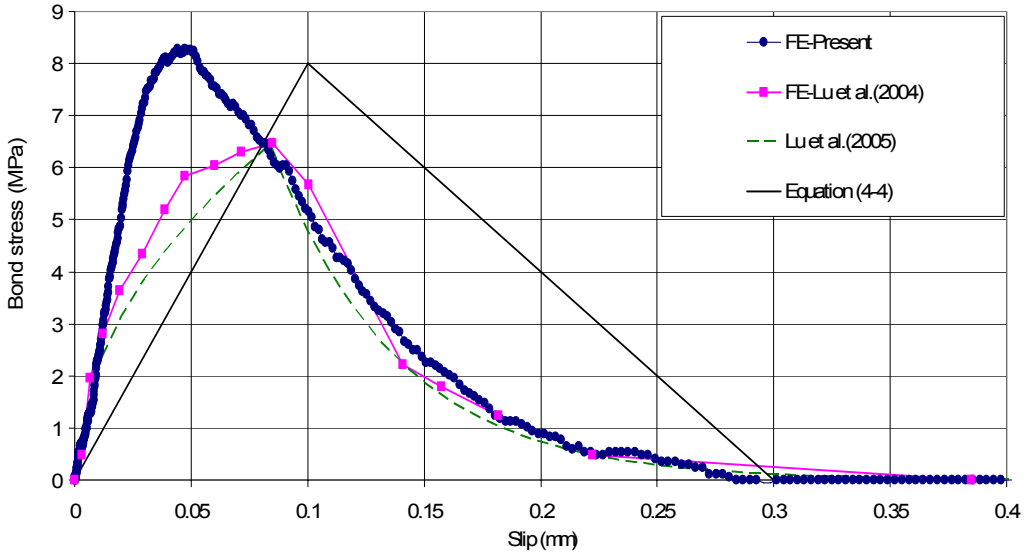

Figure 4-5 Local bond-slip curve

The bond-slip curves obtained from the test (Wu et al. 2001), the FE analysis in Lu et al. (2004) and a "simplified model" (Lu et al. 2005) are also shown for comparison. The area under the local bond-slip curve is slightly larger than that in (Lu et al. 2004), but close to that under the bi-linear curve deduced from the test data (Wu et al. 2001). That is because Lu's final simplified model (Lu et al. 2005) for bond-slip relationship prediction is based on Chen and Teng's (2001) equation. The evidence was according to Equation (4-12) presented below, the ultimate load obtained from Lu's prediction (Lu et al. 2005) is the equal to Chen and Teng's (2004) analytical prediction of the ultimate load. It should be noted that the local bond-slip curve obtained from an FE analysis is different at different locations, depending on their relative position to the micro-cracks in the concrete. The bi-linear bond-slip curve in Figure 4-5 was deduced based on the global load-displacement response of the pull-off test according to Equation (4-4) too, so it represents an average of the local bond-

slip relation over the bond length. From the local bond slip curves predicted from different FE models at a particular position, one can not tell which model is better.

$$\tau_{\max} = \frac{P_u^2}{E_p t_p b_p^2 s_f} \tag{4-4}$$

where $\tau_{\max}$ is the peak value of the bond stress; P_u is the ultimate load at the FRP end from the load slip curves; E_p is the elastic Young's modulus of the FRP plate; t_p is the thickness of the FRP plate; b_p is the FRP plate width in the test; s_f is the final slip of the bond-slip curves.

4.3 Shear dilation

Dilation is a measure of volume increase when the material is under shear. In the Mohr-Coulomb material model, a dilation angel α is used, varying from zero for non-associated flow rules to the friction angle φ for associated flow rules. According to Chandra et al. (2010), lower dilation angles are generally used for soft rocks and higher values for hard brittle rocks. A good starting estimate is $\alpha = \varphi/3$ for soft rocks and $\alpha = 2\varphi/3$ for hard rocks, and zero for very weak rocks. However, there are no clear guidelines for the selection of dilation angle α in concrete.

An associated flow rule results in plastic volume expansion in excess of that indicated by test data, and a non-associated Prandtl-Reuss flow rule does not allow

for any plastic volume expansion, which is also not correct for concrete. In the K&C concrete damage model, a partially associated flow rule combining these two rules is used. This flow rule is characterised by an input parameter ω, representing the ratio of associated plastic flow to Prandtl-Reuss plastic flow. The plastic flow is purely deviatoric for $\omega = 0$ and is associative for $\omega = 1$, and interpolated for ω in between (Baylot and Bevins 2007). It controls the amount of plastic volume change in the material.

To investigate the effects of the shear dilation on the structural behaviour of FRP-concrete bonded joints, the pull-off test done by Yao (2004) was modelled using various ω. The concrete's strength was $f_c' = 23.8MPa$. The load-slip curves are compared with test data in Figure 4-6.

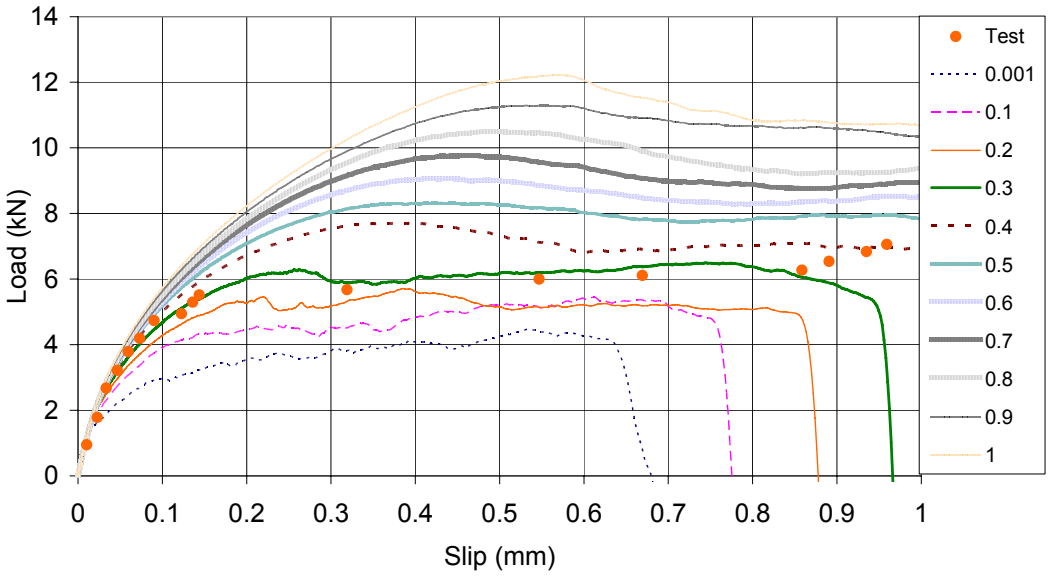

Figure 4-6 Load slip curves (FE results) with different compared with test data Concrete strength, test result from Yao (2004).

It looks like that ω=0.3 led to the best results for this specimen. The peak load increases almost linearly as ω for both concrete strength, as shown in Figure 4-7.

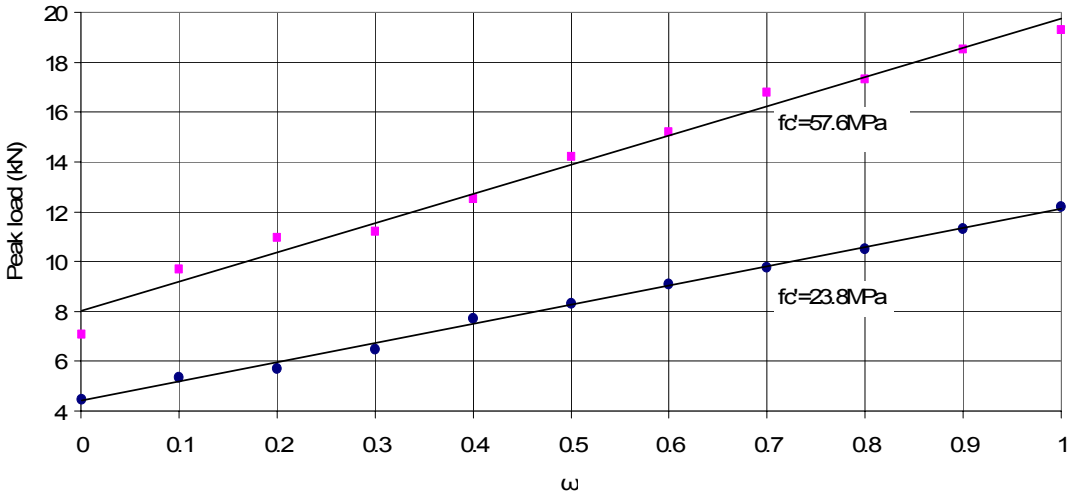

Figure 4-7 Peak Load versus ω

This can be explained by the different evolution processes of pressure and damage contours from different ω, as shown in Figure 4-8 and Figure 4-9 for $f_c' = 23.8MPa$. It can be seen that both the area of the pressure zone and the depth of the debonding zone are higher from ω=0.5 than those from ω=0.3. This is because the higher shear dilation from ω =0.5 caused stronger confinement and mobilised more elements to resist debonding, leading to higher loading capacity.

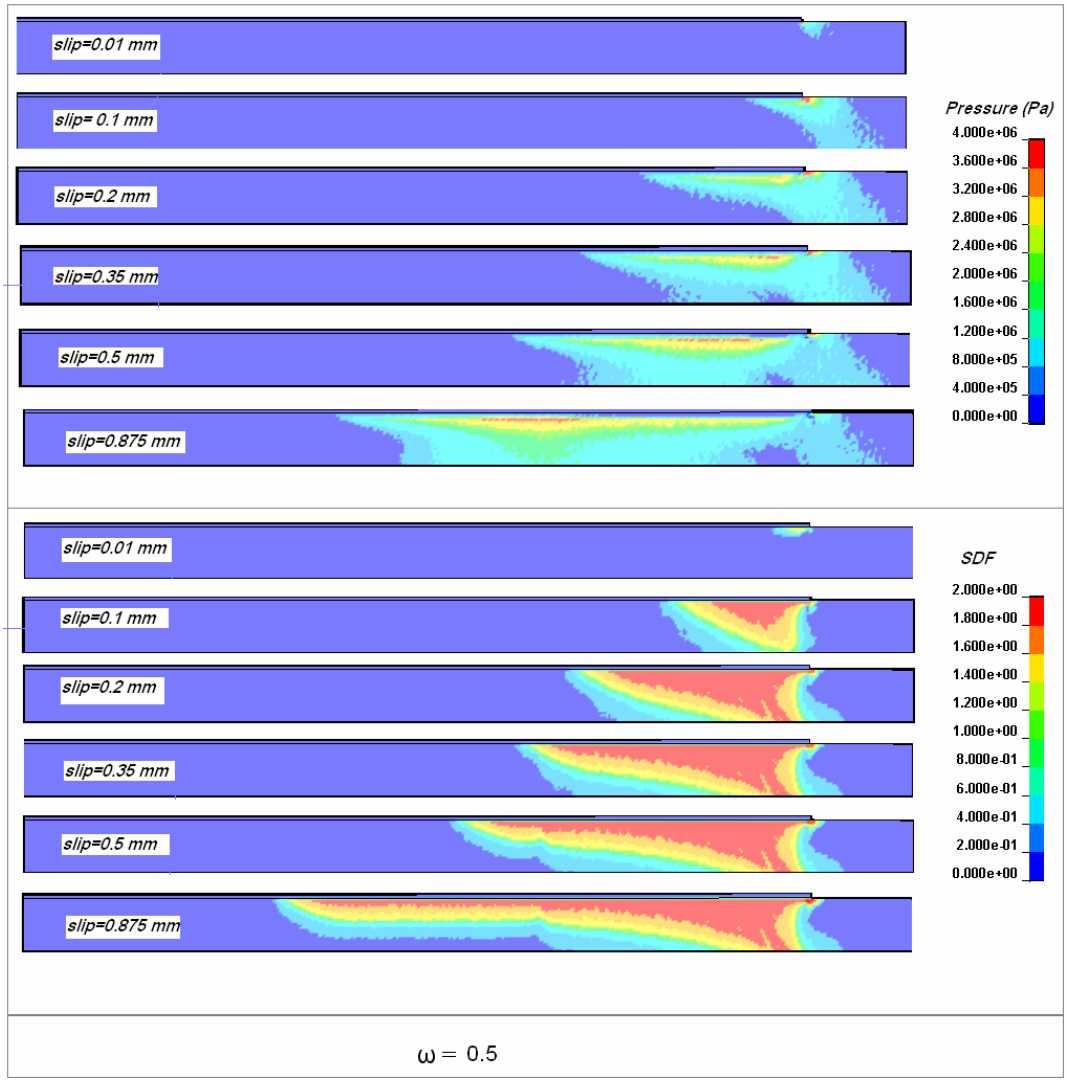

Figure 4-8 Pressure and *SDF* contours for ω=0.5

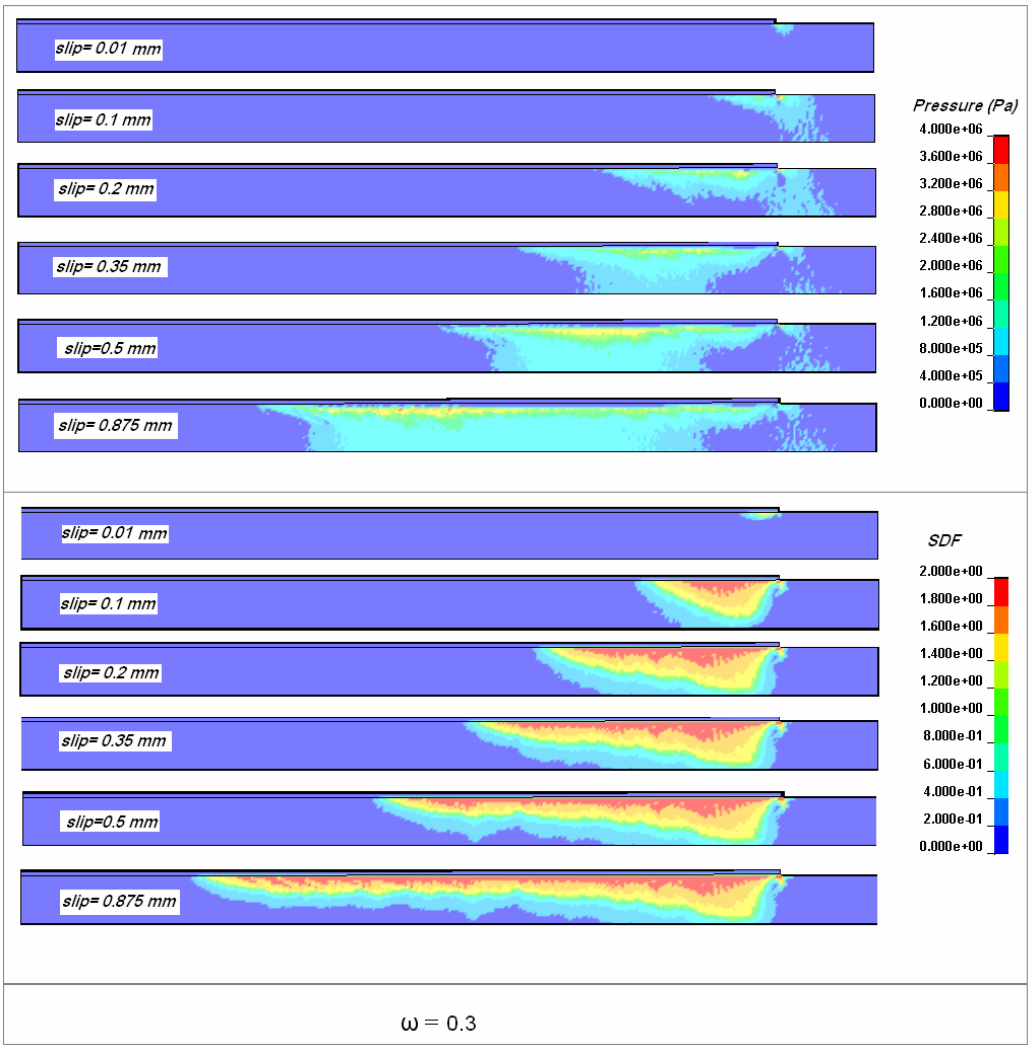

Figure 4-9 Pressure and *SDF* contours for ω=0.3

A few more FRP-concrete bonded joint specimens tested with different $f_c^{'}$ were modelled using the K&C model with various ω, including IV-12 and III-7 in Yao et al. (2005), B-1 in Ueda et al. (1999), and C4 in Wu et al. (2010). The best-fit peak loads and corresponding ω are listed in Figure 4-10. The data are also described in Table 4-1 with a best fitting curve relating ω and $f_c^{'}$ as

$$\omega = 4\times10^{-6} f_c^{'3} - 0.0003 f_c^{'2} + 0.0092 f_c^{'} + 0.2015 \quad (4\text{-}5)$$

Table 4-1 the points for determination of Equation (4-5)

Test specimen	$f_c^{'}(MPa)$	ω	P_{Test}	P_{FE}
IV-12	19.8	0.3	5.67	5.60
III-7	27.1	0.32	4.78	4.73
B-1	40.9	0.35	20.60	19.99
C4	47.1	0.4	10.64	10.16
WU-1	57.6	0.5	14.1	14.21

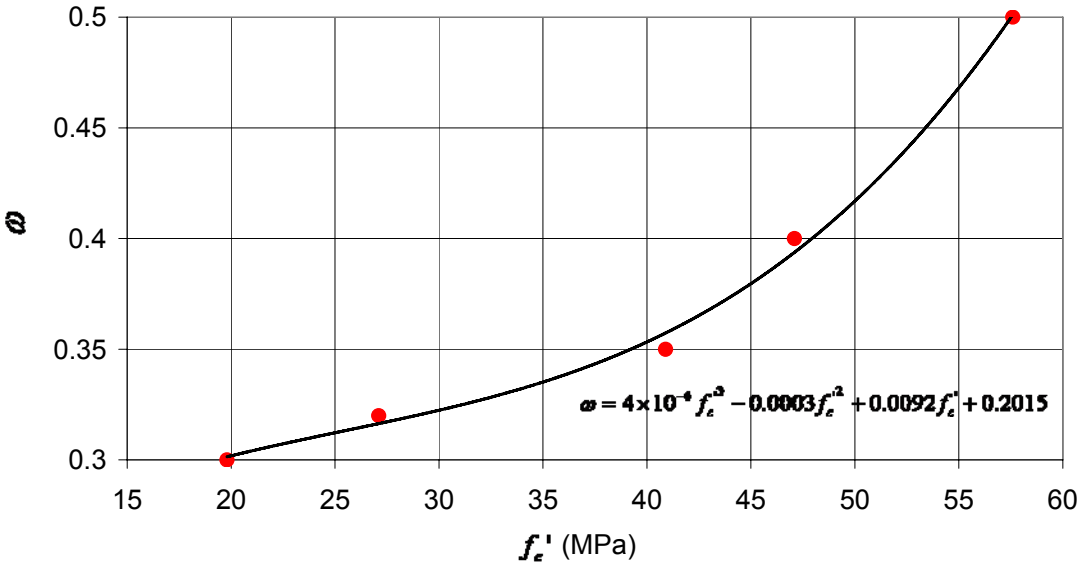

Figure 4-10 Relationship between ω and $f_c^{'}$

To examine the applicability of the above equation, a large number of FRP-concrete bonded joints tested by Chen and Teng (2001), Yao (2004), Wu et al. (2001), Björn Täljsten (1997) , Ueda et al. (1999) and Wu et al. (2010) were modelled, using ω calculated by Equation (4-5). All these specimens failed by concrete fracture only.

The results are listed in Table 4-2 and the predicted peak loads are compared with test data in Figure 4-11 . It can be seen that Equation (4-5) resulted in good agreement for most specimens and can thus be used as a sound guideline to select the dilation parameter ω in the K&C model.

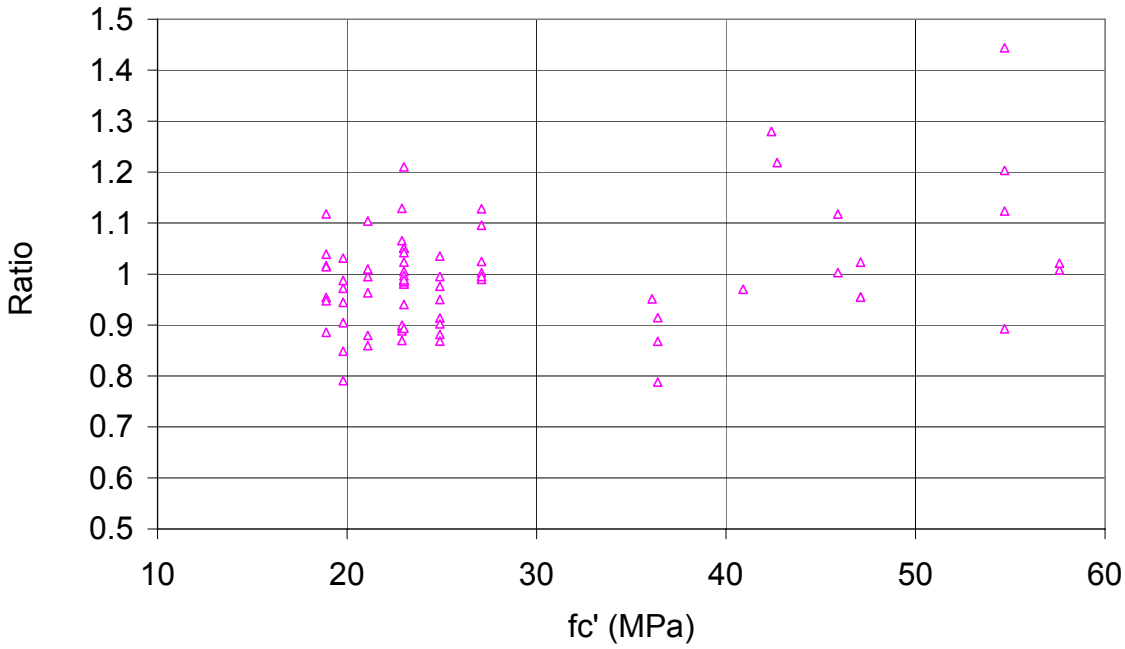

Figure 4-11 FE/Test ultimate load ratios for different concrete strengths

Table 4-2 Results of the FE modelling with concrete strength dependent dilation according to Equation (4-5)

Specimens	f_c' (MPa)	b_c (mm)	b_p (mm)	L (mm)	E_p (GPa)	t_p (mm)	ω	P_{pred} (kN)	P_{test} (kN)	P_{FE} (kN)
IV-1	18.9	150	25	95	256	0.165	0.30	5.72	5.86	5.59
IV-2	18.9	150	25	95	256	0.165	0.30	5.72	5.9	5.59
IV-5	18.9	150	25	95	256	0.165	0.30	5.72	5	5.59
IV-7	18.9	150	25	95	256	0.165	0.30	5.72	5.5	5.59
IV-9	18.9	150	25	95	256	0.165	0.30	5.72	5.38	5.59
IV-11	18.9	150	25	95	256	0.165	0.30	5.72	5.51	5.59
IV-3	19.8	150	25	95	256	0.165	0.30	5.8	5.43	5.60
IV-4	19.8	150	25	95	256	0.165	0.30	5.8	5.76	5.60
IV-6	19.8	150	25	95	256	0.165	0.30	5.8	7.08	5.60
IV-8	19.8	150	25	95	256	0.165	0.30	5.8	5.93	5.60
IV-10	19.8	150	25	95	256	0.165	0.30	5.8	6.6	5.60
IV-12	19.8	150	25	95	256	0.165	0.30	5.8	5.67	5.60
IV-14	19.8	150	25	95	256	0.165	0.30	5.8	6.19	5.60
V-1	21.1	150	15	95	256	0.165	0.30	3.71	3.81	3.79
V-2	21.1	150	15	95	256	0.165	0.30	3.71	4.41	3.79

Specimens	f_c' (MPa)	b_c (mm)	b_p (mm)	L (mm)	E_p (GPa)	t_p (mm)	ω	P_{pred} (kN)	P_{test} (kN)	P_{FE} (kN)
V-3	21.1	150	25	95	256	0.165	0.30	5.89	6.26	6.03
V-4	21.1	150	50	95	256	0.165	0.30	10.51	12.22	10.75
V-5	21.1	150	75	95	256	0.165	0.30	14.1	14.29	14.43
V-6	21.1	150	100	95	256	0.165	0.30	16.82	15.58	17.20
II-1	22.9	150	25	95	256	0.165	0.30	6.02	5.2	5.87
II-2	22.9	150	25	95	256	0.165	0.30	6.02	6.75	5.87
II-3	22.9	150	25	95	256	0.165	0.30	6.02	5.51	5.87
II-4	22.9	150	25	190	256	0.165	0.30	6.02	7.02	6.28
II-5	22.9	150	25	190	256	0.165	0.30	6.02	7.07	6.28
II-6	22.9	150	25	190	256	0.165	0.30	6.02	6.98	6.28
I-1	23	150	25	75	256	0.165	0.30	5.72	4.75	5.75
I-2	23	150	25	85	256	0.165	0.30	5.96	5.69	5.98
I-3	23	150	25	95	256	0.165	0.30	6.02	5.76	6.05
I-4	23	150	25	95	256	0.165	0.30	6.02	5.76	6.05
I-5	23	150	25	95	256	0.165	0.30	6.02	6.17	6.05
I-6	23	150	25	115	256	0.165	0.30	6.02	5.96	6.10

Specimens	f_c' (MPa)	b_c (mm)	b_p (mm)	L (mm)	E_p (GPa)	t_p (mm)	ω	P_{pred} (kN)	P_{test} (kN)	P_{FE} (kN)
I-7	23	150	25	145	256	0.165	0.30	6.02	5.95	6.20
I-8	23	150	25	190	256	0.165	0.30	6.02	6.68	6.28
I-9	23	150	25	190	256	0.165	0.30	6.02	6.35	6.28
I-10	23	150	25	95	256	0.165	0.30	6.02	6.17	6.05
I-11	23	150	25	75	256	0.165	0.30	5.72	5.72	5.75
I-12	23	150	25	85	256	0.165	0.30	5.96	6	5.98
I-13	23	150	25	95	256	0.165	0.30	6.02	6.14	6.05
I-14	23	150	25	115	256	0.165	0.30	6.02	6.19	6.10
I-15	23	150	25	145	256	0.165	0.30	6.02	6.27	6.20
I-16	23	150	25	190	256	0.165	0.30	6.02	7.03	6.28
VII-1	24.9	150	25	95	256	0.165	0.31	6.14	6.8	6.46
VII-2	24.9	150	25	95	256	0.165	0.31	6.14	6.62	6.46
VII-3	24.9	150	25	145	256	0.165	0.31	6.14	7.33	6.46
VII-4	24.9	150	25	145	256	0.165	0.31	6.14	6.49	6.46
VII-5	24.9	150	25	190	256	0.165	0.31	6.14	7.07	6.46
VII-6	24.9	150	25	190	256	0.165	0.31	6.14	7.44	6.46

Specimens	f_c' (MPa)	b_c (mm)	b_p (mm)	L (mm)	E_p (GPa)	t_p (mm)	ω	P_{pred} (kN)	P_{test} (kN)	P_{FE} (kN)
VII-7	24.9	150	25	240	256	0.165	0.31	6.14	7.16	6.46
VII-8	24.9	150	25	240	256	0.165	0.31	6.14	6.24	6.46
III-1	27.1	150	25	100	256	0.165	0.32	6.27	5.94	6.70
III-2	27.1	150	50	100	256	0.165	0.32	11.19	11.66	11.95
III-3	27.1	150	75	100	256	0.165	0.32	15.02	14.63	16.03
III-4	27.1	150	100	100	256	0.165	0.32	17.91	19.07	19.12
III-7	27.1	100	25.3	100	22.5	1.27	0.32	4.92	4.78	4.73
III-8	27.1	100	50.6	100	22.5	1.27	0.32	8.3	8.02	7.98
C1	36.1	228.6	25.4	76.2	108.48	1.016	0.33	8.90	8.46	8.05
C14	36.4	228.6	25.4	101.6	108.48	1.016	0.33	10.67	12.80	10.09
C15	36.4	152.4	25.4	152.4	108.48	1.016	0.33	10.86	11.90	10.33
C16	36.4	152.4	25.4	203.2	108.48	1.016	0.33	11.09	11.57	10.58
B-1	40.9	500	100	200	230.00	0.11	0.35	21.04	20.60	19.99
M4	42.4	100	50	75	380.00	0.165	0.36	12.72	10.00	12.80
M6	42.7	100	50	65	230.00	0.22	0.36	11.26	9.55	11.64
B-2	45.9	500	100	200	230.00	0.33	0.38	37.50	38	38.11

Specimens	f_c' (MPa)	b_c (mm)	b_p (mm)	L (mm)	E_p (GPa)	t_p (mm)	ω	P_{pred} (kN)	P_{test} (kN)	P_{FE} (kN)
B-3	45.9	500	100	200	230.00	0.33	0.38	37.50	34.1	38.11
C2	47.1	228.6	25.4	76.2	108.48	1.016	0.39	9.96	9.93	10.16
C3	47.1	228.6	25.4	76.2	108.48	1.016	0.39	9.96	10.64	10.16
C4	47.1	228.6	25.4	76.2	108.48	1.016	0.39	9.96	10.64	10.16
C100_50A	54.7	200	50	100	170.00	1.25	0.46	25.32	17.3	24.98
C200_50A	54.7	200	50	200	170.00	1.25	0.46	31.67	27.5	30.90
C300_50A	54.7	200	50	300	170.00	1.25	0.46	31.67	35.1	31.33
C400_50A	54.7	200	50	400	170.00	1.25	0.46	31.67	26.9	32.37
WU-1	57.6	100	40	250	230	0.22	0.5	11.32	14.1	14.21
WU-2	57.6	100	40	250	390	0.501	0.5	22.24	23.5	24

4.4 Rate effects on FRP-to-concrete bond behaviour

4.4.1 Dynamic Increasing Factor (DIF)

For concrete structures subjected to transient dynamic loadings, their response at very high strain rates (e.g., up to 1000/s for blast) is often sought. At such high strain rates, the apparent or engineering strength of concrete can increase significantly. This

is often described by the ratio of the dynamic to static strength, namely, the dynamic increase factor (DIF). For concrete, the DIF can be more than 2 in compression and more than 6 in tension at high strain rates (Malvar and Crawford 1998). The function relating DIF to the strain rate is treated as a material property in the K&C concrete damage model. The CEB-FIP (1993) DIF curve for concrete in compression was adopted in this study:

$$\text{DIF}= f_c / f_{cs} = (\dot{\varepsilon} / \dot{\varepsilon}_s)^{1.026\alpha_s} \text{ for } \dot{\varepsilon} \le 30s^{-1} \quad (4\text{-}14)$$

$$\text{DIF}= f_c / f_{cs} = \gamma_s (\dot{\varepsilon} / \dot{\varepsilon}_s)^{1/3} \text{ for } \dot{\varepsilon} > 30s^{-1} \quad (4\text{-}15)$$

where $\dot{\varepsilon}$ is the strain rate (from 30×10^{-6} to 300/*s*), $\dot{\varepsilon}_s$ =30×10^{-6} is the reference static strain rate, f_c is the dynamic compressive strength at $\dot{\varepsilon}$, f_{cs} is the static compressive strength at $\dot{\varepsilon}_s$, and

$$\log\gamma_s = 6.456\alpha_s - 2 \quad (4\text{-}16)$$

$$\alpha_s = 1/(5 + 9 f_{cs} / f_{co}) \quad (4\text{-}17)$$

$$f_{co} = 10MPa$$

For concrete in tension with strain rates between 10^{-6} and $160\,s^{-1}$, the Modified CEB-FIP curve proposed by Malvar and Crawford (1998) was used in this study:

$$\text{DIF}= f_t / f_{ts} = (\dot{\varepsilon} / \dot{\varepsilon}_s)^{\delta} \text{ for } \dot{\varepsilon} \le 1 s^{-1} \quad (4\text{-}18)$$

$$\text{DIF}= f_t / f_{ts} = \beta (\dot{\varepsilon} / \dot{\varepsilon}_s)^{1/3} \text{ for } \dot{\varepsilon} > 1 s^{-1} \quad (4\text{-}19)$$

where f_t is the dynamic tensile strength at $\dot{\varepsilon}$, f_{ts} is the static tensile strength at $\dot{\varepsilon}_s = 10^{-6} s^{-1}$, and

$$\log \beta = 6\delta - 2 \quad (4\text{-}20)$$

$$\delta = 1/(1 + 8 f_{cs} / f_{co}) \quad (4\text{-}21)$$

4.4.2 Dynamic Effects on Pull-off Test

The same specimen S-CFS-400-25 in (Wu et al. 2001) modelled in static analyses was used as the reference case in dynamic analyses. The same geometry and boundary conditions in Figure 4-1 were modelled. The static concrete properties are the same as the former static pull-off test modelling for the specimen before. The DIF-strain rate relations presented in the above section were used. The mesh consists of 8-noded brick elements with uniform element size 1*mm*. A constant velocity control with smoothed start was applied so that debonding happened at a constant velocity. The time increment of every step for explicit analysis should be smaller than the critical value, which equal to the time of elastic wave transforming in the material of every single element. It is calculated automatically in LSDYNA, and the user can define a scale factor that times the critical value to obtain the time increment

in each step. 0.9 is suggested for low loading rates and 0.6 for higher rates in the manual (LS-DYNA 2007). 0.5 was used in the present dynamic modeling. Figure 4-12 shows the load-slip curves from different loading rates at the loading end of the FRP.

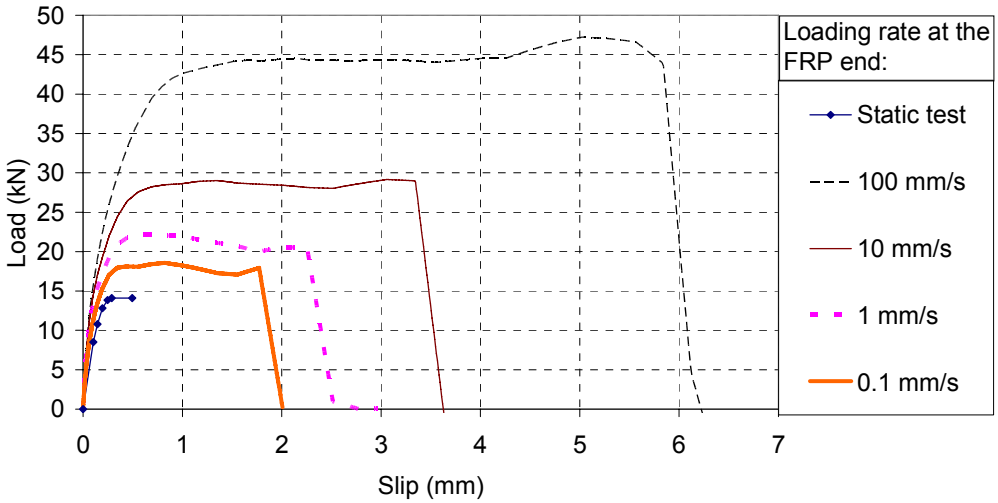

Figure 4-12 Strain rate effects on pull-off test

It can be seen that both the peak load and the final slip increase with the loading rate. For example, when the loading rate increases from 0.1*mm/s* to 100*mm/s*, P_u and the peak slip increase from 18.3*kN* to 44.3*kN*, and 0.25*mm* to 2.0*mm*, respectively. This is because both the tensile strength and the fracture energy have increased from their static counterparts due to high strain rates. Figure 4-13 shows the damage contours of the specimen at the ultimate load P_u from different loading rates. It can be clearly seen that the damage zone also increases as does the loading rate. The depth and breadth of the damage area in concrete increase almost proportionately. This indicates that, as the loading rate increases, more concrete is mobilised to resist the pull-off load, and hence delays debonding and increases the pull-off load capacity.

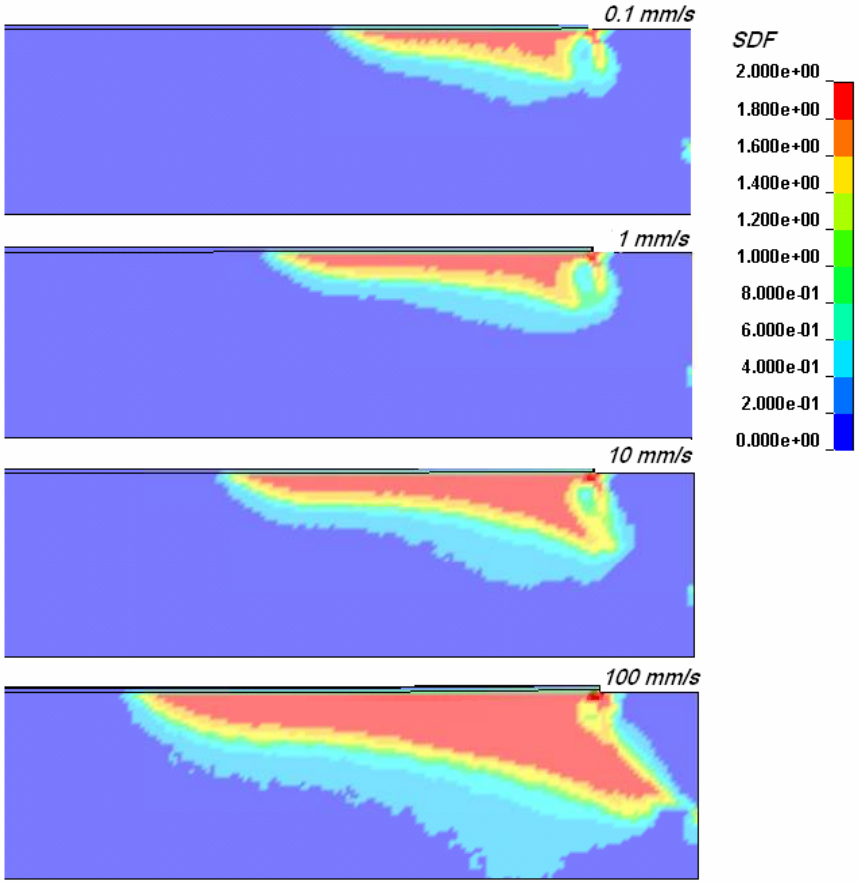

Figure 4-13 Scaled damage factor contour of the specimen when the maximum load is attained under different loading rates (note that the specimen is not plotted in full length)

4.5 Conclusions

This Chapter has presented the investigation into the modelling of the FRP-to-concrete bond behaviour using the K&C concrete damage model in LS-DYNA using the explicit integration scheme, starting from the static simulation. It has been shown that the model can simulate the static FRP-to-concrete bond behaviour, in terms of the load-carrying capacity, load-displacement behaviour and local bond-slip

behaviour with reasonable accuracy and mesh objectivity subjected to both proper localization and dilation consideration with local concrete damage model.

A preliminary finite element study on the effects of loading rate on the behaviour of FRP-to-concrete bonded pull-off tests is presented too based on the mesh-independent load-slip curves in good agreement with test data have been obtained for quasi-static loading. By considering the dynamic increase factor for concrete strength as functions of strain rate, the effects of loading rates on the load-slip curve, effective bond length, ultimate load and the damaged concrete area were elucidated. The developed numerical model will be further investigated under dynamic loadings in the following Chapters.

4.6 References

Baylot, J.T. and Bevins, T.L. (2007), "Effect of responding and failing structural components on the air blast pressures and loads on and inside of the structure", *Computers and Structures*, 85: 891–910.

Bazant, Z.P. and Oh, B.H. (1983), "Crack band theory for fracture of concrete", Materials and Structures (RILEM, Paris), 16: 155–177.

Bhatti, A.Q., Kishi, N. and Tan, K. (2011), "Impact resistant behaviour of RC slab strengthened with FRP sheet", *Materials and Structures/Materiaux et Constructions*, 5:1-10.

Boyd, A.J., Liang, N., Green, P.S. and Lammert, K. (2008), "Sprayed FRP repair of simulated impact in prestressed concrete girders", *Construction and Building Materials*, 22(3): 411-16.

Buchan, P.A. and Chen, J.F. (2007), "Blast resistance of FRP composites and polymer strengthened concrete and masonry structures – a state-of-the-art review", *Composites,* Part B (38), 509–522.

CEB-FIP (1993), Model Code 90. Lausanne.

Chandra, S., Nilsen, B. and Lu, M. (2010), "Predicting excavation methods and rock support: a case study from the Himalayan region of India", *Bull Eng Geol Environ*, 69:257–266.

Chen, G.M., Chen, J.F. and Teng, J.G. (2011), "On the finite element modelling of RC beams shear-strengthened with FRP", *Construction and Building Materials*, Article in Press.

Chen, G.M., Teng, J.G. and Chen, J.F. (2009), "Finite element simulation of IC debonding in FRP-plated RC beams: a dynamic approach", The 9th International Symposium on Fibre Reinforced Polymer for Concrete Structures (FRPRCS9), 13-15 July, Sydney, Australia.

Chen, J.F. and Tao, Y. (2010), "Finite element modelling of FRP-to-concrete bond behaviour using a plastic degradation theory based concrete damage plasticity model", Proceedings of the 5th International Conference on FRP Composites in Civil Engineering, Beijing: 45-50.

Chen, J.F. and Teng, J.G. (2001), "Anchorage strength models for FRP and steel plates bonded to concrete", *Journal of Structural Engineering, ASCE* 127(7):784–791.

Crawford, J.E., Malvar, J., Wesevich, J.W. and Raynolds, A. D. (1997), “Retrofit of reinforced concrete structures to resist blast effects”, *ACI Structural Journal*, 94 (4):371–377.

Crawford, J.E., Malvar, L.J., Morrill, K.B. and Ferritto, J.M. (2001), "Composite Retrofits to Increase the Blast Resistance of Reinforced Concrete Buildings", Proceedings of the 10th International Symposium on Interaction of the Effects of Munitions with Structures, San Diego, CA, May.

De Lorenzis, L. and La Tegola, A. (2005), "Bond of FRP laminates to concrete under impulse loading: a simple model", Proc. International Symposium on Bond Behaviour of FRP in Structures (BBFS 2005), Hong Kong, China: 503-508.

Heffernan, P.J., Wight, R.G. and Erki, M.A. (2011), "Research on the use of FRP for critical load-bearing infrastructure in conflict zones*", Journal of Composites for Construction*, 15(2):136-145.

Kim, S.W. and Vecchio, F.J. (2008), "Modelling of shear-critical reinforced concrete structures repaired with fiber-reinforced polymer composites", *Journal of Structural Engineering*, 134(8):1288-1299.

Li, X.Q., Chen, J.F. and Lu, Y. (2010a), "Meso-scale modelling of FRP-to-concrete bond behaviour using LSDYNA", Proceedings of the 5th International Conference on FRP Composites in Civil Engineering, Beijing: 494-498.

Li, X.Q., Chen, J.F. and Lu, Y. (2010b) "On mode-I fracture modelling of concrete in LS-DYNA explicit", Proceedings (CD-ROM) of the 13th International Conference on Structural Faults + Repair, Edinburgh, UK.

LSDYNA (2007), Keyword User’s Manual Version 971, Livermore Software Technology Corporation.

Lu, X.Z., Teng, J.G., Ye, L.P. and Jiang, J.J. (2005), "Bond–slip models for FRP sheets/plates bonded to concrete", *Engineering Structures*, 27:920–937.

Lu, X.Z., Ye, L.P., Teng, J.G. and Jiang, J.J. (2004), "Mesco-scale finite element model for FRP sheets/plates bonded to concrete", *Engineering structures*, 27:564-575.

Malvar, L.J., and Crawford, J.E. (1998), "Dynamic increasing factors for concrete", Twenty-Eighth DDESB Seminar, Orlando, FL, August.

Malvar, L.J., Crawford, J.E. and Morrill, K.B. (2000), "K&C Concrete material model release3—automated generation of material model input", K&C documents, August.

Malvar, L.J., Crawford, J.E., Wesevich, J.W. and Simons, D. (1997), "A plasticity concrete material model for DYNA3D*", International Journal of Impact Engineering*, 19(9-10): 847-873.

Malvar, L.J. and Simons, D. (1996), "Concrete material modeling in explicit computations", Workshop on Recent Advances in Computational Structural Dynamics and High Performance Computing, USAE Waterways Experiment Station, April 24-26.

Niroomandi, A., Maheri, A., Maheri, M., R. and Mahini, S.S. (2010), "Seismic performance of ordinary RC frames retrofitted at joints by FRP sheets", *Engineering Structures*, 32(8):2326-2336.

Pantelides, C.P. and Gergely, J. (2007), "Seismic retrofit of reinforced concrete beam-column T-joints in bridge piers with FRP composite jackets", American Concrete Institute, *ACI Special Publication*, 258:1-18.

Schwer, L.E. and Malvar, L.J. (2005), "Simplified concrete modelling with *mat_concrete_damage_rel3", JRI LS-Dyna User Week, Nagoya, Japan.

Su, X.T., Yang, Z.J. and Liu, G.H. (2010), "Monte Carlo simulation of complex cohesive fracture in random heterogeneous quasi-brittle materials: a 3D study", *International Journal of Solids and Structures*, 47(17):2336-2345.

Tarapada, R. and Debabrata, C. (2006), "Delamination in hybrid FRP laminates under low velocity impact", *Journal of Reinforced Plastics and Composites*, 25(18):1939-56.

Teng, J.G., Chen, J.F., Smith, S.T. and Lam, L. (2002), FRP-Strengthened RC Structures, John Wiley and Sons Ltd. ISBN-10: 0-471-48706-6.

Teng, J.G., Zou, X.K., De Lorenzis, L. and Xia, S.H. (2007), "Optimal performance-based design of FRP jackets for seismic retrofit of reinforced concrete frames", *Composites Part B (Engineering)*, 38(5-6):584-97.

Tu, Z.G. and Lu, Y. (2009), "Evaluation of typical concrete material models used in hydrocodes for high dynamic response simulations", *International Journal of Impact Engineering*, 36(1):132-146.

Ueda, T., Sato, Y. and Asano, Y. (1999), "Experimental study on bond strength of continuous carbon fiber sheet", Proceedings of 4th int. sym. on fiber reinforced polymer reinforcement for reinforced concrete structure: 407–416.

Wu, C., Oehlers, D.J. and Day, I. (2009), "Layered blast capacity analysis of FRP retrofitted RC member", *Advances in Structural Engineering*, 12(3): 435-449.

Wu, Y.F., Zhou, Z.Q., Yang, Q.D. and Chen, W.Q. (2010), "On shear bond strength of FRP-concrete structures*", Engineering Structures*, 32 : 897-905.

Wu, Z.S., Yuan, H., Yoshizawa, H. and Kanakubo, T. (2001), "Experimental/analytical study on interfacial fracture energy and fracture propagation along FRP-concrete interface", *ACI International SP-201-8*:133–152.

Yang, Z.J., Chen, J.F. and Proverbs, D. (2003), "Finite element modelling of concrete cover separation failure in FRP plated RC beams", *Construction and Building Materials,* 17:3-13.

Yang, Z.J., Su, X.T., Chen, J.F. and Liu, G.H. (2009), "Monte Carlo simulation of complex cohesive fracture in random heterogeneous quasi-brittle materials", *International Journal of Solids and Structures*, 46(17):3222-3234.

Yao, J. (2004), Debonding failures in reinforced concrete structures strengthened with externally bonded FRP sheets/plates, PhD thesis, Department of Civil and Structural Engineering, Hong Kong Polytechnic University, Hong Kong.

Yao, J., Teng, J.G. and Chen, J.F. (2005), "Experimental study on FRP-to-concrete bonded joints", *Composites Part B: Eng.*, 36 (2):99-113.

Chapter 5 Dynamic increase factor (DIF) for concrete in tension

5.1 Introduction

It has been introduced in Section 2.5.3 that under "uniaxial" compression, the DIF is rather a dynamic structural effect than a material property. However, it is suggested that the DIF of the tensile strength observed in dynamic tensile tests could be a genuine material effect. Consequently, it is deemed to be rational to include the DIF for the dynamic tensile strength in the material descriptions in an analysis where tension plays a dominant role.

This chapter is concerned about an appropriate incorporation of the tension DIF in a general finite element framework with local concrete material description. In particular, the pertinent issues with regard to strain localisation and the subsequent mesh dependence, especially the associated "strain rate localisation" and subsequent need of using a mesh-objective local DIF input versus strain rate relationship, are investigated. Following the Introduction, an overview of the general specifications of the tension DIF is given in Section 2. In Section 3, the scenario of direct tension test is chosen to examine the mesh-dependence in a finite element model involving dynamic strain rate effect. It is shown that a mesh-objective correction needs to be

made on the standard global DIF vs. strain rate relationship, thus forming a numerical local DIF, so as to achieve basic mesh convergence and the expected tensile strength enhancement at the specimen level. The Split Hopkinson Pressure Bar (SHPB) test for direct tension is modelled in Section 4 and the results are discussed in light of the complexity of the stress states for the high loading rates. A modified mesh-objective local DIF versus strain rate curve is proposed for FE modelling with local concrete model.

5.2 DIF and discussion on its application in FE

In the literature, the-CEB recommend DIF curve for compression (CEB-FIP 1993) and the modified CEB formula for tension (Malvar and Crawford 1998) may be the most commonly adopted formulas to model the dynamic strength enhancement for concrete under high strain rate loading. Therefore these two formulas will be used as benchmarks in the present investigation.

The CEB-FIP (1993) DIF curve for concrete in compression is expressed as:

$$DIF = f_c / f_{cs} = \left(\frac{\dot{\varepsilon}}{\dot{\varepsilon}_S} \right)^{1.026\alpha_S} \quad \text{for } \dot{\varepsilon} \le 30 s^{-1} \tag{5-1}$$

$$DIF = f_c / f_{cs} = \gamma_S \left(\frac{\dot{\varepsilon}}{\dot{\varepsilon}_S} \right)^{1/3} \quad \text{for } \dot{\varepsilon} > 30 s^{-1} \tag{5-2}$$

where $\dot{\varepsilon}$ is the strain rate (ranging from 30×10^{-6} to $300\,s^{-1}$), $\dot{\varepsilon}_s$=$30\times10^{-6}\ s^{-1}$ is the reference static strain rate, f_c is the dynamic compressive strength at $\dot{\varepsilon}$, f_{cs} is the static compressive strength at $\dot{\varepsilon}_s$, and

$$\log\gamma_s = 6.456\alpha_s - 2 \tag{5-3}$$

$$\alpha_s = 1/(5+9f_{cs}/f_{co}) \tag{5-4}$$

$$f_{co} = 10MPa = 1450\ psi \tag{5-5}$$

For concrete in tension and within a strain rate in the range of 10^{-6} to $160\,s^{-1}$, a Modified CEB-FIP (1993) curve as proposed by Malvar and Crawford (1998) is often adopted for its improved accuracy compared with the original CEB-FIP (1993) curve:

$$DIF = f_t / f_{ts} = \left(\frac{\dot{\varepsilon}}{\dot{\varepsilon}_S}\right)^{\delta} \text{ for } \dot{\varepsilon} \le 1s^{-1} \tag{5-6}$$

$$DIF = f_t / f_{ts} = \beta\left(\frac{\dot{\varepsilon}}{\dot{\varepsilon}_S}\right)^{1/3} \text{ for } \dot{\varepsilon} > 1s^{-1} \tag{5-7}$$

where f_t=dynamic tensile strength at $\dot{\varepsilon}$, f_{ts}=static tensile strength at $\dot{\varepsilon}_s$=$10^{-6}\ s^{-1}$ and

$$\log\beta = 6\delta - 2 \tag{5-8}$$

$$\delta = 1/(1 + 8 f_{cs} / f_{co}) \tag{5-9}$$

$$f_{co} = 10MPa = 1450 \ psi \tag{5-10}$$

It is particularly worth noting that in the experimental determination of the apparent dynamic strength using SHPB type of apparatus, the strain rate and the global DIF are calculated according to the stress wave time histories measured from the strain gauge sensor attached on the incident and the transmitter bars (e.g. Ross 1989; Ross et al. 1990; Tedesco et al. 1989; Tedesco et al. 1991; Li and Meng 2003). Therefore, the results are representative of the bulk or macroscopic behaviour of the sample specimens. When such "apparent" global DIF is considered in a FE model involving a local concrete model as a material parameter, issues pertinent to the localisation naturally arise, especially when the element size is much smaller than the general crack band width of the concrete, which is approximately equal to three times the maximum aggregate sizes (Bazant and Oh 1983).

Localization is an important aspect of FE modelling with local concrete model, and needs to be addressed properly. Especially in a tension dominant response, localization in a FE model essentially limits the fracture to a single element, and consequently, the stress strain curve needs to be made mesh-dependent so that the total fracture energy can be maintained as a material constant (i.e., independent of the mesh). In a quasi-static loading scenario, a typical way of handling the effect of strain localisation is incorporating a characteristic length in the description of the material strain softening, such that the product of the characteristic length and the

area under the stress strain curve in the descending branch equals a target fracture energy value.

For the dynamic analysis of concrete where the strain rate effect on the concrete tensile strength is realised through the use of the apparent DIF, which is a function of the strain rate, it is conceivable that the localisation issue would render the strain rate as evaluated from the strain to be "localised" and mesh-dependent. Based on the same logic as mentioned above on tackling the localised strain, it would be necessary to "correct" the localised strain rate, or alternatively correct the DIF versus strain rate relationship so that the actually achieved dynamic increase effect would become mesh-independent. Unfortunately, such an issue has not been properly addressed in the existing numerical modelling literature concerning the analysis of concrete under high strain rate tension. Further discussion follows.

5.3 DIF of direct tension in meso-scale FE modelling

To illustrate the issue related to the localisation of the strain rate in a FE model, a simplified direct tension test is simulated. The DIF curve expressed in Equations (5-6) and (5-7) is used directly in the model, whereas different mesh sizes are employed and the results are compared.

The specimen used in this analysis is a cylinder with a length of 50.8*mm* and a diameter of 50.8*mm*, as typically used in the standard dynamic tests (e.g. Tedesco et

al.1991). For an illustrative purpose, a simplified 2D FE model with plane stress assumption is employed. To control the occurrence of fracture, a notch is created in the middle of the specimen with a dimension of $2mm \times 2mm$ on each side, as shown in Figure 5-1. Three different meshes are chosen for investigation, with element size equal to $2mm$, $1mm$, and $0.5mm$, respectively.

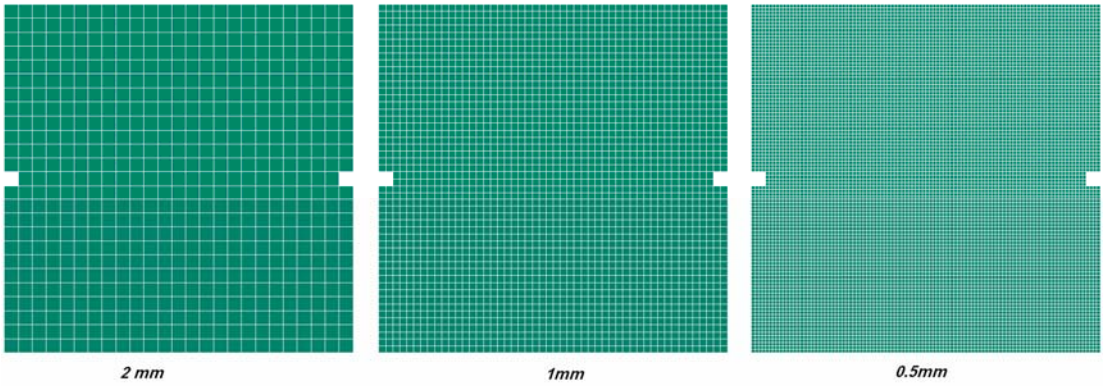

Figure 5-1 Three different meshes for simplified direct tension test

In the numerical experiment, the load is applied via imposing a velocity history in the axial (vertical) direction on the top side of the specimen, while the bottom nodes are constrained in the vertical direction. The velocity history has an initial smooth rising stage followed by a constant phase, so as to ensure that the whole specimen reaches a constant strain rate (Gray III 2000), expressed in Equation (5-11), before failure,

$$\dot{\varepsilon} = \frac{\Delta\varepsilon}{\Delta t} = \frac{\Delta d / L}{\Delta t} = \frac{v}{L} = \frac{v}{50} \tag{5-11}$$

where $\dot{\varepsilon}$ is the nominal or engineering strain rate, ε is the engineering strain, d is the displacement, t is time, L is the specimen length which is $50mm$ herein.

The concrete strength is assumed to be of a grade with $f_c^{'}$=30 MPa (static), and its static tensile strength is about 2.9 MPa . According to Equations (5-6) and (5-7), for this grade of concrete, the tension global DIF would be equal to 1.7 at a strain rate of $1\,s^{-1}$.

The specimen is first analysed with the DIF in the material model being turned off, i.e., without considering the DIF as a material property. This is for the purpose to observe how the dynamic structural effect within the specimen might affect the overall strength. Figure 5-2 shows the nominal stress, as evaluated by dividing the total axial force on the loading face by the area, versus the nominal strain relationship when the strain rate is $1\,s^{-1}$. As can be seen, the apparent dynamic strength (maximum stress on the curves) is equal to about 2.9 MPa , which is the same as the static strength. This indicates that, unlike in the case of compression as mentioned earlier, the specimen does not exhibit any increase in the dynamic tensile strength if a DIF is not included as a material property. It is also worth noting that the results from different meshes are almost identical, indicating satisfactory mesh convergence while a material DIF is not involved.

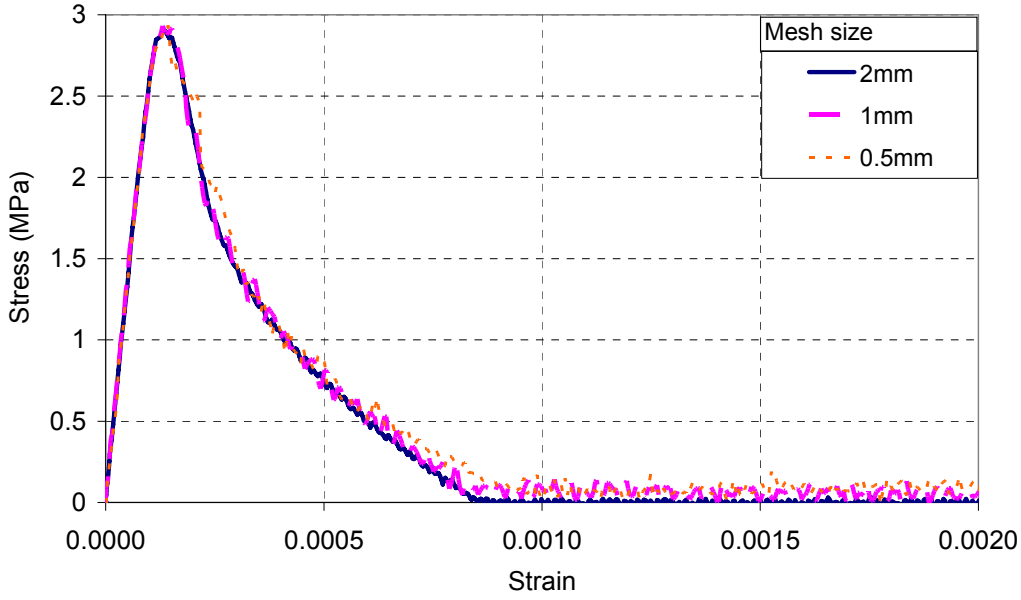

Figure 5-2 Direct tension test with DIF off, under a constant velocity 50*mm/s* (corresponding to engineering strain rate $\dot{\varepsilon}$ =1 s^{-1})

The above observation suggests that it is necessary to include the DIF in the material description for the analysis of tension if the experimentally observed dynamic tensile strength enhancement is to be represented in a FE model.

The specimen is then analysed with the DIF as expressed in Equations (5-6) and (5-7) being enabled. Figure 5-3 shows the resulting engineering stress - strain curves as obtained from models with different mesh sizes, for a strain rate of $1\,s^{-1}$. As can be expected, the achieved dynamic strength now becomes much higher than the static strength. However, the results differ considerably among the different meshes, and there is no tendency of mesh convergence. Furthermore, while the expected global DIF for $\dot{\varepsilon}=1\,s^{-1}$ is 1.7, the actually achieved apparent DIF is nearly 4 even for the lowest stress peak value of $11\,MPa$ in Figure 5-3 with a mesh size of 2mm, and it tends to increase as the mesh size further reduces. Examination of the damage

patterns in Figure 5-4 reveals that damage is concentrated within a single row of elements at the middle of the specimen where the notch is located. Note that the scaled damage factor (*SDF*) shown in the figure is an indication of the degree of damage in the concrete; 0 to 1 is the range for elastic stage while damage starts from 1.0 and total failure corresponds to *SDF* equal to 2 (LSDYNA 2007; Malvar et al. 1997). Normally, when *SDF* reaches 1.8, less than 10% of the total fracture energy of the concrete is dissipated, and even when *SDF*=1.95, the energy dissipated is still less than 50% of the total fracture energy in an element. This means *SDF* would be very close to 2.0 at the macro fracture stage.

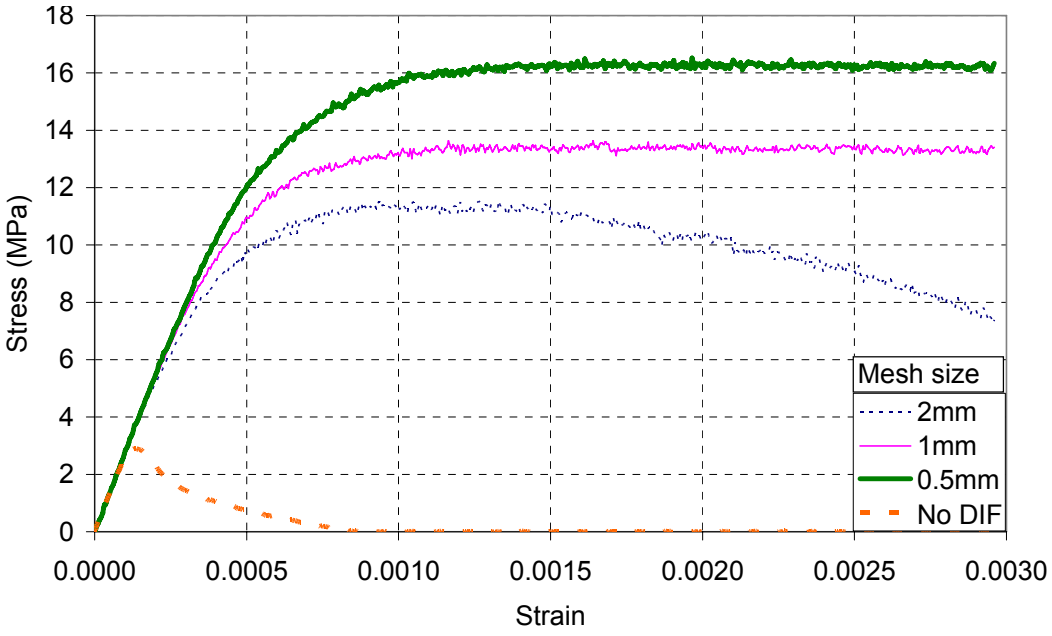

Figure 5-3 Direct tension test with DIF curve following Equations (5-6) and (5-7), under a constant velocity 50*mm/s* (corresponding to engineering strain rate $\dot{\varepsilon}$ =1 s^{-1})

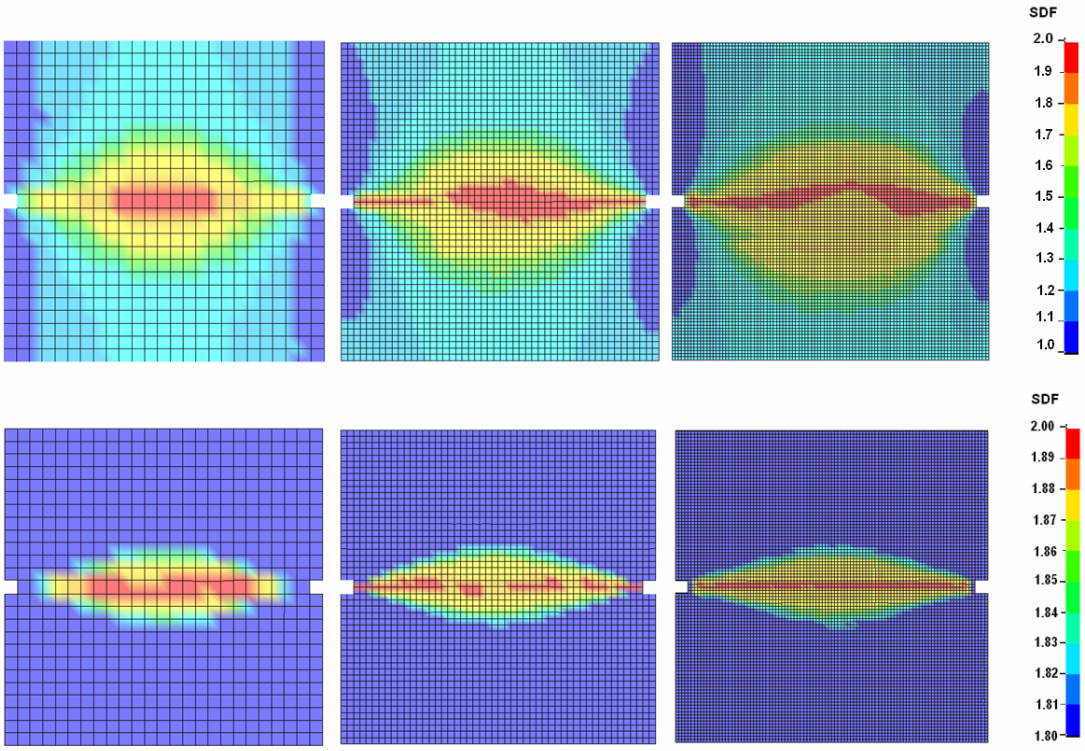

Figure 5-4 Damage patterns for $\dot{\varepsilon}$ =1 s^{-1} presented with different scale of *SDF*

Clearly, the problem is associated with the localisation of tension failure within a single element in the general FE modelling framework as presently employed. The localisation renders a concentration of the post-peak deformation to the width of the softened element. Consequently, for the same amount of the engineering strain (or overall displacement), the strain in the critical row of elements would increase proportionately as the size of the element reduces. This in turn magnifies the "strain rate" in these critical elements for the same overall loading (displacement) rate as compared to the engineering strain rate. As a result, the actually achieved DIF in the critical elements becomes much higher than the expected DIF according to the engineering strain rate. This also explains the non-convergence of meshes as illustrated in Figure 5-3, despite the fact that satisfactory mesh convergence in terms

of the strain localisation has been obtained when the strain rate effect is not involved (refer to Figure 5-2).

To rectify this problem with strain rate localisation and ensure mesh convergence in the analysis of direct tension, a mesh correction factor would have to be incorporated in the empirical tension DIF formulas of Equations (5-6) and (5-7). This is discussed in the following section.

5.4 Meso-scale FE modelling with mesh-dependent DIF

To rectify the mesh-dependent strain rate localisation effect on the DIF, it would be rational to firstly establish a reference characteristic width within which physical crack softening is deemed to take place. Such a characteristic width may be regarded as a baseline for which empirical tensile DIF formulas such as Equations (5-6) and (5-7) would apply. Similar to the suggestion made by Malvar et al. (2000), herein we adopt a characteristic width of 25.4*mm*, which is roughly three times the size of the 3/8-inch aggregates that are commonly used in concrete samples for high strain rate tests. For mesh size differing from (especially smaller than) 25.4*mm*, the computed strain rate due to localisation should be corrected by the mesh size normalised with respect to the characteristic width before the empirical DIF formula is applied. This is equivalent to introducing a correction to the local DIF formula as an input to the model, thus making the implementation more straightforward, as follows,

$$DIF = f_t / f_{ts} = \left(\frac{\dot{\varepsilon} \frac{x}{L_{c0}}}{\dot{\varepsilon}_s} \right)^{\delta} \quad \text{for } \dot{\varepsilon} \le \frac{L_{c0}}{x} s^{-1} \tag{5-12}$$

$$DIF = f_t / f_{ts} = \beta \left(\frac{\dot{\varepsilon} \frac{x}{L_{c0}}}{\dot{\varepsilon}_s} \right)^{1/3} \quad \text{for } \dot{\varepsilon} > \frac{L_{c0}}{x} s^{-1} \tag{5-13}$$

where x is the current element size in mm; L_{c0} represents the characteristic width in mm, herein $L_{c0} = 25.4\,mm$; the definition of other symbols remains the same as in Equations (5-6) to (5-10).

Figure 5-5 shows the re-calculated stress and strain curves for the specimen with three different meshes, under an engineering strain rate of $1\ s^{-1}$, but with the corrected local DIF according to Equations (5-12) and (5-13). As can be seen, mesh convergence is now satisfactorily achieved, and the dynamic strength developed in the specimen agrees well with the expected increase global DIF from the static strength.

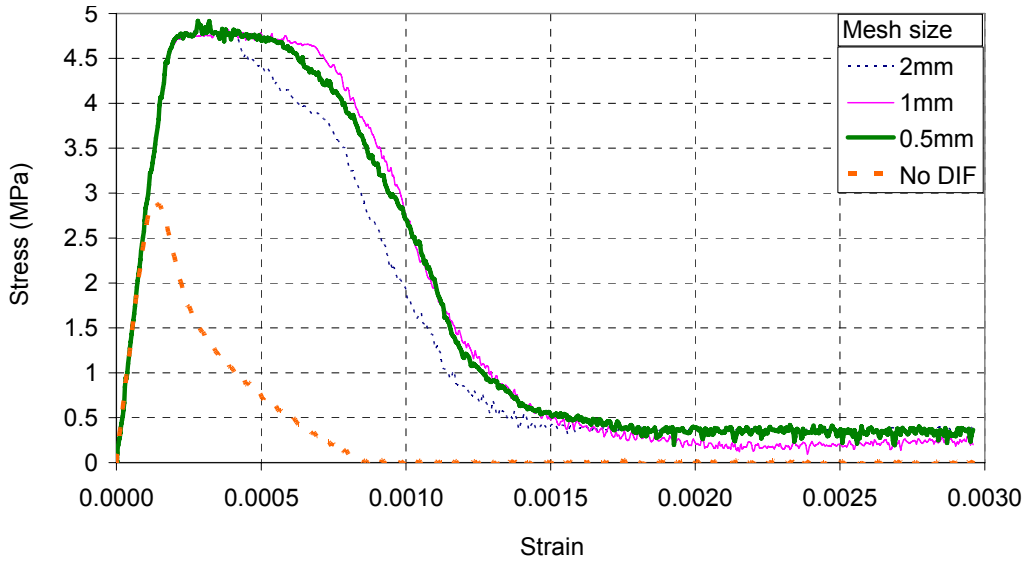

Figure 5-5 Direct tension test with corrected local DIF curve in Equations (5-12) and (5-13), under a constant velocity 50*mm/s* (corresponding to engineering strain rate $\dot{\varepsilon}$ =1 s^{-1})

Three loading rates were then simulated, namely 5*mm/s* ($\dot{\varepsilon}$=0.1 s^{-1}), 50*mm/s* and 200*mm/s* ($\dot{\varepsilon}$=4 s^{-1}) respectively and compared with Ross's (1989) test data together with the global DIF curve proposed by Malvar et al. (2000). The achieved apparent global DIF are plotted against the corresponding (engineering) strain rates and compared with the empirical curve and some physical test data in Figure 5-6.

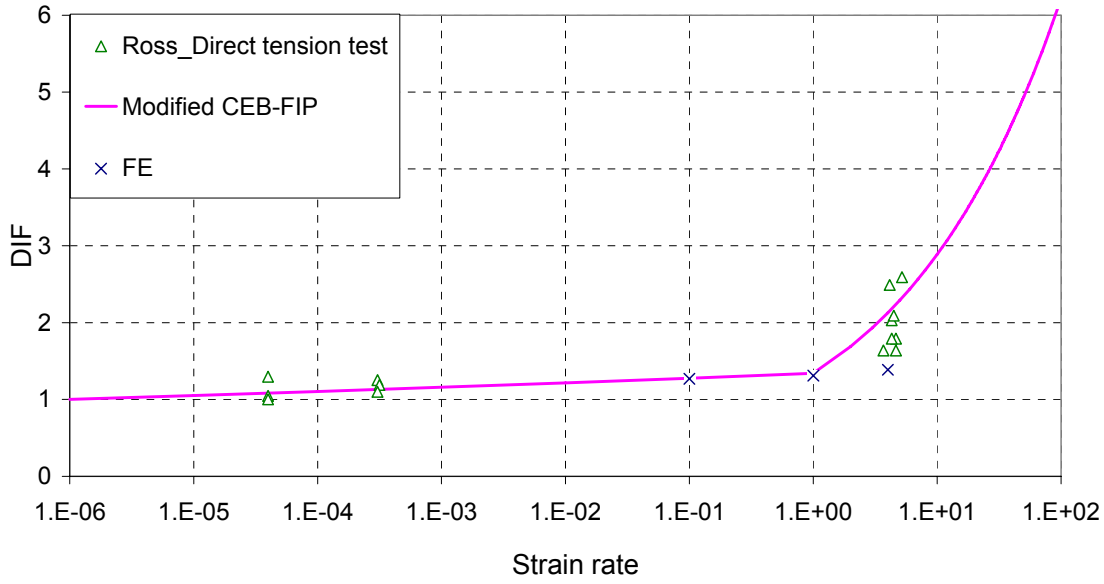

Figure 5-6 DIF from FE simulations with local DIF curve expressed in Equations (5-12) and (5-13) and comparison with empirical data for direct tension test ($f_c' = 57.7 MPa$)

From Figure 5-6, it can be found that the FE results for direct tension with the proposed mesh-corrected local DIF curve in Equations (5-12) and (5-13) show a good agreement with the empirical global DIF data, especially for the range of strain rate up to the order of $1\,s^{-1}$. Further simulation for higher strain rates, however, did not turn out as good results as in the relatively lower strain rate range. In Figure 5-6, DIF from FE simulations with local DIF curve expressed in Equations (5-12) and (5-13) for $4\,s^{-1}$ strain rate is lower than the value according to modified CEB curve and experiment results. This is explicable by the fact that the simple correction proposed in Equations (5-12) and (5-13) essentially assumes a fixed localisation of strain (and strain rate) within a single element, so the validity is limited to cases where failure does localise in a single element width, such as under quasi-static and relatively low dynamic tension. When the loading rate gets higher, however, damage tends to distribute or re-locate in a wider area due to strong transient dynamic effect, as is

evidenced in Figure 5-7 shows a comparison of the failure patterns for strain rates of 1 s^{-1} and 10 s^{-1}, respectively. This renders the localisation correction more complicated and requires further investigation.

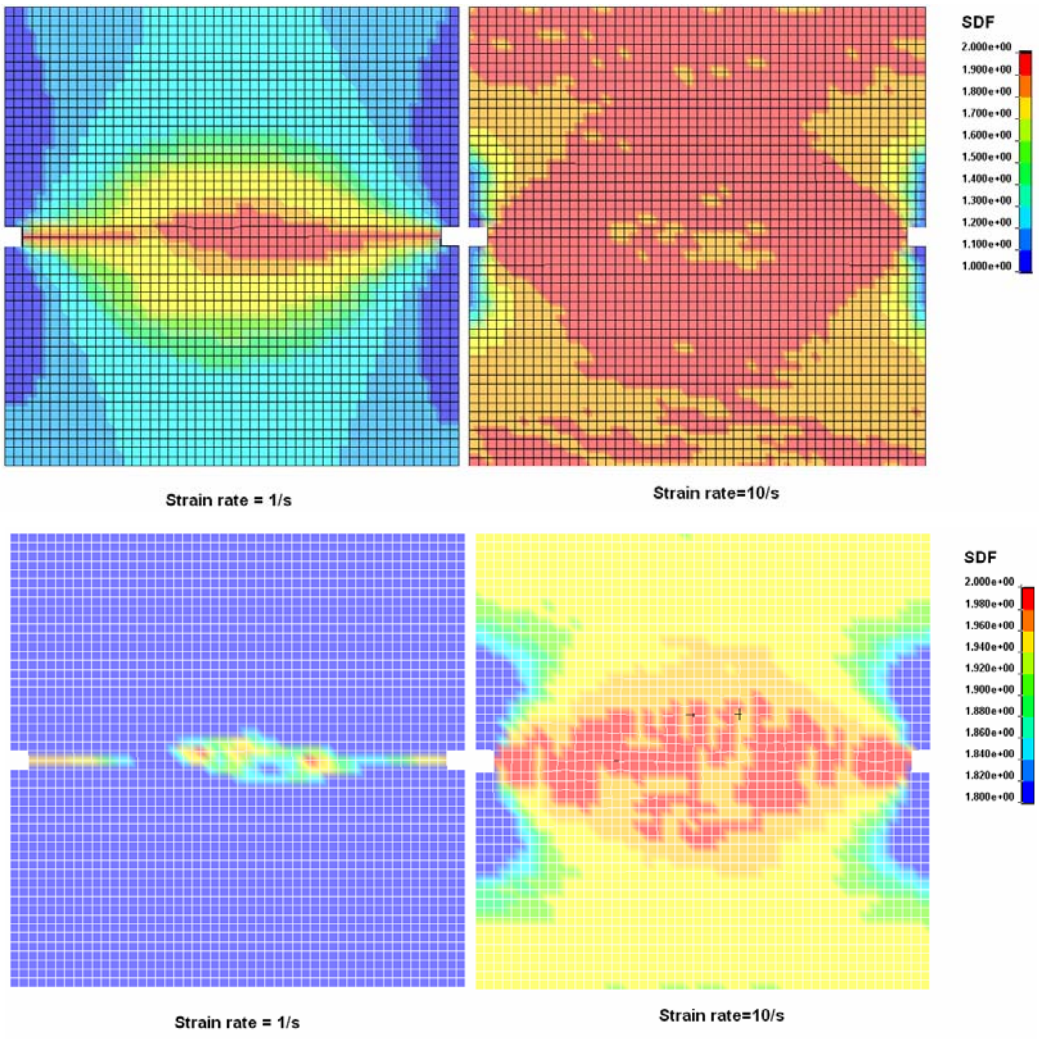

Figure 5-7 Damage contour of two different strain rates

At this juncture, it should be noted that the loading scheme in the analyses presented up to this point by imposing a velocity boundary condition is a simplified approach, and such an approach is also susceptible to concentration of failure at the loading face. To be more realistic in the comparison with real SHPB tests, in the analyses that follow, a computational model resembling the actual SHPB apparatus is

developed and employed. This would eliminate possible discrepancies arising from artificial loading conditions and make the assessment of the local DIF correction more straightforward.

5.5 Simulation of split-Hopkinson pressure bar (SHPB) for direct tension

The split-Hopkinson pressure bar testing for direct tension is modelled with the inclusion of the pressure bars in the model together with the concrete specimen. Different tensile impulses can be imposed on the incident face of the pressure bar to achieve different strain rates (Tedesco et al. 1991). To examine the adequacy of considering the local DIF at the material level, two options are examined with the current concrete model, one without any DIF, and the other with a local DIF which incorporates the simple mesh correction as proposed in Equations (5-12) and (5-13). Based on the results, a further correction to take into account the tendency of increasing spread of tension failure in the higher strain regime is introduced. Combining with the mesh correction, this provides a more comprehensive rectification of the issues in the FE modelling for dynamic tension that arise from strain / strain-rate localisation and its increased complexity due to transient dynamic effect.

5.5.1 SHPB direct tension tests

A SHPB setup for direct tension as developed by Ross (1989) is schematically shown in Figure 5-8. In this setup, two strain gauges are located at "SG1" and "SG2". SG1 is used to measure the transmitted stress wave time history and SG2 is for incident/reflected stress wave. The two strain gauges are located at the symmetric positions about the specimen, such that the start point of the reflected wave and the transmitted wave should occur at the same time. During the test, a striker (bar) impacts a tup (Tedesco et al. 1991) which is fixed on the end of what becomes the tensile incident bar (right side of the specimen). A tensile stress wave then propagates toward the specimen. The specimen is cemented between the two bars (Tedesco et al.1991; Ross 1989).

The geometry of the specimen with two squared notches is shown in Figure 5-9. The overall dimension was 50.8*mm* (2*inches*) in diameter and 50.8*mm* in length. The notch was located at the mid-length of the specimen and was 3.175*mm* square. The pressure bars were made of PH 13-8 MO stainless steel. The concrete being tested had the following properties: Young's modulus E_s =37.93*GPa*; compressive stress f_c'= 57.7*MPa*; tensile strength f_t = 4.53*MPa*; density ρ= 2405kg/m^3 (Tedesco et al. 1991).

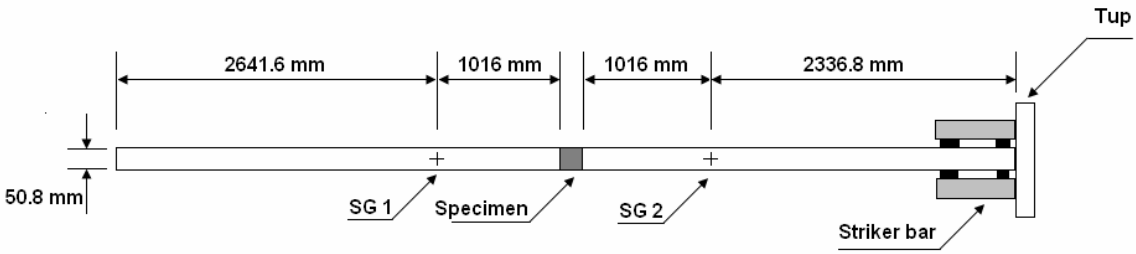

Figure 5-8 Direct tension split-Hopkinson pressure bar test (specimen cemented on both ends) (Ross 1989)

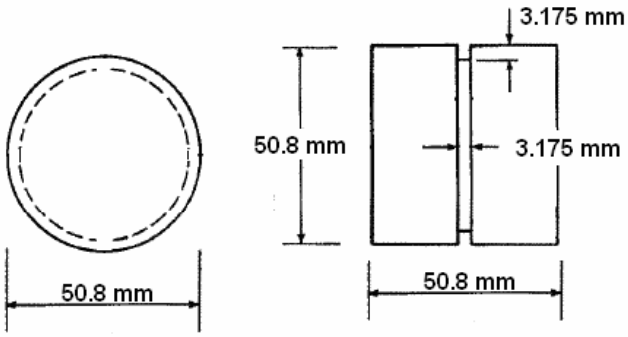

Figure 5-9 Square notched direct tension specimen (left: end view; right: plane view) (Tedesco et al. 1991)

Assuming equilibrium at failure, the dynamic tensile strength at the notch, f_{tn}, will be proportional to the transmitted stress, σ_T (Tedesco et al. 1991).

$$f_{tn} = \sigma_T A_r \tag{5-14}$$

in which

$$A_r = \frac{D_b^2}{D_n^2} \tag{5-15}$$

where A_r is the area ratio, D_b is the diameter of the Hopkinson bar, D_n is the diameter of the specimen at the notch.

Additionally, the loading rate, $\dot{\sigma}$, and the strain rate, $\dot{\varepsilon}$ in the specimen can be estimated from the following expressions:

$$\dot{\sigma} = \frac{f_{tn}}{\tau} \tag{5-16}$$

$$\dot{\varepsilon} = \frac{\dot{\sigma}}{E_s} \tag{5-17}$$

where τ is the time lag between the start of the reflected stress wave and the maximum transmitted stress, and E_s is the modulus of elasticity of the specimen. The global DIF is then calculated as the ratio between f_{tn} and the static tensile strength of the concrete f_t.

5.5.2 FE modelling with mesh-corrected DIF only

For simplicity, in the numerical modelling the above SHPB test is treated as a plane stress problem, as was done in some previous studies (e.g. Tedesco et al. 1991; Zhou and Hao 2008), and only half of the SHPB is modelled considering symmetry, see Figure 5-13. A tensile stress pulse is imposed at the end of the incident (right side) bar instead of modelling the striker. Figure 5-10 shows the typical tensile stress wave time history.

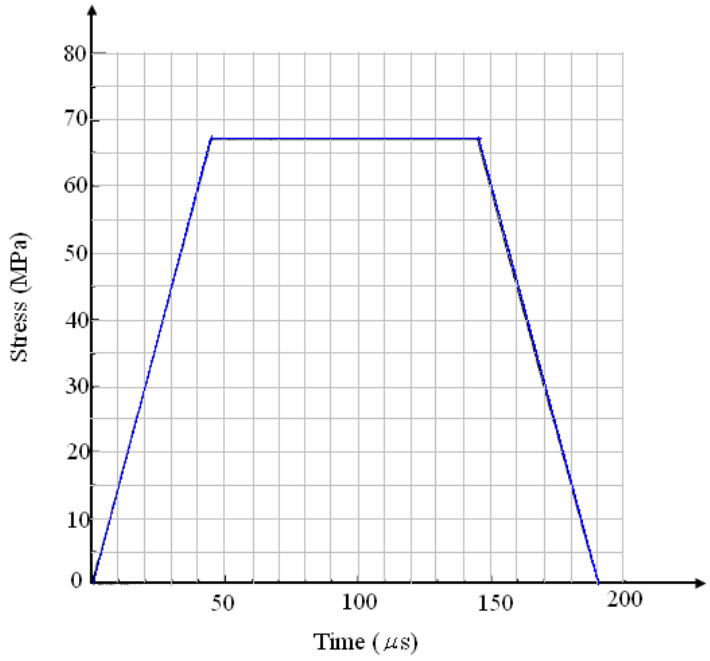

Figure 5-10 Incident stress wave time history (adopted from Tedesco et al. 1991)

To observe the effectiveness of the proposed mesh-corrected local DIF in the SHPB test setting, the concrete specimen is modelled with the mesh-corrected local DIF as expressed in Equations (5-12) and (5-13).

Figure 5-11 and Figure 5-12 shows a comparison between the computed stress waves in the pressure bars with the experimental counterparts under a nominal strain rate of $5.3\,s^{-1}$. It can be seen that the transmitted stress wave does not compare well with the test results. Further examination of the damage contour of the concrete specimen, as shown in Figure 5-13, reveals that extensive tensile damage occurs in the specimen. Such a phenomenon is different from the presumption in the implementation of the mesh-corrected DIF that tensile failure would concentrate only to a single element width, due apparently to the transient stress wave effect. This implies that the use of mesh-corrected DIF would lead to overestimation of the strain

rate effects. As a result, the FE transmitted stress value reaches 160*MPa* while the peak value as occurred during the physical experiment was only 60*MPa*. Clearly, the local DIF input curve needs to be further modified to take into account of the stress-wave induced diffusion of fractures.

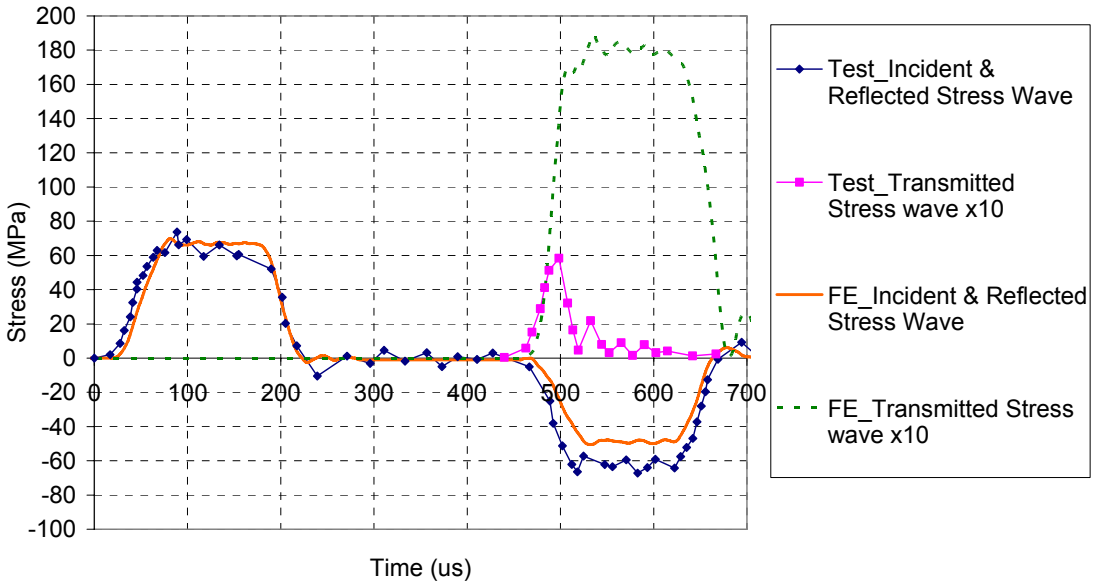

Figure 5-11 SHPB simulation results using original DIF curve (Equations (5-6) and (5-7)) compared with test data (Mesh size 1.5875 *mm* ; Incident impulse peak value 67 *MPa*)

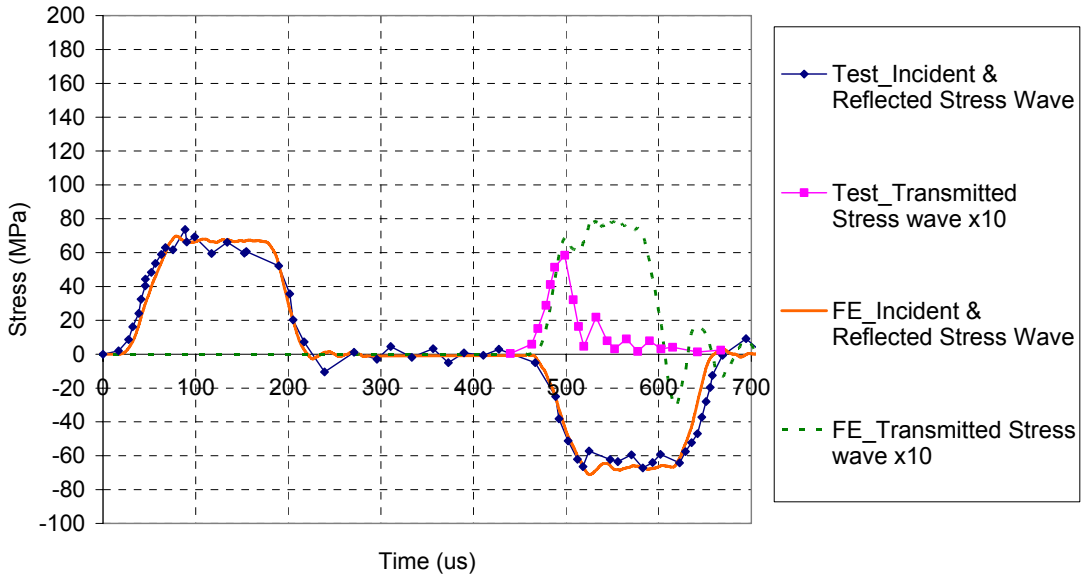

Figure 5-12 SHPB simulation results using original DIF curve (Equations (5-12) and (5-13)) compared with test data (Mesh size 1.5875 mm ; Incident impulse peak value 67 MPa)

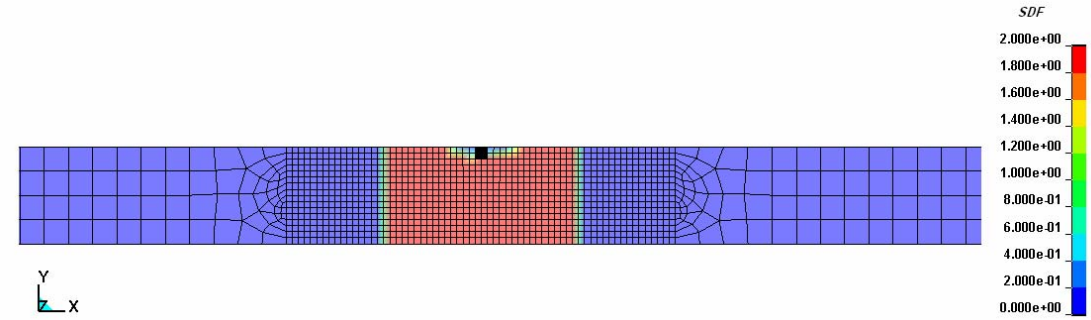

Figure 5-13 Simulated damage contour of concrete specimen at failure

5.5.3 A mesh and strain-rate dependent ("doubly corrected") DIF model for FE analysis

As presented before, for lower strain rates, i.e. $\dot{\varepsilon} < 1\ s^{-1}$, the localization tends to stick to a single element width and so when the mesh-corrected local DIF is introduced, the numerical modelling of the concrete can properly represent the dynamic enhancement of material property. However, it is also discovered that when

the strain rate is getting higher, i.e. $\dot{\varepsilon} > 1\, s^{-1}$, complication arises as the stress wave effects become more significant, especially the tendency of diffusion of the fracture across multiple elements. In this respect, it is deemed appropriate to attach the localisation correction further to the strain rate, in addition to the mesh, such that the fracture diffusion effect at higher strain rates can be reasonably incorporated.

Equations (5-18) and (5-19) present such "double-corrected" DIF curves for local concrete model. The strain rate correction of the localisation is achieved by introducing a dynamic characteristic length, such that $L_{cd} = L_{c0}(1 + \xi \lg \dot{\varepsilon})$ for $\dot{\varepsilon} > \dot{\varepsilon}_c$, where ξ is an empirical coefficient, $\dot{\varepsilon}_c$ is a numerical critical strain rate below which only the mesh objective correction on the DIF need to be made.

$$DIF = f_t / f_{ts} = \left(\frac{\dot{\varepsilon} \dfrac{x}{L_{c0}}}{\dot{\varepsilon}_S} \right)^{\delta} \quad \text{for } \dot{\varepsilon} \le \dot{\varepsilon}_c \tag{5-18}$$

$$DIF = f_t / f_{ts} = \beta \left(\frac{\dot{\varepsilon} \dfrac{x}{L_{c0}(1 + \xi \lg \dot{\varepsilon})}}{\dot{\varepsilon}_S} \right)^{1/3} \quad \text{for } \dot{\varepsilon} > \dot{\varepsilon}_c \tag{5-19}$$

$$\text{Where} \qquad \xi = 6.8^{(1-\frac{x}{L_{c0}})} - 1 \tag{5-20}$$

$$\left(\frac{\dot{\varepsilon}_c \dfrac{x}{L_{c0}}}{\dot{\varepsilon}_S}\right)^{\delta} = \beta\left(\frac{\dot{\varepsilon}_c \dfrac{x}{L_{c0}(1+\xi \lg \dot{\varepsilon}_c)}}{\dot{\varepsilon}_S}\right)^{1/3} \tag{5-21}$$

The above DIF curve with mesh & rate corrections can degenerate to the original DIF curve in Equations (5-6) and (5-7) when the mesh size, x, resumes the standard static crack band width (25.4mm) and the strain rate is relatively low (on or below the order of 1 s^{-1}).

The FE results with the above-proposed "doubly corrected" DIF are compared with the test data in Figure 5-14. A good agreement is observed.

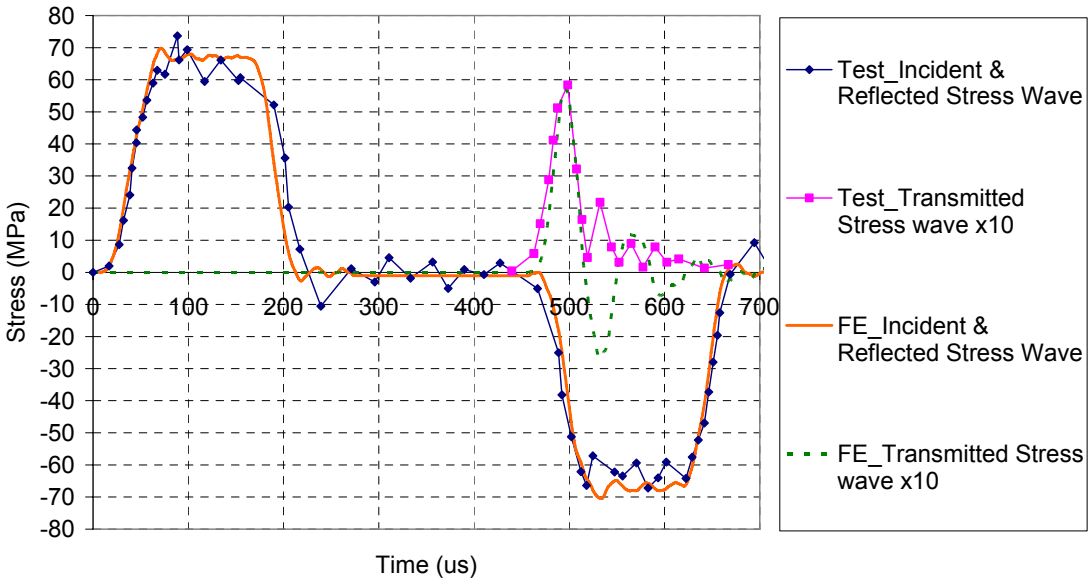

Figure 5-14 SHPB simulation results using "doubly-corrected" DIF compared with test data (Mesh size 1.5875 mm ; Incident impulse peak value 67MPa)

A mesh dependence evaluation is also performed for the "doubly corrected" local DIF, as shown in Figure 5-15. Results demonstrate satisfactory mesh convergence.

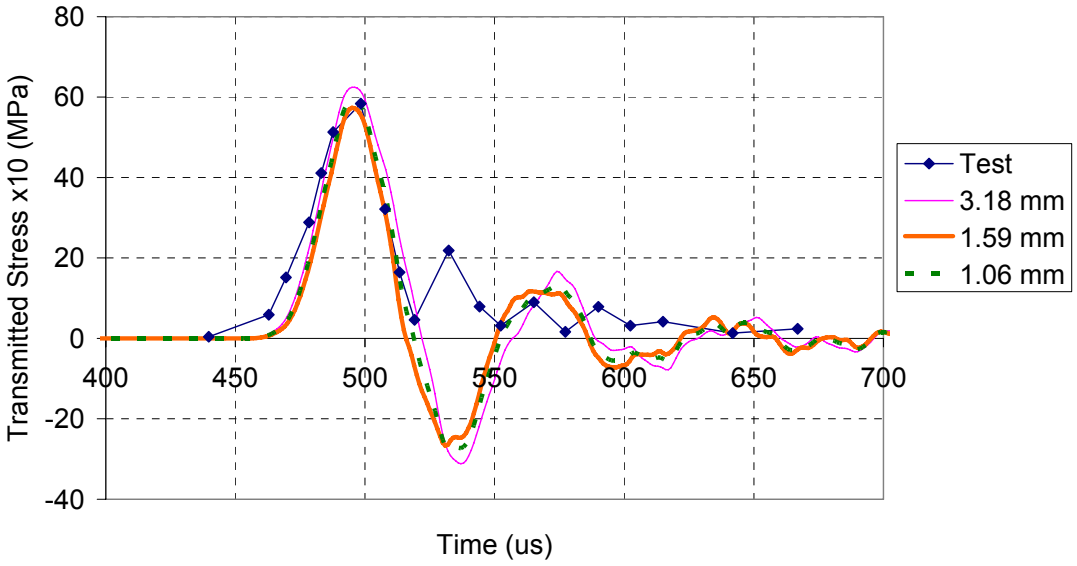

Figure 5-15 Transmitted stress wave FE results with different mesh sizes ("double-corrected", mesh and rate dependent, local DIF, Incident impulse peak value 67*MPa*)

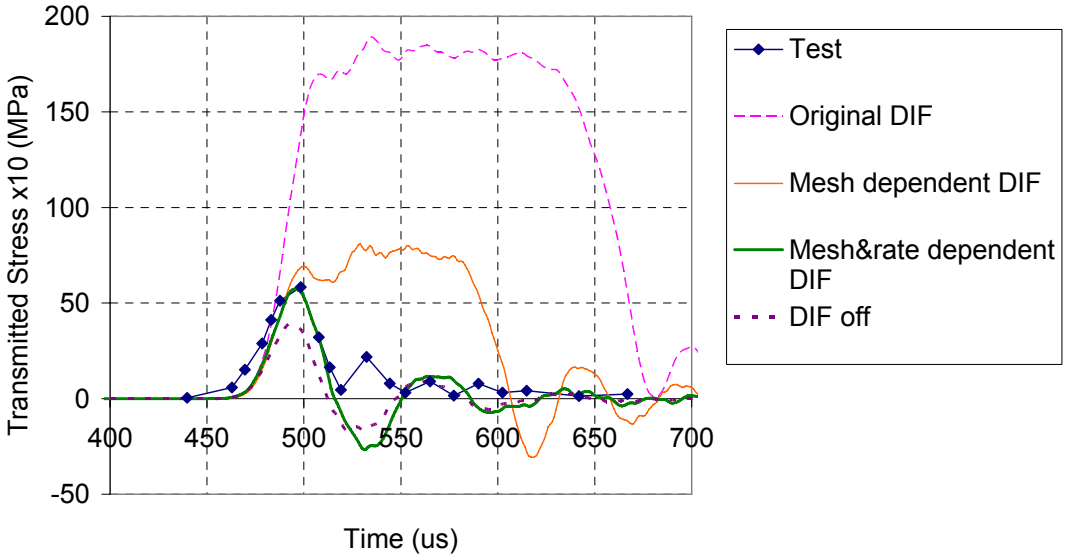

Figure 5-16 Transmitted stress wave FE results with different DIF options (mesh size=1.5875*mm*, Incident impulse peak value 67*MPa*)

Two more tests with different peak impulses, namely 26.5 MPa and 75 MPa , are simulated and the results are compared with the test data in Figure 5-17 and Figure 5-18. The FE stress wave time histories match the tests well. A further comparison between the experimentally and numerically determined strain rates for different input stress pulses is presented in Table 5-1. The strain rates obtained from the current model are nearly the same as the experiment results.

As is demonstrated from the above analyses and comparisons, the introduction of the corrections to the DIF with a local concrete material model is both logical and numerically effective. As with the physical problem itself, when the strain rate becomes higher, the stress wave effect will be increasingly more complicated. Although in principle the basis for the proposed double corrections on the DIF is deemed to remain valid, the exact formulation needs to be further validated. In this regard, continued research will be required.

The next section presents a case study in which a FE model with the proposed "doubly-corrected" DIF is employed to model the response of a concrete beam under an impact load.

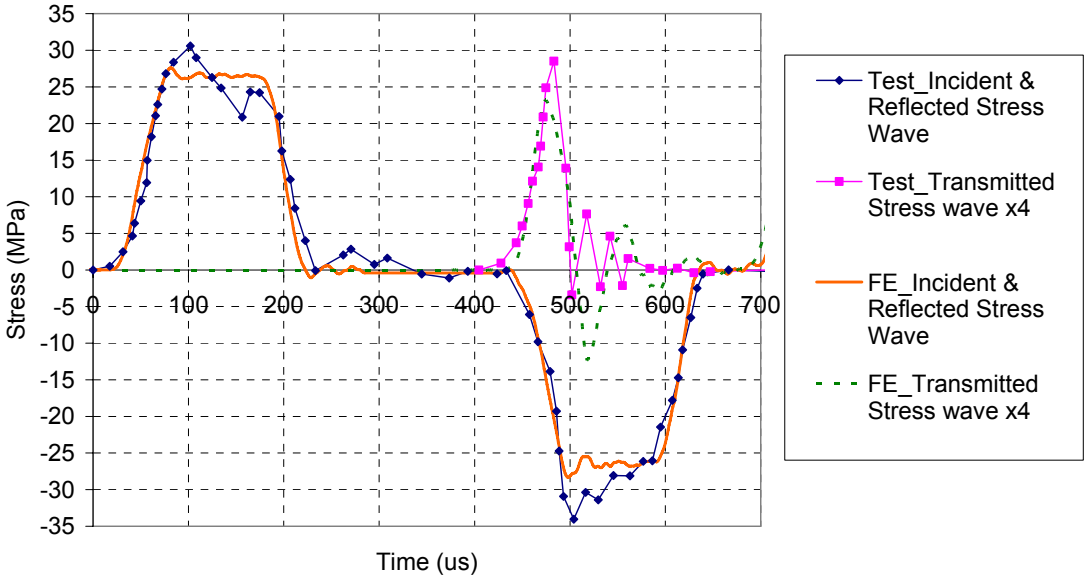

Figure 5-17 SHPB test modelling results compared with test data for "double-corrected", mesh and rate dependent, local DIF (Mesh size 1.5875*mm*; Incident impulse peak value 26.5*MPa*)

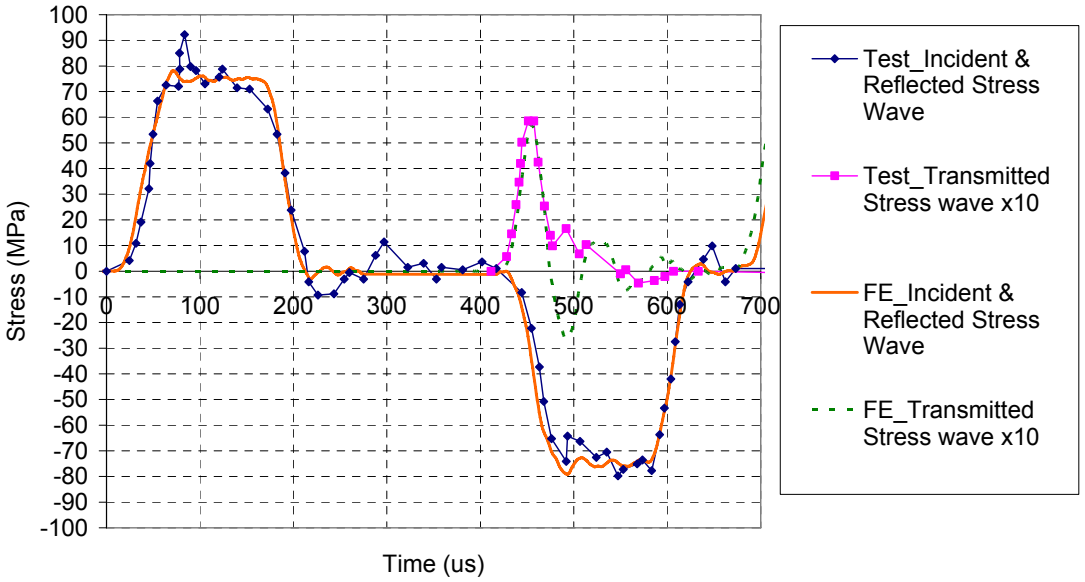

Figure 5-18 SHPB test modelling results compared with test data for "double-corrected", mesh and rate dependent, local DIF (Mesh size 1.5875mm; Incident impulse peak value 75*MPa*)

Table 5-1 experimentally and numerically determined strain rates

Incident stress (MPa)	Experimental (s^{-1})	FE_current model (s^{-1})	FE_Tedesco et al.1991 (s^{-1})
26.5	4.9	4.54	6.10
67	5.3	5.64	6.78
75	5.8	5.79	9.32

5.6 Modelling of impact test with the proposed "doubly-corrected" DIF

An impact test performed by Du et al.(1992) is modelled with the proposed DIF incorporating both mesh and rate corrections, i.e. Equations (5-14) and (5-15), to further verify the adequacy of the DIF corrections in dealing with localisation in FE modelling. The test set-up and the dimensions of the specimen are shown in Figure 5-19.

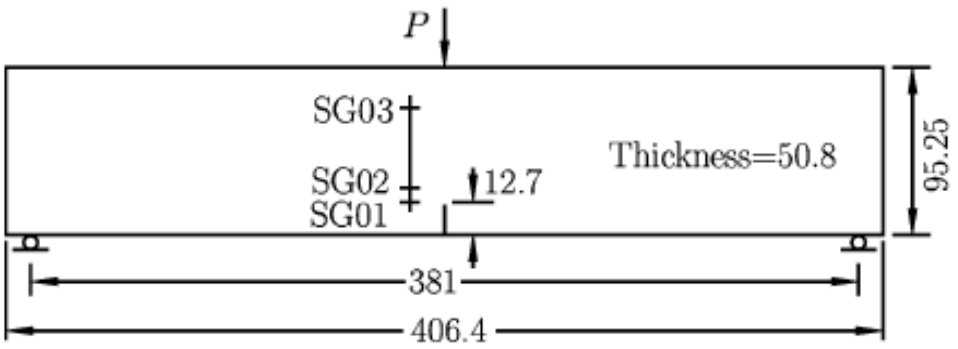

Figure 5-19 Impact test of a concrete beam (unit: *mm*) Su et al. 2010.

In the FE model, the three-point bend impact test of concrete prism is simplified as a 2D plane stress problem. The impact load history as obtained from the test is used as the input loading condition. The support condition is treated as simply-supported in the FE model, and this is confirmed as adequate by checking the resulting natural frequency of the specimen against the measured counterpart. Figure 5-20 shows the impact loading history employed in the analysis.

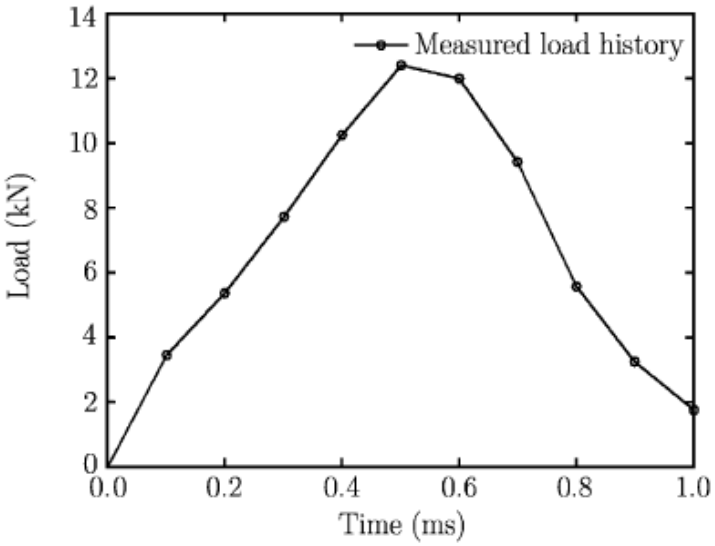

Figure 5-20 Input load history (after Su et al. 2010)

During the actual test, three strain gauges were located at three selected points as shown in Figure 5-19, where "SG" indicates strain gauges. The horizontal distance from the middle notch to the three strain gauges is 12.7*mm* (0.5*inch*). The distance from the centre of the strain gauge to the bottom of the beam is 12.7*mm*, 25.4*mm*, and 76.2*mm* for SG01, SG02 and SG03, respectively.

In the model, the properties of concrete are defined by specifying an unconfined compressive strength f_c' of 53*MPa*, which corresponds to a Young's modulus E_s of

34.48*GPa*, as observed from the test. Other properties include: Poisson's ratio $\nu = 0.2$, density $\rho = 2.5 \times 10^{-6} kg/mm^3$. The Mode I fracture energy is $G_f = 152$ *N/m*.

Figure 5-21 shows a comparison of the computed strain time histories without considering DIF with the experimental results. It can be observed that the strain response from the FE model without DIF at SG03 is quite close to the experimental result. But for SG01 and SG02, the computed strains are all markedly lower than the test results.

FE results from using the "original DIF" and the "mesh dependent only DIF" are presented in Figure 5-22 and Figure 5-23, respectively. The computed results appear to significantly over-predict the strain response as compared with test data in both modelling conditions.

Finally, Figure 5-24 presents the FE results with the incorporation of the doubly-corrected DIF. As can be seen, the computed results improve considerably from the models mentioned above and they compare very well with the experimental data.

The above comparisons further confirm that the proposal of introducing mesh and rate dependent corrections to the DIF in FE modelling with a local concrete model is a rational and also effective way. With such corrections it is possible to achieve realistic and consistent representation of the strain rate effect on the dynamic response of concrete under high rate loadings.

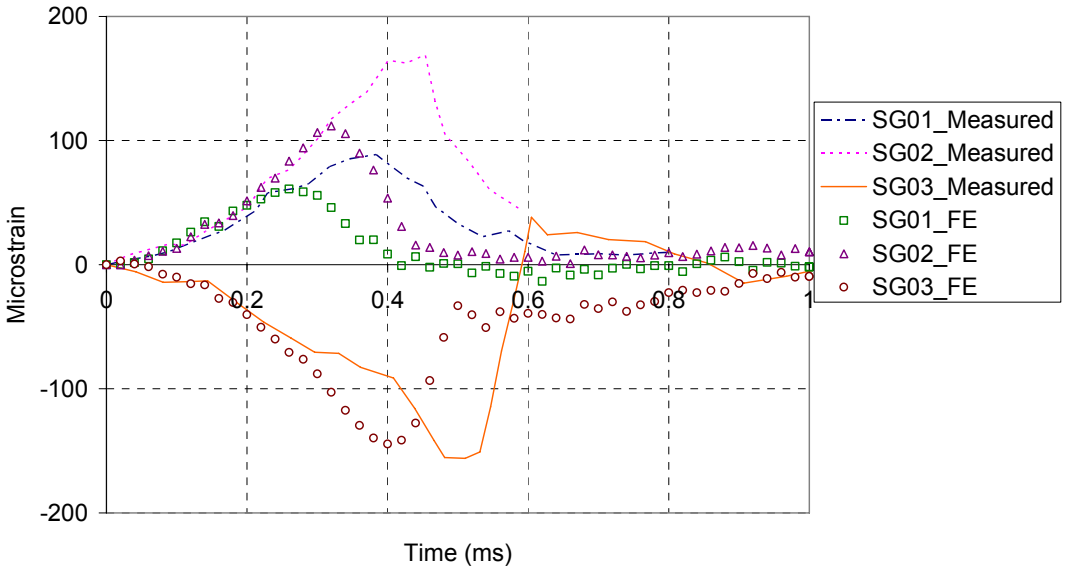

Figure 5-21 Strain time history (DIF OFF)

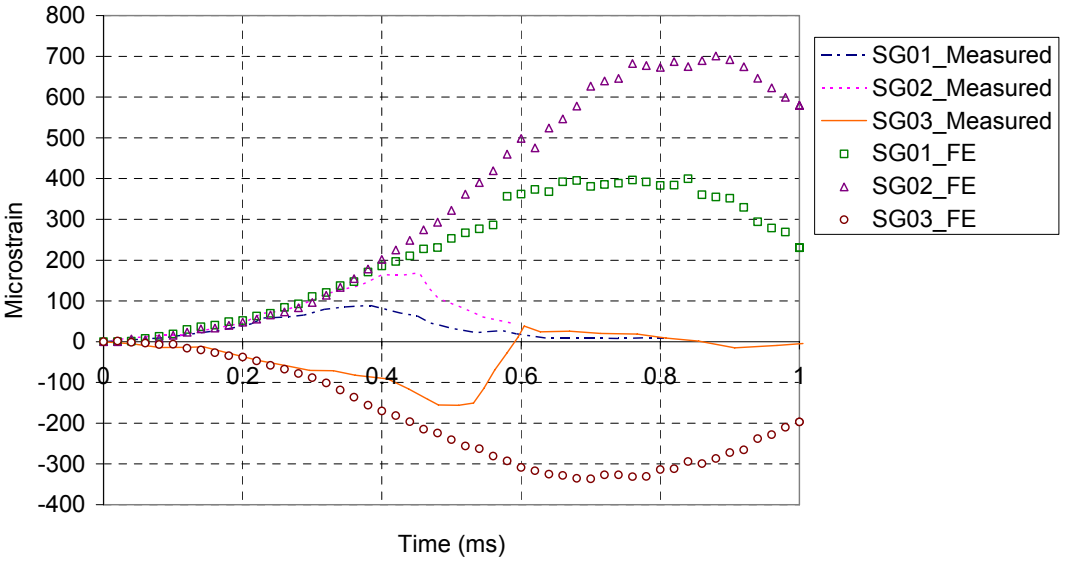

Figure 5-22 Strain time history (DIF Original input)

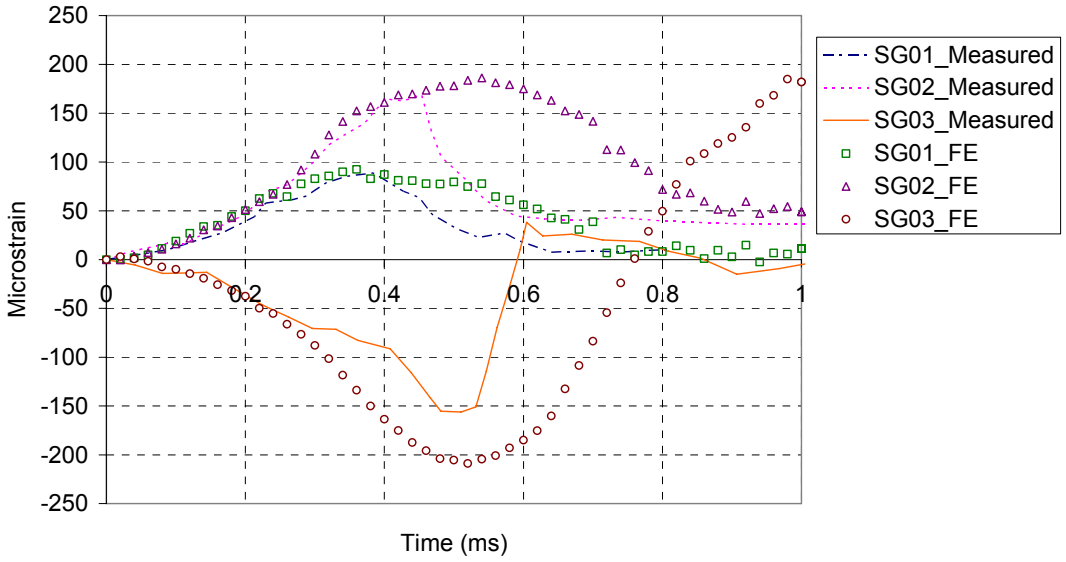

Figure 5-23 Strain time history (mesh-corrected local DIF input)

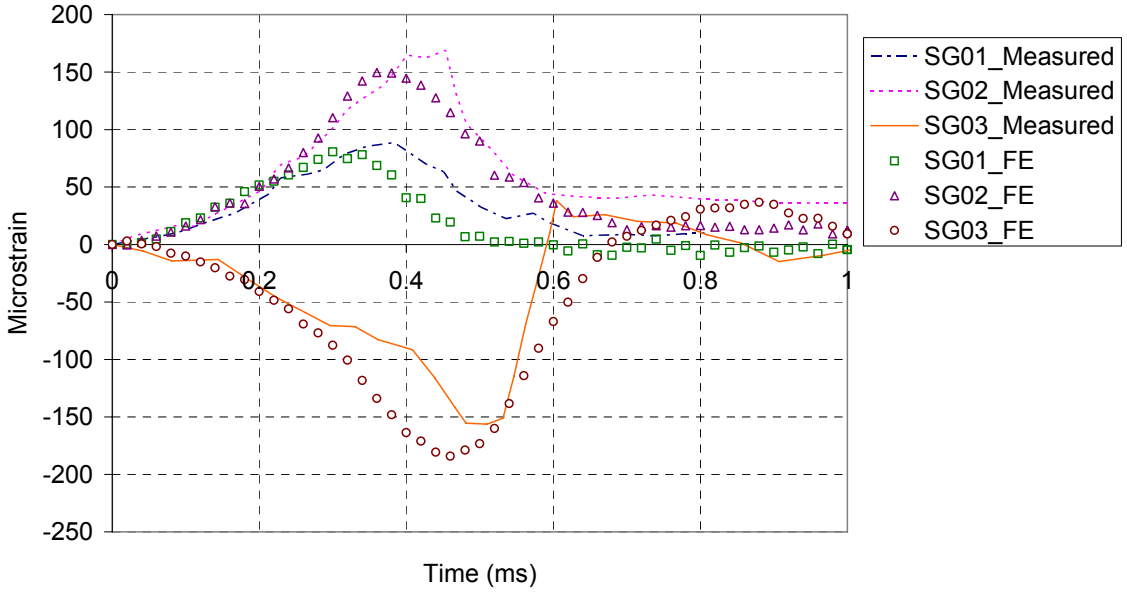

Figure 5-24 Strain time history ("double-corrected", mesh and rate, local DIF input)

5.7 Conclusions

Based on the FE modelling studies presented in this chapter, the following conclusions may be drawn:

1) The dynamic tensile strength increase (tension DIF) is demonstrated to be a genuine material property for concrete in tension. This observation is supported by a variety of tension-dominated modelling analyses, ranging from simplified direct tension, SHPB tension test, to three-point bend impact test. Without considering the DIF at the material property level, it is not possible to reproduce reasonably the relevant experimental results from the FE models.

2) However, the commonly adopted empirical global DIF curves can not be applied directly in the FE analysis with a local concrete material model without discrimination; this is particular the case in tension-dominated responses due to the well-known localisation of fracture, which naturally extends to strain-rate localisation in the case of dynamic loading. To rectify this problem and enable mesh convergence, a mesh-correction factor is proposed to be introduced in the local DIF input. Moreover, due to the complexity in the stress and strain distribution when the loading/strain rate is high, a rate correction factor is further incorporated. Thus, a "doubly-corrected" local DIF versus strain rate relationship is proposed for FE applications.

3) The appropriateness of the proposed doubly corrected local DIF is confirmed by various mesh convergence modelling studies and comparison of the computed results with experimental data. Although the specific correction parameters in the current study may be dependent upon to the concrete model employed (i.e., the K&C model), the approach is generally applicable and can be easily extended to other local material models.

5.8 Reference

Bazant, Z.P. and Oh, B.H. (1983), "Crack band theory for fracture of concrete", *Materials and structures*, 16(93):155-177.

Brace, W.F. and Jones, A.H. (1971), "Comparison of uniaxial deformation in shock and static loading of three rocks", *J Geophys Res.* 13: 4913–4921.

Bischoff, P.H. and Perry, S.H. (1991), "Compression behaviour of concrete at high strain-rates", *Mater Struct.* 24: 425–450.

CEB-FIP (1993), Model Code 90. Lausanne.

Du, J., Yon, J.H., Hawkins, N.M., Arakawa, K. and Kobayashi, A.S.(1992), "Fracture process zone for concrete for dynamic loading", *ACI Materials Journal*, 89: 252-258.

Gray III, G.T. (2000), "Classic Slplit Hopkinson Pressure Bar Testing", *ASM Handbook, Mechanical testing and evaluation*, 8: 462-476.

Hentz S., Donze, F.V. and Daudeville, L. (2004), “Discrete element modelling of concrete submitted to dynamic loading at high strain rates”, *Computer structure,* 82: 2509-2524.

Li, Q.M. and Meng, H. (2003), “About the Dynamic strength enhancement of concrete like materials in a split Hopkinson pressure bar test”, *Int J Solids Struct*. , 40: 343-360.

LSDYNA (2007), Keyword User’s Manual Version 971, Livermore Software Technology Corporation.

Lu, Y., Song, Z. and Tu, Z. (2010), “Analysis of dynamic response of concrete using a mesoscale model incorporating 3D effects”, *Int J Protective Structures*, 1(2):197-217.

Lu, Y.B. and Li, Q.M. (2011), “About the dynamic uniaxial tensile strength of concrete-like material”, *International journal of impact engineering*, 38: 171-180.

Malvar, L. J., Crawford, J. E., Wesevich, J. W. and Simons, D. (1997), "A plasticity concrete material model for DYNA3D″, *International Journal of Impact Engineering*, 19(9-10): 847-873.

Malvar, L.J. and Crawford, J.E. (1998), “Dynamic increasing factors for concrete”, Twenty-Eight DDESB Seminar, Orlando, August.

Malvar, L. J., Crawford, J. E. and Morrill, K. B. (2000), "K&C Concrete material model release3—automated generation of material model input", K&C documents, August.

Ross C. A. (1989), Split-Hopkinson pressure bar tests. Final Report, Air Force Engineering and Services Center, Tyndall AFB, Fl, ESL-TR-88-82.

Ross, C.A., Thompson, P. Y. and Tedesco, J. W.(1990), “Split-Hopkinson Pressure-Bar tests on Concrete and Mortar in Tension and Compression”, *Materials Journal*, 86(5): 475-481.

Su, X.T., Yang, Z.J. and Liu, G. (2010), "Finite element modelling of complex 3D static and dynamic crack propagation by embedding cohesive elements in ABAQUS", *Acta Mechanica Solida Sinica*, 23(3): 271-282.

Tedesco, J.W., Ross, C.A. and Brunair, R.M. (1989), “Numerical analysis of dynamic split cylinder tests”, *Comput. Struct*., 32: 609-624.

Tedesco, J.W., Ross, C.A., McGill, P.B. and O’Neil B.P. (1991), “Numerical analysis of high strain rate concrete direct tension tests”, *Computers& structures*, 40(2): 313-327.

Zhang, M., Wu, H.J., Li, Q.M. and Huang, F.L. (2009), “Further invesgtigation on the dynamic compressive strength enhancement of concrete-like materials based on split Hopkinson pressure bar tests. Part I: Experiments”, *International Journal of Impact Engineering*, 36:1327-1334.

Zhou, X.Q. and Hao, H. (2008), “Mesoscale modelling of concrete tensile failure mechanism at high strain rates”, *Computers and Structures*, 86(21-22): 2013–2026.

Chapter 6 Dynamic FRP to concrete bond-slip model

6.1 Introduction

The United Sates Department of State reported that globally there were 10,999 terrorist attacks in 2009, and people worldwide killed, injured, or kidnapped as a result of terrorism were 53,897 (USDS 2010). Social services and civilian capacity-buildings are highlighted as the terrorism targets in Moscow (2010), London (2005), Madrid (2004), Istanbul (2003) and New York (2001). Attacks directed towards vulnerable structures may cause considerable damage and loss of life. Therefore, increasing the resistance of structures, including military or critical government buildings, important transport terminals, chemical, petroleum and nuclear plants, directed towards high strain rates are of crucial importance due to their high risk of terrorist attack. In-site enhancing of RC structures using externally bonded steel plates has previously been attempted by increasing the flexural strength of beams, walls and slabs. FRP composites are now being utilised instead of steel due to their higher strengths, better corrosion resistance and greater ease of transportation and handling (Buchan and Chen 2007).

For FRP strengthened concrete structures, the bond behaviour between the FRP and concrete is one of the most important aspects of the strengthening. A significant

amount of empirical (Pellegrin et al. 2008; Ueda et al. 1999; Wu et al. 2001; Yao 2004), analytical (Chen and Teng 2001) and numerical investigations (Li et al. 2010; Lu et al. 2005; Lu et al. 2004) has been conducted for static debonding behaviour. However, little attention has been paid to the bond behaviour in high energy events. The bond behaviour under high strain rates may significantly differ from that under the static state due to the concrete strength enhancement from strain rate effects and damage induced by the impact wave travelling through the interface.

Current design guidelines for structural response analysis under high energy events such as TM5 (1990) and ASCE (1997), still use single degree freedom (SDOF) systems to perform dynamic analysis. These guidelines are for general structure use but no advice is provided for retrofit RC structures against impulsive load. Wu et al. (2009) formulates a layered model that allows for both FRP strengthening and the consideration of strain rate effects on the blast resistant capacity of flexural structural members. It is incorporated into a SDOF model for dynamic analyses. However, the SDOF model is only sufficient for analyzing the peak response of the structure under non-oscillatory loads. An in-depth understanding of the structural behaviour under high energy events is required.

Although the finite element (FE) methods based on continuum mechanics approaches can be used to analyze large scale structural response to blast, it is still rarely used in design because of its perceived complexity and expense due to the numerous difficulties and challenges involved in modelling bonded interface between FRP and concrete (Wu et al. 2009).

Perfect bond has been normally assumed in FE modelling (Nam et al. 2009; Schmidt and Cheng 2009). But the application of the perfect bond is conditional that debonding occurs in the concrete layer, so the concrete dynamic properties is properly captured and the FE mesh should be close or smaller than the normal debonding depth, which is approximately 2-5mm (Lu et al. 2004). For computational cost consideration, perfect bond modelling is normally suitable for the analysis of FRP-to-concrete bonded test joints, not for structural elements such as beams, columns or slabs, when the element size requirement is in meso-scale. A bond-slip model is used for solving these problems so that a layer of interface element describing the FRP-to-concrete bond mechanics can be employed and macro-scale elements could be used in FE modelling. For modelling large scale structures strengthened with FRP under high strain rates, there is a lack of comprehensive dynamic bond slip model to properly capture the FRP-to-concrete bond behaviour under high strain rates.

De Lorenzis and La Tegola's (2005) analytical research conducted on the bond behaviour for high energy invents. They developed an analytical solution for the bond-slip model under impulsive loading, which expresses the impulsive to static maximum stress ratio $\tau_{\max} / \tau_{\max\_s}$ as a function of the ratio of the total duration of the impulse propagation time in the FRP total bond length to the one in the effective bond length t_a / t_e. It was assumed that the bond length was significantly larger than the effective bond length. The analysis was restricted to the linear region only of the bond-slip law without considering softening, nonlinearity, and it was analyzed in a

static framework due to the assumption that the effect of inertia forces was neglected. This interface model has been applied into the numerical analysis recently, i.e. Nam et al. (2010), but there was a lack of layered capacity analysis (Wu et al. 2009) regarding the mesh convergence study in that numerical modelling, also the bond behaviour comparison between the test and the numerical was not discussed. This study attempts to find a more appropriate dynamic bond-slip model for high strain rate events via numerical experiment, and then validate the proposed model by comparing with test results. This chapter mainly concerns deriving the dynamic bond-slip model.

The bond behaviour of an FRP laminate bonded to a concrete element across an existing crack is similar to that in a simple shear test on FRP-to-concrete bonded joints, where the FRP is pulled (De Lorenzis and La Tegola 2005), so it is possible to develop a bond-slip model under different slip rates using the pull-off test by properly modelling the concrete with dynamic effects. The mesh and rate dependent dynamic increasing factor (DIF) for local K&C concrete damage model presented in Chapter 5 is applied in the meso-scale modelling of pull-off test with perfect bond assumption as in Lu et al. (2004).

The bond-slip model with DIF effect is developed in 2 steps: 1) the development of a slip rate dependent dynamic bond-slip model based on the model-II fracture energy. Here the DIF for bond-slip relationship is dependent on the slip rate and defined as the ratio of the dynamic to static maximum stress ratio $\tau_{\max} / \tau_{\max\_s}$. The DIF for bond-slip relationship at a particular slip rate is equal to the square root of the

dynamic to static fracture energy ratio; 2) the DIF versus slip rate for bond-slip relationship is applied to the static bond-slip model of Lu et al. (2005) to make it suitable for dynamic situations.

6.2 Finite element modelling

6.2.1 FE model

The development of the DIF for bond-slip relationship is purely numerical here as there are no dynamic experiment results available to the best knowledge of the author. Concrete modelling is the main aspect of modelling debonding of FRP from concrete prism as the debonding mostly happens in a thin layer of concrete adjacent to the FRP (Lu et al. 2004). In this chapter, the K&C concrete damage model with the "double corrected" concrete local DIF is introduced to the meso-scale dynamic pull-off test.

The concrete was modelled using the K&C concrete damage model (Malvar et al. 1997). The crack band localized width, lw, is set equal to the element characteristic length h_c, so that the Mode I static fracture energy G_{fs}^{I} remains a material constant in each element. The fracture energy is controlled by the uniaxial tensile stress (σ) - strain (ε) curve:

$$\int \sigma d\varepsilon = \frac{G_{fs}^{I}}{h_c} \tag{6-1}$$

The FRP-to-concrete pull-off test specimen S-CFS-400-25 reported in Wu et al. (2001) was adopted as the reference case in this study. The test specimen consisted of a 275×100×100*mm* (length × width × depth) concrete prism bonded with a 0.22*mm* thick and 40*mm* wide FRP sheet with a bond length of 250*mm*. The concrete had a cylindrical compressive strength of 57.6*MPa*. The FRP had a modulus of elasticity of 230*GPa*. The same FE geometry and boundary conditions as Lu et al. (2004) were adopted (Figure 6-1).

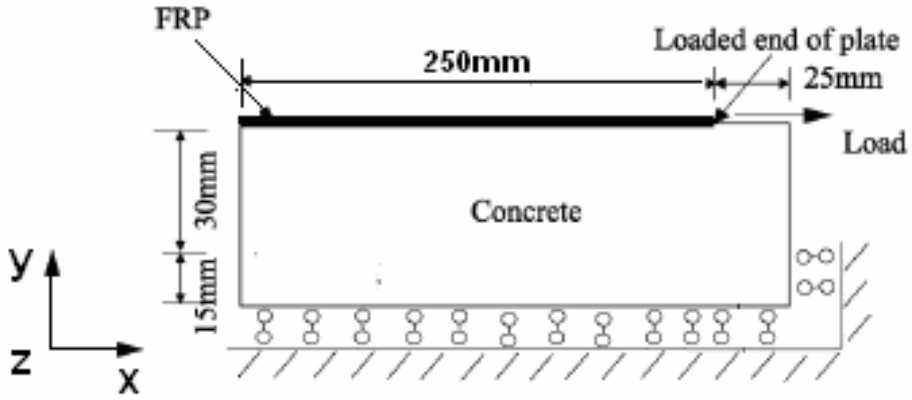

Figure 6-1 Pull-off test FE model geometry

The concrete prism included in the FE model has a height of 45*mm*, which is generally much smaller than the actual concrete prism in a bond test. The exclusion of the rest of the concrete prism leads to a reduced computational effort but has little effect on the FE results. The test was modelled as a 2D plane stress problem but the predicted results including loads, stresses, strains and slips are corrected according to Chen and Teng's (2001) width effect factor β_w so that they can be compared with test results.

$$\beta_w = \sqrt{\frac{2 - b_p / b_c}{1 + b_p / b_c}} \tag{6-2}$$

The FRP was modelled as an isotropic linear elastic material with a thickness t_p =1 mm and Young's modulus E_p = 50.6 GPa so that its axial rigidity $E_p t_p$ remains the same as in the test. Because debonding of FRP in the pull-off test mostly occurs at a small distance beneath the adhesive-concrete interface in the concrete, the FRP was assumed to be perfectly bonded to the concrete prism as in Lu et al. (2004). The specimen was loaded with a time dependent displacement at the loaded end.

6.2.2 Loading scheme

The FRP is loaded under displacement control with a constant velocity at the FRP end. This guarantees debonding occurs at a constant slip rate, equal to the velocity loading rate at the FRP end because the failure occurs at the constant velocity at the FRP end no matter what the exact values of the slip rate at different local positions. As the concrete prism is reduced in size, the slip rate is the relative slip rate between the FRP ends to the bottom of the 45mm height numerical specimen. To avoid numerical instability, the constant velocity control was added with a smooth start which only takes 5% of the total loading time, ensuring that the acceleration, velocity and displacement all starts from 0.

The smooth curve was defined with "*DEFINE_CURVE_SMOOTH" in LSYNA (Figure 6-2). Here T_{rise} is the duration of rising time; T_{start} is the start time; T_{end} is the

end time. In this study, T_{rise} was set equal to 5% of the total loading time. The distance is equal to the integration of the velocity under the velocity time.

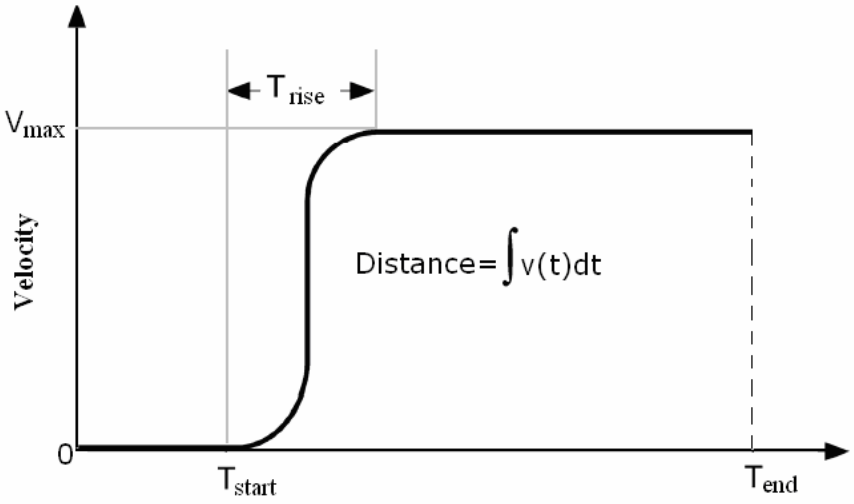

Figure 6-2: Define smooth curve in LSDYNA (LSDYNA Keywords Manual 2007)

6.2.3 Mesh objectivity

At first, the concrete DIF was turned off and the produced load slip relationships corresponding to different loading rates at the FRP loaded end are compared with the test static data in Figure 6-3. Clearly, loading rates has little effect when the DIF is not considered. However, based the work of Chapter 5, DIF is a genius material property exists which must be included in FE modeling for high strain rate events. If the global DIF versus strain rate relationship (Marlvar et al. 1998) is introduced directly, mesh convergence can not be achieved (Figure 6-4). Whereas, with the "double corrected" DIF, the concrete local DIF presented in Chapter 5, mesh objectivity is achieved showed (Figure 6-5).

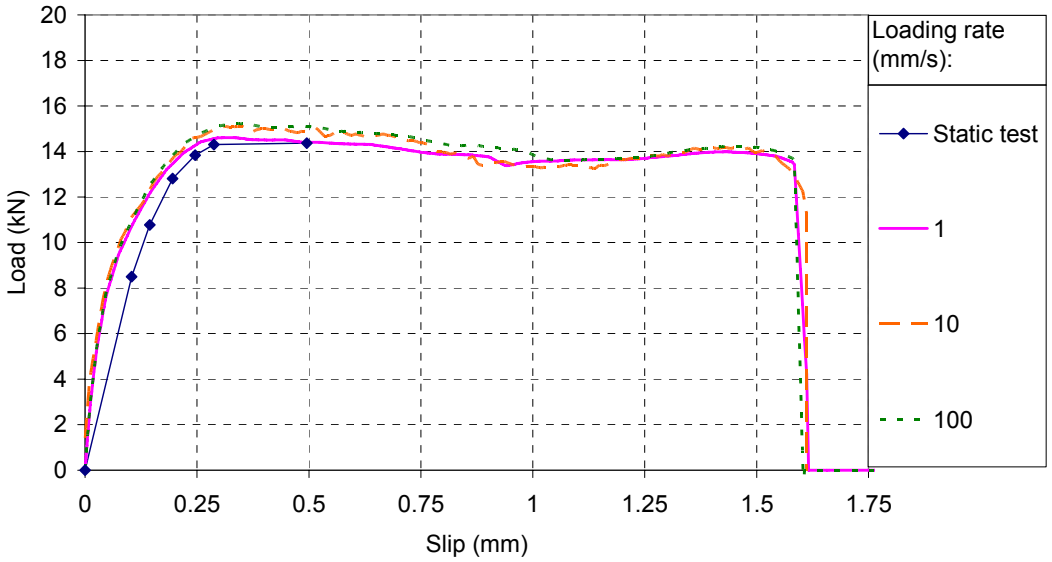

Figure 6-3: Load slip curves for different loading rates (DIF off, mesh size 1*mm*)

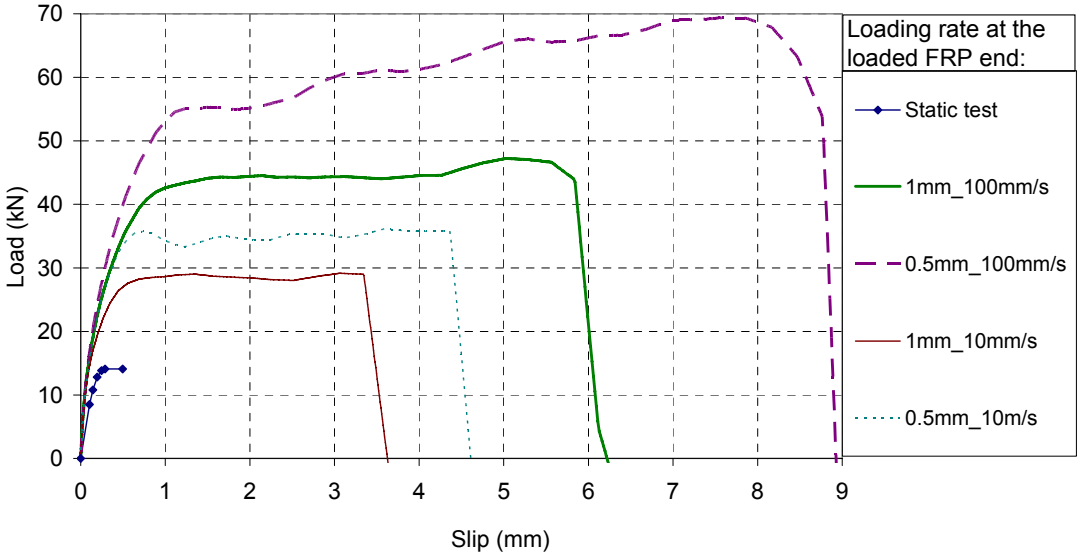

Figure 6-4: Load slip curves for different mesh sizes and different loading rates (Original global DIF versus strain rate relationship)

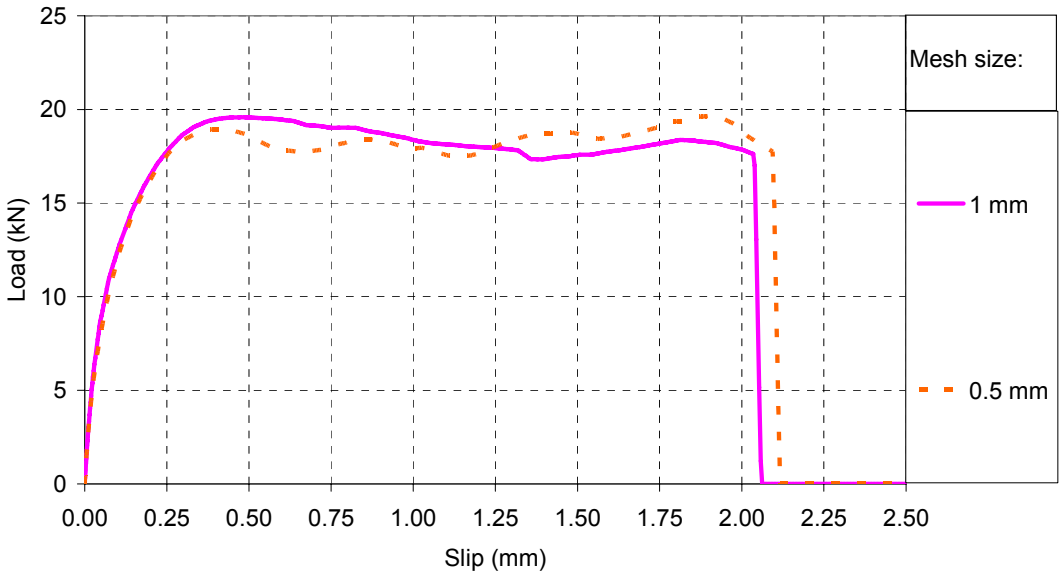

Figure 6-5: Mesh convergence with mesh and rate dependent concrete local DIF (loading rate 100*mm/s*)

6.3 DIF for bond-slip relationship

6.3.1 Effect of slip rates to DIF for bond-slip relationship

The predicted load displacement curves for the reference specimen under different loading rates are presented in Figure 6-6. Clearly the peak load and the slip at the final failure are all increased with the loading rate.

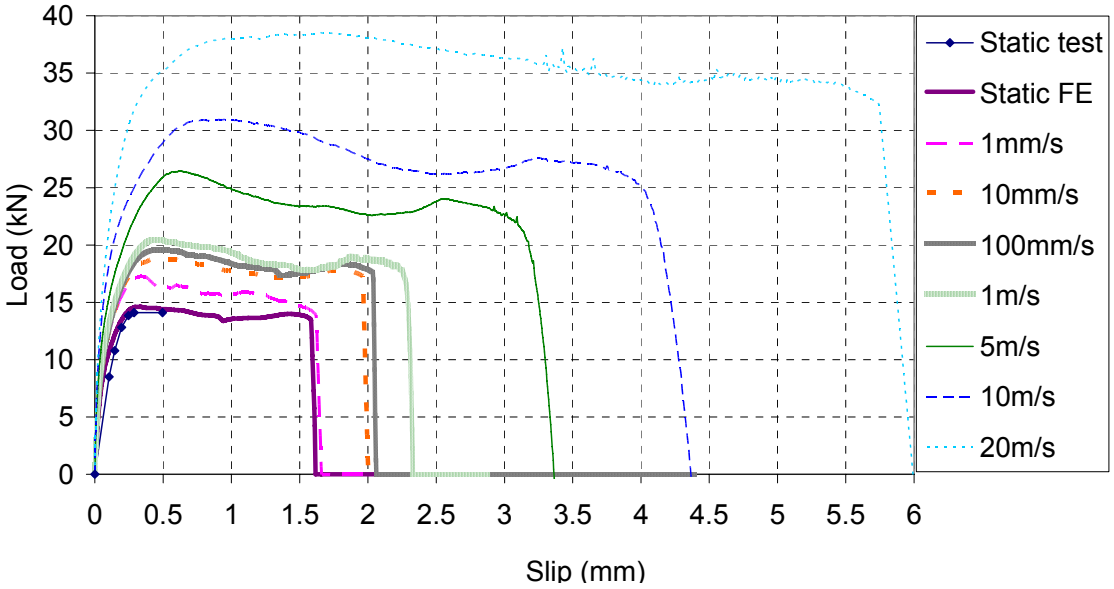

Figure 6-6: Load slip curves for different loading rates at the FRP end (mesh size 1*mm*)

The DIF for bond-slip relationship at a particular slip rate is here defined as the square root of the dynamic to static fracture energy ratio. Because the concrete DIF only affects the strength of the concrete but not its Young's modulus, the load slip curves and local bond-slip curves for different loading rates should have the same initial slip for the simplified bi-linear model.

There were three steps involved in obtaining the DIF for bond-slip relationship based on energy: 1) the local bond-slip curves were obtained over the whole bond length, and the Mode II fracture energy was calculated from the local bond-slip curves located in a relatively stable zone where the shape of the local bond-slip curves were similar and the area under these curves were almost equal to each other; 2) the static bond-slip curve was simplified as bilinear. The maximum bond stress for the static state and the fracture energy were calculated; 3) calculate the dynamic state fracture energies under different slip rates.

The predicted static local bond slip and bilinear simplification are presented in Figure 6-7.

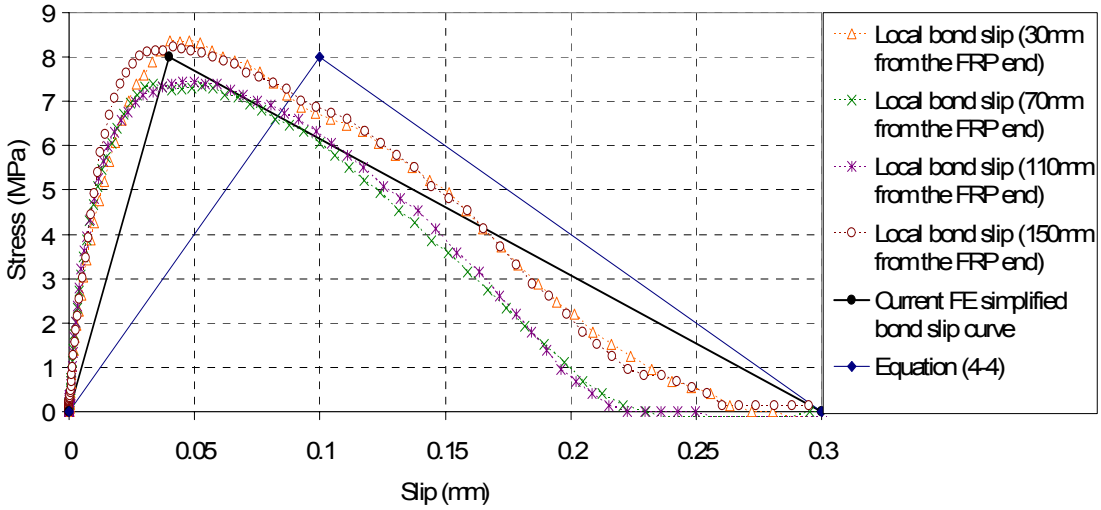

Figure 6-7: Static bond-slip relationship for S-CFS-400-25 reported in Wu et al. (2001)

From Figure 6-7, the stable zone for the specific case is approximately from 30mm away from the FRP end. The area under the current FE simplified bond slip curve is almost equal to the area under the local bond slip curves in the stable zone and the bond slip relationship obtained from the test results in Wu et al. (2001).

The simplified triangle bond-slip curves under different slip rates are presented in Figure 6-8 to Figure 6-10. Figure 6-8 and Figure 6-9 show two cases for bilinear simplification under slip rates of 1*mm/s* and 1*m/s*. Figure 6-10 presents the simplified dynamic bond-slip curves for the different slip rates.

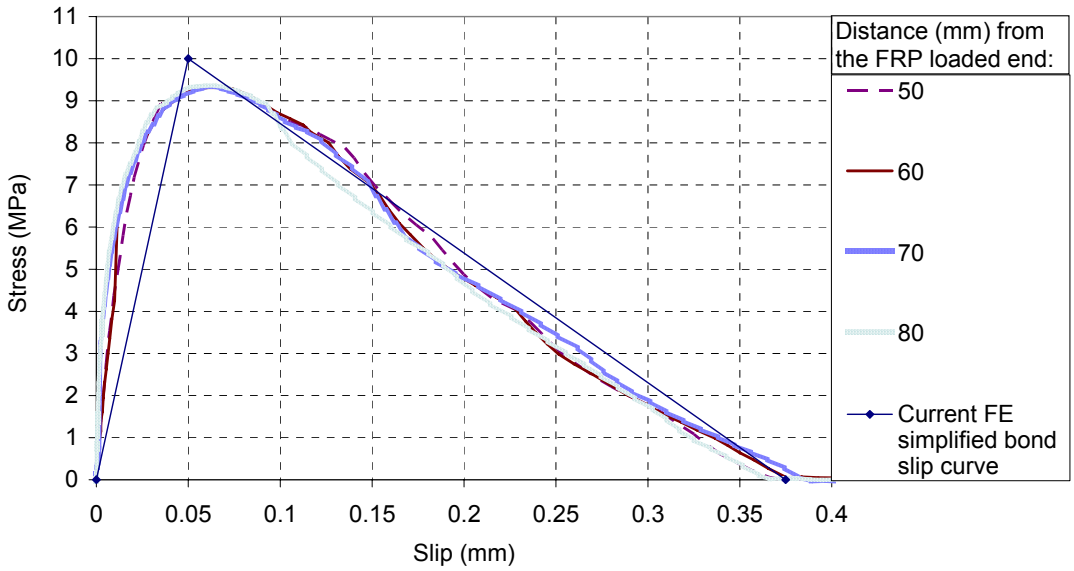

Figure 6-8 Local bond-slip curves at slip rate=1*mm/s*

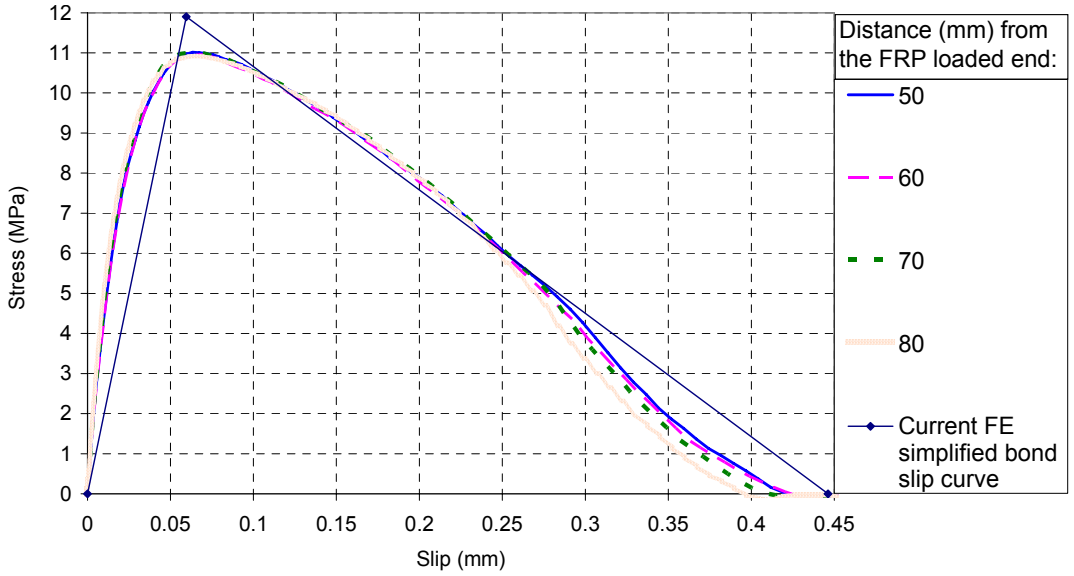

Figure 6-9 Local bond-slip curves at slip rate=1*m/s*

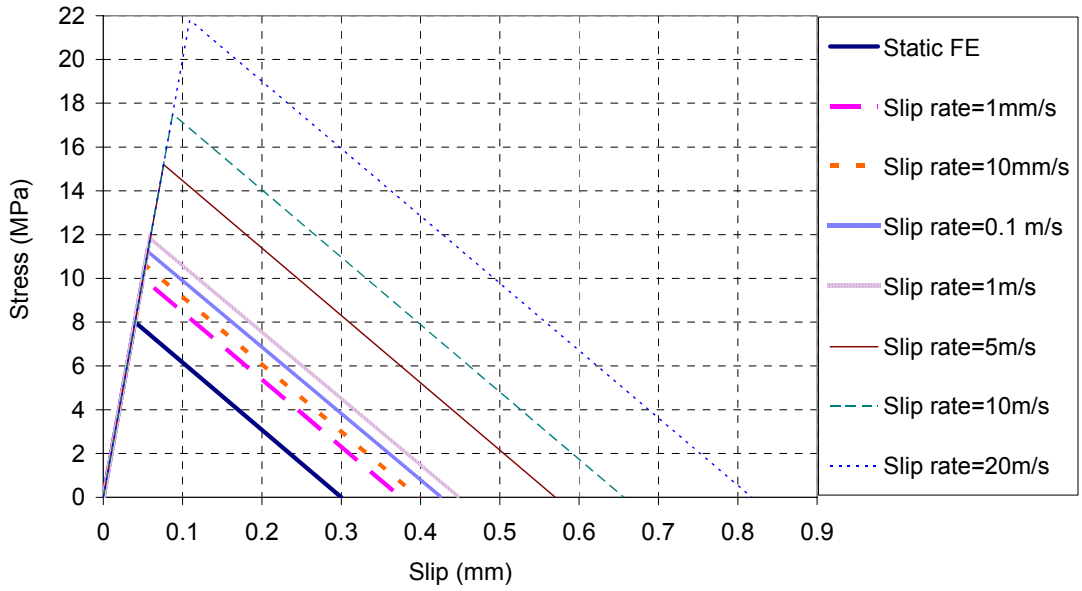

Figure 6-10: Simplified different bond-slip curves under different slip rates for S-CFS-400-25 reported in Wu et al. (2001)

The bilinear simplification presented in Figure 6-8 and Figure 6-9 was obtained based on energy equilibrium and keeping the hardening and softening slops of the local bond-slip curves under different slip rates constant. The DIF for the bond-slip relationship, α_{DIF}, at a slip rate $\dot{s}$ is equal to the square root of the fracture energy under the local bond-slip curve for different slip rate:

$$\alpha_{DIF} = \sqrt{\frac{G_f^{II}}{G_{fs}^{II}}} \tag{6-4}$$

where G_f^{II} is the dynamic shear fracture energy in N/mm; and G_{fs}^{II} is the static shear fracture energy in *N/mm*. For a bilinear bond-slip relationship, the following relationships stand based on the assumptions mentioned earlier:

$$\frac{\tau_{\max}}{\tau_{\max\_s}} = \frac{s_0}{s_{0s}} = \frac{s_f}{s_{fs}} = \alpha_{DIF} \tag{6-5}$$

in which $\tau_{\max}$ is the maximum dynamic bond stress in *MPa*; s_0 is the slip at the maximum dynamic bond stress in mm; s_f is the maximum dynamic slip at failure in mm; $\tau_{\max\_s}$ is the static maximum bond stress unit: *MPa*; s_{0s} is the slip at the maximum static bond stress in mm; and s_{fs} is the maximum static slip at failure in *mm*.

The load slip curves under different slip rates were used for double check the dynamic fracture energy. The external performance of the ultimate load (Figure 6-6) at the FRP loaded end is also a function of the bond-slip fracture energy. Equation (6-3) referred from Wu et al. (2001) for the relationships about bond stress, slips and loads at FRP end were used for double check whether the simplification can be inversely operated to the numerical output ultimate loads for different loading rate cases.

$$\tau_{\max} = \frac{P_u^2}{E_p t_p b_p^2 s_f} \tag{6-3}$$

where $\tau_{\max}$ is the peak value of the bond stress; P_u is the ultimate load at the FRP end from the load slip curves; E_P is the elastic Young's modulus of the FRP plate; t_p is the thickness of the FRP plate; b_p is the FRP plate width; s_f is the final slip of the bond-slip curves.

The FE predicted ultimate loads $P_{\max\_FE}$ and the ultimate load calculated from the simplified bond-slip model presented in Figure 6-10 are compared in Table 6-1.

Table 6-1 DIF for bond-slip relationship, bond stress, slip and load for S-CFS-400-25

Slip rate (m/s)	DIF for bond-slip relationship α_{DIF}	$\tau_{\max}(MPa)$	$s_f(mm)$	$P_{\max\_caculated}(kN)$	$P_{\max\_FE}(kN)$
Static (1×10^{-7})	1.00	8.0	0.300	13.9	14.3
1×10^{-3}	1.25	10.0	0.375	17.4	17.3
1×10^{-2}	1.32	10.6	0.398	18.5	18.8
1×10^{-1}	1.41	11.3	0.424	19.7	19.6
1	1.49	11.9	0.446	20.7	20.5
5	1.90	15.2	0.57	26.5	26.5
10	2.19	17.5	0.656	30.5	30.8
20	2.72	21.8	0.818	38.0	38.0

6.3.2 Determination of α_{DIF} versus $\dot{s}$ relationship

Yao (2004) recorded 1.2mm final displacements at the loaded end of FRP in 10 minutes. This represents an average loading rate of $2\times10^{-6}\ m/s$. The final displacement and total loading time varies depending on many factors. A slip rate which is one scale smaller than the above scale, $1\times10^{-7}\ m/s$, is chosen as the static slip rate. All slip rates are normalised in the following analysis in establishing a simple formula for the DIF for bond-slip relationship under different slip rates. Note that the DIF for bond-slip relationship, α_{DIF}, versus the normalized slip rate is

independent of the FRP and concrete prism width ratio effect. It only includes the effect of concrete strength $f_c^{'}$.

Test specimens Yao II-5 in Yao (2004), with $f_c^{'}$=23.8MPa, E_p = 256GPa and FRP thickness t_p=0.165mm, was analyzed in the same way of the reference case. The DIF for bond-slip and slip rate relationship is present below in Figure 6-11. Figure 6-12 and Figure 6-13 are the trend line analysis plots for two different slip ranges.

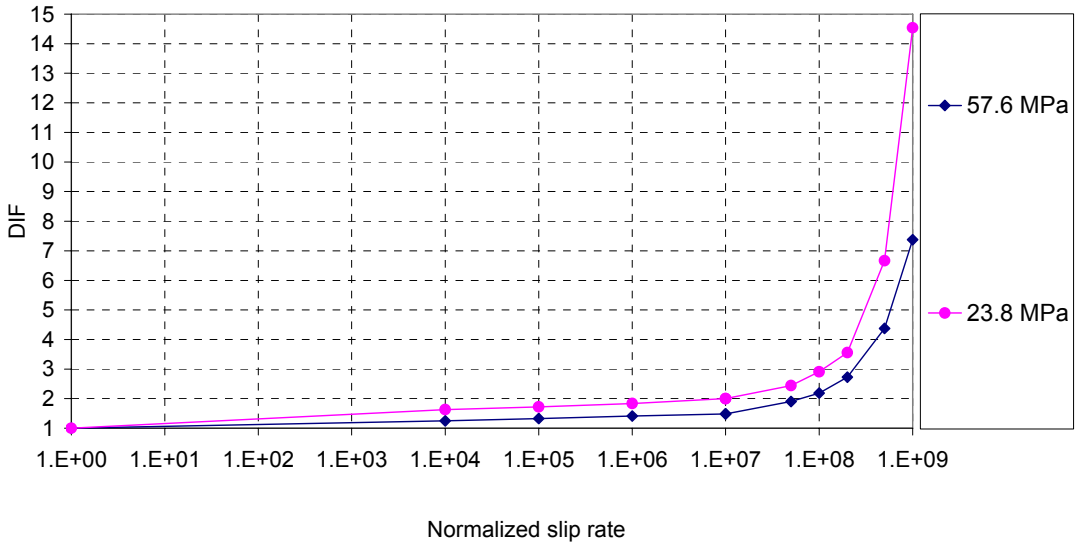

Figure 6-11: DIF for bond-slip relationship versus normalized slip rate for concrete strength fc'=57.6MPa and 23.8MPa

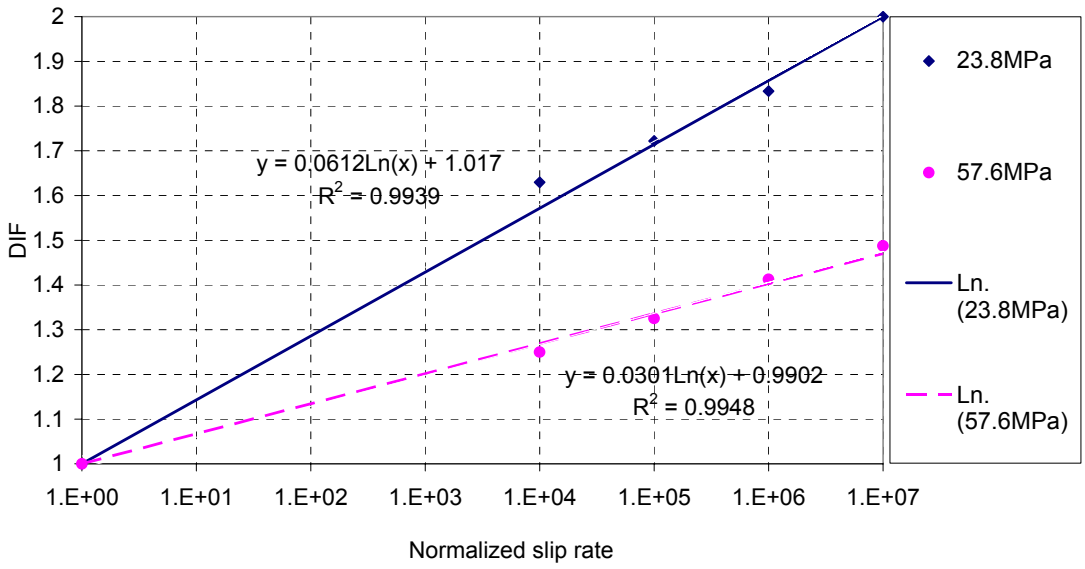

Figure 6-12: Trend line analysis for DIF for bond-slip relationship versus normalized slip rate at lower slip rate

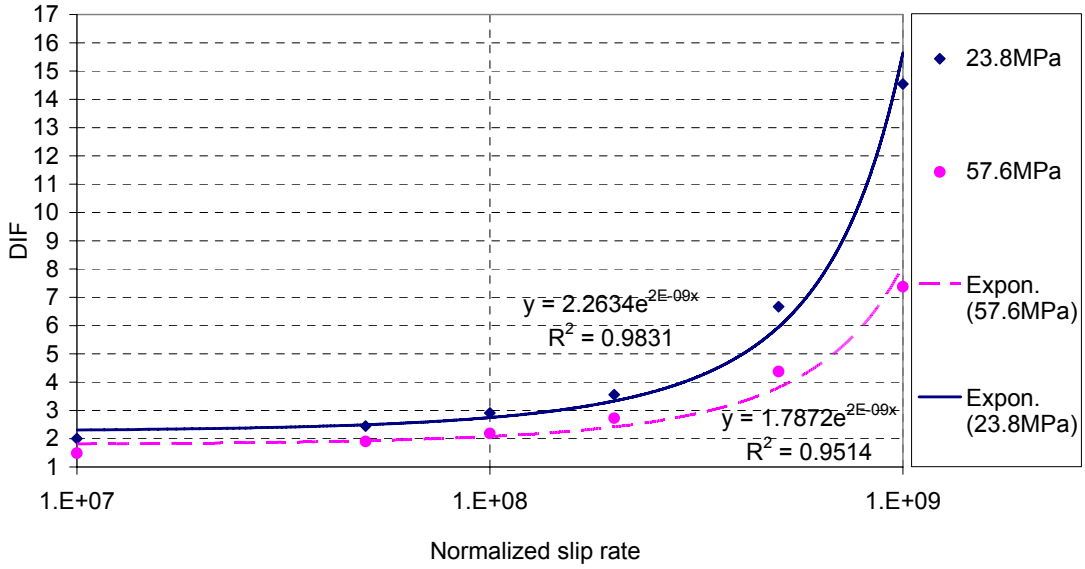

Figure 6-13: Trend line analysis for DIF for bond-slip relationship versus normalized slip rate at higher slip rate

From the trend analysis for DIF for bond-slip relationship versus normalized slip rate for concrete strength f_c'=57.6 *MPa* and 23.8 *MPa* a DIF versus slip rate relationship is derived and presented in Equations (6-6) to (6-10):

$$\alpha_{DIF} = \alpha \ln\left(\frac{\dot{s}}{\dot{s}_s}\right) + 1 \qquad \text{When } \dot{s} \le 1 m/s \qquad (6\text{-}6)$$

$$\alpha_{DIF} = \beta \times e^{\gamma} \qquad \text{When } \dot{s} > 1 m/s \qquad (6\text{-}7)$$

Where α_{DIF} is the DIF for bond-slip relationship at slip rate $\dot{s}$

f_{cs} = static cylinder compressive stress of the concrete in MPa

f_{co} =10 MPa

$\dot{s}$ = slip rate (in m/s)

$\dot{s}_s$ = static slip rate=1×10^{-7} m/s

$$\alpha = 0.123\left(\frac{f_{cs}}{f_{co}}\right)^{-0.80} \qquad (6\text{-}8)$$

$$\beta = 2.852\left(\frac{f_{cs}}{f_{co}}\right)^{-0.27} \qquad (6\text{-}9)$$

$$\gamma = 2 \times 10^{-9}\left(\frac{\dot{s}}{\dot{s}_s}\right) \qquad (6\text{-}10)$$

6.3.3 Verification of DIF for bond-slip relationship versus slip rate formula

The DIF for bond-slip relationship presented in Equations (6-6) to (6-10) was suitable for $f_c^{'} = 57.6 MPa$ and $f_c^{'} = 23.7 MPa$. A different test specimen FE model for a third concrete strength in between was analyzed to verity the proposed model.

Specimen B1 with f_c'=40.9MPa reported in Ueda et al. (1999) was chosen for this purpose. The slip rate and corresponding DIF for bond-slip relationship was obtained with repeating the numerical modelling analysis in the same way of the reference case. Then the points were compared with the proposed formulas Equations (6-6) to (6-10). The results shown in Figure 6-14 indicate that the proposed model is in closed agreement with the FE predicts for different concrete strengths.

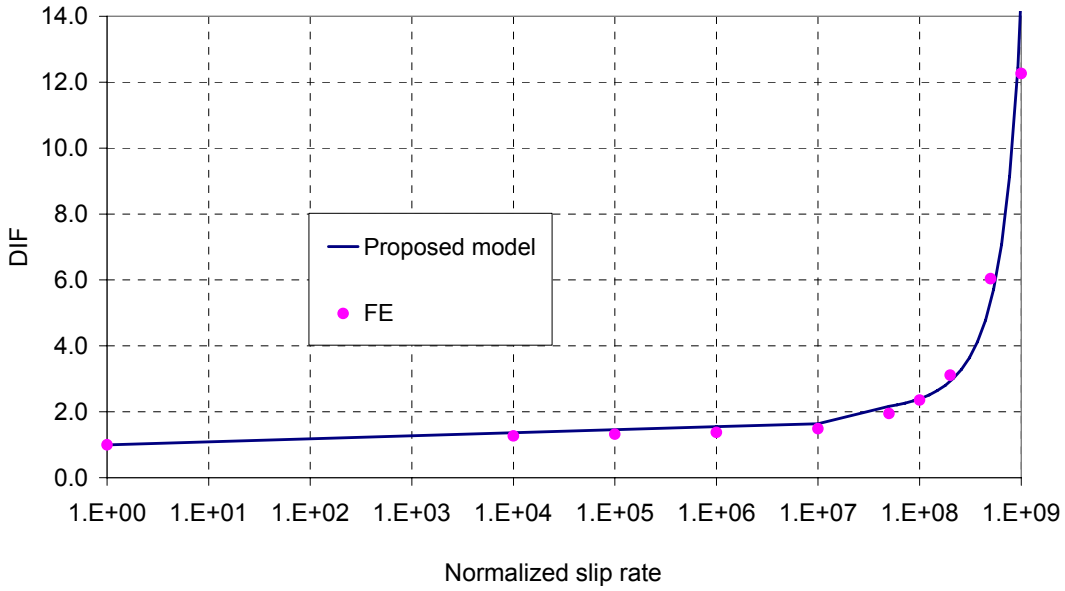

Figure 6-14: Verification with f_c'=40.9*MPa* (Specimen B1 in Ueda et al. 1999)

6.4 A Dynamic bond-slip model

Many existing static bond-slip models were analyzed and compared with numerous tests results in Chapter 4. The current FE model can give very good comparability with the test results, Chen and Teng (2001) analytical solution and Lu et al's (2005) static bond-slip model. Lu et al's (2005) static bond-slip model is chosen as the

static base for a dynamic bond-slip model. The DIF for bond-slip relationship versus slip rate relationship obtained was added to the static bond-slip giving a dynamic bond-slip model.

Equations (6-11) to (6-18) present the dynamic bond-slip relationship at bond slip rate $\dot{s}$. When $\dot{s} = 1 \times 10^{-7}\ m/s$, it reduces to the bilinear static bond slip model proposed in Lu et al. (2005).

$$\tau_{\max} = 1.5\alpha_{DIF}\beta_w f_t \tag{6-11}$$

$$s_0 = 0.0195\tau_{\max} f_t \tag{6-12}$$

$$G_f^{II} = 0.308\alpha_{DIF}^2\beta_w^2\sqrt{f_t} \tag{6-13}$$

$$s_f = 2G_{fs}^{II}/\tau_{\max} \tag{6-14}$$

$$\tau = \tau_{\max}\frac{s}{s_0} \text{ if } s \le s_0 \tag{6-15}$$

$$\tau = \tau_{\max}\frac{s_f - s}{s_f - s_0} \text{ if } s_0 < s \le s_f \tag{6-16}$$

$$\tau = 0 \text{ if } s > s_f \tag{6-17}$$

$$f_t = 0.53\sqrt{f_c'} \tag{6-18}$$

Where τ_{max} is the dynamic peak bond stress; s_0 is the dynamic slip corresponding to τ_{max}; G_f^{II} is the dynamic bond slip fracture energy; s_f is the maximum dynamic slip at failure.

The application of the bond-slip relationship in FE model needs to employ an interface element, e.g. spring element or cohesive element, with material properties in shear and normal direction defined according to the bond-slip mode. The cohesive traction-separation law (Abaqus 2008; LSDYNA 2007) can be chosen to describe the constitutive mode of FRP to concrete bond interface material property. The available traction-separation models assume initially linear elastic behavior followed by the initiation and evolution of damage. The entire basis is supposed to start from the static state which is the material base of the dynamic scope. A dynamic increasing proposal should be included for the cohesive element so that the slip rate effects, DIF for bond-slip relationship, can be added.

6.5 Conclusions

This chapter is about the development of a dynamic bond-slip model with numerical experiment. The K&C concrete model and the concrete local DIF discussed in Chapter 5 was introduced into the meso-scale pull-off test modelling. The DIF for bond-slip relationship was then introduced to Lu et al's (2005) static bond-slip model forming a new dynamic bond-slip model.

The proposed slip rate dependent bond-slip model gives the possibility to properly model the FRP-to-concrete bond behaviour under dynamic loads, and the dynamic bond-slip model alsomakes it possible to use large element sizes to model large scaled structures, because meso-scale concrete elements sizes and induced high computational cost can not be avoided for numerical modelling without a proper bond-slip model.

Introducing the dynamic bond-slip model into FE application has also been briefly discussed. The proposed dynamic bond slip model was pure numerical. It will be validated and discussed by modelling application results compared with tests results in impact tests and blast experiments in the following chapters.

6.6 References

Abaqus Analysis Manual (2008), Abaqus Aanalysis: User's Manual, Dassault Systèmes.

American Society of Civil Engineers (1997), Design of Blast Resistant Buildings in Petrochemical Facilities, ASCE, USA.

Buchan, P.A. and Chen, J.F. (2007), "Blast resistance of FRP composites and polymer strengthened concrete and masonry structures – a state-of-the-art review", *Composites*, Part B (38), 509–522.

Chen, J.F. and Teng, J.G. (2001), "Anchorage strength models for FRP and steel plates bonded to concrete", *Journal of Structural Engineering, ASCE*, 127(7):784–791.

De Lorenzis, L. and La Tegola, A. (2005), "Bond of FRP laminates to concrete under impulse loading: a simple model", Proc. International Symposium on Bond Behaviour of FRP in Structures (BBFS 2005), Hong Kong, China: 503-508.

Li, X.Q., Chen, J.F. and Lu, Y. (2010), "Meso-scale modelling of FRP-to-concrete bond behaviour using LSDYNA", Proceedings of the 5th International Conference on FRP Composites in Civil Engineering, Beijing: 494-498.

LSDYNA (2007), Keyword User's Manual Version 971, Livermore Software Technology Corporation.

LSDYNA (2010), Keyword User's Manual Version 971/ Rev 5., Livermore Software Technology Corporation.

Lu, X.Z., Teng, J.G., Ye, L.P. and Jiang, J.J. (2005), "Bond–slip models for FRP sheets/plates bonded to concrete", *Engineering Structures*, 27:920–937.

Lu, X.Z., Ye, L.P., Teng, J.G. and Jiang, J.J. (2004), "Mesco-scale finite element model for FRP sheets/plates bonded to concrete", *Engineering structures*, 27: 564-575.

Malvar, L.J., Crawford, J.E., Wesevich, J.W. and Simons, D. (1997), "A plasticity concrete material model for DYNA3D", *International Journal of Impact Engineering*, 19(9-10): 847-873.

Malvar, L.J. and Crawford, J.E. (1998), "Dynamic increasing factors for concrete", Twenty-Eight DDESB Seminar, Orlando, August.

Nam, J.M., Kim, H.J., Kim, S.B., Yi, N.H. and Kim, J.H.J. (2010), "Numerical evaluation of the retrofit effectiveness for GFRP retrofitted concrete slab subjected to blast pressure", *Composite Structures*, 92:1212–1222.

Nam, J.W., Kim, H.J., Kim, S.B., Kim, J.H.J. and Byun, K.J. (2009), "Analytical study of finite element models for FRP retrofitted concrete structure under blast loads", *International Journal of Damage Mechanics*, 18(5): 461-490.

Pellegrin, C., Tinazzi, D. and Modena, C. (2008), "Experimental study on bond behavior between concrete and FRP reinforcement", *Journal of Composites for Construction*, 12(2):180-189.

Schmidt, M.E. and Cheng, L.J. (2009), "Impact response of externally strengthened unreinforced masonry walls using CFRP", *Journal of Composites for Construction*, 13(4): 252-261.

TM5-1300 (1990), Structures to Resist the Effect of Accidental Explosions, US Department of the Army, Navy and Air Force Technical Manual.

Ueda, T., Sato, Y. and Asano, Y. (1999), "Experimental study on bond strength of continuous carbon fiber sheet", Proceedings of 4th int. sym. on fiber reinforced polymer reinforcement for reinforced concrete structure: 407–416.

United States Department of State- Office of the Coordinator for Counterterrorism. (2010), "Country Reports on Terrorism 2009", Released August.

Wu, C., Oehlers, D.J. and Day, I. (2009), "Layered blast capacity analysis of FRP retrofitted RC member", *Advances in Structural Engineering*, 12(3): 435-449.

Wu, Z.S., Yuan, H., Yoshizawa, H. and Kanakubo, T. (2001), "Experimental/analytical study on interfacial fracture energy and fracture propagation along FRP-concrete interface", ACI *International,* SP 201(8): 133–152.

Yao, J. (2004), Debonding Failures in Reinforced Concrete Structures Strengthened with Externally Bonded FRP Sheets/Plates, PhD thesis, Department of Civil and Structural Engineering, Hong Kong Polytechnic University, Hong Kong.

Chapter 7 FRP-to-concrete bond impact tests

7.1 Introduction

Concrete structures may be exposed to dynamic loads due to impact in their working lives, such as damage of transportation infrastructure due to impact incidents. FRP retrofitting techniques offer a promising solution to these problems (Boyd et al. 2008; Kabir and Shafei 2009; Suter 2006; Uddin et al. 2006; Zhang et al. 2006).

The main characteristics of impact load are high loading rates and short periods of duration that result in high material strain rates. The bond behaviour at high loading rates may be quite different from the static state, because the dynamic increase effect due to high strain rate and the debonding mostly happens in the concrete layer adjacent to the FRP unless the adhesive is very weak or proper surface treatment has not been followed (Lu et al. 2004).

There have already been a series of studies on concrete beams with externally bonded FRP plate under impact loading (Erki and Meier 1999; Tang and Saadatmanesh 2003; Hosny et al. 2006; White et al. 2001) but they mainly focused on the global response including flexural capacity, stiffness, energy absorption and ductility of the strengthened beams. Little attention has been paid to the FRP-to-concrete bond behaviour in high strain rate events.

A set of bending test specimens similar to the ones in Sena Cruz et al. (2004) for static test were designed and tested under impact in this study to study the dynamic bond-slip behaviour. Two symmetric concrete blocks were connected with compressive reinforcement bars only. The FRP was applied on the tensile face. The mid-span deflection at the failure was designed to be small (less than 5%) compared with the span. When the specimen was under an impact load at the centre, the FRP was only suffered from tensile force at the mid-span providing the similar bond-slip mechanics like pull-off tests discussed in previous chapters.

The static experiments were conducted in the structure laboratory at the University of Edinburgh. The impact tests were conducted at Heriot-Watt University. The tests were conducted collectively by three PhD students, Xiaoqin Li, Lei Mao and Zhenhuan Song, and two MEng students, Andrew Sheil and Rory O'Sullivan, at the University of Edinburgh, under the supervision of Dr Jian-fei Chen, Prof. Yong Lu, Dr Tim Stratford of the University of Edinburgh and Prof. Ian May of Heriot-Watt University.

The specimen design and casting were conducted by Andrew Sheil and Rory O'Sullivan under the supervision of Dr Jian-fei Chen and Dr Tim Stratford in the University of Edinburgh. The experimental design was done by the author Xiaoqin Li under Dr Jian-fei Chen and Prof. Yong Lu's supervision. Strain gauge application, wiring, painting and pretesting for both static and dynamic test were conducted by Xiaoqin Li and Zhenhuan song. The cameror setting up and monitoring were done by Andrew Sheil and Rory O'Sullivan for both static and dynamic tests. The accelerator

application and monitoring for the impact test was operated by Lei Mao. Andrew Sheil, Rory O'Sullivan and Xiaoqin Li cooperated in the static tests under the direction of Dr Jian-fei Chen and Dr Tim Stratford at the structure lab of the University of Edinburgh. The impact tests were conducted by Andrew Sheil, Rory O'Sullivan, Xiaoqin Li, Zhenhuan Song and Lei Mao at the structure lab of Heriot-Watt University under the supervision of Prof. Yong Lu, Prof. Ian May and Dr Jian-fei Chen.

7.2 Specimen design

Six steel reinforced concrete specimens with FRP plate bonded at the bottom were designed and constructed by Andrew Sheil and Rory O'Sullivan under the supervision of their supervisor Dr Chen.

Each test specimen consisted of two separate concrete blocks, joined by two 12*mm* diameter steel reinforcements to transfer compressive forces between them. Three double leg stirrups were included in each concrete block to prevent shear failure. Ready-mix concrete was placed into the prepared in plywood formwork with 5*mm* cardboards wrapped in cling films in the middle to form the gap between the two concrete blocks. The geometry and reinforcement details are shown in Figure 7-1. The test value (28 days between pouring and testing) compressive cylinder strength of the concrete f_c' was 24.24*MPa*. The characteristic yield strength for the 6*mm* diameter steel bars was 275*MPa* and that for the 12 *mm* bars was 500*MPa*.

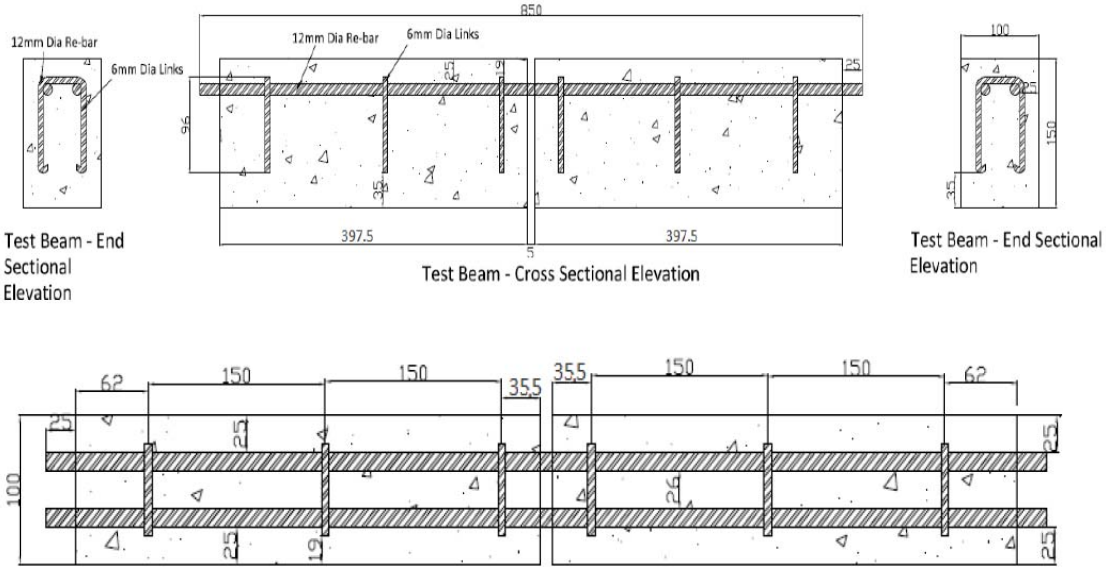

Figure 7-1Test specimens (Sheil 2011)

A 50*mm* wide and 605*mm* long FRP plate was first bonded to the underside of both blocks symmetrically, giving a bond length of 300*mm* on both blocks. An additional 100*mm* wide FRP plate was applied onto the second block to ensure that failure would occur in the other (test) block. Figure 7-2 shows test specimens before and after the second CFRP plate was applied on the un-tested block.

Figure 7-2 Test specimens before and after application of the second CFRP plate (Sheil 2011)

Under static loading, the expected bond force in the FRP at debonding failure may be estimated from Chen and Teng's (2001) bond strength model:

$$F_f = 0.427\beta_L\beta_w\sqrt{f_c'}b_pL_e \tag{7-1}$$

in which

$$\beta_L = \begin{cases} 1 & if \quad L \geq L_e \\ \sin\dfrac{\pi L}{2L_e} & if \quad L < L_e \end{cases} \tag{7-2}$$

$$\beta_w = \sqrt{\frac{2-b_p/b_c}{1+b_p/b_c}} \tag{7-3}$$

$$L_e = \sqrt{\frac{E_P t_P}{\sqrt{f_c'}}} \tag{7-4}$$

where F_f=ultimate force in the FRP; β_w= width ratio coefficient; β_L=bond length coefficient; b_P=bond FRP plate width; b_c=concrete prism width; L_e=effective bond length; L=actual bond length of FRP plate; $\varepsilon_{rupture}$=rupture strain of FRP, f_c'= concrete cylinder compressive strength; E_P= Young's modulus of the FRP plate; t_P= thickness of the CFRP plate. Details of the test FRP plate are listed in Table 7-1. The failure load of the specimen can be estimated from the loading arrangement once the maximum FRP force is found.

Table 7-1 FRP plate details

E_P	t_P	b_P	b_c	L_e	L	$\varepsilon_{rupture}$	β_L	β_w
$170\,GPa$	$1.4\,mm$	$50\,mm$	$100\,mm$	$220\,mm$	$300\,mm$	2.2%	1	1

7.3 Experimental design

7.3.1 Static test

Two specimens were tested statically, one under 4-point bending and one under 3-point bending. The distance between the two symmetric applied load locations for the 4-point bending test was $110mm$. The boundary and loading condition analysis for the half of the specimen are plotted in Figure 7-3.

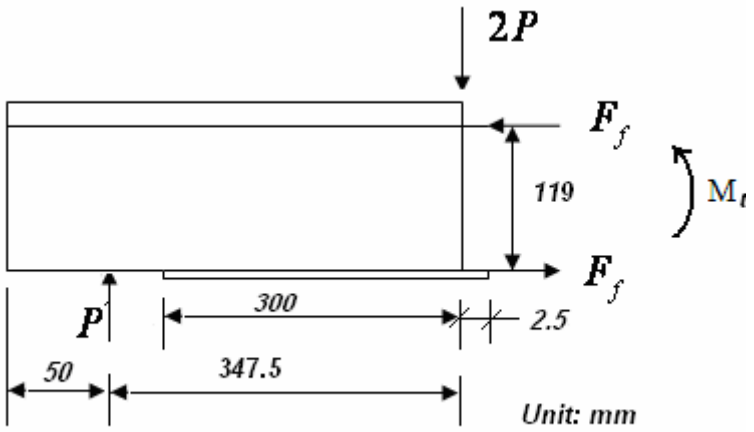

Figure 7-3 Half-span loading condition analysis of the beam

According to moment equilibrium, the ultimate load applied at the middle span for the static test was estimated to be $16.0\,kN$ for 3-point bending and $19.0\,kN$ for 4-point bending.

7.3.2 Impact test

The following approximate calculations were made before the impact tests to guide the choice of the drop height and drop weight.

7.3.2.1 FRP rupture and FRP debonding consideration

An initial range of impact load may be defined by estimating the FRP rupture load under static condition. The FRP rupture force, P_r, is $261.8\,kN$ from the FRP Young's modulus and rupture strain, so the maximum force applied load under three point bending can be found to be $180\,kN$ based on static equilibrium (i.e. neglecting the dynamic effect) (Figure 7-3). Accordingly, an initial range for the impact load F_m is $16kN < F_m < 180kN$, of which the $16\,kN$ was from the 3-ponits static state prediction.

7.3.2.2 Shear capacity consideration

It is generally assumed that the shear deformation has little effect on the distribution of flexural stresses for slender beams, i.e. the length is at least 10 times the depth (Hughes and Soeurs 1982). However the test specimens in this study had a length to depth ratio of 4.7. The transverse shear effects therefore cannot be neglected. The

static shear strength of the specimens may be estimated from Hughes and Soeurs (1982), with $Q_0 = 0.7 f_t bh = 29.4kN$. The vibration modes of a pin-ended beam are presented in Figure 16 of Hughes and Soeurs (1982). The first mode dynamic shear capacity which is the smallest dynamic shear capacity of all the vibration modes (Hughes and Soeurs 1982) for a simply supported RC beam under an impact load at mid-span is:

$$\frac{Q_1}{Q_0} = 1.56 \tag{7-5}$$

where Q_0 and Q_1 are the static and dynamic shear capacity respectively. Based on this estimation, shear failure may occur when the impact force is equal or higher than $92.3kN$. Therefore the impact load range is reduced to $16kN \le F_m \le 92.3kN$ to ensure that shear failure does not occur.

7.3.2.3 Energy consideration

For a pin-ended beam with uniformly distributed mass, the first modal mass m_e is half of the beam mass m_b between the two supports. If the current specimens are treated as such beams, $m_e = 13\ kg$. The striker used in the test had a mass of $m_s = 200\ kg$. The initial kinetic energy at the beginning of impact U_0 is equal to $\frac{1}{2} m_s v_0^2$, where v_0 is the velocity of the striker at the time of contact. If the energy dissipated in everywhere else apart from the FRP-to-concrete bond is neglected, the

kinetic energy of the striker at the contact time shall equal the kinetic energy of the striker and the specimen after impact plus the energy dissipated at the FRP-to-concrete bond. The fracture energy G_{fs}^{II} may be estimated from Lu et al's (2005) model to be 500 N/m :

$$f_{ts} = 0.53\sqrt{f_{cs}^{'}} = 2.65MPa \tag{7-6}$$

$$G_{fs}^{II} = 0.308\beta_w\sqrt{f_{ts}} \tag{7-7}$$

Assuming complete debonding at the test side of the specimen and no debonding at the other side, the total debonding energy can be found from G_{fs}^{II} times the bond area as is 7.5 $N.m$, neglecting any dynamic increase factor.

In dynamic case the debonding energy may be higher due to strain rate effect. In Chen and May (2010), a strain rate of 32.5/s in the reinforcement was reported when the impact velocity was 7.3m/s in a 2.7m span continuous concrete beam (with a 100kg striker at 3m drop height). The same striker but with different drop heights were used in this current study. As the test specimens were also different, the strain rates must be different in the current study to those in Chen and May (2010). However, this strain rate reported in Chen and May (2010) was used as initial estimation here. The tensile strength of the concrete was assumed to be increased due to dynamic increasing factor (DIF) in tension. The DIF was 5.74 at a strain rate of 32.5/s according to Malvar and Crawford (1998). Therefore the dynamic fracture energy was estimated as 16474 N/m so the debonding energy was increased to

251 $N.m$. The impact time duration Δt was assumed to be 1.8ms according to Chen and May (2010)'s test results, so the impact force for total debonding was 86.8 kN assuming a triangle impulse. This is in the range $16kN \le F_m \le 92.3kN$ as established earlier.

According to Hughes and Speirs (1982), the velocity loss needed to be considered too. The velocity at impact is $v_0 = 0.95\sqrt{2gh}$, where $g = 9.8m/s^2$ and h is the drop height. The impact load is assumed to be a triangle impulse and 1.8 ms impact time duration according to Chen and May (2010).

A drop height of 2.27 m was estimated to be the upper limit to induce total debonding based on the energy calculation earlier However we did not start from such a high drop height 2.27m and the reasons are listed below:

1) The energy dissipated in the damage zone was neglected. High drop heights may cause excessive damage in the impact zone which was not considered;

2) Calculations above was based on a strain rate 32/s which was recorded in Chen and May (2010). But as discussed previously in reality the strain rate would be smaller than this due to different specimen conditions and lower drop heights;

3) The bond might be damaged before the debonding process due to the compressive stress wave transmitted there and reflected as tensile stress wave, so lower drop height should be used rather than starting from 2.27m directly.

Accordingly, 3 different drop heights were defined and listed in Table 7-2 below based on 1.8ms impact time duration and triangle impulse assumptions.

Table 7-2 Design drop heights

Test Reference	Specimen ID	Drop heights $h\,(mm)$	Estimated impact velocity $v_0\,(m/s)$	Estimated max impact force $F_{m\_p}\,(kN)$
Impact test 1 (IT1)	4	200	1.9	25
Impact test 2 (IT2)	3	100	1.3	18
Impact test 3 (IT3)	6	400	2.7	37
Impact test 4 (IT4)	5	100	1.3	18

7.4 Static bending tests

7.4.1 Test preparation and procedure

Two specimens were tested under static loading: one under 3-point bending and 4-point bending as shown in Figure 7-4. Loading was applied manually at a rate of about 3 kN/min.

3 – Point Bending 4 – Point Bending

Figure 7-4 3-point and 4-point bending tests

In the three point bending test, the load was applied through a 50*mm* wide plastic plate and a 50*mm* wide steel plate to distribute the load equally on both sides of the 5*mm* gap. In the 4-point bending test, two point loads with a 110*mm* distance in between were applied. The test specimens were simply supported at both ends with a support spacing (span) of 700*mm*. The middle section of the specimens was painted to create a random black and white pattern for digital image analysis (Figure 7-4). A reference plate was placed under the mid-span of the specimen for the same purpose.

Figure 7-5 Test set up

Five strain gauges were installed for each specimen in the FRP on the test with a specimen of 50*mm* with the first gauge (SG1) located beneath the centre of the notch to measure the longitudinal FRP strains. Figure 7-6 shows the FRP geometry with and strain gauge locations. Data were recorded at 1 *Hz* during test. Two synchronised cameras were used to take pictures of the test specimen and loading dial of the test machine at two seconds intervals, allowing load and the displacement readings from PIV (Particle Image Velocimetry), which is an optical technique for measuring the displacement of the particle pattern, to be matched with the strain readings. Finally all tests were recorded using a high speed camera capturing 600 frames per second which was used to capture the debonding process and help identify the type of failure.

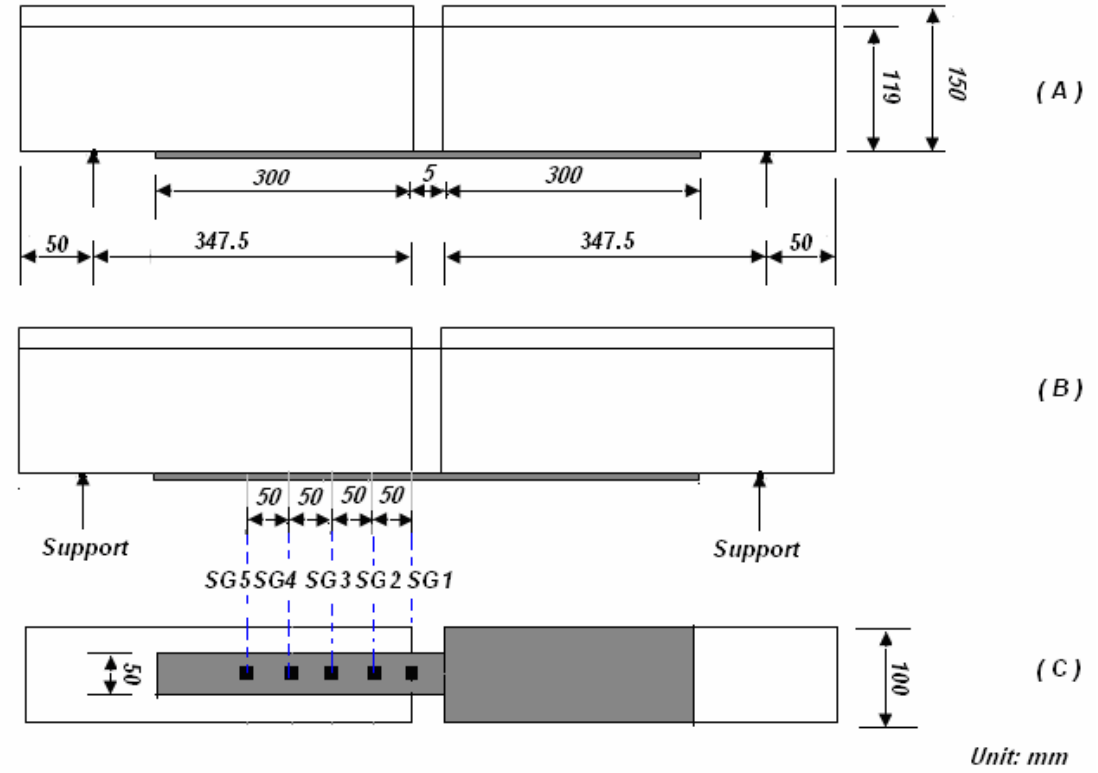

Figure 7-6 FRP geometry, strain gauge locations and support positions in the static tests

7.4.2 Test results

7.4.2.1 Static 4-point bending test

Specimen 1 tested under 4-point bending test failed due to shear crack induced debonding failure at about 500 seconds with an ultimate load of 26 kN. The load deflection curve of the test is presented in Figure 7-7.

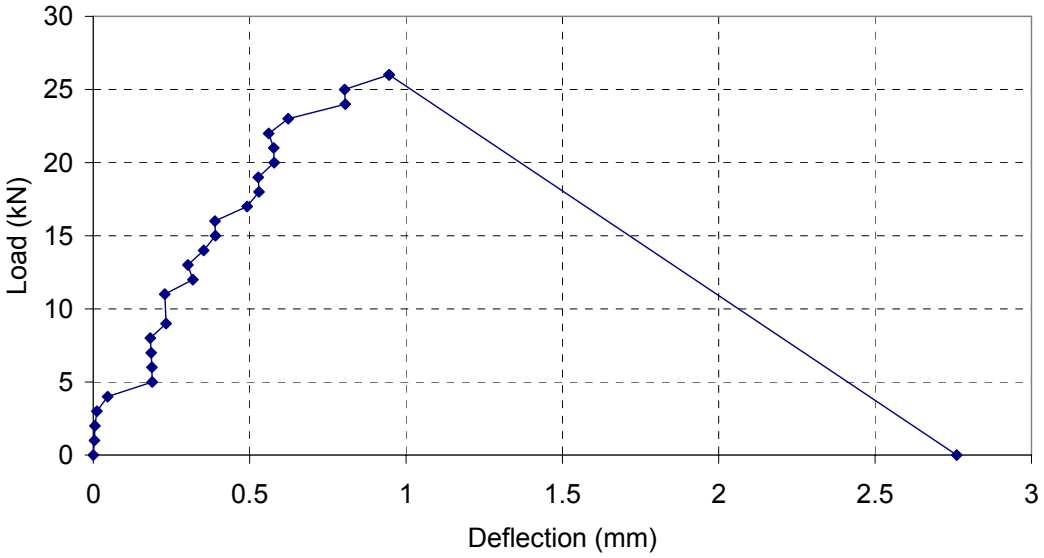

Figure 7-7 Static 4-point bending test: load deflection curve

The measured load-strain history on the FRP is shown in Figure 7-8, for the strain gauge locations in Figure 7-6.

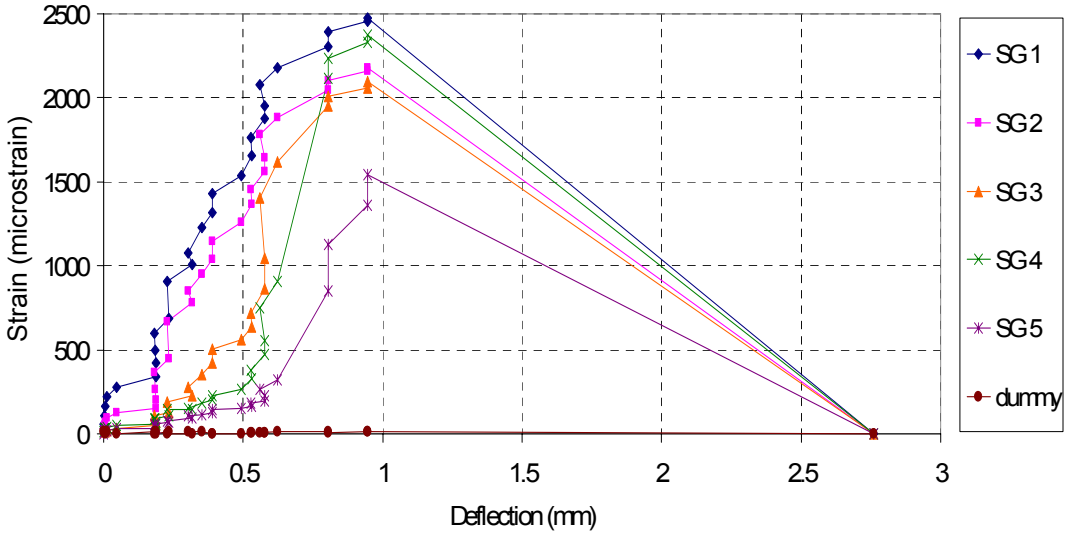

Figure 7-8 Static 4-point bending test strain-deflection curves (SG1, SG2, SG3, SG4 and SG5 in Figure 7-6 respectively)

The shear crack developed at 130*mm* from the 5*mm* gap and at an angle of 40° as shown in Figure 7-9. The failure mode was quite brittle as the load drops sharply to

zero as soon as it reaches the maximum mid span deflection 2.7*mm* at 500*s*. The type of failure mode experienced was shear crack induced interfacial debonding. Debonding developed just above the CFRP plate and propagated towards the plate end removing a thin layer of concrete.

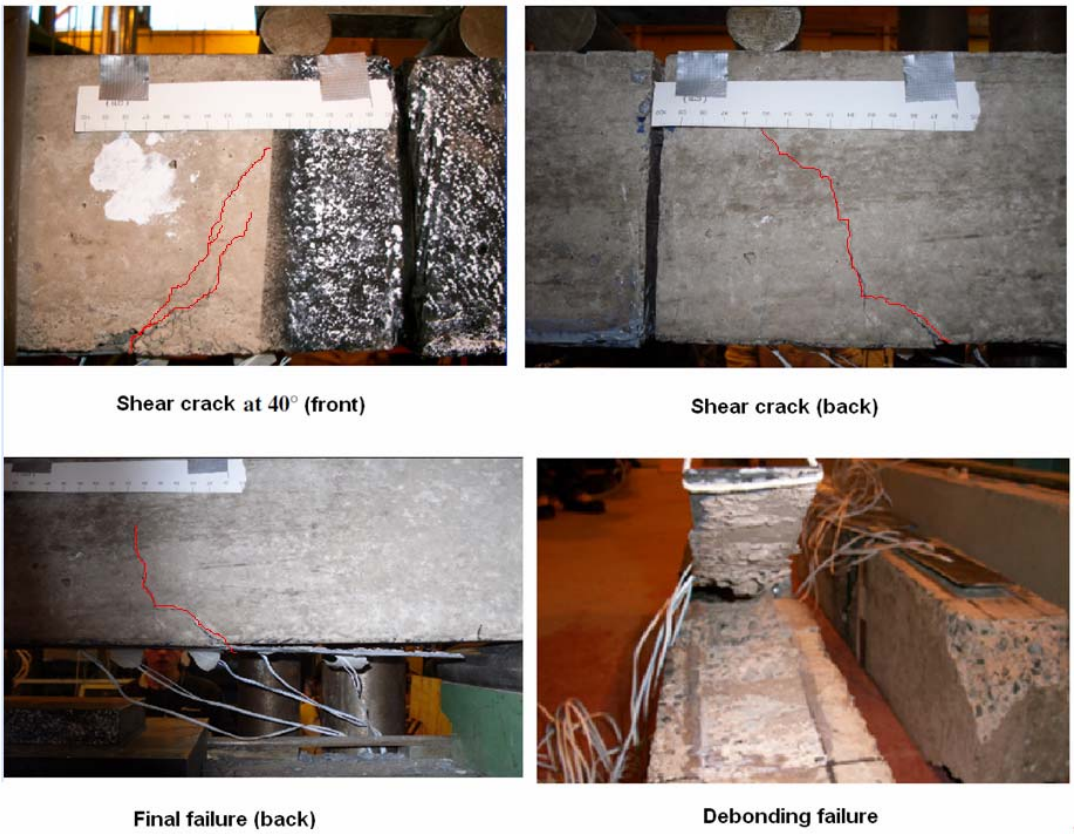

Figure 7-9 Failure mode of Specimen 1 under static 4-point bending test

7.4.2.2 Static 3-point bending test

Specimen 2 was tested under 3-point bending and it failed due to shear crack induced debonding failure at about 220 seconds with an ultimate load of 18 *kN*. The load deflection relationship is shown in Figure 7-10.

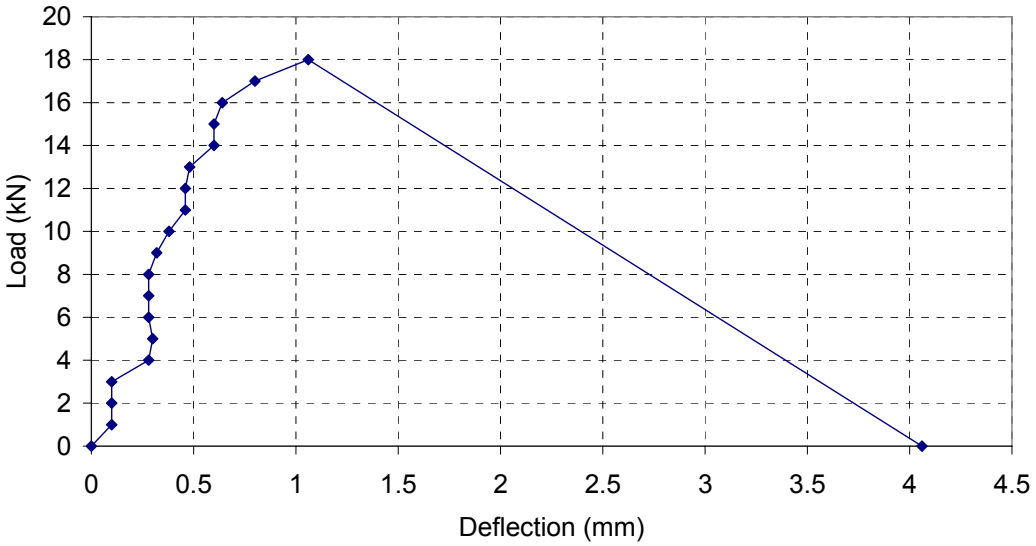

Figure 7-10 Static 3-point bending test: load deflection curve

The strain measurements along the FRP are presented in Figure 7-11 .

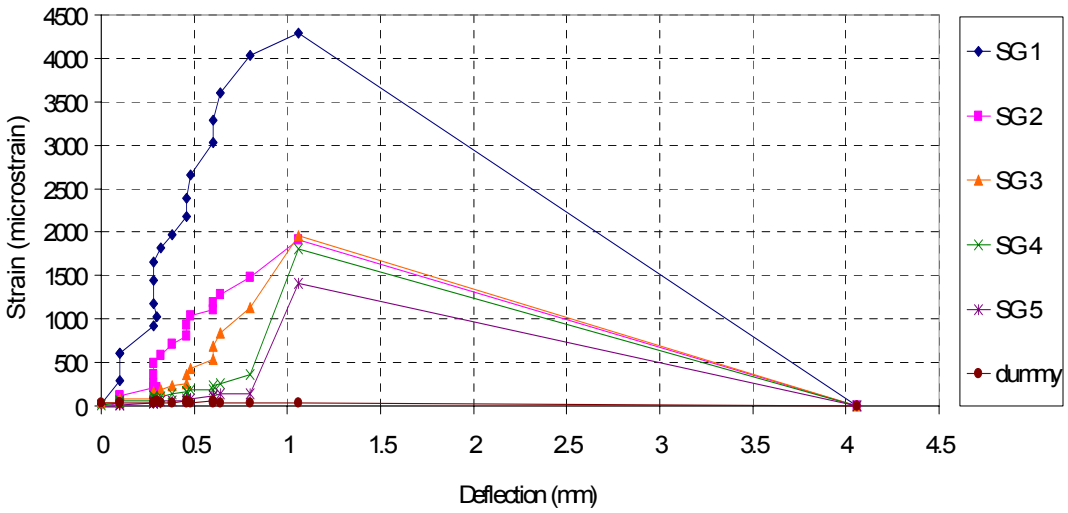

Figure 7-11 Static 3-point bending test strain-deflection curves

A shear crack developed at 50*mm* from the 5*mm* gap and at an angle of 42° as shown in Figure 7-12. The failure was quite brittle as the load drops sharply to zero as soon as it reaches the maximum mid span deflection of 4*mm* at 220*s*. The type of failure mode experienced was shear crack induced interfacial debonding. Debonding

developed just above the CFRP plate and propagated towards the plate end removing just the bottom layer concrete less than 1*mm* thick.

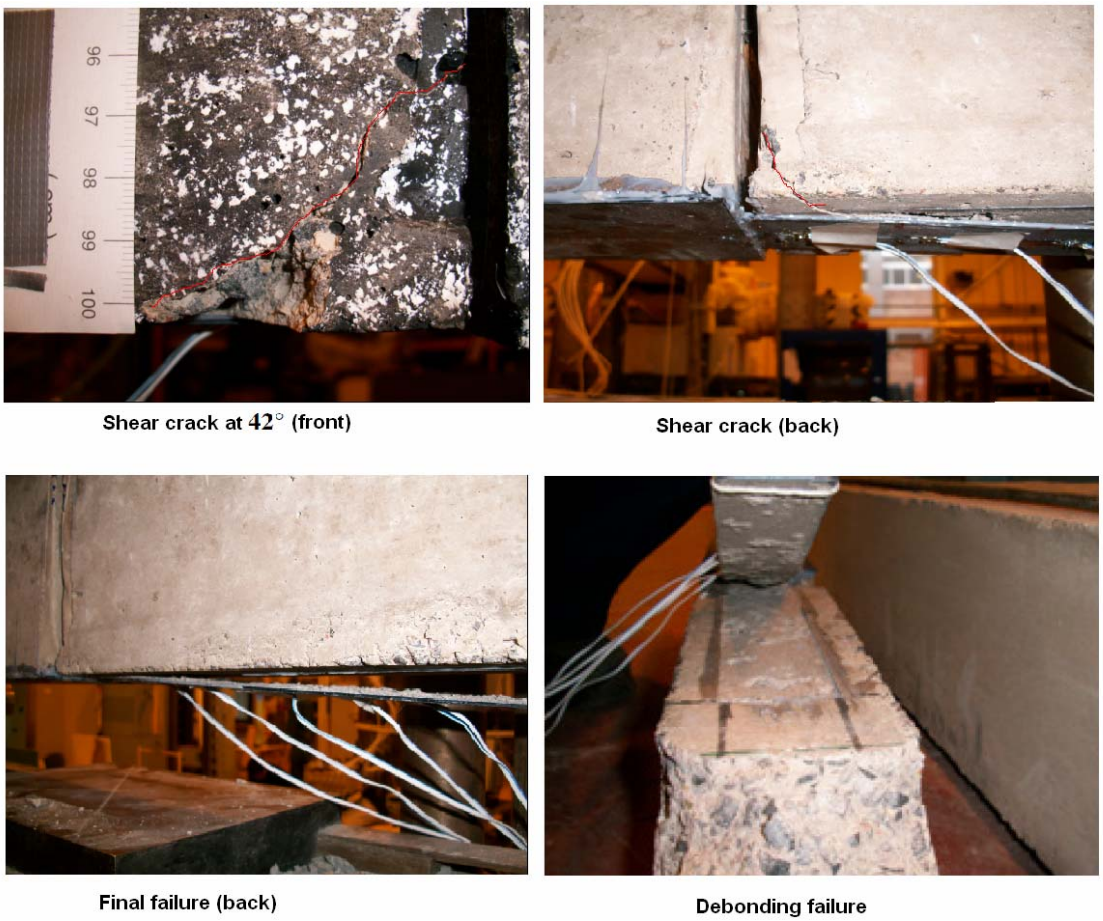

Figure 7-12 Failure mode of Specimen 2 under static 3-point bending test

7.5 Impact tests

7.5.1 Test preparation and procedure

Figure 7-13 shows the impact test arrangement with a test specimen in position.

Figure 7-13 Impact test arrangement

The impact test rig consisted of a frame with two vertical steel angle legs used to guide the striker. The striker was lifted, using a winch, by a steel wire rope that was attached to the striker by an electromagnet. When the striker was at the required height it was released by switching off the magnet. To prevent an accidental release of the striker owing to a failure of the magnet, there was a mechanical link between the rope and striker, which was released prior to switching off the magnet. The striker comprised a 200 kg mass, a flat mild steel contact face with 100 mm diameter and the load cell (Chen and May 2010). The beam was pin supported (Figure 7-13). The distance between the centers of the two supports was 660mm (Figure 7-14). Four impact tests were conducted with details listed in Table 7-2.

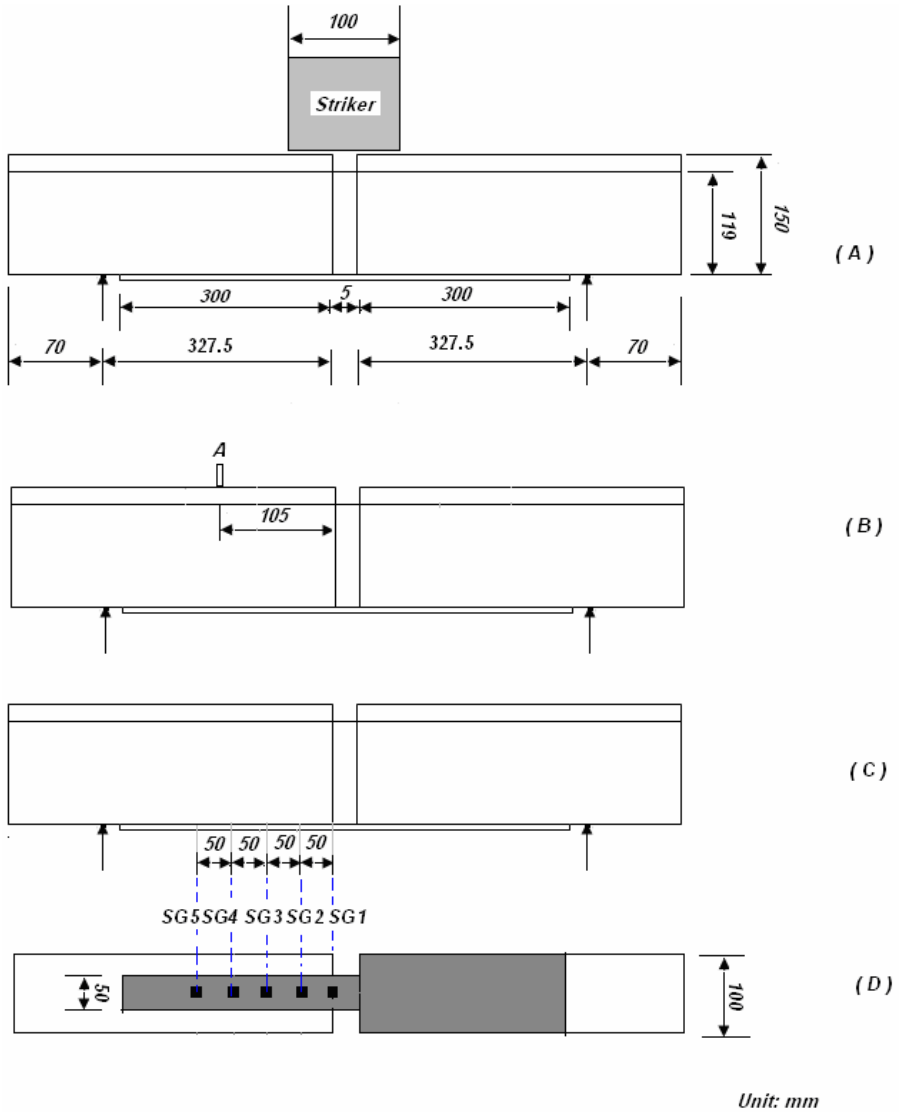

Figure 7-14 Impact test geometry, loading position, accelerator and strain gauge locations (A point in (B) is the location for the accelerometer)

For the impact test, strains were recorded at a 10,000 *Hz* for the first two impact tests (IT 1 and IT2) and 15,000 *Hz* for the other two (IT3 and IT4). The acceleration of the test specimen was measured using an accelerometer. The impact force and the reactions were measured with load cells placed at the striker and the support respectively. The recording frequency of the impact load was the same as strains. Again all tests were recorded using a high speed camera capturing 1,200 frames per

second. The maximum mid-span deflection was determined through PIV analysis of the recordings and the type of failure experienced could also be identified using these recordings.

7.5.2 Test results

7.5.2.1 Impact test 1 (IT1)-Drop height 200*mm*

The drop height for IT1 was 200*mm*. The impact and reaction force time histories are presented in Figure 7-15. The maximum peak impact load was 56.25 kN appeared at 1.4 ms and. The strain measurement is presented in Figure 7-16 and acceleration time history is presented in Figure 7-17. The maximum acceleration was approximately $200 \times 9.8 m/s^2$ (200g). The failure mode of IT1 was debonding. Figure 7-18 shows the development of the failure process.

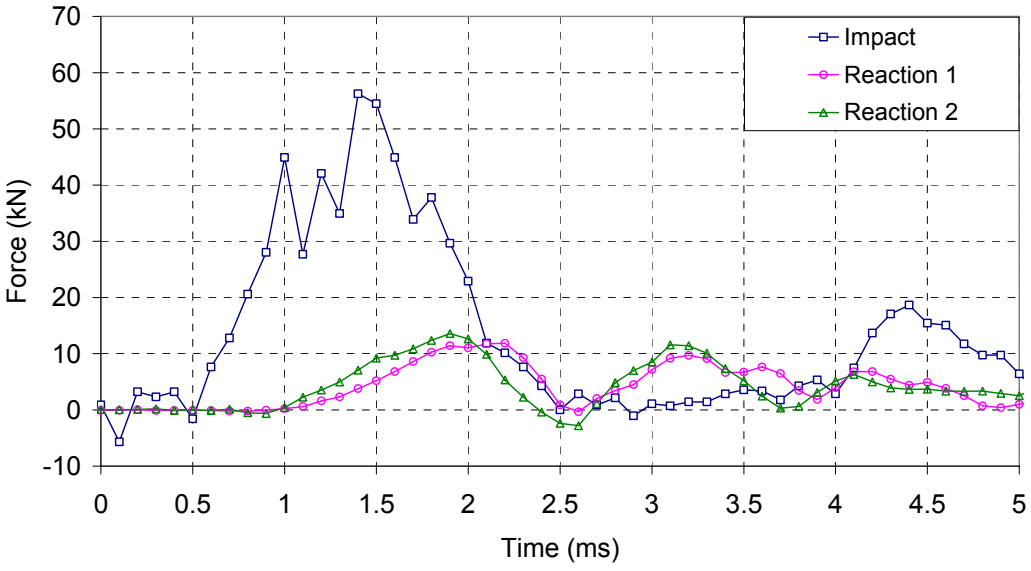

Figure 7-15 Impact and reaction force time history (IT1_200*mm* drop height)

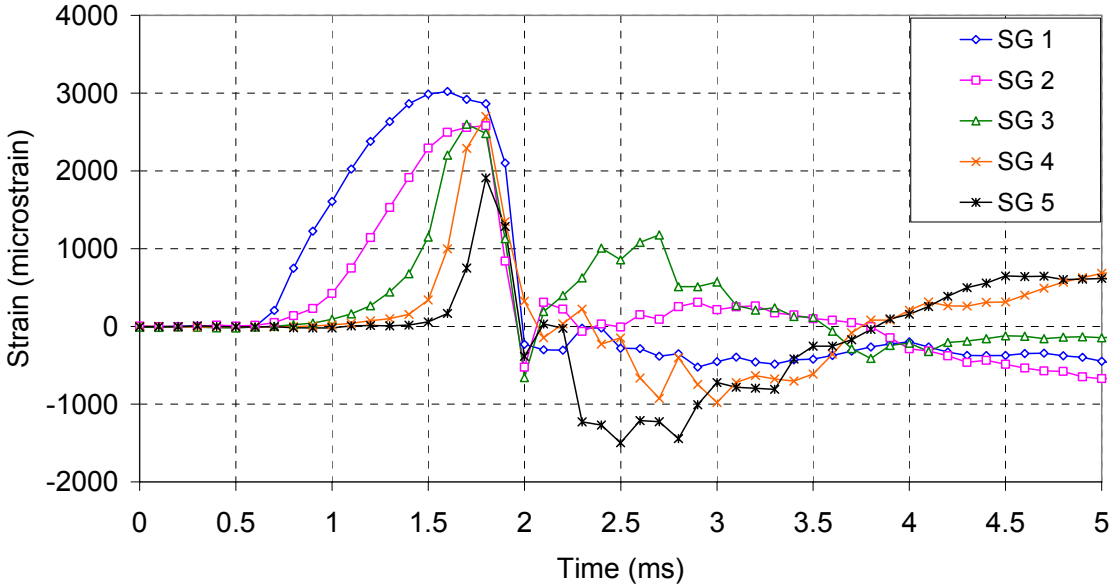

Figure 7-16 Strain time history (IT1_200*mm* drop height)

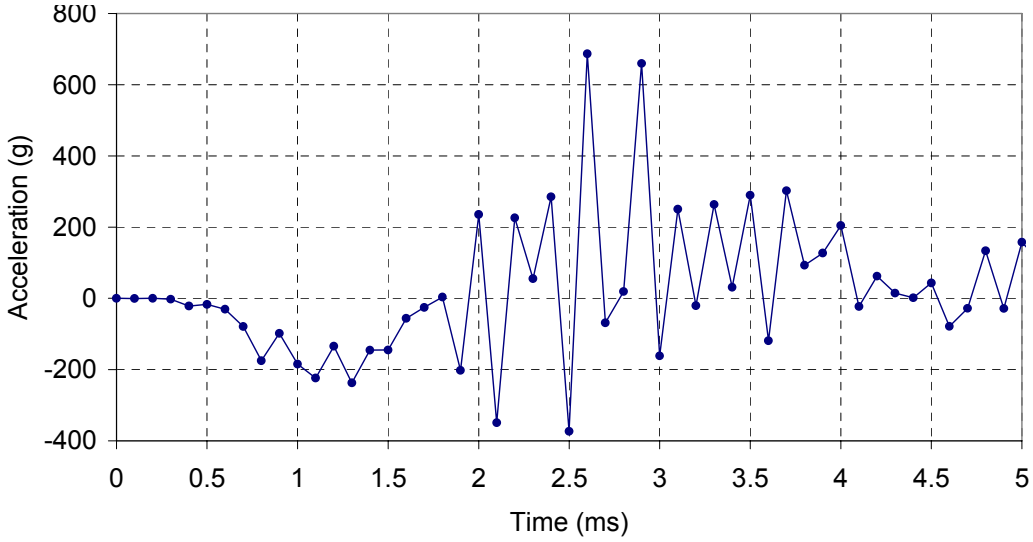

Figure 7-17 Impact acceleration time history (IT1_200*mm* drop height) (Acceleration measured at position A in Figure 7-14)

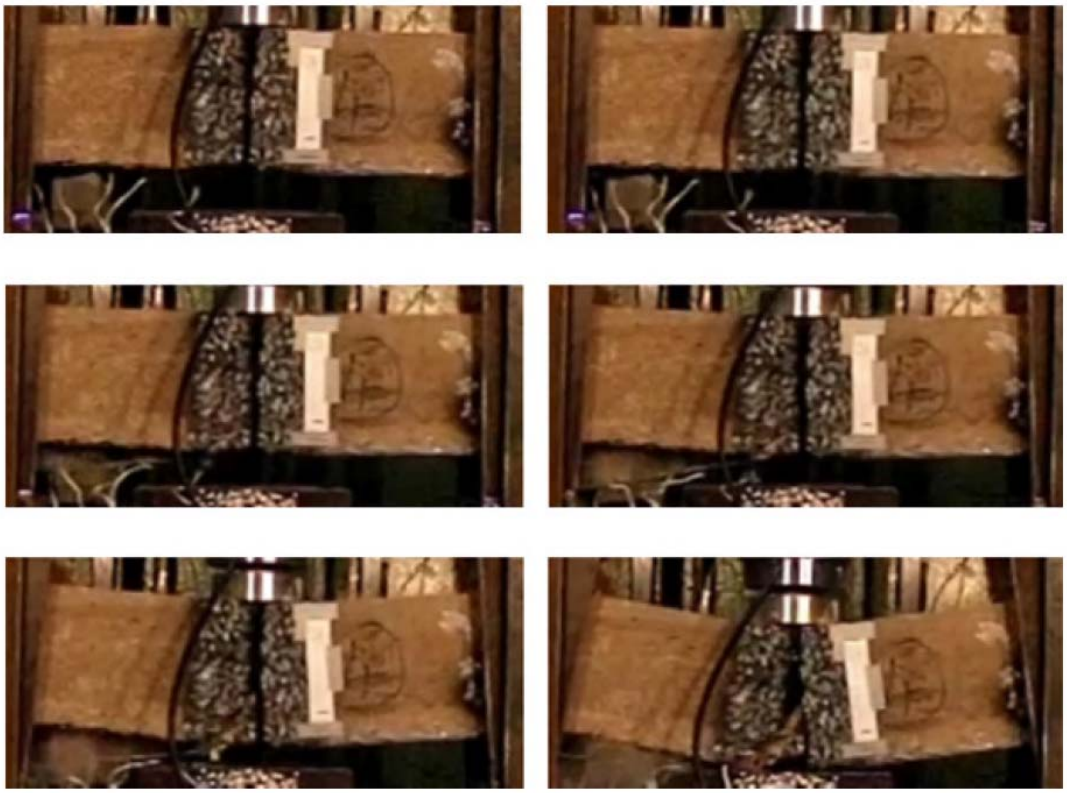

Figure 7-18 Failure process of IT1

A shear crack was also identified at an angle of 45° which developed and widened as the debonding propagated towards the middle gap. This shear crack was very similar to the one experienced during the three-point bending static loading test. For the static test, it was shear-crack induced debonding. The surface preparation appeared to be insufficient and the adhesive layer was too thin to offer enough bond strength as only a very thin layer of concrete mortar no aggregate was removed from the concrete surface with the CFRP plate. The final failure pattern of the specimen is presented in Figure 7-19, and the maximum deflection during the debonding failure process from the PIV analysis was 3*mm* for IT1.

Figure 7-19 IT1 (Impact test 1)

7.5.2.2 Impact test 2 (IT2)-Drop height 100*mm*

The drop height was 100*mm* for IT2. The impact load time history is presented in Figure 7-20. The maximum peak impact load was 35 *kN* appeared at 3.5 *ms* . The strain measurements are presented in Figure 7-21. Note that SG3 data was missed during the test. The acceleration time history is presented in Figure 7-22. The maximum acceleration was $100 \times 9.8 m/s^2$ (100g) approximately.

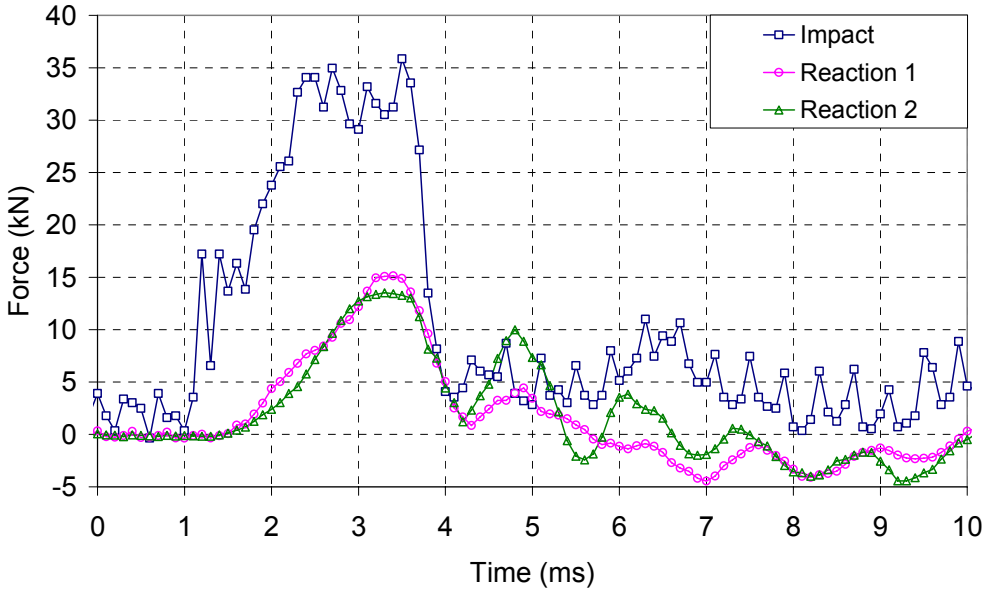

Figure 7-20 Impact and reaction force time history (IT2_100*mm* drop height)

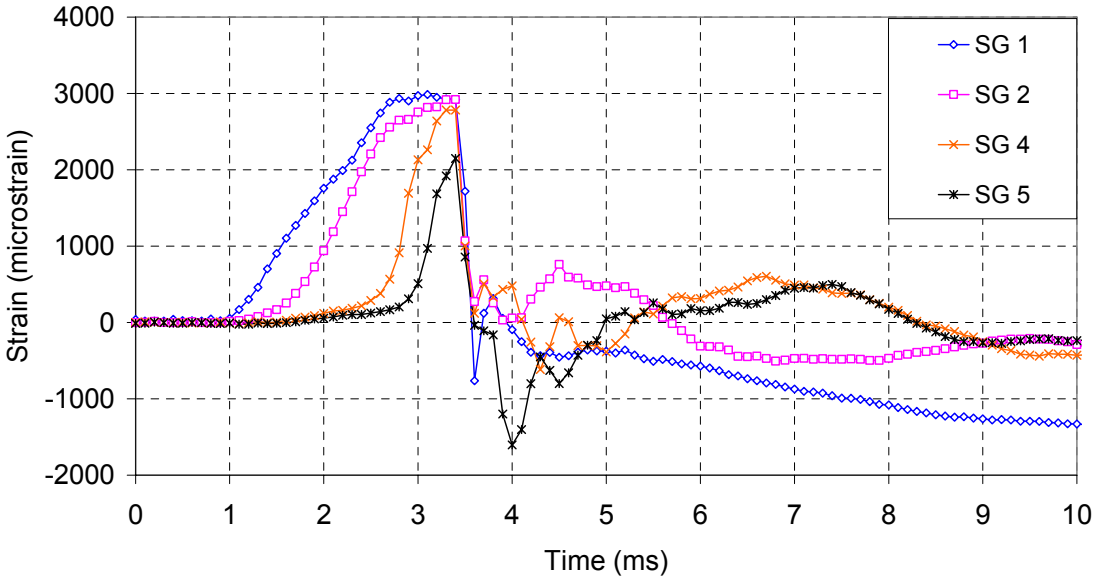

Figure 7-21 Impact strain measurement time history (IT2_100*mm* drop height; please note error occurred at SG1 and data reading was not captured)

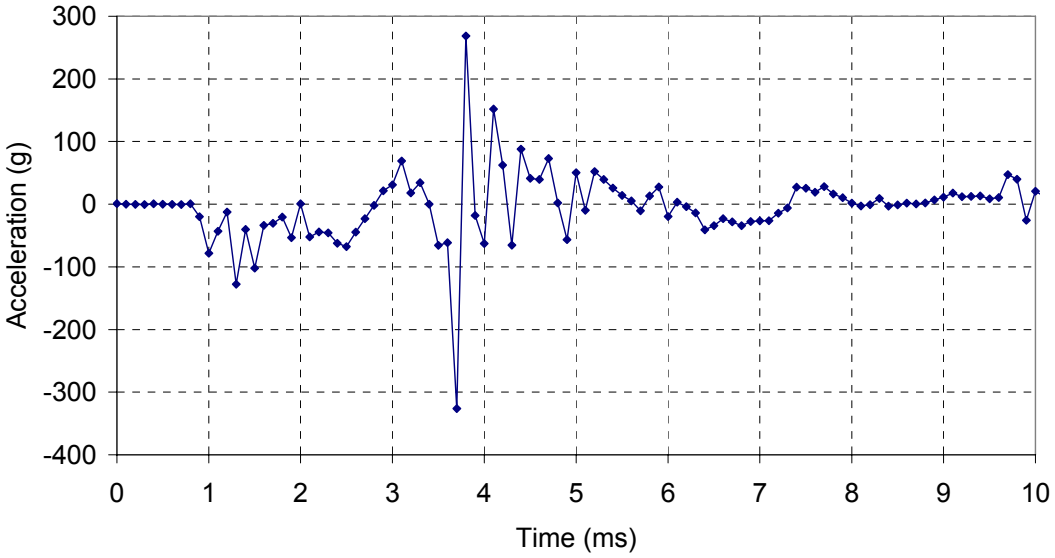

Figure 7-22 Impact acceleration time history (IT2_100*mm* drop height) (acceleration measured at position A in Figure 7-14)

The failure mode was debonding too. A shear crack was also identified at an angle of 50° which widened as the debonding propagated towards the middle gap. Figure 7-23 shows the development of the failure process in picture two before plate debonding. The final failure mode is presented in Figure 7-24 and the maximum deflection during the debonding failure process from the PIV analysis was 2*mm* for IT2.

Figure 7-23 Failure process of IT2

Figure 7-24 IT2 failure mode

7.5.2.3 Impact test 3 (IT3)-Drop height 400*mm*

The drop height was 400*mm*. The impact load the support load time history is presented in Figure 7-25. The maximum peak impact load appeared at 1.4 *ms* and the peak load was 56.25 *kN* . The strain gauge measurement is presented in Figure 7-26 and acceleration time history was presented in Figure 7-27. The maximum acceleration was $400 \times 9.8 m/s^2$ (400g) approximately.

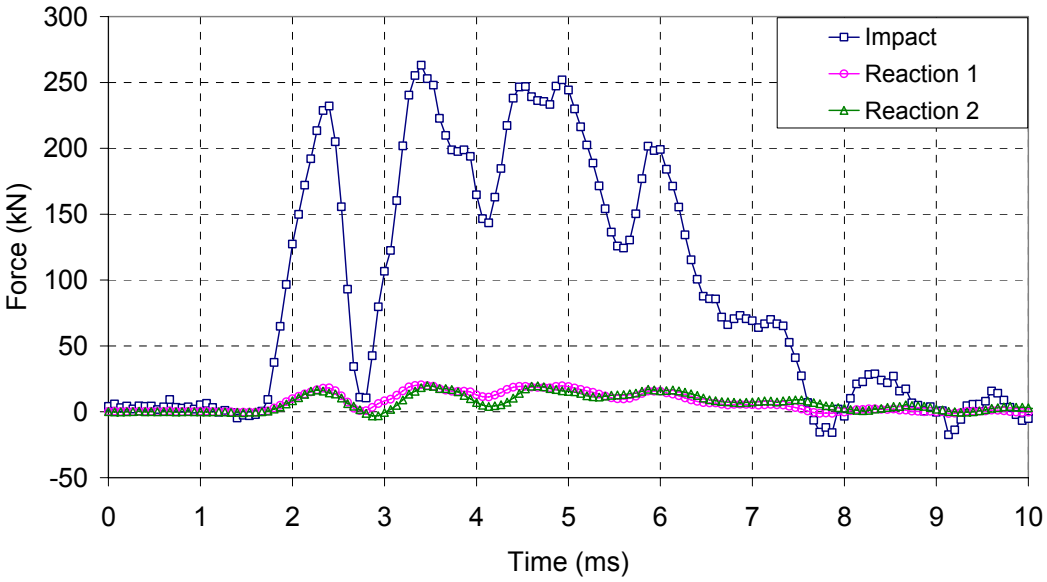

Figure 7-25 Impact and reaction force time history (IT3_400 *mm* drop height)

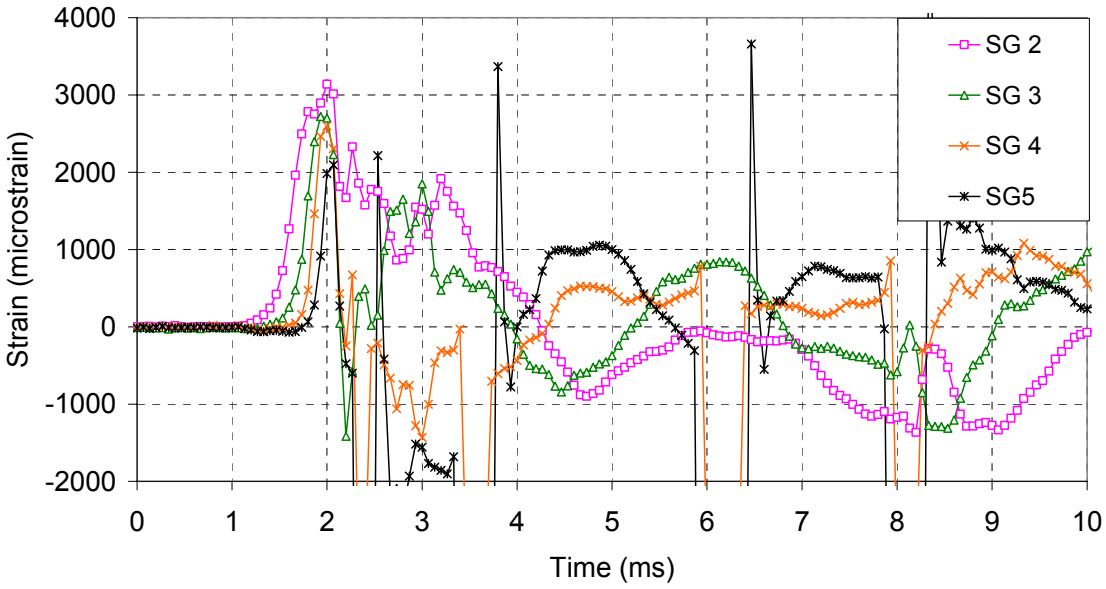

Figure 7-26 Impact strain measurement time history (IT3_400*mm* drop height; please note error occurred at SG1 and data reading was not captured)

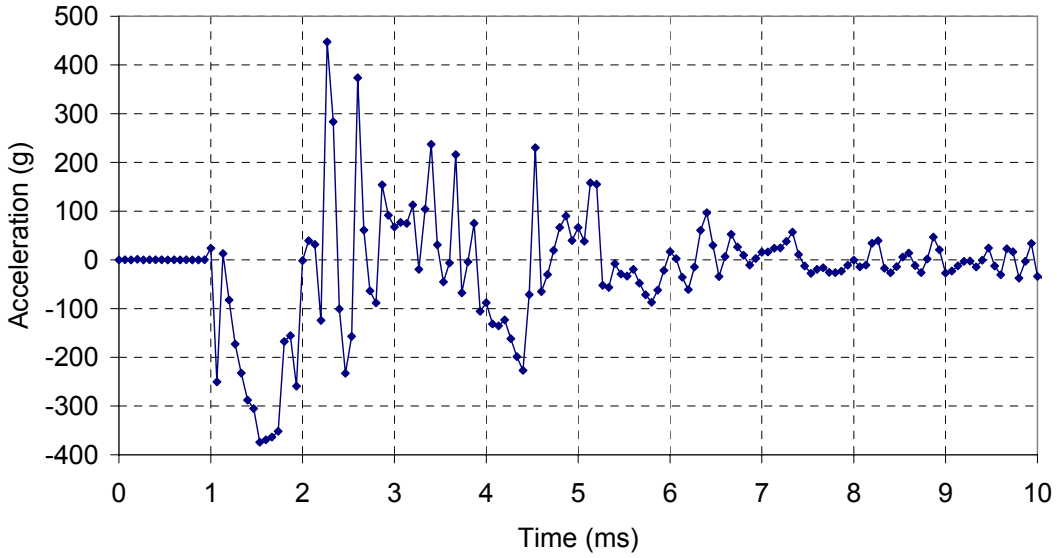

Figure 7-27 Impact acceleration time history (IT3_400*mm* drop height) (The accelerator locates at position A in Figure 7-14)

Impact zone damage was quite significant for IT3 due to the increased drop height to 400*mm* compared to the other drop heights, which could be check from Figure 7-28.

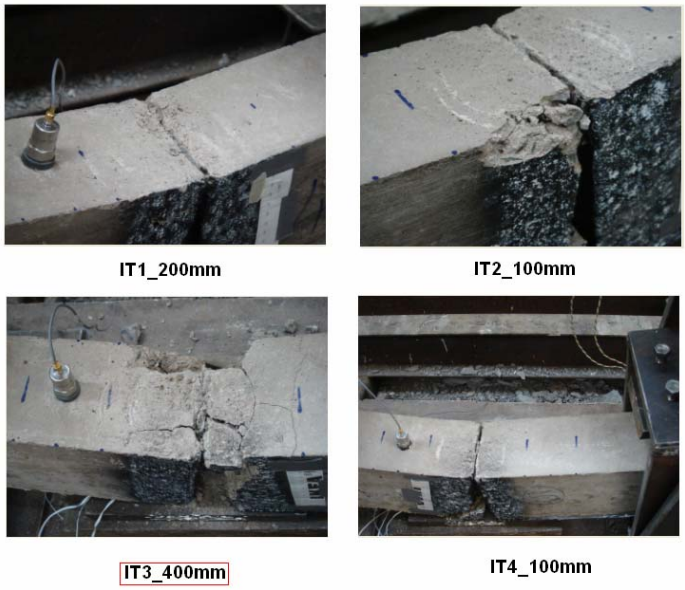

Figure 7-28 Impact zone damage

Figure 7-29 shows the development of the failure mode along with the maximum deflection in picture two prior to plate debonding. The failure mode was debonding with a small shear crack at an angle of 45° very close to the middle gap as shown in Figure 7-30. The maximum deflection during the debonding failure process from the PIV analysis was 6*mm* for IT3.

Figure 7-29 Failure process of IT3

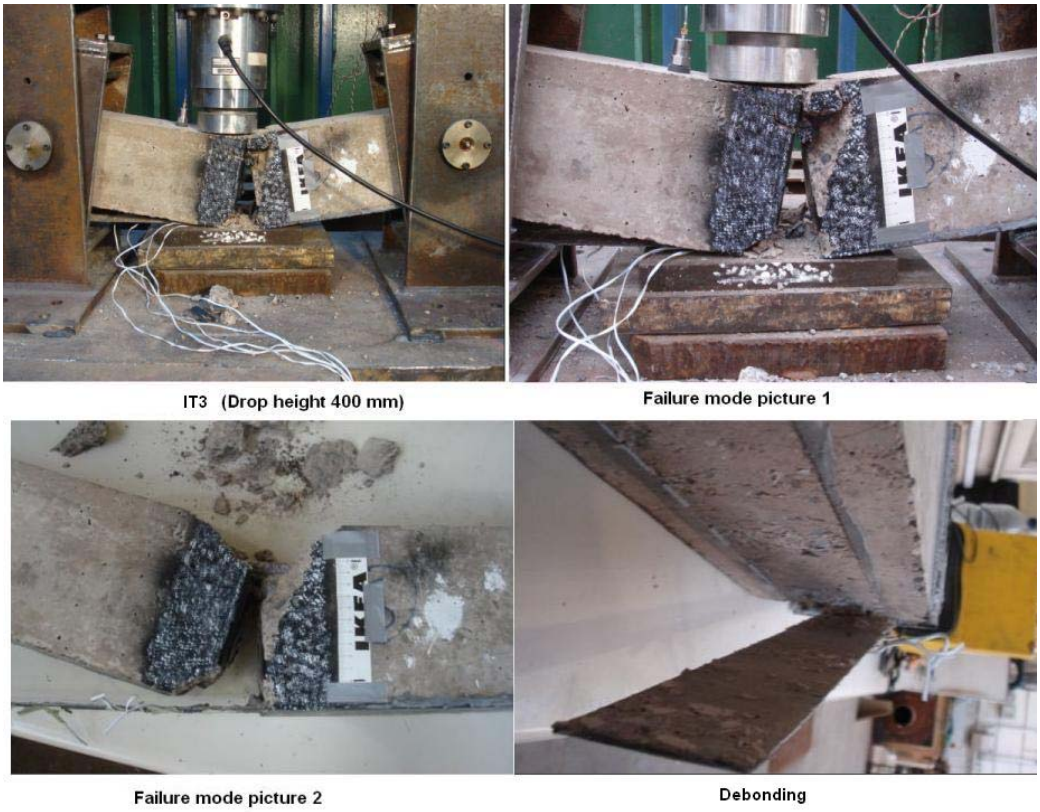

Figure 7-30 IT3 failure mode

7.5.2.4 Impact test 4 (IT4)-Drop height 100*mm*

The drop height was 100*mm* same as IT2. The impact load the support load time history is presented in Figure 7-31. The maximum peak impact load appeared at 2 *ms* and the peak load was150 *kN* . The strain gauge measurement is presented in Figure 7-32. The acceleration time history is presented in Figure 7-33 and maximum acceleration was $200 \times 9.8 m/s^2$ (200g) approximately.

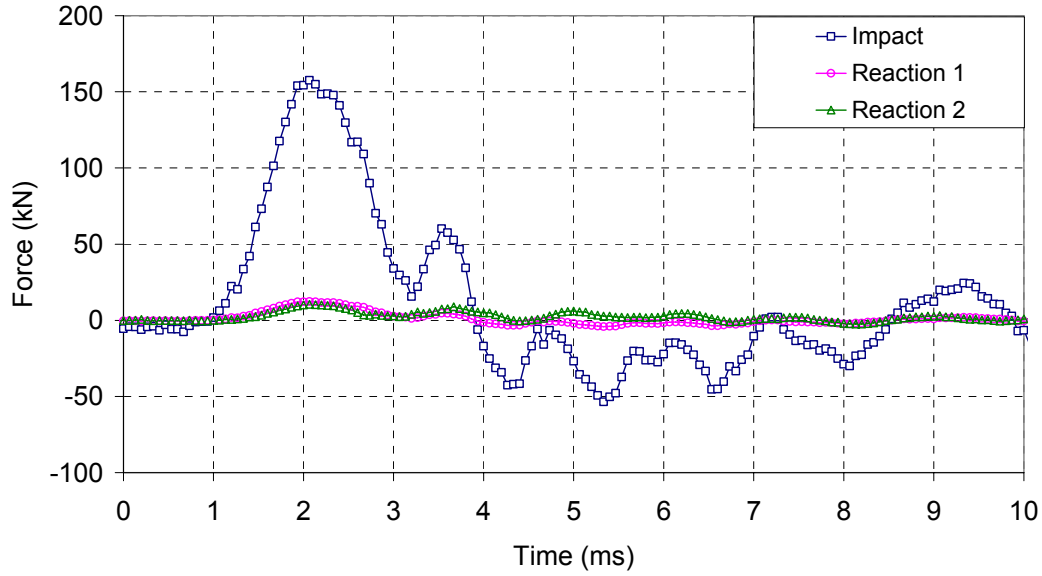

Figure 7-31 Impact and reaction force time history (IT4_100*mm* drop height)

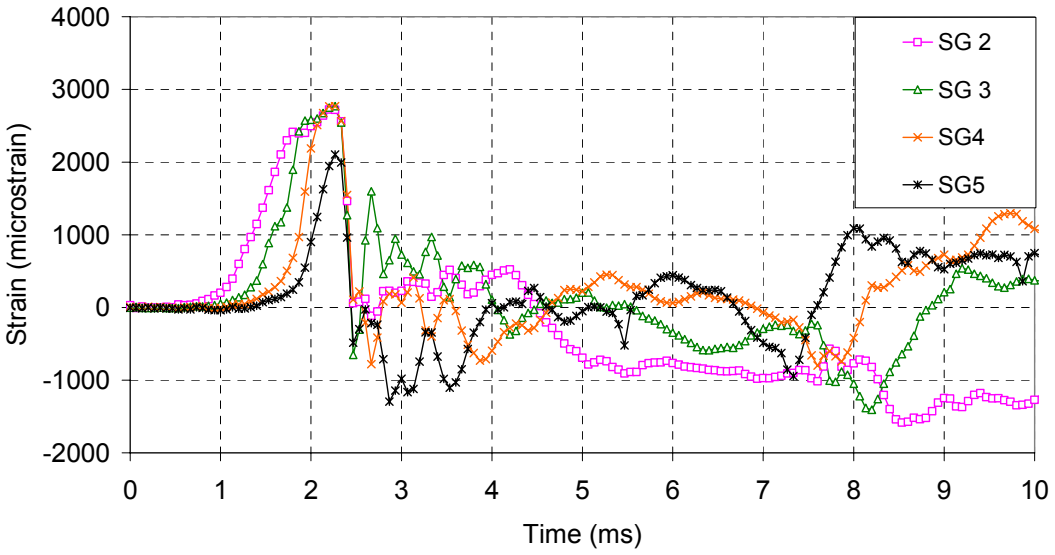

Figure 7-32 Impact strain measurement time history (IT4_100*mm* drop height; please note error occurred at SG1 and data reading was not captured)

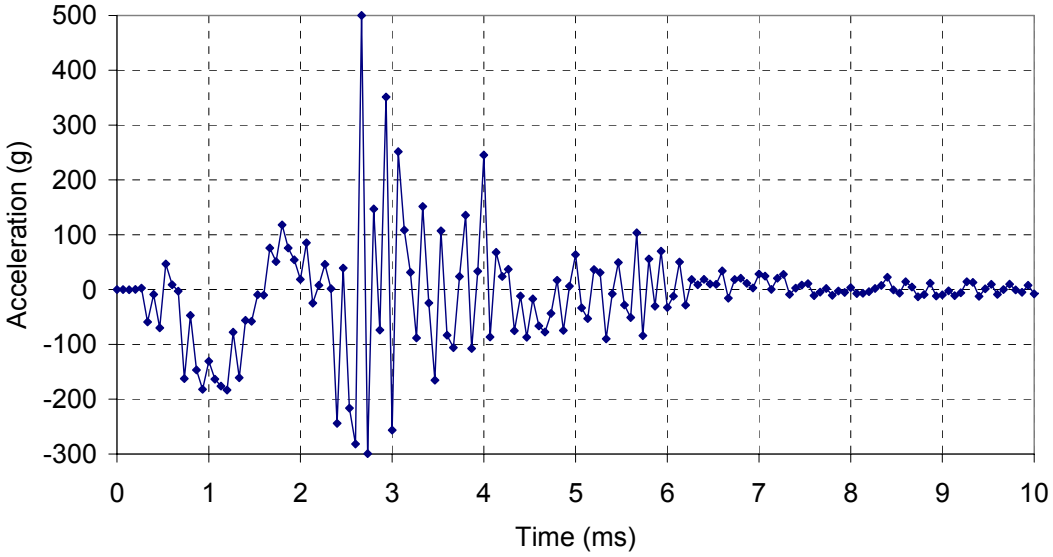

Figure 7-33 Impact acceleration time history (IT4_100*mm* drop height) (The accelerator locates at position A in Figure 7-14)

The failure mode was also debonding. A shear crack developed at an angle of 50° which widened as the debonding propagated towards the middle gap. The debonding depth was still very thin and just with mortar but no aggregate, less than 2*mm* thickness. Figure 7-34 shows the development of the failure mode including the shear crack along with the test specimen immediately before plate debonding in picture two. The final failure mode is presented in Figure 7-35 and the maximum deflection during the debonding failure process from the PIV analysis was 0*mm* for IT4.

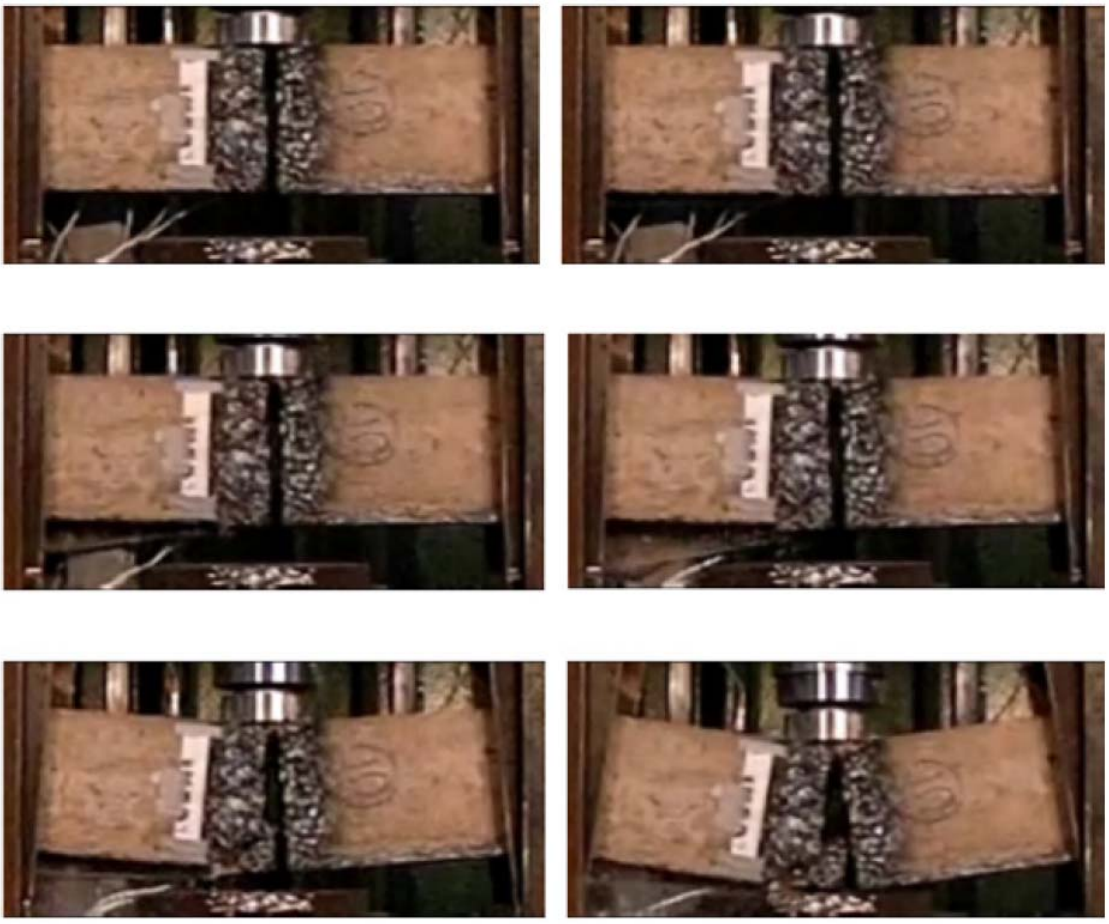

Figure 7-34 Failure process of IT4

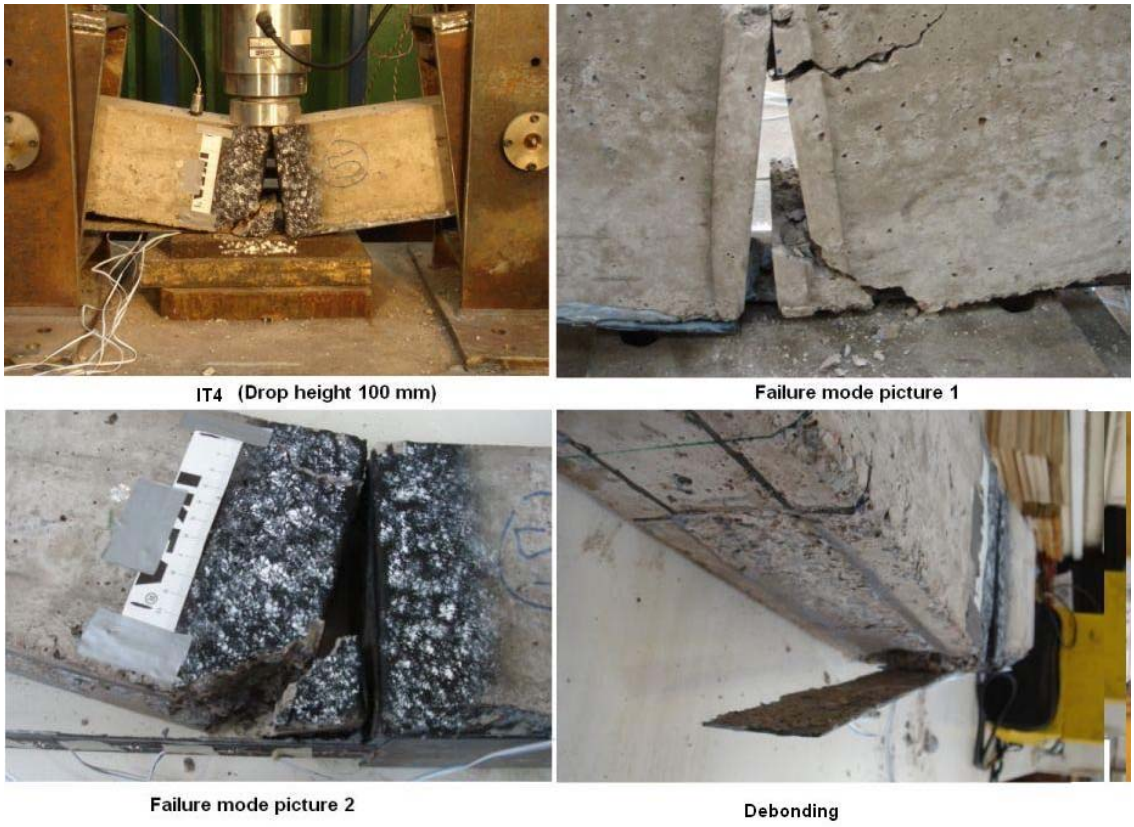

Figure 7-35 IT4 failure mode

7.6 Analyses

7.6.1 Summary of test results

For both the static and impact tests, the debonding process was instant and the beam behaved quite brittle. Table 7-3 summarises the results from the static and impact tests.

Table 7-3 Summary of the test results (strain unit: $\mu\varepsilon$)

	IT3	IT1	IT4	IT2	ST2(3-point)	ST1(4-point)
Striker drop height (mm)	400	200	100	100	Static	Static
Peak impact load at first impulse (kN)	232	56	158	36	18	26
Time duration of the first impulse (ms)	1.1	2.0	1.2	3.0	500	250
Impulse of the first impulse ($N \cdot s$)	128	56	94	82	--------	--------
Maximum acceleration ($\times 9.8 m/s^2$)	400	200	100	100	0	0
Maximum strain rate (s^{-1})	16.5	12.9	9.3	7.8	3.3×10^{-4}	1.5×10^{-5}
Maximum strain at SG1	N/A	3021	N/A	2985	4292	2478
Maximum strain at SG2	3141	2581	2770	2919	2000	2180
Maximum strain at SG3	2720	2560	2770	N/A	1843	2085
Maximum strain at SG4	2601	2560	2720	2782	1808	2372
Maximum strain at SG5	2095	1909	2105	2147	1408	1606
Shear crack angle ($\circ$)	45	45	50	50	42	40
Distance between shear crack start point and the notch (mm)	30	50	60	55	40	120
Estimated mid-span deflection at failure (mm)	6	3	0	2	4.06	2.7

The final failure patterns of the impact test specimens were all very similar to the 3-point bending test specimen with a shear crack close to the mid notch.

The failure mode for the static test was shear-crack induced debonding. For the impact test, debonding failure was observed for all the four impact tests, however it was hard to determine exactly which type of debonding failure mode was in reality for the impact tests: 1) Plate end debonding might be first estimated, because according to the frames (Figure 7-18, Figure 7-23, Figure 7-29 and Figure 7-34) it can be discovered the shear crack developed significantly after the debonding happening at the plate end. However, there were only 2 to 3 frames within the first impulse, of which the time duration is only around 2 ms , with low resolution to judge the failure mode and the shear crack actually occurred before it significantly developed; 2) The strain time histories of the impact tests (Figure 7-16, Figure 7-21, Figure 7-26 and Figure 7-32) presented in former section can tell the strain development of the FRP started from the middle notch to the FRP end, and the time gap between the start of SG1 and SG5 was 0.5 to 1ms. The peak strain of SG1 also always happened before the peak of SG5. So there is still a possibility that the failure mode was shear crack induced debonding.

7.6.2 Test repeatability

The repeatability of the impact tests was not good according to test results for IT2 and IT4 presented in Table 7-3. The two impact load time histories for the two specimens with the same drop height of 100mm have significant differences. But the

impulse for IT4 and IT2, which was equal to the area of the first impulse, were close to each other so the difference of the maximum strain measurements and final shear failure crack were close to each other too. The impulse for IT1 of which the drop height was 200*mm* was smaller than the results obtained from 100*mm* drop height. That was not expected as if the striker had a higher drop height the impulse was expected to be greater due to the higher impact velocity with the same striker. The possible reasons for poor repeatability are listed:

1) The limitation of the number of the test specimens. There were only 4 specimens. Normally for beam specimen tests, a larger number of test specimens were preferred, e.g. over 80 long beams tested in Hughes and Soeurs (1982).

2) Low data recording frequency. For IT1 and IT2 conducted in the first day of impact tests, the recording frequency was set to 10,000*Hz*, but for IT3 and IT4 in the next day, it was increased to 15,000*Hz*. The change of the sampling rate did matter as some points may be missed. As presented in Figure 7-15, Figure 7-20, Figure 7-25 and Figure 7-31, the load time history was not continues enough and there are only 20 to 30 data for the first impulse. Consequently, the peak values recorded for IT1 and IT2 could be slightly lower compared to the other two tests.

3) Also, the first mode mass of the beam was less than 30*kg*, but the striker was 200*kg* with an impact ranging up to 2000 kN. When the load was in the order of 10 kN, the resolution may not be good enough and the accuracy of the load measurement may be not high.

4) Finally, the poor surface treatment. Less than 1mm mortar was attached to the FRP without any aggregate attached. Also the random micro differences between the impact contact-zones of the surface on the concrete specimens also introduced quite significant distinctions between IT2 and IT4 even under the same drop height. These differences may significantly affect the impact time duration. Clearly the impact time duration of IT4 is only half of IT2, and the peak load of the impulse was strongly dependent on the time duration of the first impulse.

7.6.3 Bond behavior

From Table 7-3, the smallest peak impact load was $56\,kN$ for IT1. Assuming it was uniformly distributed in the $100\,mm$ diameter impact zone, the peak value of the impact stress was approximately $7MPa$. When the compressive stress wave travelled to the FRP bond, it reflected as a tensile wave. $7MPa$ is nearly more than 2 times the concrete tensile strength of $2.65\,MPa$. Meanwhile the stress wave speed travelling in the concrete is approximately $3.15\times10^3\,m/s$ according to CEB-FIP (1993).

$$V_c = \sqrt{\frac{E_c}{\rho_c}} \tag{7-8}$$

in which

$$E_c = 18.275(f_c'/10)^{1/3} \tag{7-9}$$

where E_c is the concrete Young's modulus; ρ_c is the density of concrete; V_c is the wave speed. It took less than $0.5\,ms$ for the stress wave to travel from the top surface of the specimen to the FRP bond line. That is one scale smaller than the time duration of the debonding process approximately equal to $3\,ms$. FRP-to-concrete bond may be damaged before the bond strength is mobilised, causing reduction of the bond strength.

The shear crack angle and distance between shear cracks start point and the notch indicate that the impact test failure mode were close to the 3-point static bending test. According to Table 7-3, the SG1 strain readings for the impact test specimens, which were right under the impact zone, were all higher than the value which obtained from the 3-point static bending, but lower than 4-point bending. Other strain readings were higher than the 3-point and 4-point static bending tests. These indicate the bond was enhanced due to the higher strain rates compared to static tests.

The behavior of the bond was complex due to various enhancing and weakening factors. According to strain measurements, enhancement was greater.

The mid-span deflection at the first impulse failure was small, less than 6mm which is less than 1% of the span ($700mm$), so bending effect of the specimen may be considered minimal. In future tests, better surface treatments should be followed to ensure that failure occurs in the concrete. If the strain gauges were closely applied on the FRP, it is possible to measure the local bond-slip relationship under impact load. Also, it may be necessary to have plenty of specimens. The striker and load cell

resolution must be well controlled as well as the impact contact surface treatment. The drop height prediction should be well established before tests as the failure mode should be debonding failure only but not shear failure. The data recording frequency should be higher enough to capture all important features.

7.7 Conclusions

This chapter has presented a set of FRP-to-concrete bond test under impact load. The measured strain time histories of the strain gauges along the bond length can report the FRP-to-concrete bond behaviour under high strain rates induced by the impact load. The analyses indicate the behavior of the bond was complex, with a combination of enhancement due to strain rate effects and weakening due to the reflected tensile stress waves at the bond. According to the strain measurement, enhancement was greater. The test results can be used to validate the proposed dynamic bond-slip model in Chapter 6, and this will be discussed in the next Chapter. However, according to the test results, the repeatbility was poor and the thickness of the debonding layers of concrete which was adjacent to the FRP plates were all too thin, less than 1mm. Improvements like better surface treatments, thicker adhesive layer and more specimen numbers are necessary for conducting the future tests.

7.8 References

Boyd, A.J., Liang, N., Green, P.S. and Lammert, K. (2008), "Sprayed FRP repair of simulated impact in prestressed concrete girders", *Construction and Building Materials*, 22(3): 411-16.

CEB-FIP (1993), Model Code 90. Lausanne.

Chen, J.F. and Teng, J.G. (2001), "Anchorage strength models for FRP and steel plates bonded to concrete", *Journal of Structural Engineering*, *ASCE*, 127(7):784–791.

Chen, Y. and May, I.M. (2010), "Reinforced concrete members under drop-weight impacts", *Proc. of the Inst. of Civ. Eng*., 162(1): 45-56.

Erki, M.A. and Meier, U. (1999), "Impact loading of concrete beams externally strengthened with CFRP laminates", *Journal of Composites for Construction*, 3(3):117-125.

Hosny, A., Shaheen, H., Abdelrahman, A. and Elafandy, T. (2006), "Performance of reinforced concrete beams strengthened by hybrid FRP laminates", *Cement and Concrete Composites*, 28(10):906-913.

Hughes, G. and Soeurs, D.M. (1982), An Investigation of the Beam Impact Problem, Wexham Springs, Cement and Concrete Association, Technical Report 546, ISBN 0721012469.

Kabir, M.Z. and Shafei, E. (2009), "Analytical and numerical study of FRP retrofitted RC beams under low velocity impact", *Cientia Iranica*, 16(5): 415-428.

Lu, X.Z., Ye, L.P., Teng, J.G. and Jiang, J.J. (2004), "Mesco-scale finite element model for FRP sheets/plates bonded to concrete", *Engineering structures*, 27:564-575.

Malvar, L.J. and Crawford, J.E. (1998), "Dynamic increasing factors for concrete", Twenty-Eighth DDESB Seminar, Orlando, FL, August.

O'Sullivan, R. (2011), "FRP-to-concrete bond behaviour under impact loading", MEng Thesis, the University of Edinburgh.

Sena Cruz, J.M., Barros, J.A.O. and Gettu, R. (2004), Bond Behavior of Near-Surface Mounted CFRP Laminate Strips under Monotonic and Cyclic Loading, Report No. 04 DEC/E-04, Department of Civil Engineering, University of Minho, Guimarães.

Sheil, A. (2011), "FRP-to-concrete bond behaviour under impact loading", MEng Thesis, the University of Edinburgh.

Suter, R. (2006), "Reinforcement of bridge piers with FRP sheets to resist vehicle impact", *Structures and Extreme Events. IABSE Symposium*, 1: 242-243.

Tang, T.P. and Saadatmanesh, H. (2003), "Behavior of Concrete Beams Strengthened with Fiber-Reinforced Polymer Laminates under Impact Loading", *Journal of Composites for Construction*, 7(3):209-219.

Uddin, N., Shelar, K.V. and Fouad, F. (2006), "Impact response of autoclave aerated concrete/FRP sandwich structures", *Proceedings of the Structures Congress and Exposition*, 214: 1-10.

White, T.W., Soudki, K.A. and Erki, M.A.(2001), "Response of RC Beams Strengthened with CFRP Laminates and Subjected to a High Rate of Loading", *Journal of Composites for Construction*, 5(3):153-162.

Yu, D., Kwaka, J.B., Parka, S. and Lee, J. (2010), "Dynamic responses of PCB under product-level free drop impact", *Microelectronics Reliability*, 50(7): 1028-1038.

Zhang, Y., Cai, C.S., Shi, X.M. and Wang, C. (2006), "Vehicle-induced dynamic performance of FRP versus concrete slab bridge", *Journal of Bridge Engineering*, 11(4): 410-419.

Chapter 8 Modelling of impact test

8.1 Introduction

The quasi-static behaviour of concrete beams strengthened with FRP has been well documented in recent years and some researches have also been conducted on experimental investigation regarding with the effects of dynamic loading, i.e. impact and explosion (e.g. Erki and Meier 1999; Kabir and Shafei 2009; Tang and Saadatmanesh 2003; White et al. 2001; Wu et al. 2009). These studies indicate that strengthening with FRP increased the flexural capacity and stiffness but reduced the energy absorption and ductility. Most of the literature on this focused on the experimental observation of the structural global response and the effects of strengthening but did not address the bond behaviour between the FRP and the concrete in detail. However, it's has been discovered that the catastrophic and explosive failure of strengthened beams produced by debonding of FRP from the concrete has often limited the efficiency of strengthening in design applications (Buchana and Chen 2007; Subramaniama et al. 2008), indicating the bond does affect FRP strengthened concrete structures for impact and blast events. The debonding mostly occurs in the concrete layer unless the adhesive layer is very weak or proper surface treatment has not been followed, and debonding failure model is tension dominated (Chen and Teng 2001; Lu et al. 2004; Lu et al.2005), so the

concrete material properties does affect the bond. The fracture mechanics of the brittle materials such as concrete are strongly dependent on the loading velocity (Sharon et al. 1996). Many studies have been conducted on the relationship between the strain rate and the strength dynamic increasing factor using the split Hopkinson pressure bar (SHPB) test and modelling (i.e. Ross.1989; Ross et al. 1990; Tedesco et al. 1989; Tedesco et al.1991; Li and Meng. 2003). The recent work done by Lu and Li (2011) suggested that the concrete tensile dynamic increasing factor (DIF) due to the strain rate is a genuine material effect rather than the effects from inertia force of the structure. The numerical investigation and comparison presented in Chapter 5 also indicated that DIF should be considered as a genuine concrete material property and modelling with the proposed concrete local DIF give reliable FE results compared with test data both for SHPB (Tedesco et al. 1991) and notched concrete beam impact tests (Du et al. 1992). A slip rate dependent dynamic bond-slip model has been proposed in Chapter 6 via numerical experiments on pull-off test modelling under different loading rates. FRP strengthened specimens with FRP retrofitted concrete beam was tested with impact load presented in Chapter 7. It has been discovered that both enhancement due to strain rate effects and damage from the stress wave exist for the FRP-to-concrete bond and the enhancement is greater. The concrete local DIF in Chapter 5 and the proposed dynamic bond-slip model in Chapter 6 are employed to model the impact test presented in Chapter 7.

Two different loading schemes, one modelling a striker and another using the impact load from the test measurement, are discussed respectively and compared in Section 8.2. The 100*mm* drop height was chosen for the first numerical modelling as we got

two samples, IT2 (impact test 2) and IT4 (impact test 4), both at 100*mm* drop height for test repeatability consideration. A uniformly distributed pressure load equivalent to the measured impact load is finally chosen to be applied at the impact zone instead of modelling striker. FE modelling with and without concrete local DIF was analyzed with perfect bond assumption. The dynamic bond-slip model was also introduced with a layer of interface elements and all of the four tests, IT1, IT2, IT3 and IT4 were modelled and compared.

8.2 Impact test modelling with striker

8.2.1 FE model

The attempt was to model the impact test with the striker. The beam was idealized as a 2D plane stress problem so only a single slice of concrete in the beam width direction (z-direction in Figure 8-1) was modeled using the 3D solid element. In order to reduce the computational effort, only half of the specimen was modeled

The elevation of the model is presented in Figure 8-1. A pin-end boundary condition, with both vertical and horizontal restraints, was applied at the support "A". Horizontal restraints were applied at "B" and "C" for symmetry. Both FRP and steel reinforcement bar was assumed to be perfectly bonded to the concrete.

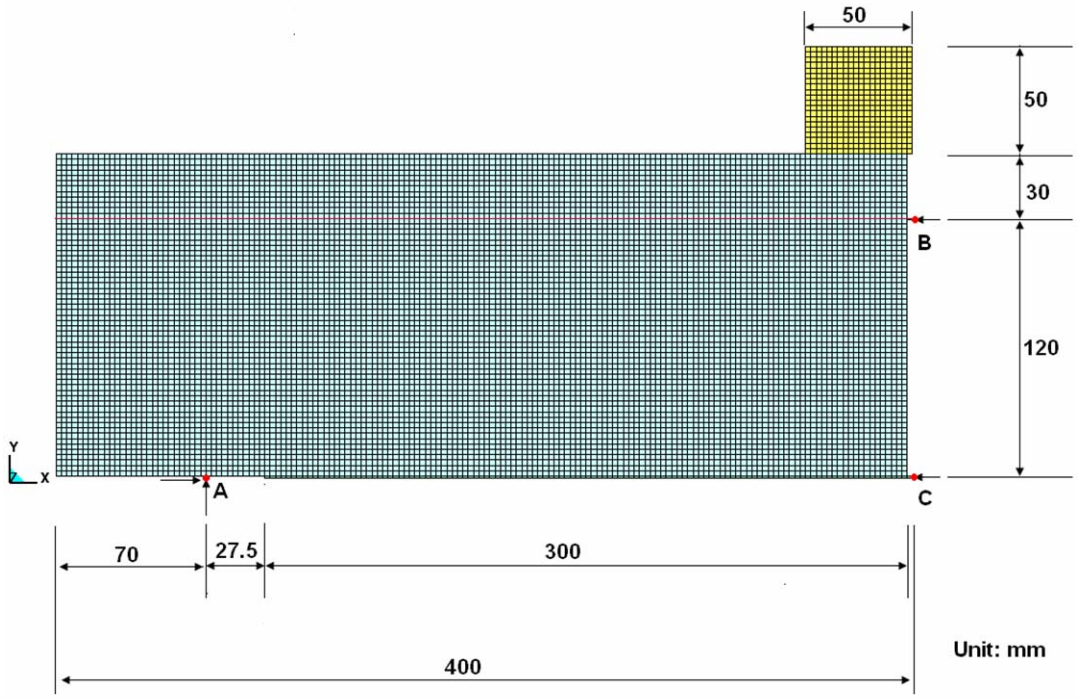

Figure 8-1 Elevation of the impact test model

The striker was simplified as a cube. The striker to concrete surface contact was set as the "automatic contact surface to surface" in LS-DYNA. The adopted mesh consists of 2.5*mm* square elements.

The K&C concrete damage model together with the concrete local DIF proposed in Chapter 5 were chosen to represent the concrete. The concrete compressive cylinder strength f_c' was 25 MPa . The local concrete localization width was set as the element characteristic length according the numerical localization investigation in Chapter 3 and Chapter 5. The dilation parameter was set as 0.3 based on Chapter 4. FE modeling with and without mesh and rate dependent local DIF for the impact test with 100*mm* drop height was conducted and the predicting are compared to test results of IT2 and IT4.

Because FRP rupture was not experienced in the test, the FRP was modeled as linear elastic material for simplification. The thickness of the FRP plate was 1.4*mm*, the Young's modulus was 170 *GPa* , and Poisson's ratio was 0.3. The test was modelled as a 2D plane stress problem but the predicted results including strains and slips are corrected according to Chen and Teng (2001)'s width effect factor β_w so that they can be compared with test results:

$$\beta_w = \sqrt{\frac{2 - b_c / b_f}{1 + b_c / b_f}} \tag{8-1}$$

where b_c is the width of concrete prism and b_f is width of the FRP plate. In the tests, b_c =100*mm* and b_f =50*mm*.

Beam elements were chosen for modeling the steel reinforcement bars, which had a density of $7.8 \times 10^3 kg/m^3$, the elastic Young's modulus of 200 *GPa* and the Poisson's ratio of 0.3. The cross section of the beam element for numerical simplification was based on equivalent area as in Figure 8-2. The original cross section was firstly simplified as an equivalent area which is uniformly distributed at through the width of the section; then a single slice of the cross section was adopted, of which the thickness for the slice was the thickness of the 2D concrete model. Finally the steel reinforcement bar area of the single slice was simplified as two equivalent beam elements sections for modeling the reinforcement.

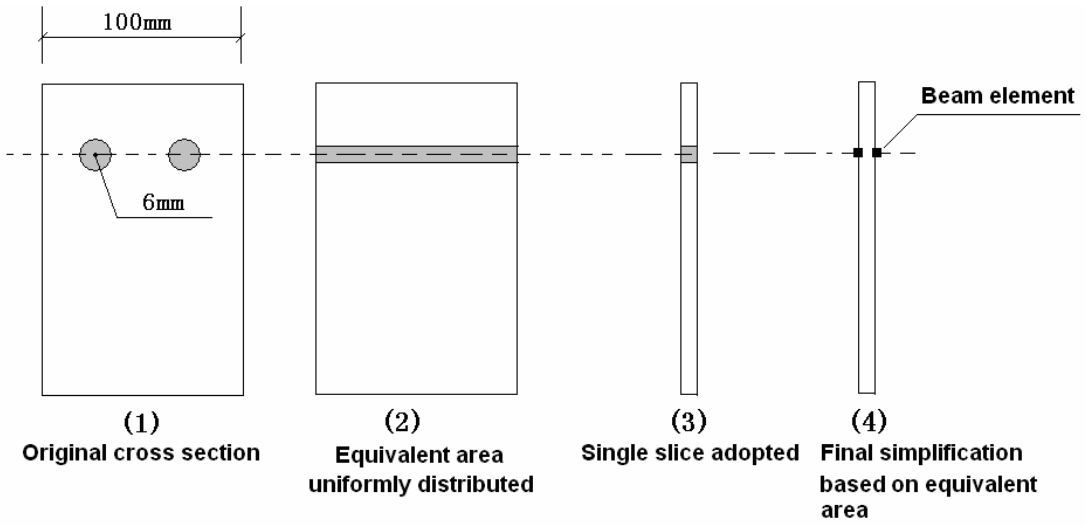

Figure 8-2 Representation of the reinforcement bars in the FE model

The striker had a mass of 200 kg , with a flat mild steel contact face. The striker was modelled as a cuboid as shown in Figure 8-1. As the total impact weight was 200kg in the tests, the density of the cuboids was set as $4.0\times10^5\ kg/m^3$ to account for the actual mass. The Young's modulus of steel (200 GPa) was adopted for the striker.

The modeling was started from the contact point with the following initial velocity assigned to the striker:

$$v_0 = 95\%\sqrt{2gh} \tag{8-2}$$

where v_0 is the initial velocity; $g=9.8m/s^2$ is the acceleration of gravity; and h is the drop height. The 95% is due to 5% gravitational potential energy loss estimation during the drop (Hughes and Speirs 1982). The initial velocity was added to all nodes and elements of the striker before the impact contact time.

8.2.2 FE results and discussion

The impact load time history was compared in Figure 8-3. The strain gauge locations were given in Figure 8-4. The strain predictions from the FE were compared with the test data in Figure 8-5. The strains gauge 1 (SG1) reading for IT4 and strain gauge 3 (SG3) reading for IT2 were missing due to gauge error in the test. The damage contour of the specimen without DIF and with mesh and rate dependent concrete local DIF are compared in Figure 8-6.

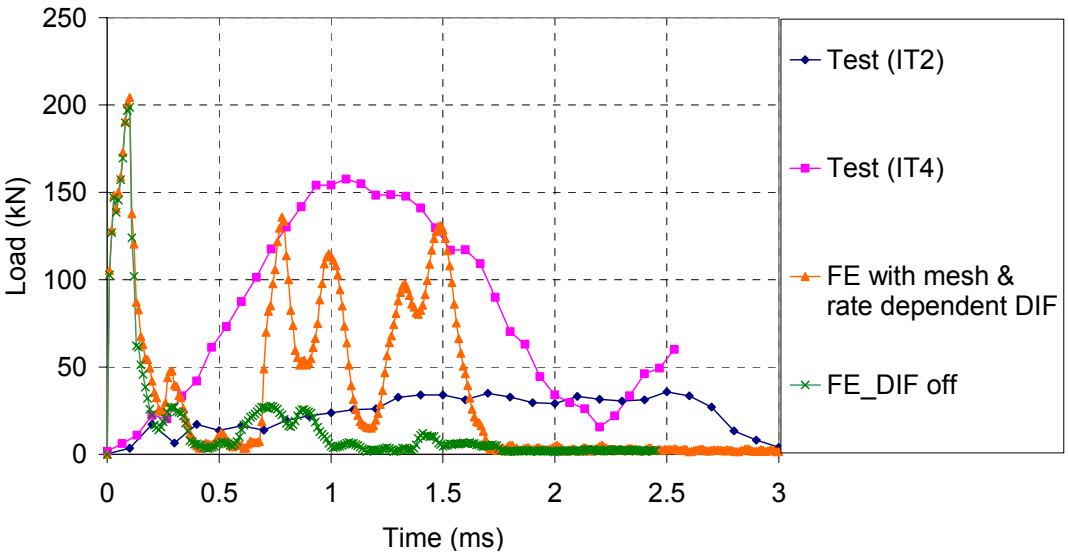

Figure 8-3 Impact load time history comparison between test and the numerical predictions (Drop height = 100mm)

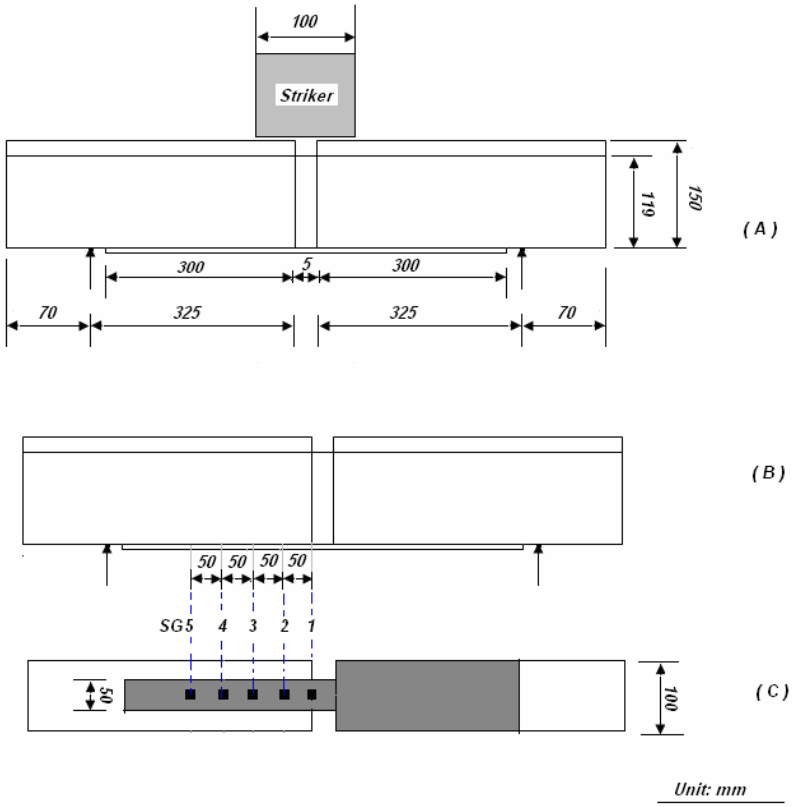

Figure 8-4 Strain gauge locations for the impact tests

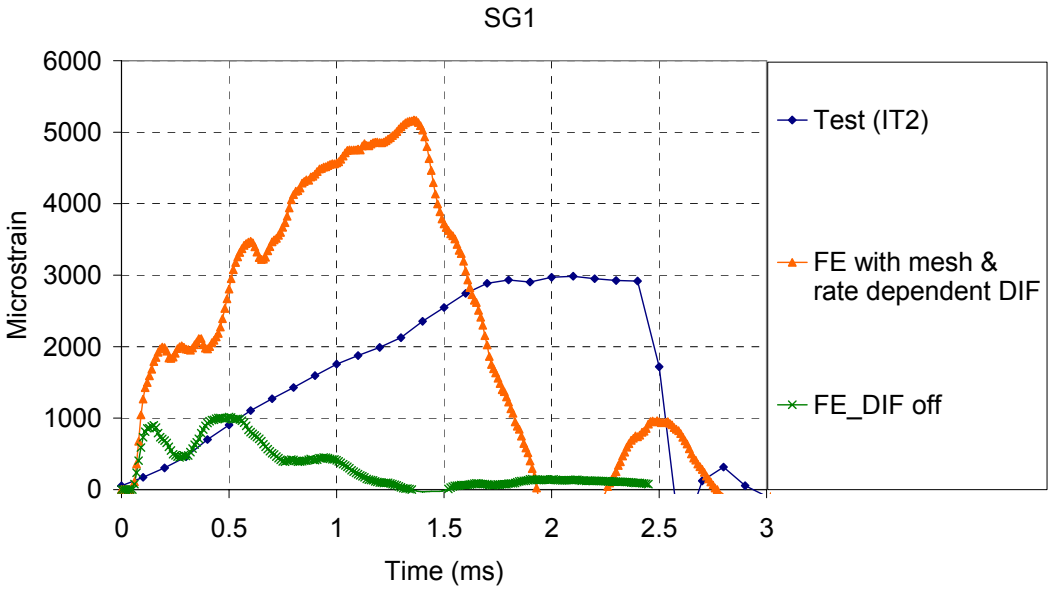

Figure 8-5 Strain time histories at SG1

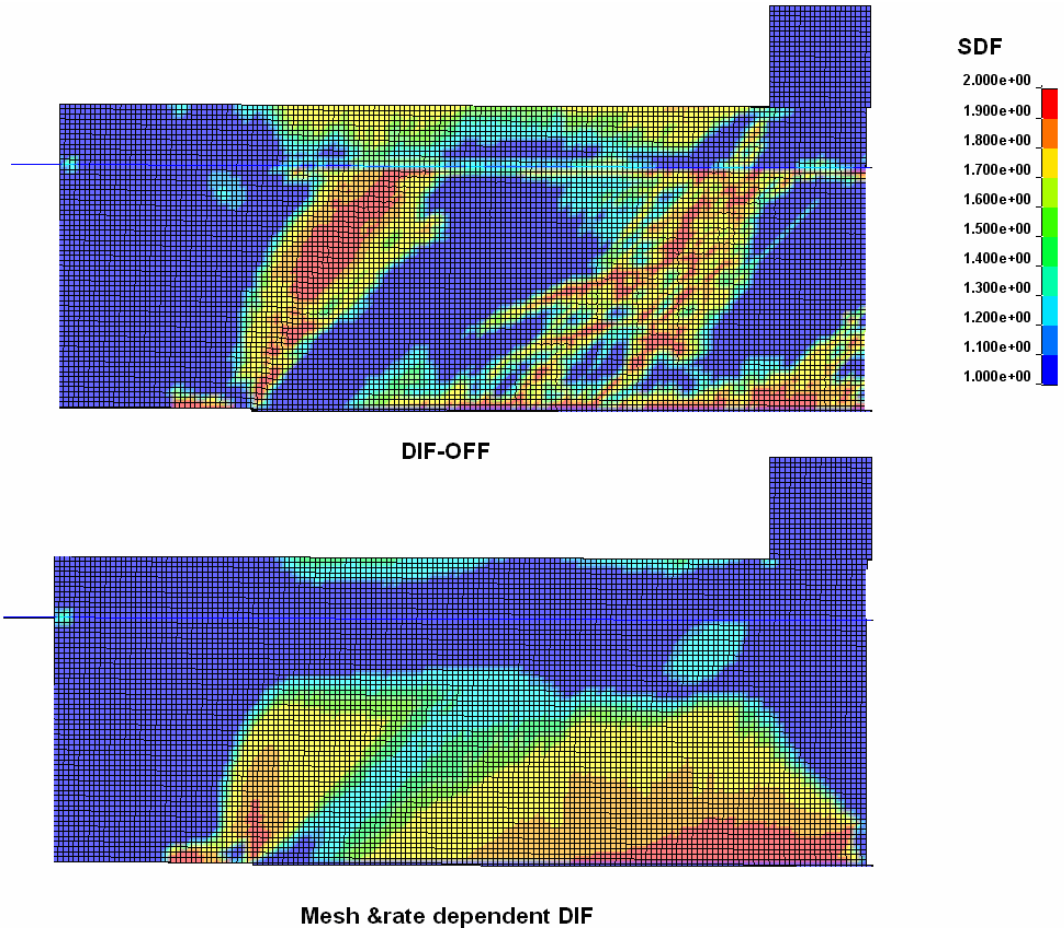

Figure 8-6 Damage contour at 2*ms*

From Figure 8-3, the impact duration of the first impulse has great differences compared with the test data: the time duration of the first impulse for IT2 is 3*ms* and it is 2*ms* for IT4 but the numerical model is 0.5*ms*; For IT2 the peak impact load measured is 35 kN and for IT4 it is 150 kN. However it is 200 kN for the impact test modeling with striker. Also, the strain measurements are significantly affected by the concrete DIF. The comparison is presented in Figure 8-5 and Table 8-1. The FE peak strain prediction without DIF was only 1000 $\mu\varepsilon$ which were much lower than the test results of 3000 to 2000 $\mu\varepsilon$.

Table 8-1 Peak strain value: FE model with striker and tests (Unit: $\mu\varepsilon$)

	SG1	SG2	SG3	SG5	SG6
IT2(100 mm drop height)	3000	2918	N/A	2783	2147
IT4(100 mm drop height)	N/A	2720	2769	2770	2104
FE_DIF OFF	1000	920	778	762	598
FE_Mesh and rate dependent DIF	5106	4325	3000	2176	1453

Also, the damage pattern (Figure 8-6) indicates too much damage is predicted in the FE model without DIF compared with the test results (Figure 8-7 and Figure 8-8). In the test, only one shear crack appeared at the position close to the mid gap where the FRP was pulled. The failure pattern for the FE model with mesh and rate dependent DIF is closer to the test. Too much shear failure happened at the concrete prism for the FE model without DIF. So although both of the two FE models with modelling impact under striker can not match the test results, it seems DIF should be included in the concrete model and this will be further discussed in the following section.

Figure 8-7 Failure mode of IT2

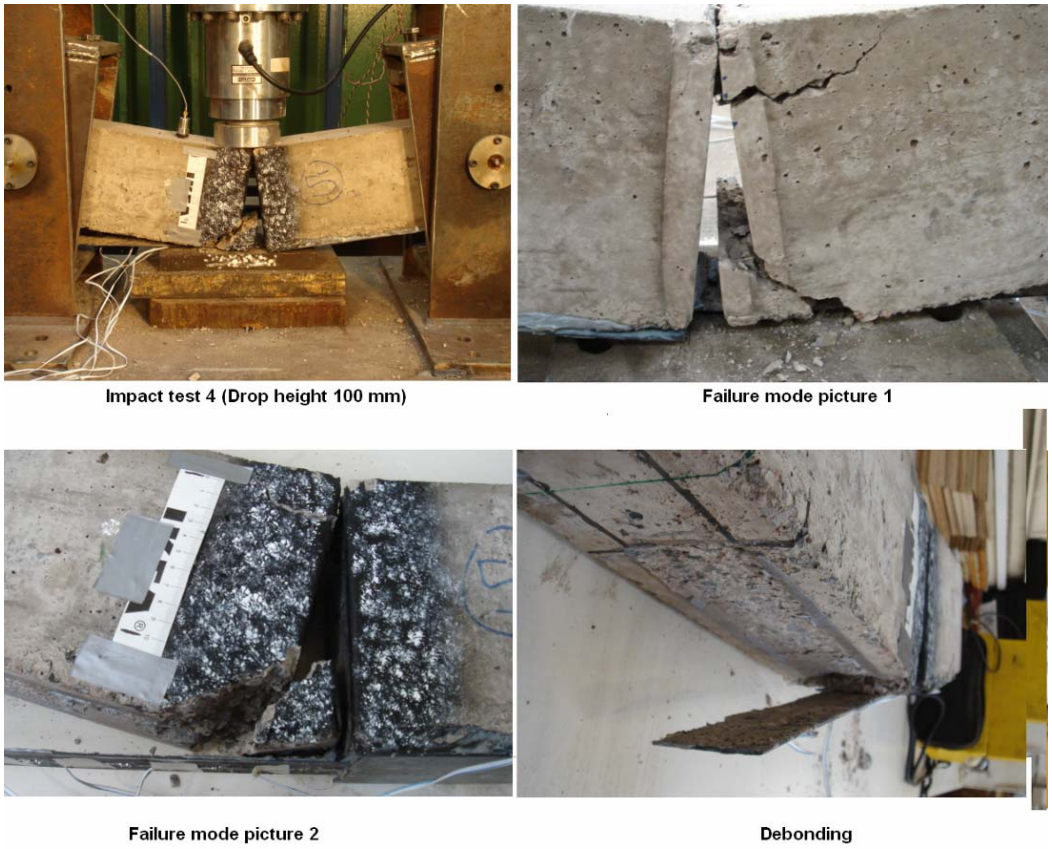

Figure 8-8 Failure mode of IT 4

It is clearly, the FE prediction of the impact load is higher than that in the test and the impact duration is shorter than in the test causing higher strains than in the experiments. The incomparability of FE prediction with the test results, and the poor test repeatability between IT2 and IT4 are probably due to the complexity at the impact interface between the striker and the specimen. As the impact force time history was recorded during the tests so it's possible to do the modelling with the impact force applied directly, without having to model the complex interface behaviour. All the numerical investigations in the rest of this chapter were therefore conducted with impact load directly applied to the specimens.

8.3 Modelling with impact pressure load

8.3.1 FE model

The impact load was treated as a uniformly distributed pressure load applied at an $100 \times 100 mm^2$ impact zone for the whole specimen. All the other numerical modeling aspects were the same as the model issue presented in Section 8.2.1. IT2 was firstly chosen as the sample case for study, with the pressure load time history as shown in Figure 8-9.

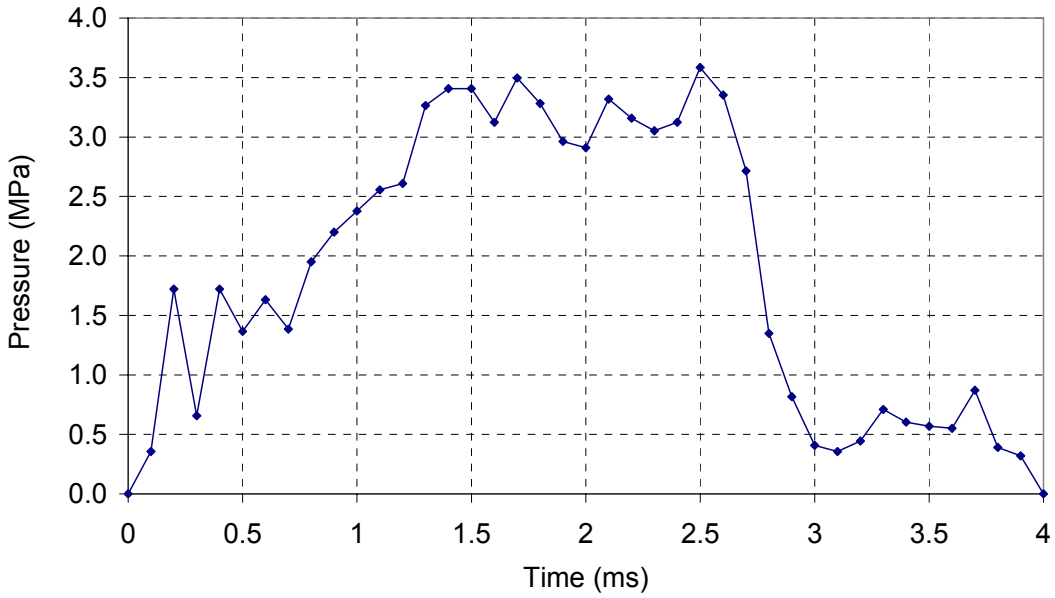

Figure 8-9 Impact pressure load on IT2, drop height 100mm

8.3.2 FE results and discussion

The mesh and rate dependent concrete local DIF was employed. The damage contour presented in Figure 8-10 shows the debonding process still started from the mid span

of the specimen like what behaved in the FE model with the striker. The "*SDF*" in Figure 8-10 is the scaled damage factor for the concrete model. "0< *SDF* <1"means no damage, " *SDF* >1" damage with material softening, and " *SDF* =2" full damage.

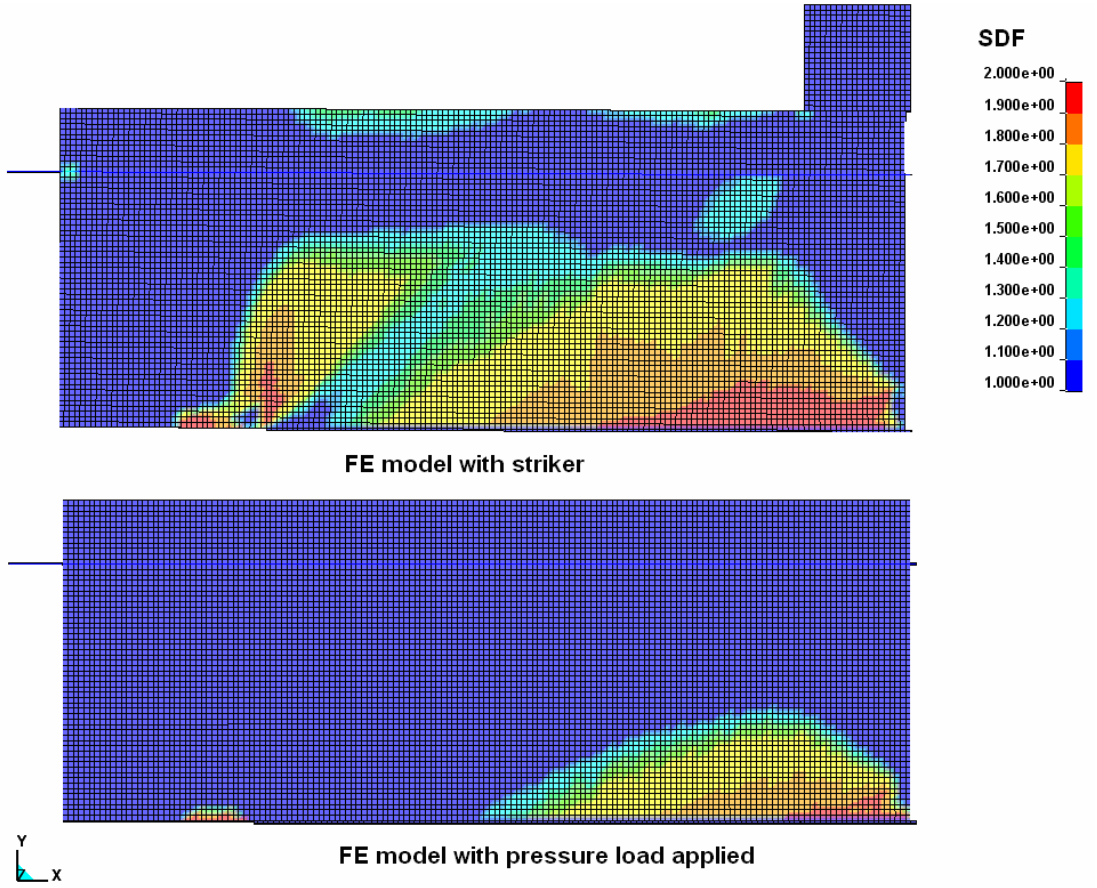

Figure 8-10 Damage contour of the impact test with mesh and rate dependent concrete local DIF for two loading schemes (striker vs. pressure load; mesh size 2.5mm)

In the test, total FRP debonding occurred with a very thin layer of mortar (approximately 1*mm*) attached to the FRP (e.g. Figure 8-8). However, total debonding does not occur in the numerical model. The debonding of the FE model starts at the mid-span and reaches a debonded length of less than 50*mm* for test IT2.

Three element sizes, 10*mm*, 5*mm*, 2.5*mm*, were used for mesh convergence analysis. The SG1 reading comparison is given in Figure 8-11. Mesh convergence is achieved at 5*mm* element size. It is seen that the FE prediction at SG1 is in very good agreement with the test result.

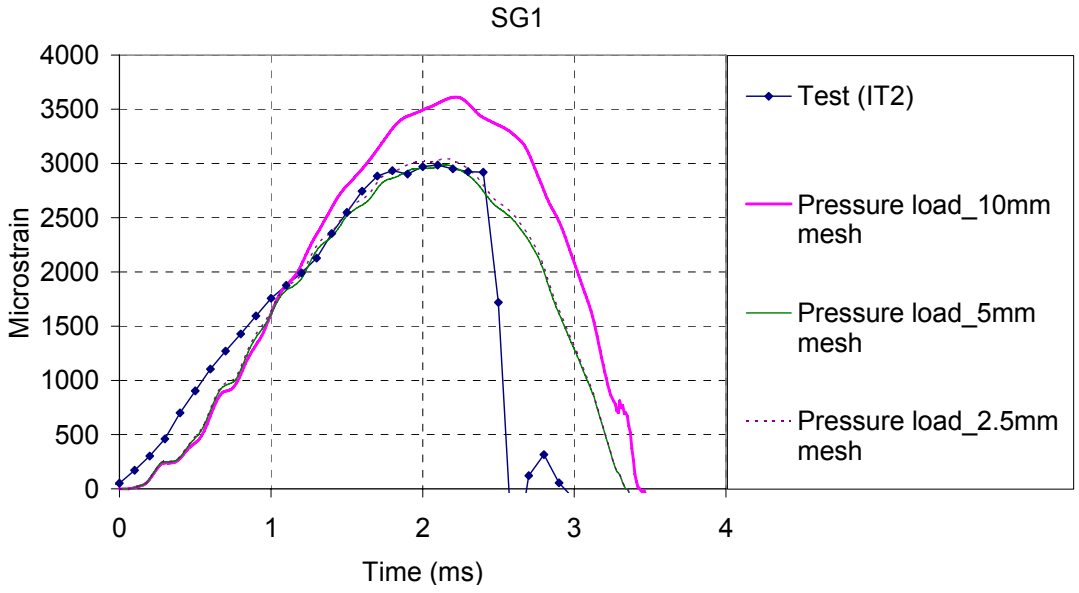

Figure 8-11 SG1 readings for test IT2 (Mesh and rate dependent concrete DIF employed)

However, the other strains outputs do not match with the test results well: The closer the strain gauge location to the mid span where debonding starts, the better the FE strain prediction is in agreement with the test as shown in Table 8-2. Note that the strain gauge at SG3 was faulty in the test.

Table 8-2 Peak strain value: FE model under pressure load (Unit: $\mu\varepsilon$)

	SG1	SG2	SG3	SG4	SG5
IT2 (100 mm drop height)	3000	2918	N/A	2783	2147
FE (pressure load)	3000	2000	1212	726	384

The poor match for strain measurements except that at SG1 is mostly due to the difference in the failure mode as mentioned above. Total debonding occurred at the test, but only at less than 50*mm* from the middle gap in the FE simulation. Among various possible causes, the most plausible could be: 1) the FRP-to-concrete bond was in a poorer state in the test so that the FE model over estimates the strength, and 2) the impact load is under estimated. These two factors are investigated here.

First, a numerical attempt was done with an impact load 20% higher than the measured from test IT2. The predicted damage pattern is shown in Figure 8-12. Clearly the debonded length in this case is longer than the original one. The strain outputs are compared in Figure 8-13 to Figure 8-16.

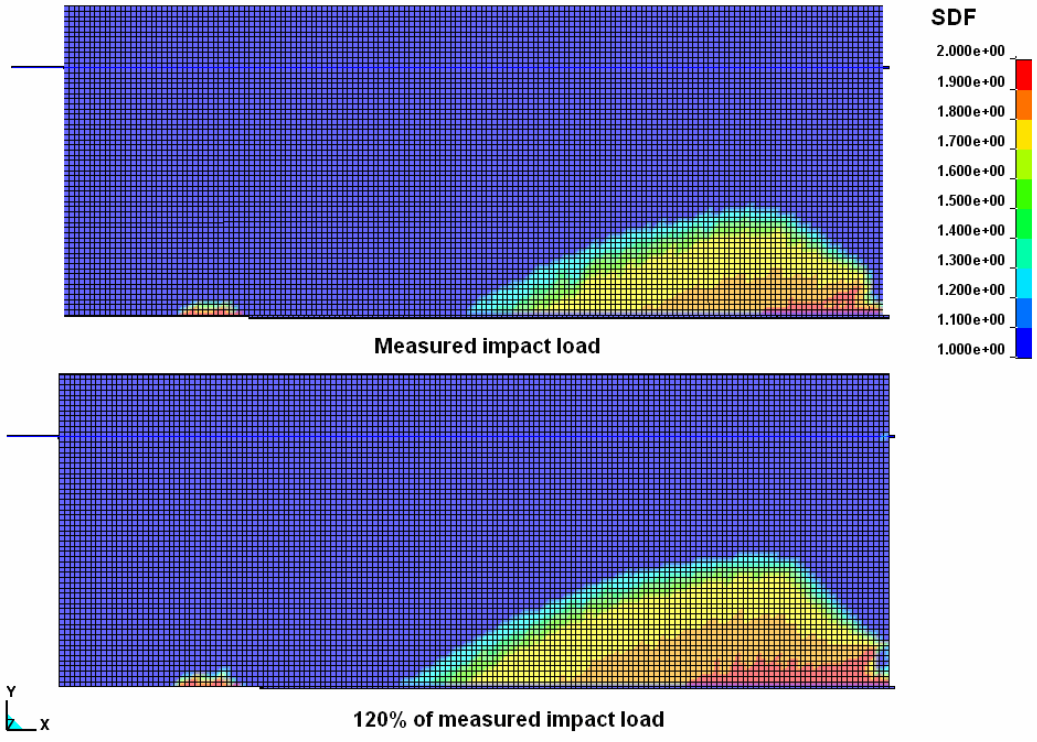

Figure 8-12 Damage contour under measured impact load and 120% measured impact load

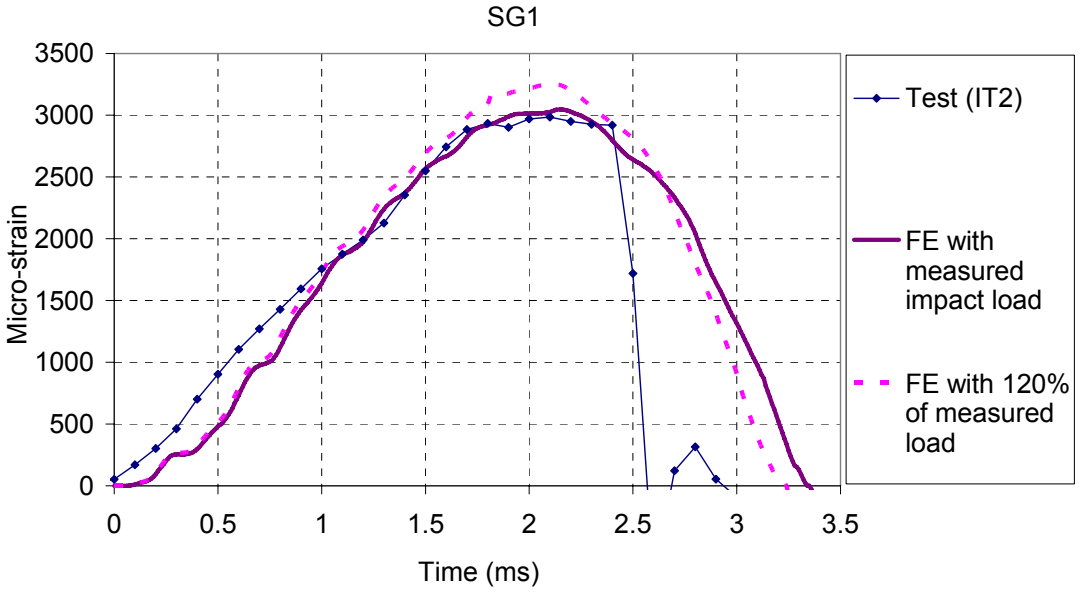

Figure 8-13 SG1: Test, FE with measured impact load and with 120% measured impact load

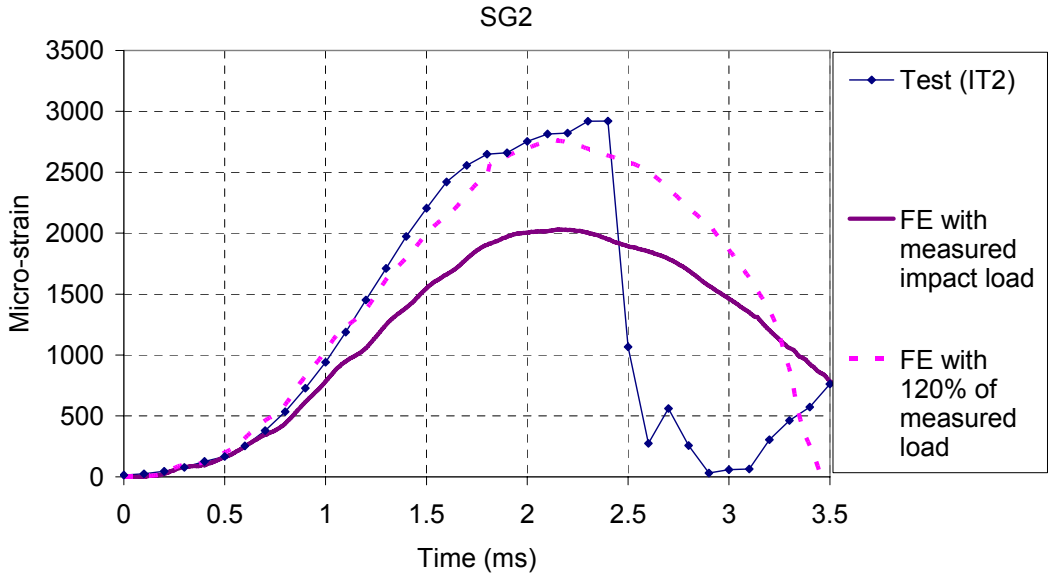

Figure 8-14 SG2: Test, FE with measured impact load and with 120% measured impact load

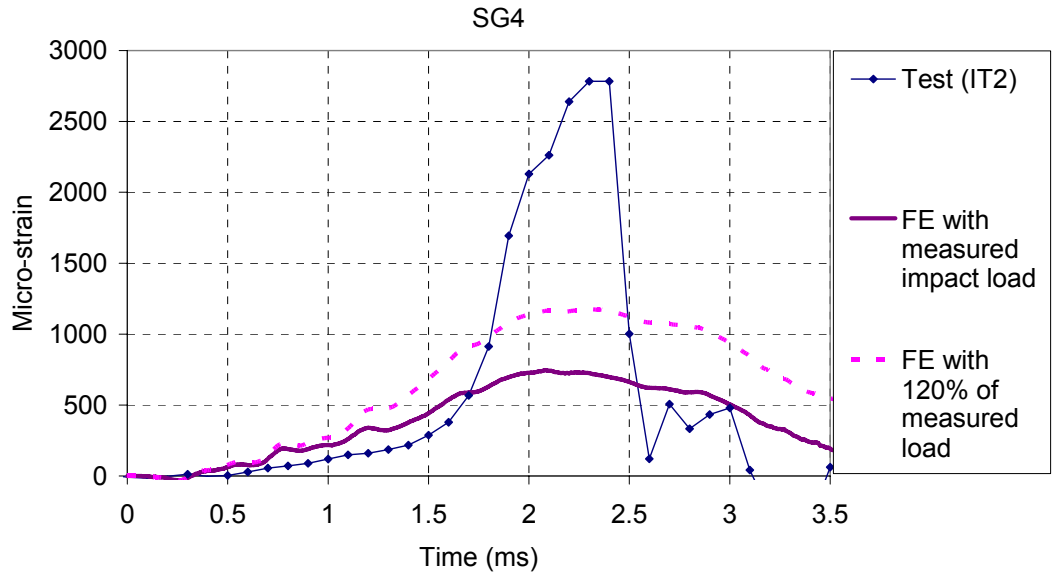

Figure 8-15 SG4: Test, FE with measured impact load and with 120% measured impact load

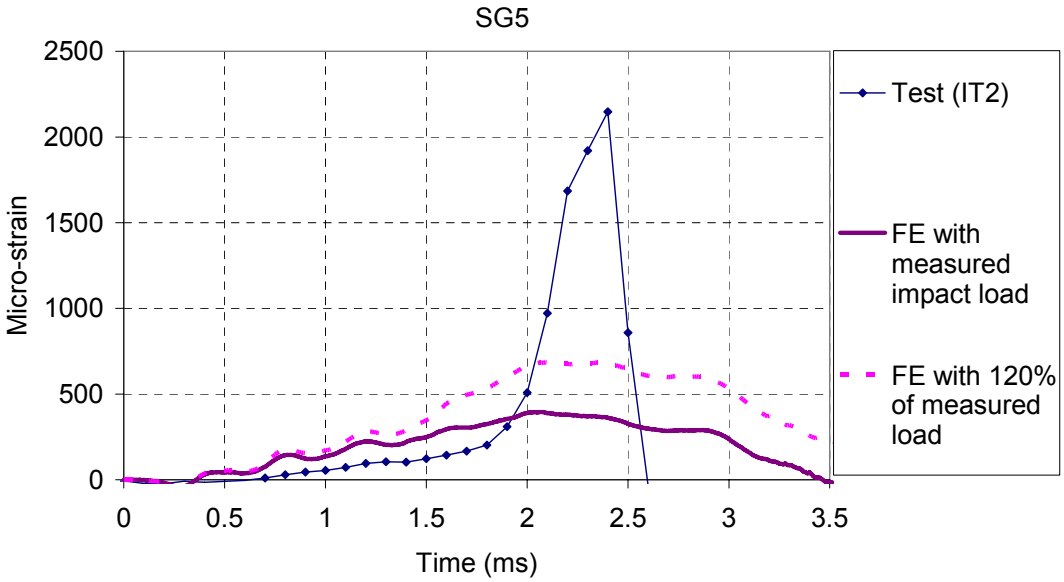

Figure 8-16 SG5: Test, FE with measured impact load and with 120% measured impact load

From Figure 8-13, the FE predicted peak strain at SG1 increases slightly due to the increase of the impact load. However, the predicted SG2 strain increases significantly and give a good agreement with the test value as shown in Figure 8-14,

because the debonding length for the case with 20% impact load is over 50*mm* starting from the middle span where SG2 is located at 50*mm* away from the mid span. For the case when the measured impact load is applied, the SG2 output is much lower than the test results as the debonding has not been developed so far. The strain outputs of SG4 (Figure 8-15) and SG5 (Figure 8-16) also indicate that the more damage occurs at the bond, the closer the strain outputs agree with the test results. The unmatched SG4 and SG5 FE strain outputs to the test results are still due to the debonding failure does not happen there. Accordingly, it is clear that there are the two main possible causes:

1) The inaccuracy of the load measurement. As presented in Figure 8-13 and Figure 8-14, with adding 20% more impact load to FE, SG 1 output is only slightly increased whereas the debonded length is increased and SG2 output is significantly increased. There was just one choice of striker with the load cell fixed to it at Heriot-Watt University at the time of test. The measurement range of the load cell in the test was up to $2000\,kN$. Due to the low impact heights used in the test; the peak load measured was only around $100\,kN$ for test IT4 and $35\,kN$ for test IT2.

2) The method of surface treatment. The surface treatment might not offer sufficient bond strength in the test. In the test, total debonding occurred with less than 1mm mortar attached to the FRP. However, in the FE total debonding failure does not happen. In the numerical model the debonding depth of the concrete adjacent to FRP was thicker due to the ideal bond assumption.

The above two possible causes were further investigated here with two more numerical attempts: one under 250% measured impact load and one with the strength of concrete within 10*mm* adjacent to the FRP reduced to 5 *MPa* . The predicted strains are compared in Figure 8-17 to Figure 8-20.

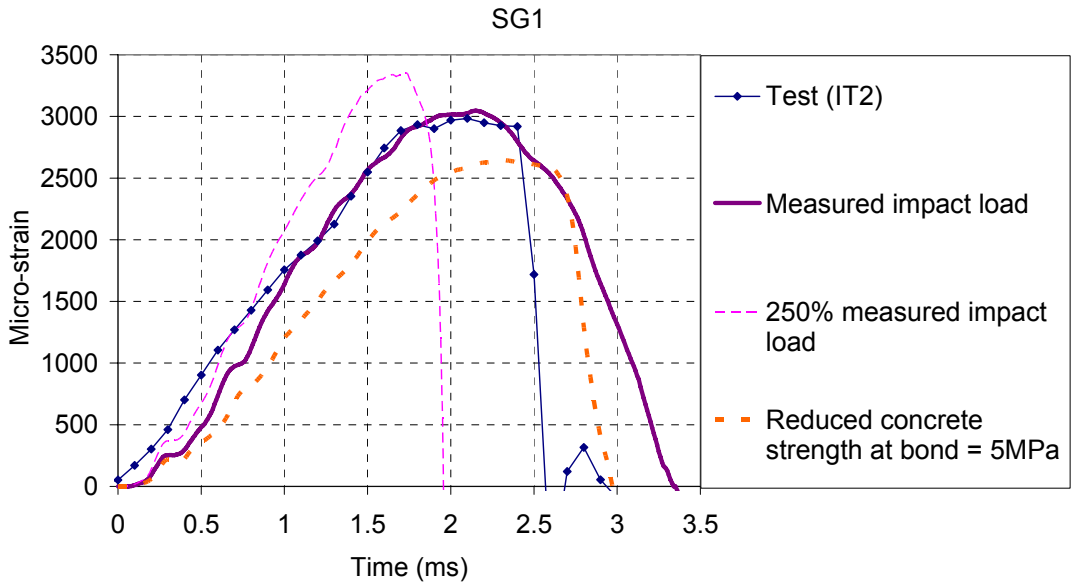

Figure 8-17 SG1 (Test, FE with measured impact load, and two total debonding cases <1> 250% measured impact load; <2> reduced concrete strength at bond = 5*MPa*)

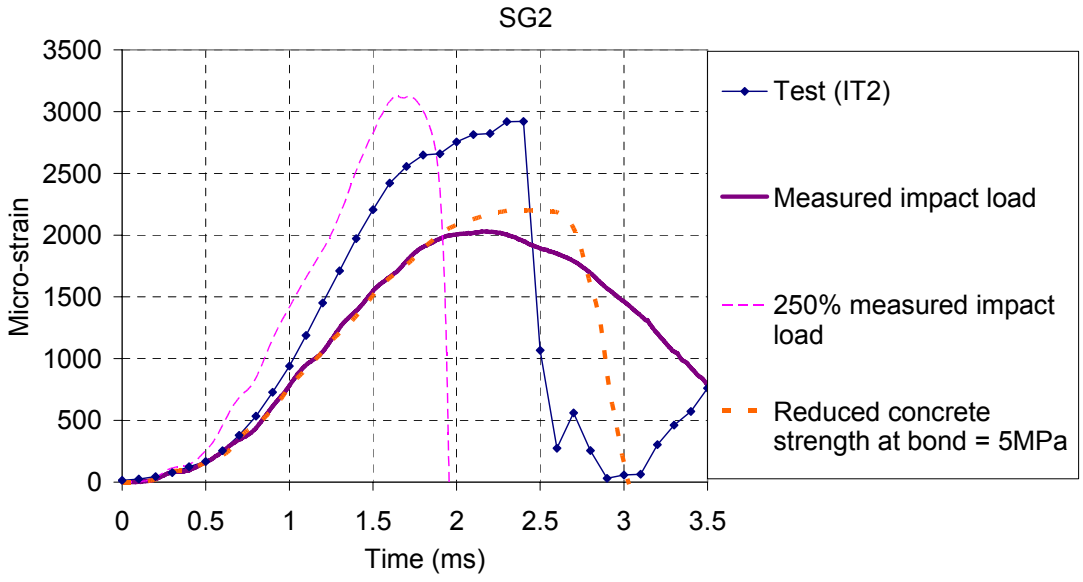

Figure 8-18 SG2 (Test, FE with measured impact load, and two total debonding cases <1> 250% measured impact load; <2> reduced concrete strength at bond = 5*MPa*)

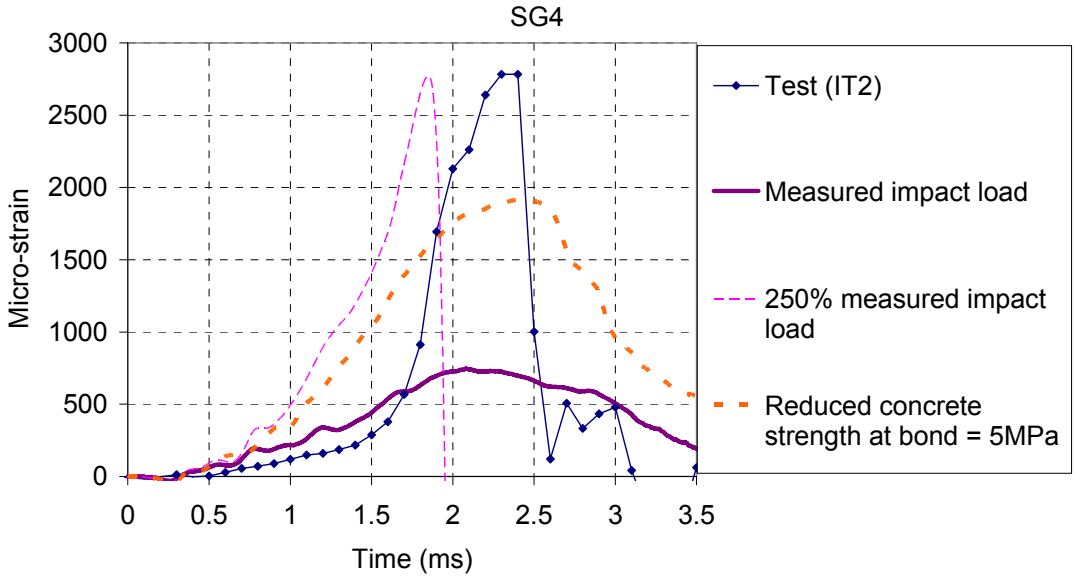

Figure 8-19 SG4 (Test, FE with measured impact load, and two total debonding cases <1> 250% measured impact load; <2> reduced concrete strength at bond = 5*MPa*)

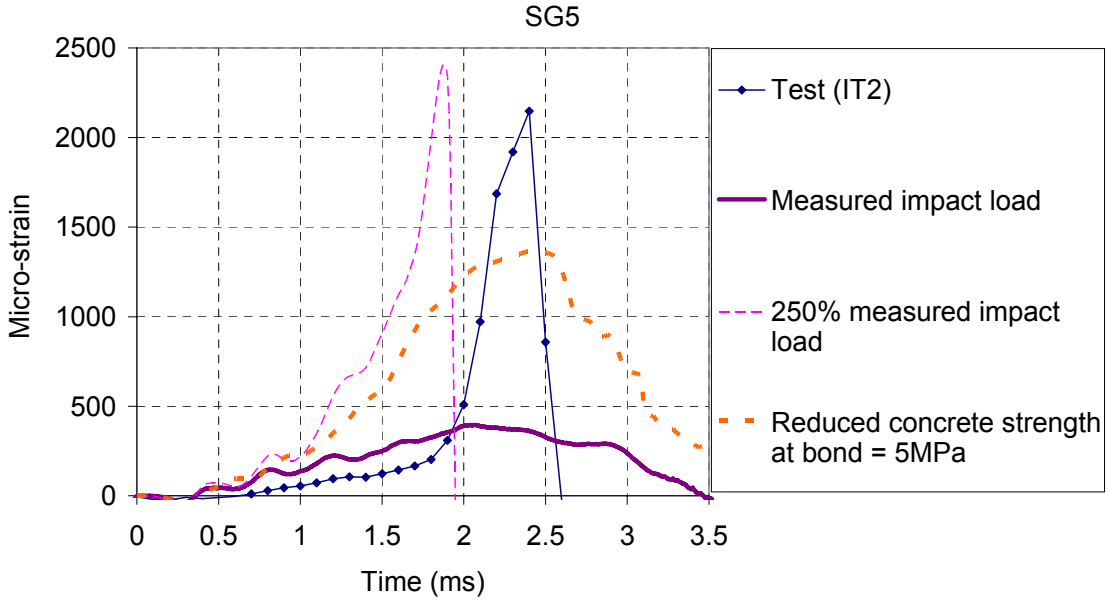

Figure 8-20 SG5 (Test, FE with measured impact load, and two total debonding cases <1> 250% measured impact load; <2> reduced concrete strength at bond = 5*MPa*)

The FE model indicates that total debonding occurs when 250% measured impact load is applied. The peak value at SG1 is higher than the test. When the concrete strength at the bond is reduced to 5 *MPa* , the peak value at SG1 is lower than the test.

Other strain time histories are also close to the test results for both cases, but the strains for the case with 250% impact load are higher than those for the case with a reduced concrete strength at the bond. These indicate that the differences of failure modes between test and FE with measured impact load may be a combination of the two reasons discussed above.

Again, effects of the DIF were also investigated via modeling impact test with and without concrete local DIF under uniformly distributed impact loading. Figure 8-21 shows the SG1 strain with and without concrete local DIF. Figure 8-22 is the damage contour comparison. It is demonstrated that concrete local DIF must be included in the FE model for impact test or else the concrete was too weak to offer enough bond strength inducing the strain peak value at SG1, not giving agreement with the test result and the damage of the specimen in FE model without concrete local DIF in Figure 8-22 was not reliable because too much shear failure occurs compared to the test (Figure 8-7).

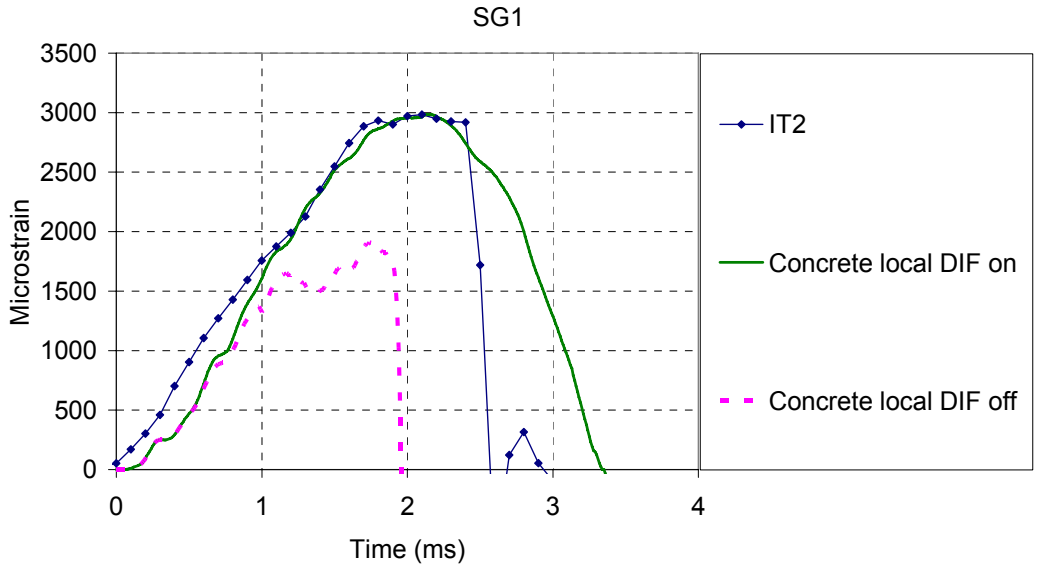

Figure 8-21 SG1 strain for IT2 (concrete local DIF on and off; mesh size 2.5*mm*)

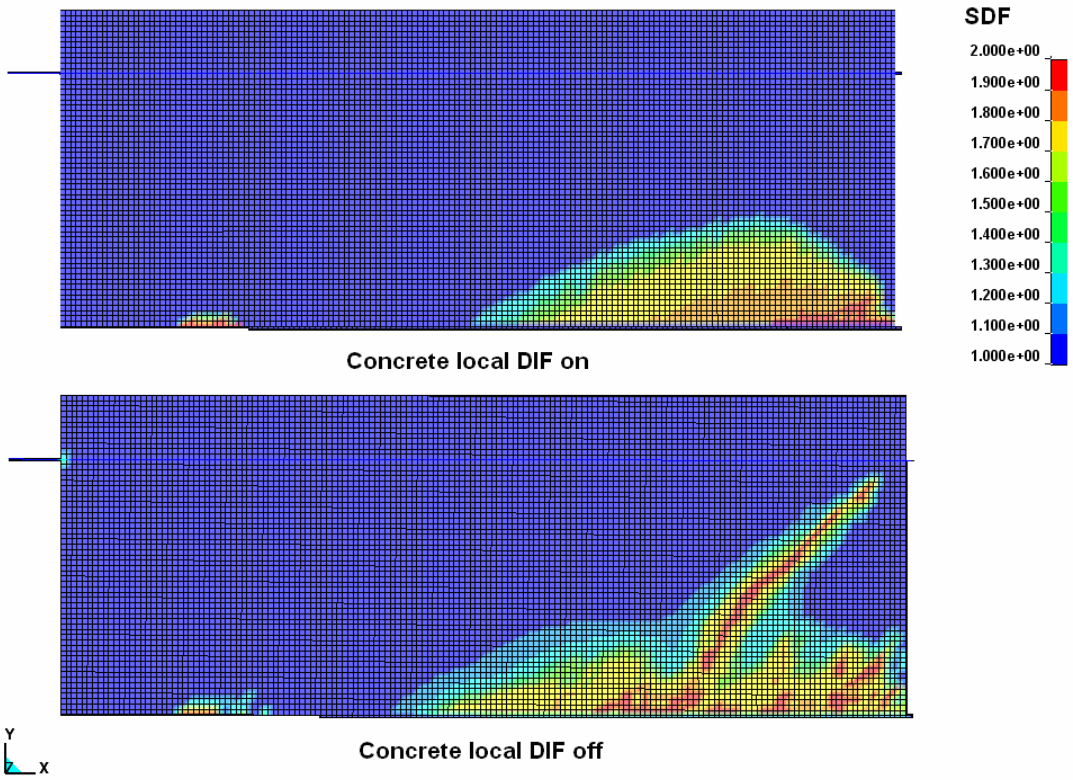

Figure 8-22 Damage contour comparison (Modelling with and without concrete local DIF; perfect bond condition)

8.4 Modelling with dynamic bond-slip model

The FE model with perfect bond assumption and mesh and rate dependent concrete local DIF gave reasonable numerical strain outputs. However from mesh convergence study that only when the element size reaches 5*mm*, mesh convergence can be achieved. The modelling is greatly restricted by computation resources as it has already been very expensive for such a half specimen with plane stress simplification (2.5 or 5*mm* elements with mesh and rate concrete local DIF), so it is difficult to be applied in modelling any larger structures.

The aim of introducing the bond-slip models is to solve this type of problems, in which larger element size can be adopted and the bond-slip mechanics can still be well performed at the same time. In this section, the dynamic bond-slip model proposed in Chapter 6 was employed. IT2 was chosen to do the mesh convergence study and compared with test and FE results with perfect bond assumption. Then all the four tests were modelled.

One thing need to be highlighted here is the failure mode of the impact tests was debonding failure not exactly in the concrete layer but with a very thin mortar attached to the FRP plate because the adhesive applied on the test specimens was very thin. It has been discussed in the former section that FE strain close to the middle gap is in agreement with the test, where debonding occurred. Meanwhile, the debonding started from the middle notch then propagated to the FRP end and from the test result it could be discovered that the debonding depth was thick enough at the middle notch there which is quite different from the other positions along the debonded FRP. Accordingly, the agreement between the SG1 readings from the test and FE was the best among all the strain gauge readings.

8.4.1 FE model

The model was the same as the previous model in Section 8.3.1, except that a layer of interface elements between concrete and FRP was employed. Two element sizes, 10*mm* and 5*mm*, were chosen for the case study to check the mesh objectivity. The elevation view of the specimen with interface element is shown in Figure 8-23.

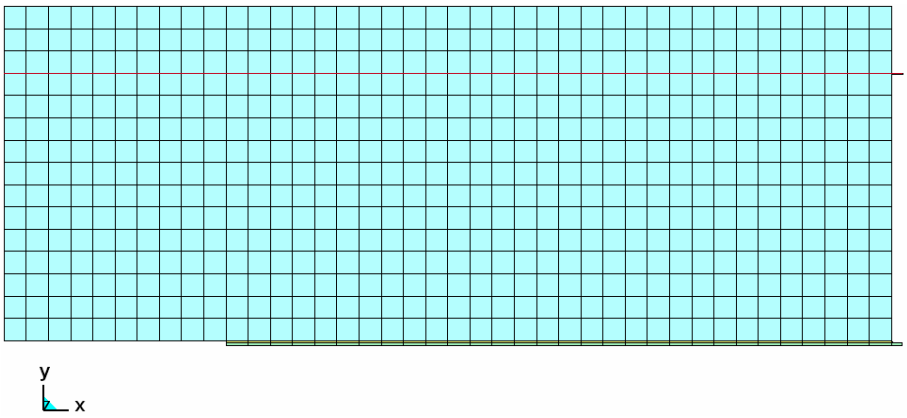

Figure 8-23 FE model with interface element (10*mm* mesh size)

8.4.2 Interface with dynamic bond-slip relationship

The application of the bond-slip relationship in FE model needs to employ an interface element, e.g. cohesive element, with material properties in shear and normal directions defined according to the bond-slip mode. The cohesive traction-separation law (Abaqus 2008; LSDYNA 2007) can be chosen to describe the constitutive mode of FRP to concrete bond interface material property. The traction-separation model assumes initially linear elastic behavior followed by the initiation and evolution of damage. A dynamic increasing proposal should be included for the cohesive element so that the slip rate effects, Mode II DIF, can be added to the static case.

The material 169 in LS-DYNA, *MAT ARUP ADHESIVE, was adopted to model the interface in this study. This material model was written for adhesive bond in aluminum structure by ARUP. The plasticity model is not volume-conserving, and hence avoids the spuriously high tensile stresses that can develop if adhesive is modeled using traditional elastic-plastic material model (LSDYNA 2007). It is assumed that the smallest dimension of the element is the through-thickens

dimension of the bond, which is dominated in the failure criteria of the material. The model has rate effects included but just two points of the states are defined, one is the static state and another is the maximum strain rate state. The material 240 in LS-DYNA, "*MAT COHESIVE MIXED MODE ELASTOPLASTIC RATE" (LSDYNA 2010) is a better choice as its rate effects function related to the strain rate/ slip rate is a logarithmic relationship which match the current proposed dynamic bond-slip relationship in Chapter 6 better. However, this material model is only available for LS-DYNA version 5 or higher. The new LS-DYNA package 5.1.1 requires the license support from higher version ANSYS 13.0, but it is not available at the School of the University of Edinburgh. Therefore the DIF versus slip rate equation presented in Chapter 6 could not be employed. Instead, the simpler rate effects model, "*MAT ARUP ADHESIVE", was chosen.

The peak stress and fracture energies in shear and normal directions can be chosen as functions of an equivalent strain rate $\dot{\varepsilon}_{eq}$. It is presented by:

$$\dot{\varepsilon}_{eq} = \frac{\sqrt{\dot{u}_1^2 + \dot{u}_2^2 + \dot{u}_3^2}}{t} \tag{8-3}$$

$\dot{u}_1, \dot{u}_2$ and $\dot{u}_3$ are the velocities in the normal and two shear directions. Here if the thickness of the cohesive element t is set to 1, the equivalent strain rate $\dot{\varepsilon}_{eq}$ is equal to the slip rate $\dot{s}$. Then the DIF curve of which the variable is slip rate can be successfully introduced. The properties for the interface element in the directions are defined as follows.

8.4.2.1 Shear mode (Mode II)

The initial shear stiffness of the bond-slip model as defined by Lu et al. (2005) is:

$$K_G = K_{aG}K_{cG}/(K_{aG} + K_{cG}) \tag{8-4}$$

where $K_{aG} = G_a / t_a$ and $K_{cG} = G_c / t_c$. G_a and G_c are the shear modulus of the adhesive and concrete respectively, t_a is the thickness of the adhesive, which can also has a general range of 2 to 3mm, t_c is the depth of the debonding zone adjacent to the adhesive and FRP in the concrete, which may be taken as 10mm as in Lu et al. (2005). In the current numerical model, $K_{aG} = G_a / t_a$=5GPa/mm and t_c=10mm.

The shear modulus input for the Mode II of the interface element is:

$$G = K_G t \tag{8-5}$$

where t is the numerical thickness of the interface element. It has physical meaning only if when $t = t_{physic}$, where the physic thickness (Equation (8-6)):

$$t_{physic} = \frac{t_a t_c}{t_a + t_c} \tag{8-6}$$

The damage evolution can be controlled by the energy; the static fracture energy is used as the basement from Equation (6-11) in Chapter 6.

8.4.2.2 Normal mode (Mode I)

The Young's modulus of adhesive E_a, Young's modulus of concrete E_c, Poisson's ratio for adhesive υ_a, Poisson's ratio for concrete υ_c and t_a were known values. The normal elastic initial stiffness can be obtained from:

$$K_E = K_{aE} K_{cE} /(K_{aE} + K_{cE}) \tag{8-9}$$

where $K_{aE} = E_a / t_a$ and $K_{cE} = E_c / t_c$. The Young's modulus input for the Mode I of the interface material is:

$$E = K_E t \tag{8-10}$$

Damage evolution based on energy is also used in the normal direction. Because for debonding failure mode damage always happens in the concrete layer, the static fracture energy G_{fs}^I is the static fracture energy of the concrete according to CEB-FIP (1990):

$$G_{fs}^I = 0.03\left(\frac{f_c^{'}}{10}\right)^{0.7} \tag{8-11}$$

8.4.2.3 DIF for dynamic bond-slip model

In this study, the static slip rate was set as $1\times10^{-7} m/s$ and the maximum dynamic slip rate $1 m/s$. The "$1 m/s$" is sufficient as the upper limit of the slip rate, as the

strain rate measurement from the test is approximately $1\times10^{-3}\ s^{-1}$ (Figure 8-24). The total bond length is $300\,mm$. So the slip rate should be approximately no more than $0.3\,m/s$ if the relative slip at the free end of the FRP is negligible.

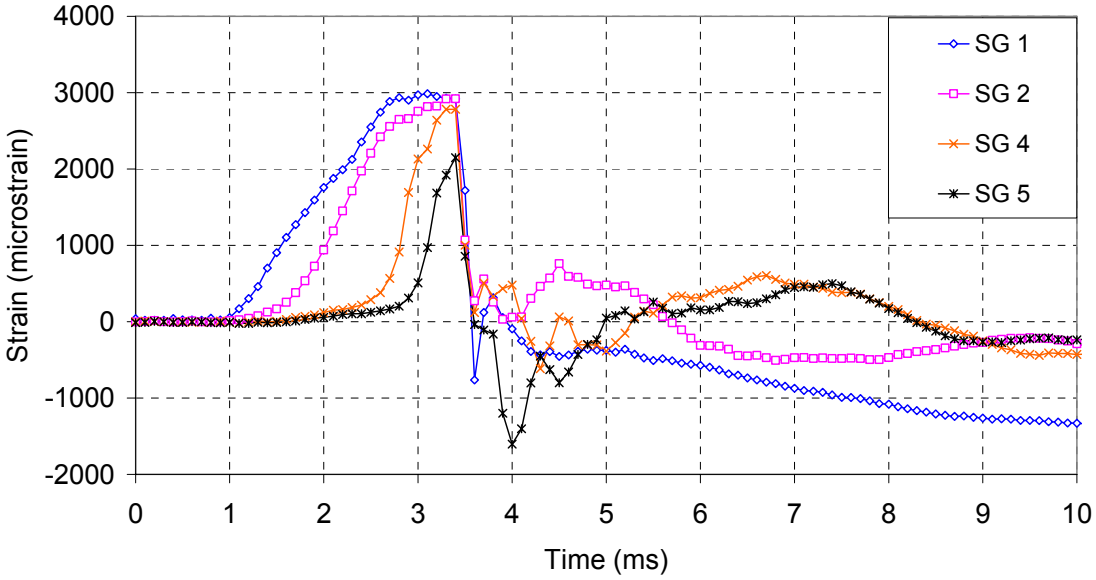

Figure 8-24 Impact strain measurement time history (IT2_100*mm* drop height)

According to Equations (6-6) to (6-10) in Chapter 6, the DIF factor at the slip rate is:

$$\alpha_{DIF} = \alpha \ln\left(\frac{\dot{s}}{\dot{s}_s}\right)+1 = 0.123\times\left(\frac{25}{10}\right)^{-0.8}\ln\left(\frac{1}{1\times10^{-7}}\right)+1 = 1.95 \qquad (8\text{-}12)$$

8.4.3 FE results

The FE predictions of strain at SG1 for IT 2 are compared in Figure 8-25.

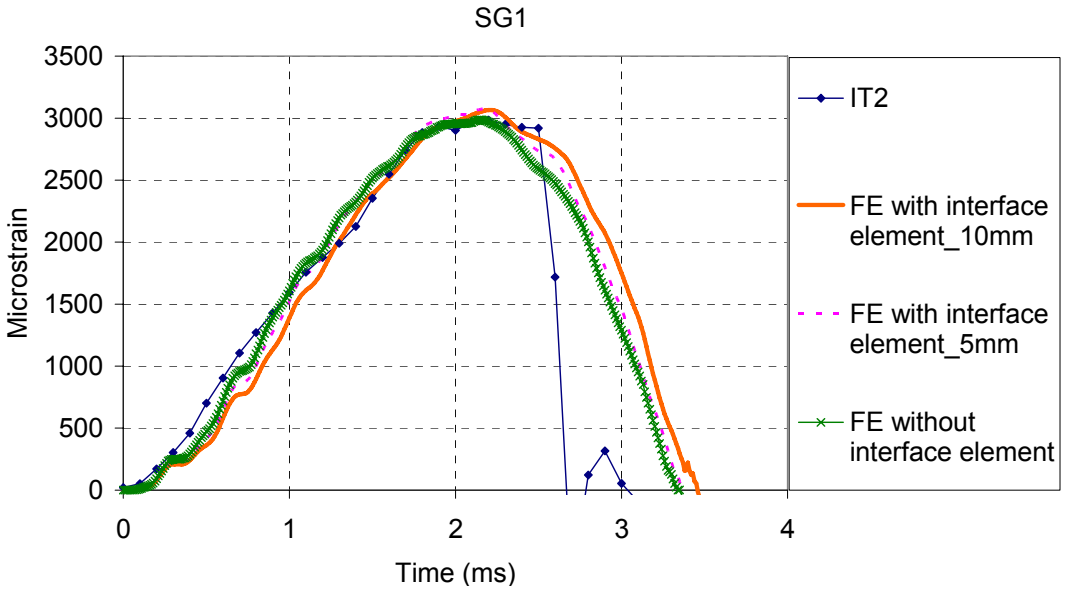

Figure 8-25 Strain at SG1 for IT2 (element size for FE with interface element is 10*mm* and for FE without interface element is 2.5*mm*)

Clearly SG1 maximum value from the FE model with dynamic bond slip model applied together with interface elements with 10*mm* and 5*mm* element size is very close to the results from the FE model without interface element but with mesh and rate dependent concrete local DIF with 2.5*mm* element size. This indicates that mesh convergence is achieved and the dynamic bond slip model proposed with "*MAT ARUP ADHESIVE" worked well with larger element sizes. The maximum strain readings for all the strain gauges are shown in Table 8-3.

Table 8-3 Peak strain comparison: FE model with interface element (Unit: $\mu\varepsilon$)

	SG1	SG2	SG3	SG4	SG5
Test IT2	3000	2918	N/A	2783	2147
FE without interface elements (fine mesh)	3000	2000	1212	726	384
FE with interface element (10*mm* mesh)	3065	2293	1431	843	462

Table 8-3 indicates that the strain gauge reading from the macro-scale FE model with interface element was slightly higher than the value reading from the meso-scale FE model without interface element due to the damage pattern difference of the two cases. However the difference is not too much and the strains at the same locations are at the same scale for the two.

Also the same simulations were done for the rest of the 3 tests. The measured impact load time histories are presented in Section 7.5. The impact test peak loads measured are listed in Table 8-4. The modelling results compared with test data are given in Figure 8-26, Figure 8-27, Figure 8-28, Figure 8-29 and Table 8-5.

Table 8-4 Impact test peak loads measured

	IT1	IT2	IT3	IT4
Peak value of impact load measured (kN)	58	35	262	158

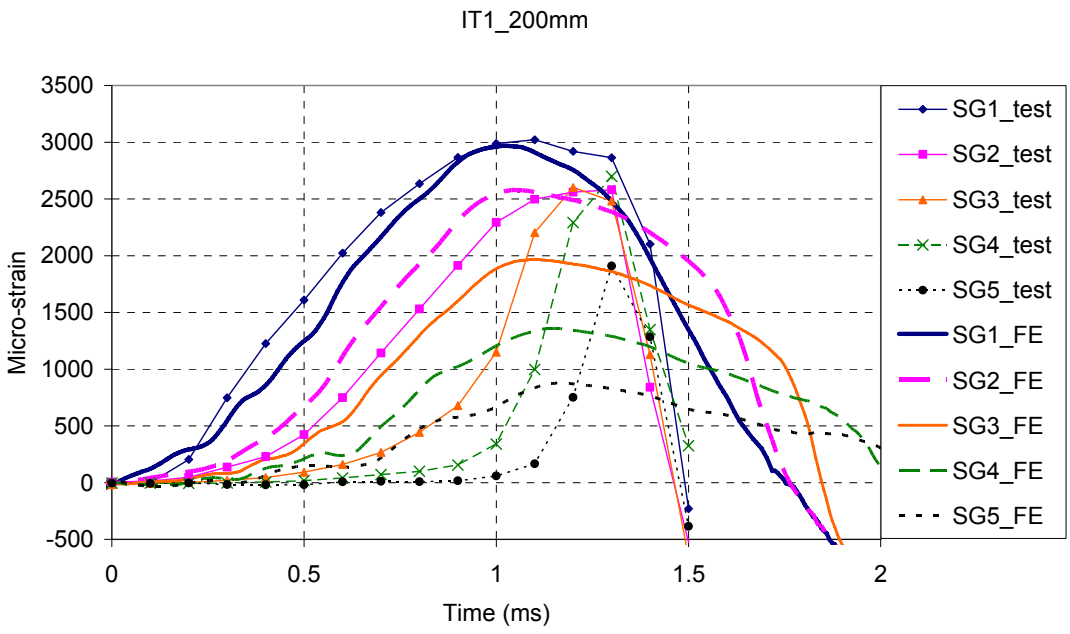

Figure 8-26 Strain comparisons: FE versus Test (IT1)

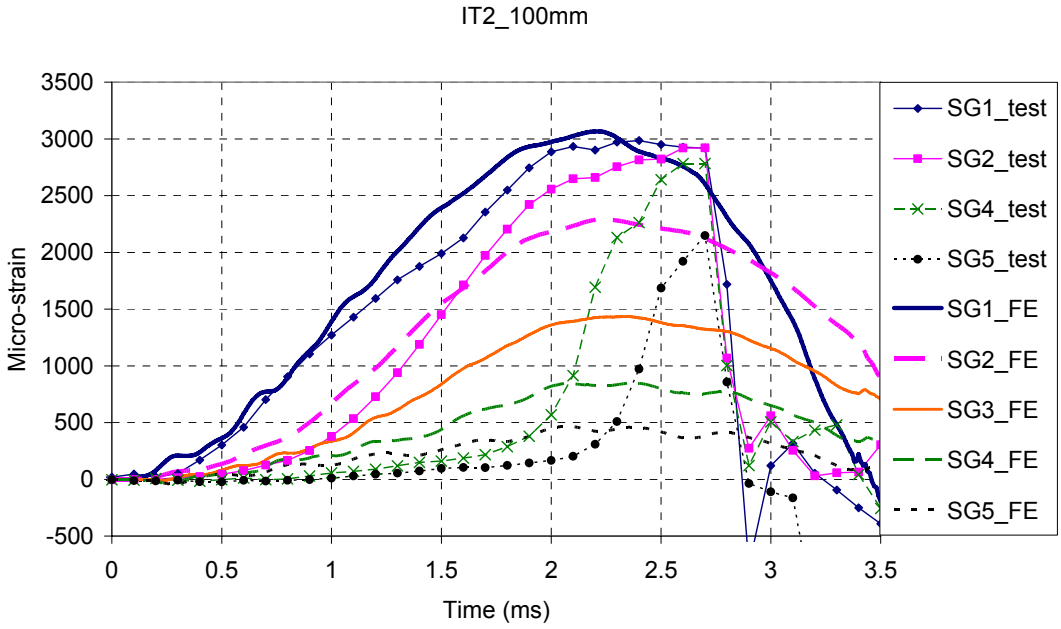

Figure 8-27 Strain comparisons: FE versus Test (IT2) (SG3 test data missing)

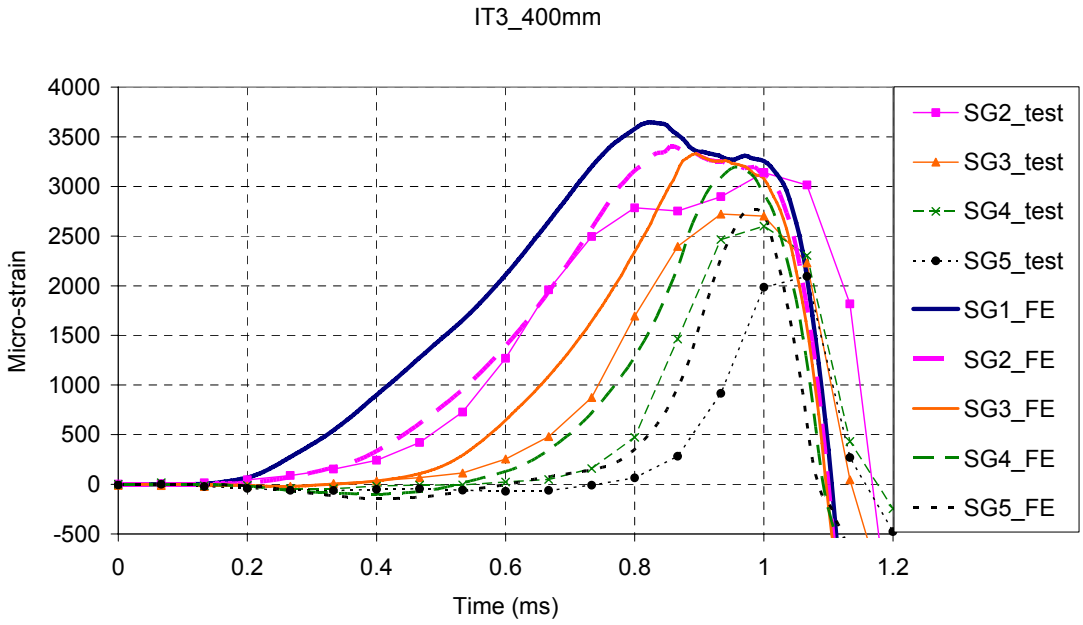

Figure 8-28 Strain comparisons: FE versus Test (IT3) (SG1 test data missing)

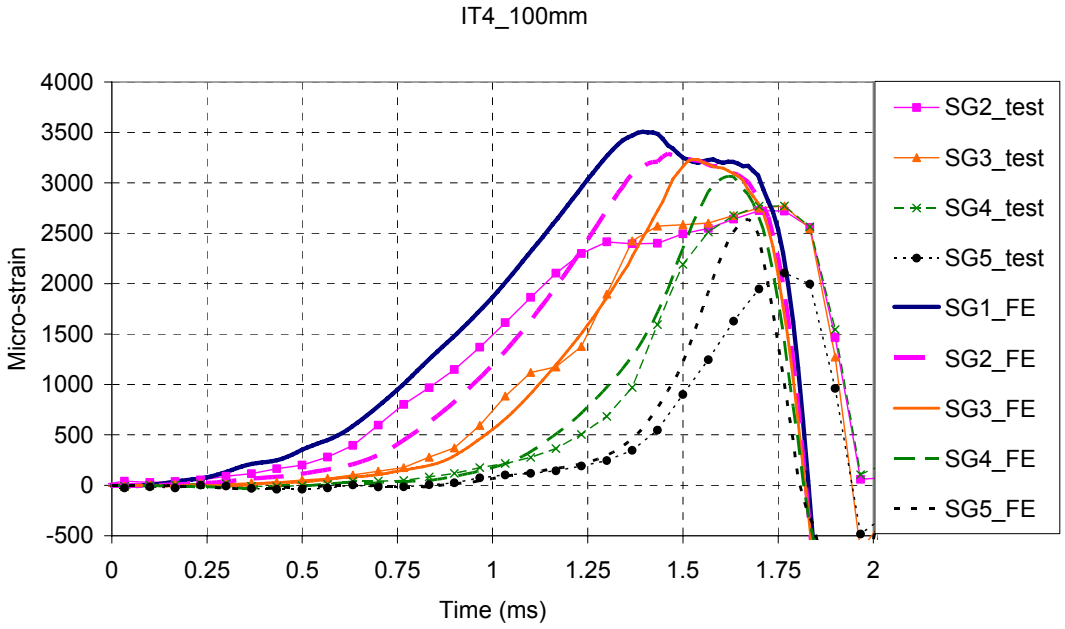

Figure 8-29 Strain comparisons: FE versus Test (IT4) (SG1 data missing)

Table 8-5 Strain peak value comparison (Test Vs. FE model; Unit: $\mu\varepsilon$)

		SG1	SG2	SG3	SG4	SG5
IT1	Test	3021	2581	2560	2560	1909
	FE	3000	2578	1963	1358	867
IT2	Test	2996	2918	N/A	2783	2147
	FE	3065	2293	1431	843	462
IT3	Test	N/A	3141	2720	2601	2095
	FE	3641	3364	3260	3130	2764
IT4	Test	N/A	2770	2770	2720	2105
	FE	3500	3271	3233	3065	2637

The results are in reasonable agreement both in the slops of the curves and the peak values to the test results at locations where debonding occur, especially at SG1 for all the tests as the debonding starts here.

As presented in Table 8-4 and Table 8-5, for tests IT1 and IT2, the peak value of the impact force was lower than $60\,kN$, and total debonding did not occur in FE model but happened in real test due to the poor surface treatment or inaccuracy of the load measurements. As a result, only SG1 peak values are close to the test results, for SG2 to SG5 the FE strain peak value are all lower than test measurements. However, for IT3 and IT4, of which the peak value of the impact force were higher than $150\,kN$, total debonding happened in both FE and experiments, for SG2 to SG5 the strain peak values from FE are all higher than the test results. This is another evidence of the interface did not offer enough bond in the test due to the poor application. In numerical modelling the interface element definition was based on good bond condition leading to debonding happens in the concrete layer adjacent to the FRP. Though the peak value does not match the tests perfectly but at the same scale, the slop performs quite well (Figure 8-28 and Figure 8-29), indicating the strain rates at the interface elements were well captured.

8.5 Conclusions

This chapter has presented a study on the FE modelling of the impact tests. A typical specimen was first modelled using two options: 1) explicitly including the striker in

the model and 2) without including the striker but use the measured impact load directly. It was concluded that explicitly modelling the striker does not produce satisfactory predictions because of the complex impact behaviour at the striker-specimen interface. The measured impact load time history was therefore used in the modelling. A mesh convergence analysis was also conduced.

The FE predictions of test IT2 indicated possible errors in load measurements and improper surface treatment in the tests, resulting in that total debonding occurred in the test but not in the numerical simulations. However the FE predicted strain at SG1, where debonding occurred in both test and FE, was in good agreement with the test observation.

The predictions with and without concrete local DIF in the model with a striker showed that when the DIF is not considered, the strain-time history is far too low compared with the test. It has been concluded that only when concrete local DIF is considered, the predictions can give good match with the test results. If the DIF is not considered, the predictions are too low and the damage pattern does not match the test.

The dynamic bond-slip model was also implemented into the model and the mesh convergence was achieved at 10*mm*. The results are in reasonable good agreement in terms of both the slops of the curves and the peak values with test results at locations where debonding occur.

8.6 References

Buchana, P.A. and Chen, J.F. (2007), “Blast resistance of FRP composites and polymer strengthened concrete and masonry structures – A state-of-the-art review”, *Composites Part B: Engineering*, 38(5-6):509-522.

Camanho, P.P. and Davila, C.G. (2002), "Mixed-mode decohesion finite elements for the simulation of delamination in composite materials”, *NASA Technical Paper*, 211737: 42.

CEB-FIP (1993), Model Code 90. Lausanne.

Chen, J.F. and Teng, J.G. (2001), "Anchorage strength models for FRP and steel plates bonded to concrete", *Journal of Structural Engineering, ASCE,* 127(7):784–791.

Du, J., Yon, J.H., Hawkins, N.M., Arakawa, K. and Kobayashi, A.S. (1992), “Fracture process zone for concrete for dynamic loading”, *ACI Materials Journal*, 89: 252-258.

Erki, M.A. and Meier, U. (1999), “Impact loading of concrete beams externally strengthened with CFRP laminates”, *Journal of Composites for Construction*, 3(3):117-125.

Hughes, G. and Speirs, D.M. (1982), An Investigation of The Beam Impact Problem,Wexham Springs,Cement and Concrete Association, ISBN0 7210 12469.

Kabir, M.Z. and Shafei, E. (2009), “Analytical and numerical study of FRP retrofitted RC beams under low velocity impact”, *Transaction A: Civil Engineering*, 16(5): 415-428.

LSDYNA (2007), Keyword User’s Manual Version 971, Livermore Software Technology Corporation.

LSDYNA (2010), Keyword User's Manual Version 971/Rev 5, Livermore Software Technology Corporation.

Lu, Y.B. and Li, Q.M. (2011), "About the dynamic uniaxial tensile strength of concrete-like material", *International journal of impact engineering*, 38: 171-180.

Lu, X.Z., Teng, J.G., Ye, L.P. and Jiang, J.J. (2005), "Bond–slip models for FRP sheets/plates bonded to concrete", *Engineering Structures*, 27:920–937.

Lu, X.Z., Ye, L.P., Teng, J.G. and Jiang, J.J. (2004). "Mesco-scale finite element model for FRP sheets/plates bonded to concrete", *Engineering structures*, 27:564-575.

Ross C.A. (1989), Split-Hopkinson pressure bar tests. Final Report, Air Force Engineering and Services Center, Tyndall AFB, Fl, ESL-TR-88-82.

Ross, C.A., Thompson, P.Y., and Tedesco, J.W. (1990), "Split-Hopkinson Pressure-Bar tests on Concrete and Mortar in Tension and Compression", *Materials Journal*, 86(5): 475-481.

Sharon, E., Gross, S.P. and Fineberg, J. (1996), "Energy Dissipation in Dynamic Fracture", *Phys Rev Lett*. 76(12):2117-2120.

Su, X.T., Yang, Z.J. and Liu, G. (2010), "Finite element modelling of complex 3D static and dynamic crack propagation by embedding cohesive elements in ABAQUS", *Acta Mechanica Solida Sinica*, 23(3): 271-282.

Subramaniama, K.V., Ali-Ahmadb, M. and Ghosn, M. (2008), "Freeze–thaw degradation of FRP–concrete interface: Impact on cohesive fracture response", *Engineering Fracture Mechanics*, 75(13): 3924-3940.

Tang, T.P. and Saadatmanesh, H. (2003),"Behavior of Concrete Beams Strengthened with Fiber-Reinforced Polymer Laminates under Impact Loading", *Journal of Composites for Construction*, 7(3):209-219.

Tedesco, J.W., Ross, C.A. and Brunair, R.M. (1989), "Numerical analysis of dynamic split cylinder tests", *Comput. Struct*., 32: 609-624.

Tedesco, J.W., Ross, C.A., McGill, P.B. and O'Neil B.P. (1991), "Numerical analysis of high strain rate concrete direct tension tests", *Computers& structures*, 40(2): 313-327.

White, T.W., Soudki, K.A. and Erki, M.A. (2001), "Response of RC Beams Strengthened with CFRP Laminates and Subjected to a High Rate of Loading", *Journal of Composites for Construction*, 5(3):153-162.

Wu, C., Oehlers, D.J., Rebentrost, M., Leach, J. and Whittaker, A.S. (2009), "Blast testing of ultra-high performance fibre and FRP-retrofitted concrete slabs", *Engineering Structures*, 31(9): 2060-2069.

Chapter 9 Modelling of FRP strengthened concrete slabs under blast

9.1 Introduction

The modelling of impact tests presented in Chapter 8 indicates that reasonable numerical results can be achieved under an impact loading condition with employing the proposed mesh and rate dependent concrete local DIF (Chapter 5) and dynamic bond slip model (Chapter 6). The aim of this Chapter is to further investigate into the numerical simulation under blast and evaluate the effectiveness of the proposed concrete local DIF and dynamic bond-slip models in such loading conditions.

A review of blast resistance of fibre reinforcement polymer (FRP) strengthened concrete structures was conducted by Buchan and Chen (2007) comprehensively demonstrates that FRP and polymer retrofitting can significantly increase the blast resistance of a structure through increasing the strength and suppressing fragmentation. More recent FRP blast protection research on concrete structures (e.g. Nam et al. 2009a ; Nam et al. 2009b; Razaqpur et al. 2007; Razaqpur et al. 2009; Wu et al. 2009a; Wu et al. 2009b) also indicate the FRP strengthening is effective on improving the resistance of the test specimens as compared with the ones without FRP strengthening. Despite the overall effectiveness, debonding failure has normally

been observed in the experiment, and this shows that the bond behaviour is critical for blast protection. However, much of the existing research has been rather qualitative when comes to the detailed mechanisms of FRP strengthened structures under blast loading. For example, even in a very recent numerical simulation conducted by Nam et al. (2010), modelling of bond-slip is still limited to a simple model proposed by De Lorenzis and La Tegola (2005) with various simplifications (see details in Chapter 6), which only has a linear elastic hardening part without consideration of softening.

In the present numerical study, the concrete local DIF and a dynamic bond-slip model as described in the previous chapters are employed. An experimental case involving reinforced concrete slabs, without and with strengthening by externally applied FRP plates, under blast load is chosen for the numerical simulation. The experiment was conducted by Wu et al. (2009a), and the response of the specimens was generally in a global bending mode and thus is considered to be suitable for an examination concerning the simulation of the dynamic bond behaviour. The effect of involving concrete local DIF as proposed in this chapter is firstly examined from the simulation of the reinforced concrete slab without FRP. Subsequently, the application of dynamic bond-slip model is evaluated from modelling the FRP retrofitted slab. In the last part, a numerical parametric study is presented and discussed regarding the effects of FRP for blast-resistant strengthening.

9.2 2D numerical simplification

9.2.1 Experimental cases considered

The test set-up of the benchmark experiment considered herein (Wu et al. 2009a), including the support boundary condition is shown in Figure 9-1. The test slab was supported with pins at the two short ends, while the two long sides were un-supported, resulting in a one way slab boundary condition. The explosive charge was positioned right above the centre of the mid-span. Different charge sizes and stand-off distances were considered in different tests.

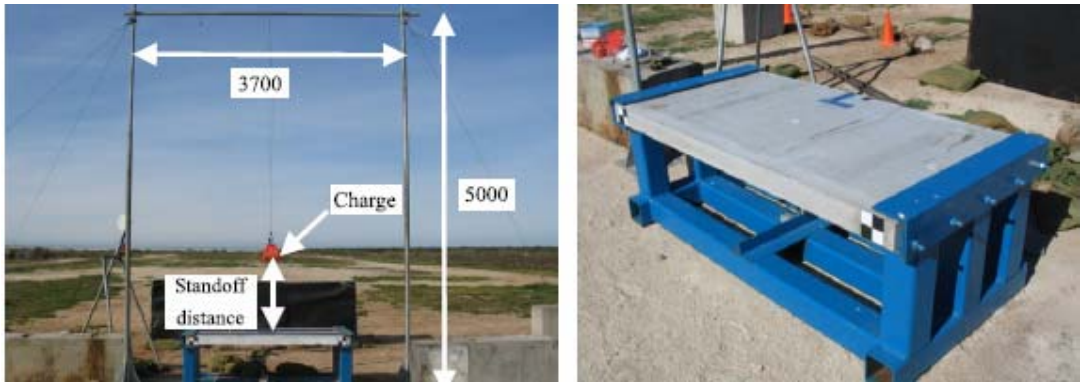

Figure 9-1 Charge support frame and test fixture (Unit: *mm*) (Wu et al 2009a)

The specimen details are shown in Figure 9-2. These specimens were reinforced with double steel meshes of 12*mm* diameter and spacing at 100*mm* in the major bending plane and 200*mm* in the minor plane, respectively. The thickness of the concrete cover was 10*mm*. The concrete had a cylinder compressive strength of 39.5 *MPa* . The reinforcement had yield strength of 600 *MPa* and Young's modulus of 200 *GPa* . For the strengthened specimens, externally bonded FRP plates were adhesively

bonded to the compression face of the slab. Layers of 2.8*mm*-thick CFRP plates were used to strengthen the specimens.

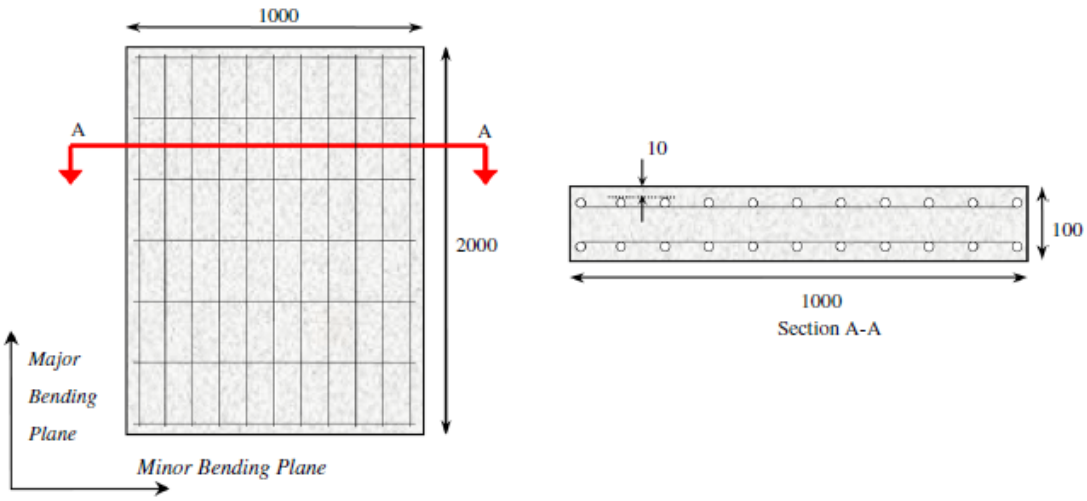

Figure 9-2 Geometry of the specimens (Unit: *mm*) (Wu et al. 2009a)

9.2.2 Basic modeling considerations

To fully capture the bending behaviour is an important requirement for the present modelling study. Considering that in the present FE model K&C concrete damage model and 8-node hexahedral solid elements in LS-DYNA are to be used, and based on the previous experiences (Wu et al. 2009b; White et al. 2001), a minimum of 10 layers is considered to be appropriate in the slab thickness direction.

To ensure an affordable computational cost for the modelling of the full-size test slab, a simplified 2D axial symmetric simulation is adopted. Previous numerical studies (Zhou and Hao 2007; Lu et al. 2005) tend to indicate that modelling the initial detonation and propagation of the hemi-spherical blast wave using a 2D axis-symmetric simulation is good enough as compared with a full 3D simulation.

For the current model, the blast was generated by a point charge in the test. When modelling an air zone with a point charge using the 2D axis-symmetric model, the air zone is equivalent to a cylinder. According to the one way slab boundary support condition in reality, the simplified 2D slab slice put in the 2D axial symmetric air zone was treated as plane stress boundary condition. The current 2D axial symmetric simulation can only estimate the behaviour of the centre cut section of the slab.

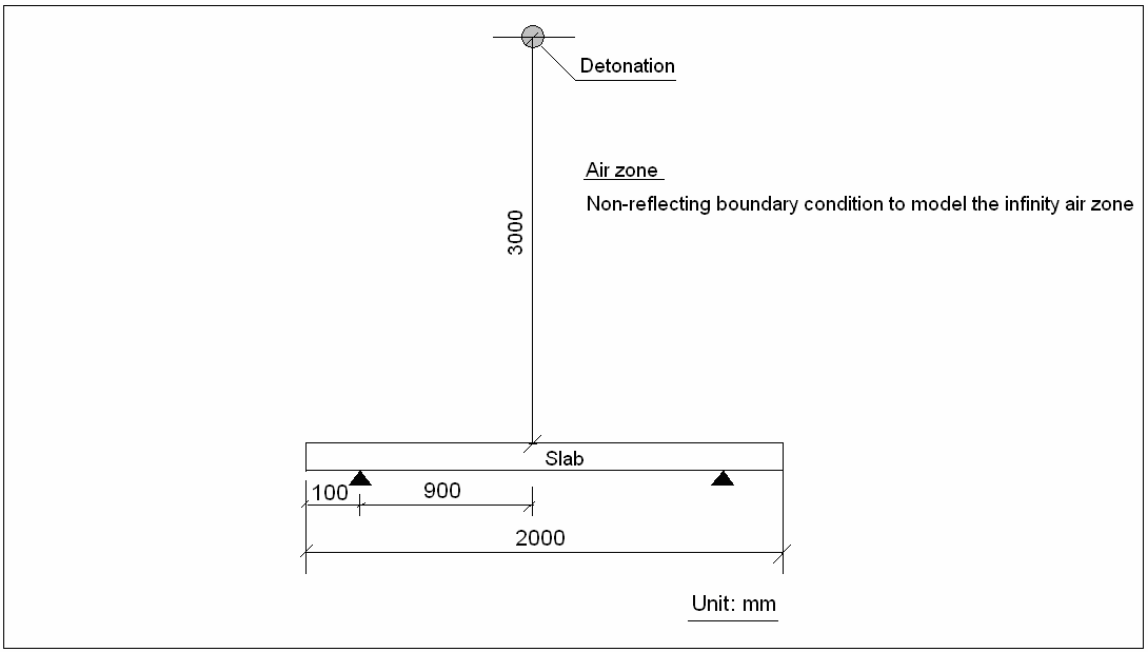

Figure 9-3 2D axial symmetric model sketch for concrete slab under blast load

9.3 Blast test modelling for reinforced concrete slab

9.3.1 FE model for RC slab without FRP

The blast test of the reinforced concrete slab, without FRP, is firstly modeled for a mesh convergence study. K&C concrete damage model together with the concrete local DIF presented in Chapter 5 is employed.

Beam elements are chosen for modeling the steel reinforcement bars. The cross section definition for the 2D axial symmetric model is based on an area equivalence which is same as the simplification considered in Chapter 8 (Figure 8-2). The plastic kinematical material model is selected to model the steel, for which the density is $7.8\times10^{3}\,kg/m^{3}$, the elastic Young's modulus is $200\,GPa$, the Poisson's ratio is 0.3 and the yield stress is $600\,MPa$. In the FE model, the steel reinforcement is assumed to be perfectly bonded to the concrete.

Two tests described in Wu et al. (2009a) are considered herein, namely Slab NRC-1 tested with a charge of $1007\,g$ (TNT equivalent) at a standoff distance $3.0\,m$, and NRC-2 with $8139\,g$ TNT at the same standoff distance are modelled. Three different mesh sizes, namely $10mm$, $5mm$ and $2.5mm$, corresponding respectively to 10 layers, 20 layers and 40 layers of division through the slab thickness, are examined.

Coupling between the air and the solid slab is realized using the coupling mechanism for modeling fluid-structure interaction (FSI), i.e. *CONSTRAINED_LAGRANGE_IN_SOLID, in the numerical simulation. The structure is constructed from Lagrange solid entities to the multi-material fluids. Air and high explosive material (TNT) are modeled by ALE formulation with an Euler processor. Air is modeled by an ideal gas

equation of state, of which the pressure is related to the energy by Equation (9-1) (LSDYNA 2007).

$$p = (\gamma - 1)\rho e \tag{9-1}$$

where γ is a constant which is equal to 1.4 for ideal gas; ρ is the density which is equal to 1.225 kg/m^3; e is the air initial internal energy equal to 2.086×10^5 kJ/kg.

High explosives are typically modeled by using the Jones–Wilkins–Lee (JWL) equation of state, which models the pressure generated by chemical energy in an explosion. It can be written in the form (LSDYNA 2007):

$$p = A(1-\frac{\omega}{R_1 v})e^{-R_1 v} + B(1-\frac{\omega}{R_2 v})e^{-R_2 v} + \frac{\omega E}{v} \tag{9-2}$$

where p is the hydrostatic pressure; v is the specific volume; E is the specific internal energy; A, B, R_1, R_2 and ω are explosive material constant. For TNT, the following parameters are valid (Dobrazt and Crawford 1985): the density ρ_0 =1590 kg/m^3; A =371.20 GPa; B =3.231 GPa; R_1 =4.15; R_2 =0.95; ω =0.3; E_0 = 6.0 kJ/cc; also for TNT material definitions the detonation velocity D =6930 m/s; Chapman-Jouguet pressure P_{CJ} = 21.0GPa.

It is useful to note that the most widely used approach for blast wave scaling is Hopkinson's law (Baker et al. 1983) which establishes that similar explosive waves are produced at identical scaled distances when two different charges of the same

explosive and with the same geometry are detonated in the same atmosphere. Thus, any distance R from an explosive charge W in kilograms of TNT can be transformed into a characteristic scaled distance Z in meters presented in Equation (9-3).

$$Z = R / W^{1/3} \tag{9-3}$$

9.3.2 FE results and discussion

The reflected pressure wave at the mid-span and 20*mm* away from the support are compared with the test measurements to check whether the air pressures due to the corresponding TNT charges and stand off distances are properly modelled in the numerical simulation. Figure 9-4 shows the pressure transducer (PT) locations. Figure 9-5 presents comparisons between the computed and measured results for the reflected pressure time histories at mid-span (PT1) and the location 20*mm* away from the support (PT2) for test for NCR-1.

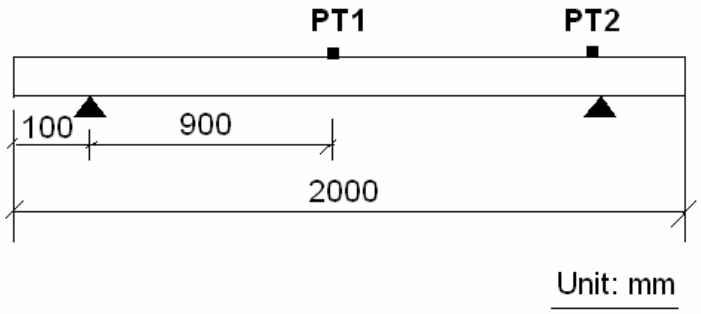

Figure 9-4 Pressure transducer (PT) locations

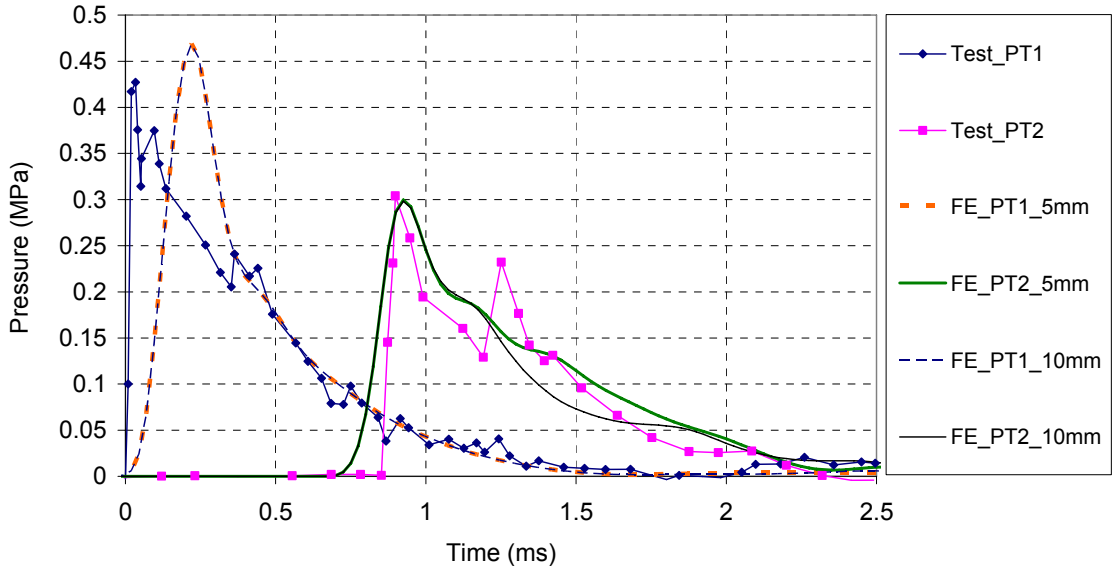

Figure 9-5 Comparison of computed and measure reflected pressure time histories for NCR-1 at mid-span(PT1) and 20mm away from the support (PT2) (10*mm* mesh size and 5*mm* mesh sizes)

From Figure 9-5, it can be observed that the mesh size of the concrete slab has little effect on the reflected wave, and the FE pressure time histories at the two locations compare reasonably well with the test results.

The slab mid-span deflection time histories obtained using different mesh sizes for NCR-1 are compared with the test results in Figure 9-6. It can be observed clearly that, even though the reflected pressure time histories are almost identical (Figure 9-5), using a 10-layers division (10*mm* mesh size) through the thickness is not sufficient enough. Satisfactory mesh convergence is achieved at 5*mm* element size (20 layers of elements division). Therefore, the rest of the FE analysis is carried out with this element size.

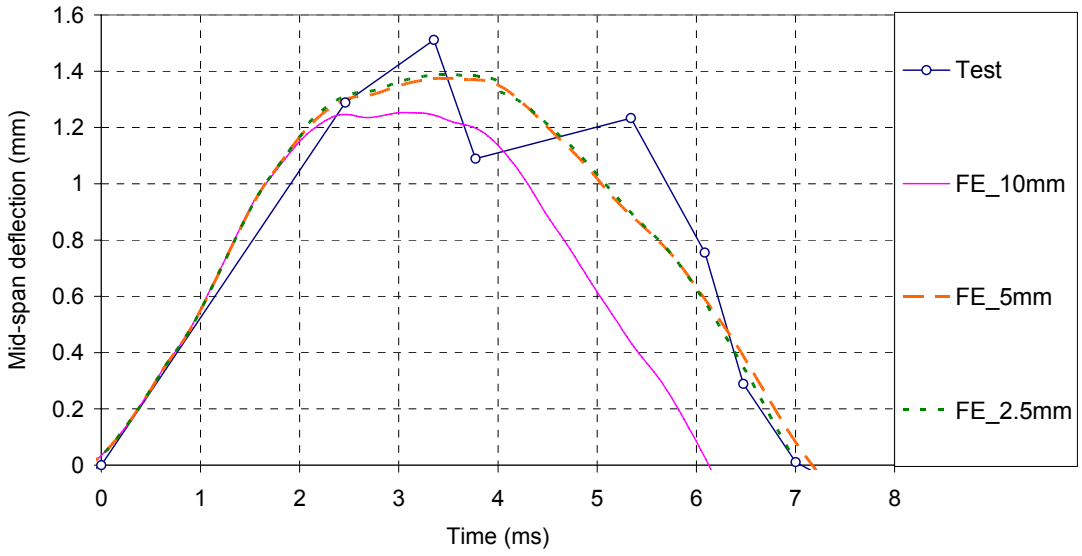

Figure 9-6 Mid-span deflection time history comparison for layered capacity analysis NCR-1 (with concrete local DIF applied)

Following the mesh convergence study, a comparison of the computed deflections with and without considering the concrete local DIF is presented in Figure 9-7.

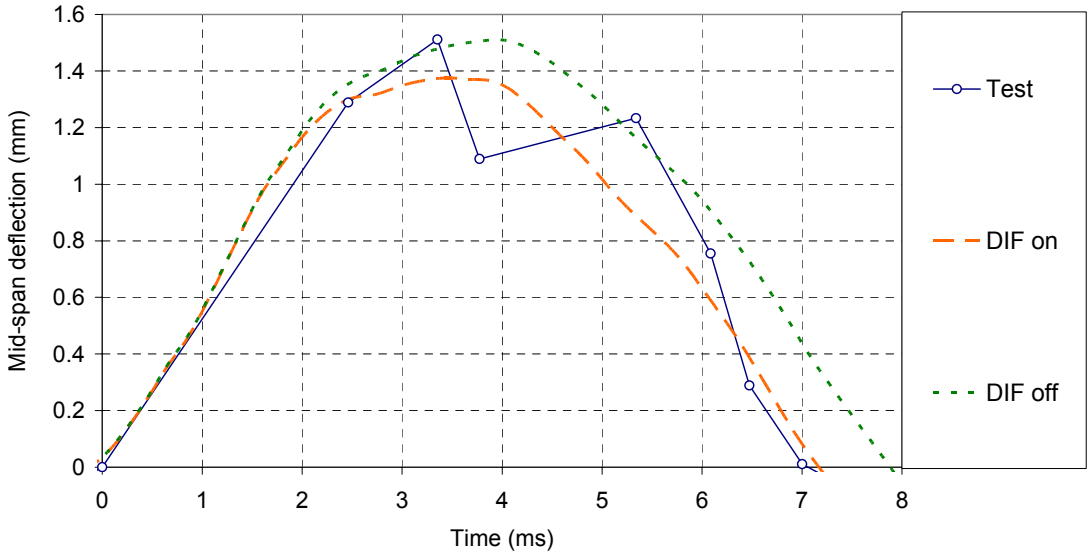

Figure 9-7 Mid-span deflection time histories for NCR-1 (With and without concrete local DIF)

From this comparison, it is difficult to observe the effect of considering or not considering the DIF, and this is because the blast loading with a maximum

overpressure of 0.45*MPa* is low for NCR-1. From the numerical results the beam still behaves nearly linear elastic and most of the stress distribution of the concrete for NCR-1 is still lower than its static tensile strength and the plastic strain in the critical regions is small. This situation can be checked from the scaled damage factor *SDF* contour for NCR-1 when the maximum mid-span deflection is reached, see in Figure 9-8. *SDF* is the scaled damage factor for the concrete model, which is a function of the effective plastic strain. "0< *SDF* <1"means no damage, "*SDF* >1" damage with material softening, and "*SDF* =2" full damage.

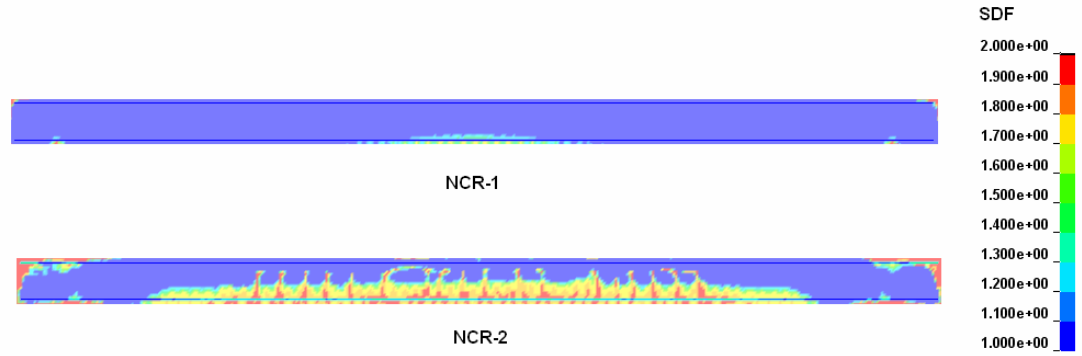

Figure 9-8 Scaled damage (*SDF*) contour of NCR-1 and NCR-2 at maximum mid-span deflection with mesh &rate dependent concrete local DIF

Another case, NCR-2, with a smaller scaled distance of 1.5 $m/kg^{1/3}$ is modelled and its *SDF* contour is plotted in Figure 9-8 as well. Comparing to NCR-1 where little damage occurs, NCR-2 exhibits much more significant damage. The pressure time histories for NCR-2 are shown in Figure 9-9 and the comparison of the maximum deflections with and without concrete local DIF is given in Figure 9-10.

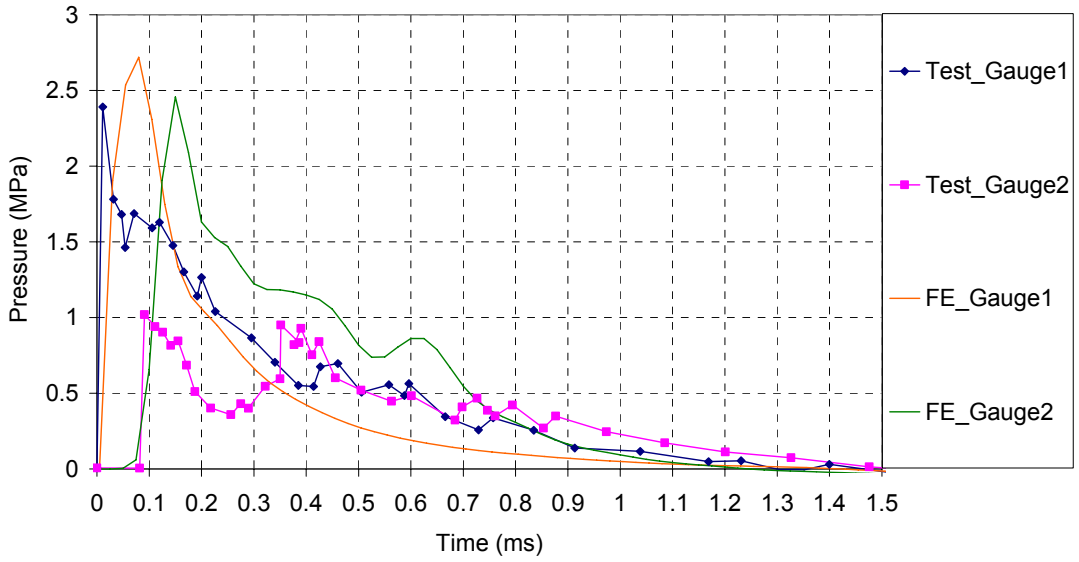

Figure 9-9 Reflected pressure time history comparison for NCR-2 at mid-span (PT1) and 20*mm* away from the support (PT 2)

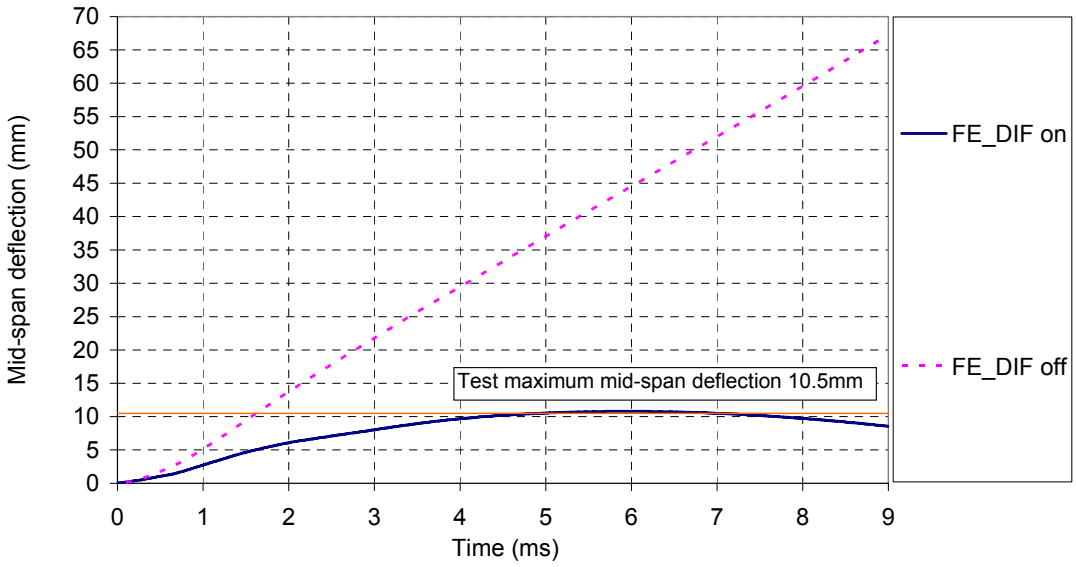

Figure 9-10 Mid-span deflection time history for NCR-2 (With and without concrete local DIF)

From the modelling results for NCR-2 in Figure 9-10, the maximum mid-span deflection is very close to the test with concrete local DIF incorporated, whereas it is significantly larger than the measured result without DIF. A comparison of the *SDF*

damage contour for NCR-2 from models with and without considering concrete local DIF is presented in Figure 9-11 and Figure 9-12.

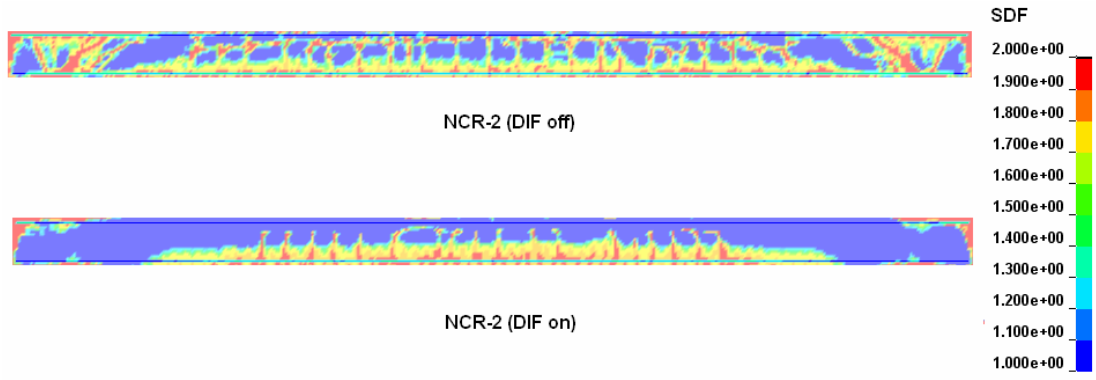

Figure 9-11 NCR-2: Comparison of *SDF* contours (DIF off vs. DIF on) at 6*ms*

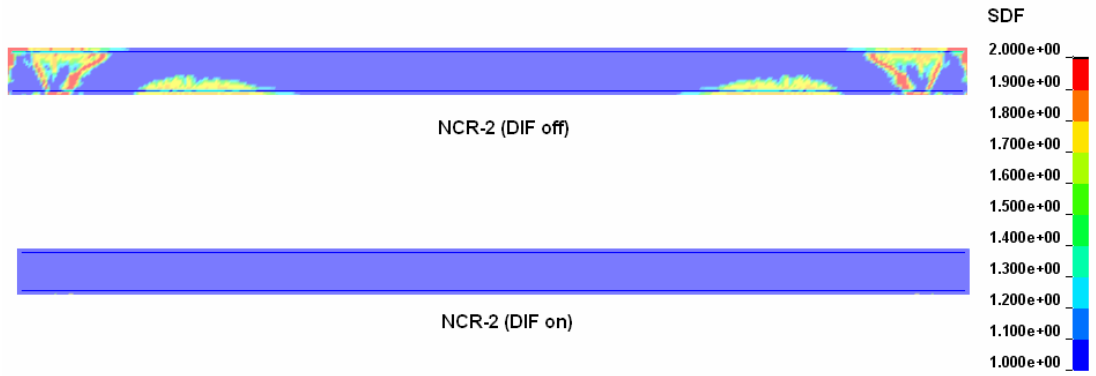

Figure 9-12 NCR-2: Comparison of *SDF* contours (DIF off vs. DIF on) at 1*ms*

From the damage contours it can be observed that significant shear cracks occur at two ends of the slab for the model without concrete local DIF, leading to a support-end shear failure mode which does not agree with the experimental observation. It can be found from the contour that even at the very beginning, herein at 1 ms when the peak overpressure has just passed (in Figure 9-9), the shear crack has already formed. The *SDF* time histories of 4 elements in Figure 9-13 located at the shear

crack are presented in Figure 9-14. The effective stress ($\Delta\sigma_{eff}$) time histories of these elements are presented in Figure 9-15.

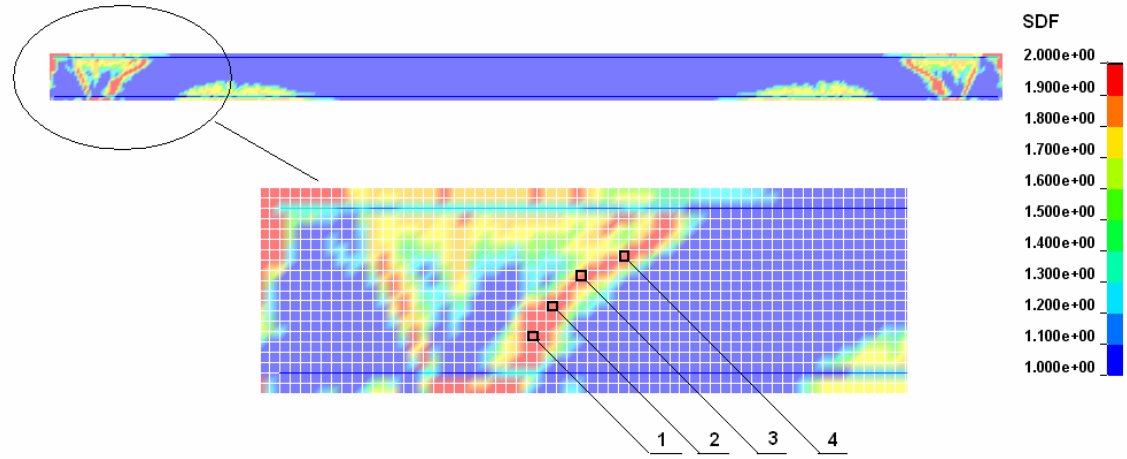

Figure 9-13 Picked elements for NCR-2 model

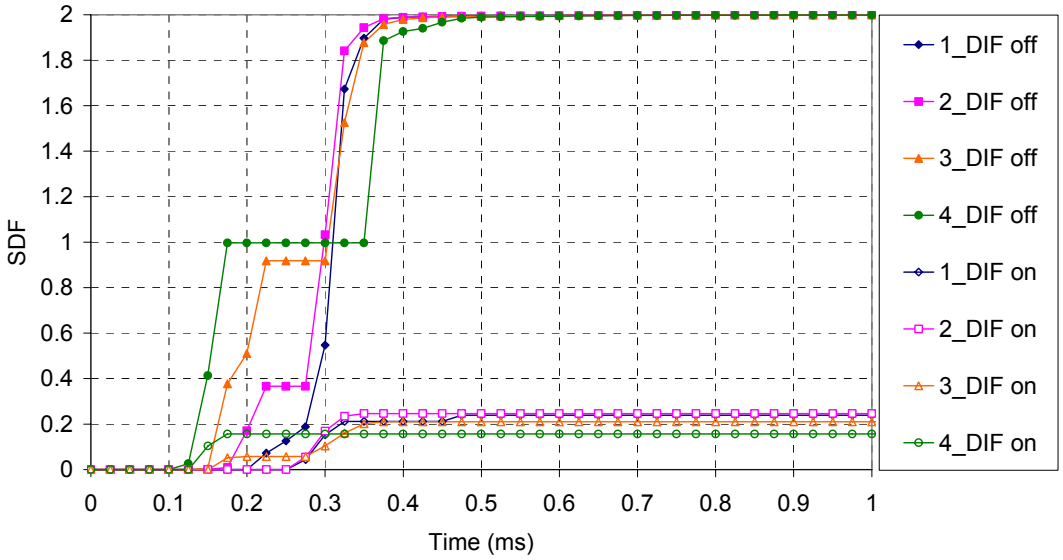

Figure 9-14 *SDF* time histories of selected elements at the shear cracks for NCR-2 models (with and without concrete local DIF)

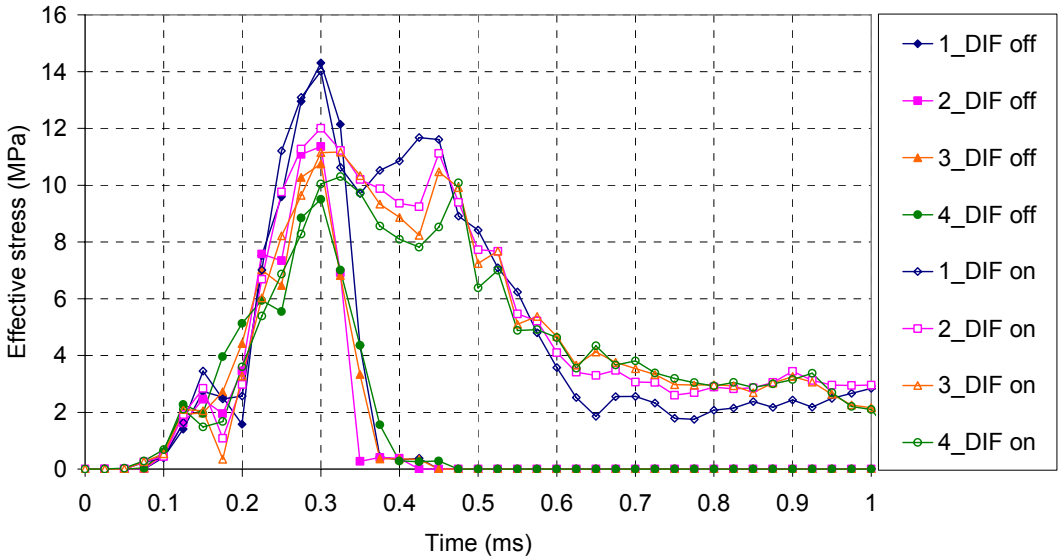

Figure 9-15 Effective stress time histories of selected elements at the shear crack for NCR-2 models (with and without concrete local DIF)

The slope of the effective stress shows little difference for different elements in Figure 9-15. The peak value of the effective stress for the same element shows little difference but the damage of the elements was totally different according to Figure 9-14 and Figure 9-15. For K&C concrete damage model the enhanced value of effective stress $\Delta\sigma_e$ of the failure surface is obtained by the current, or so call "un-enhanced", effective stress $\Delta\sigma_{eff}$ times the rate enhancement factor r_f (Equation (9-4)). The rate enhancement factor r_f is related to the local strain rate defined by concrete local DIF input presented in Chapter 5.

$$\Delta\sigma_e = r_f \Delta\sigma_{eff} \tag{9-4}$$

Without concrete local DIF, the failure surface $\Delta\sigma_e$ is not enhanced so the failure of the elements occurs (Figure 9-14) as soon as the effective stress $\Delta\sigma_{eff}$ reaches the

peak value (Figure 9-15). With concrete local DIF included, the failure surface $\Delta\sigma_e$ is enhanced, so that no shear crack damage at the supports is observed in Figure 9-11 and Figure 9-12.

The excessive mid-span deflection as shown in Figure 9-10 without considering DIF is mainly due to the concrete shear failure at the supports, which was not reliable. Concrete local DIF must be included or else the slab would behave too weak to resist the blast pressure.

The global response herein represented by the maximum mid-span deflection, of the FE model with 5mm element size of the two slabs match the test results very well. This indicates that the mesh and rate dependent concrete local DIF application with K&C concrete damage model can properly model the concrete structure behaviour under blast load. The peak reflected overpressure and the maximum values of the mid-span deflection in both NRC-1 and NRC-2 are summarised in Table 9-1, showing a reasonable comparison with the test results.

Table 9-1 Blast test for reinforced concrete slab

Blast test		NCR-1	NCR-2
Stand-off distance R (m)		3	3
Explosive charge W (kg)		1.007	8.139
Scaled distance to mid-span Z $(m/kg^{1/3})$		3	1.5
Peak reflected overpressure at PT1(MPa)	Measured	0.42	2.39
	TM5	0.33	2.52
	FE	0.47	2.71
Peak reflected overpressure at PT2 (MPa)	Measured	0.3	1.0
	TM5	0.29	2.16
	FE	0.3	2.45
Maximum mid-span deflection (mm)	Measured	1.5	10.5
	FE	1.4	10.7

9.4 Blast test modelling for FRP-retrofitted concrete slab

9.4.1 FE model

The FRP strengthened specimen test RET-1 in Wu et al. (2009a) is chosen to do the blast test modeling for FRP-retrofitted concrete slab. For test RET-1 the standoff distance was $1.5\,m$, TNT charge was $1.044\,kg$ and the scaled distance was equal to 1.5 approximately.

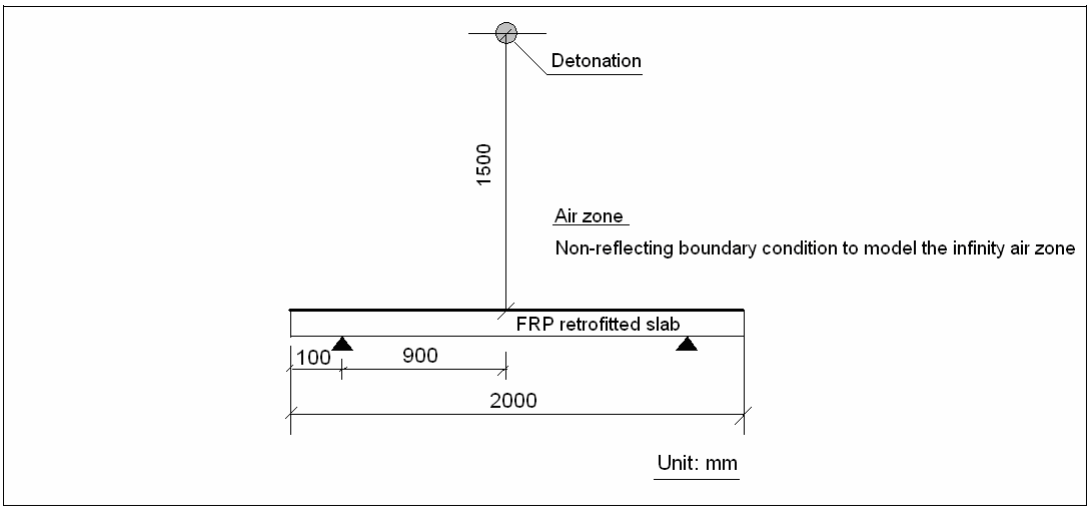

Figure 9-16 2D axial symmetric model sketch for FRP retrofitted concrete slab under blast load

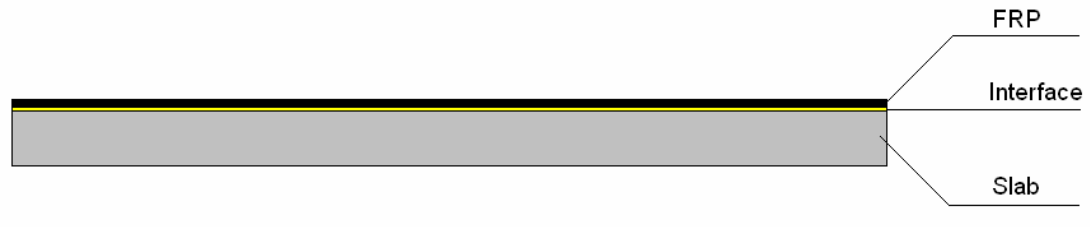

Figure 9-17 Sketch of FRP retrofitting

The basic model for the reinforced concrete slab is the same as the previous model, while FRP is added together with interface elements. The FRP plate of 2.8*mm* thickness is modelled as linear elastic with the Young's modulus equal to 205 *GPa* and the Poisson's ratio 0.3. Mesh size of 5*mm* is chosen.

Material 169 in LS-DYNA, *MAT_ARUP_ADHESIVE, is used to model the interface. This material model was originally written for adhesive bond in aluminum structures by ARUP. This plasticity model is not volume-conserving, and hence avoids the spuriously high tensile stresses that can develop if adhesive is modeled using traditional elastic-plastic material model (LSDYNA 2007). It is assumed that the smallest dimension of the element is the through-thickness dimension of the bond,

which is dominated in the failure criteria of the material. The model has rate effects included but just two points of the states are defined, one is the static state and another is the maximum strain rate state.

The geometry of the interface element was set with 1mm in thickness. The bond-slip model properties relating to the shear and normal directions are defined using the same method as presented in Section 8.4.2 in Chapter 8.

For the current simulation, the static slip rate is set as $1\times10^{-7}\,m/s$ as discussed in Chapter 6 and Chapter 8. Since test RET-1 had the same scaled standoff distance as test NCR-2, these two tests were effectively subjected to similar blast load with similar overpressure time histories. It is discovered that the maximum velocity during the test was up to nearly $100\,m/s$ at the top surface of the specimen for NCR-2. According to Equation (8-3), the equivalent local strain rate $\dot{\varepsilon}_{eq}$ for the $1\,mm$ thick interface element under a $100\,m/s$ slip rate is estimated to be on the order of $10^5/s$.

The DIF factor α_{DIF} for the maximum tensile stress and shear stress at a strain rate of $10^5/s$ is found to be around 14:

$$\alpha_{DIF}=\beta\times e^{\gamma}=2.852\left(\frac{f_{cs}}{10}\right)^{-0.27}\times e^{2\times10^{-9}\left(\frac{10^2}{10^{-7}}\right)}=14 \qquad (9\text{-}5)$$

The definitions of parameters in Equation (9-5) can be found from Equations (6-4) to (6-8) in Chapter 6.

9.4.2 FE results and discussion

The test and modelling results for NCR-2 and RET-1 are listed and compared in Table 9-2.

Table 9-2 Comparison of results for NCR-2 and RET-1 with the same scaled distance

Blast test		NCR-2	RET-1
Stand-off distance $R\,(m)$		3	1.5
Explosive charge $W\,(kg)$		8.139	1.044
Scaled distance to mid-span $Z\,(m/kg^{1/3})$		1.5	1.5
Peak reflected overpressure at Gauge1(MPa)	Measured	2.39	2.08
	TM5	2.52	2.53
	FE	2.71	2.9
Peak reflected overpressure at Gauge 2 (MPa)	Measured	1.0	0.89
	TM5	2.16	1.47
	FE	2.45	2.5
Maximum mid-span deflection (mm)	Measured	10.5	3.5
	FE	10.7	3.4

The modelling results indicate that simulations using the proposed mesh and rate dependent DIF together with the proposed dynamic bond-slip model can properly reproduce the global behaviour of the FRP strengthened concrete slab under blast load. The peak values of the overpressure for model NCR-2 and RET-1 are close to each other due to the same scaled distances of $1.5\,m/kg^{1/3}$. A comparison of the *SDF* damage contour of RET-1 and NCR-2 is presented in Figure 9-18. It can be observed

that FRP strengthening has improved the resistance of the slab under blast with reduced damage.

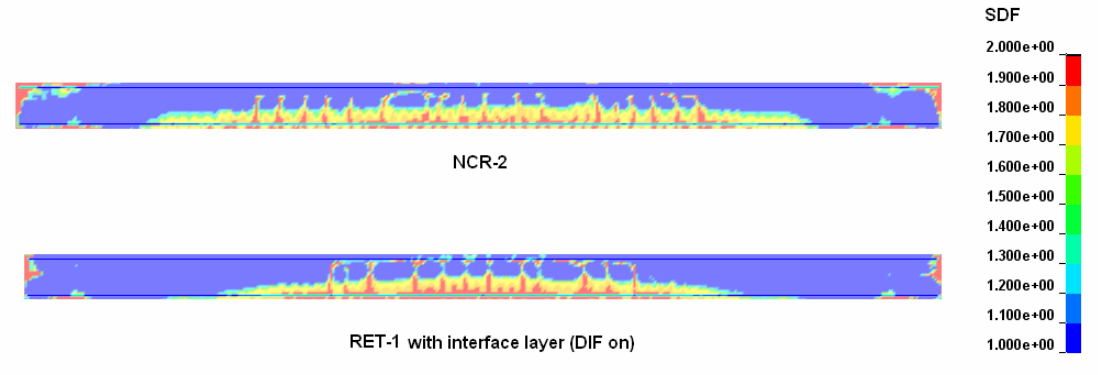

Figure 9-18 Scaled damage (*SDF*) contour of NCR-2 and RET-1 at maximum mid-span deflection with mesh and rate dependent DIF and dynamic bond-sip model

Three different case studies with regard to the application of the proposed dynamic bond-slip model are conducted, with the bond being modelled with a perfect bond condition, with and without interface, respectively. A comparison of the deflection time histories with the test results is illustrated in Figure 9-19. It is noted that in all the three model cases the mesh and rate dependent concrete local DIF is applied. A comparison of the damage contours is presented in Figure 9-20.

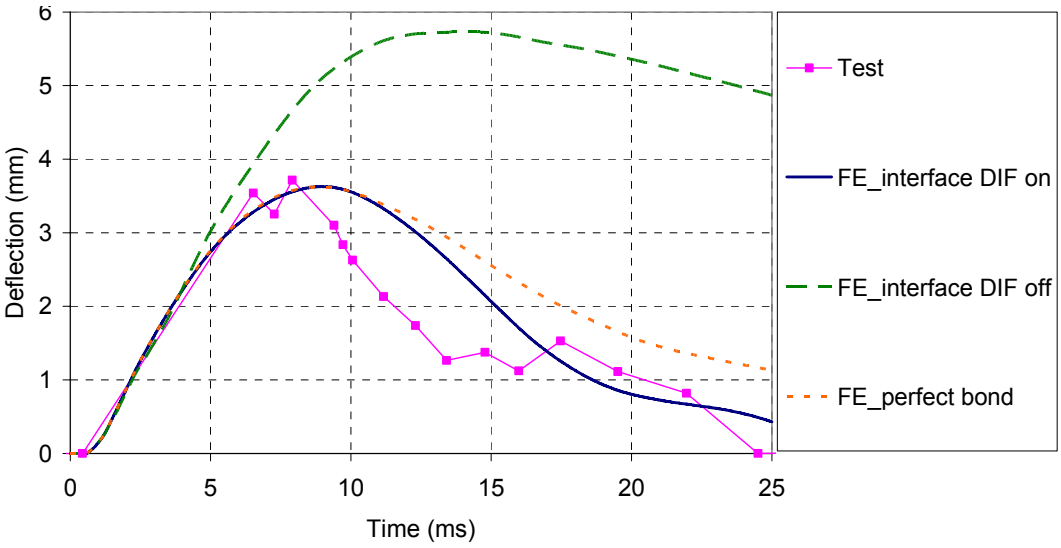

Figure 9-19 Mid-span deflection time histories for RET-1 (with and without DIF for bond-slip relationship; concrete local DIF on; mesh size 5*mm*)

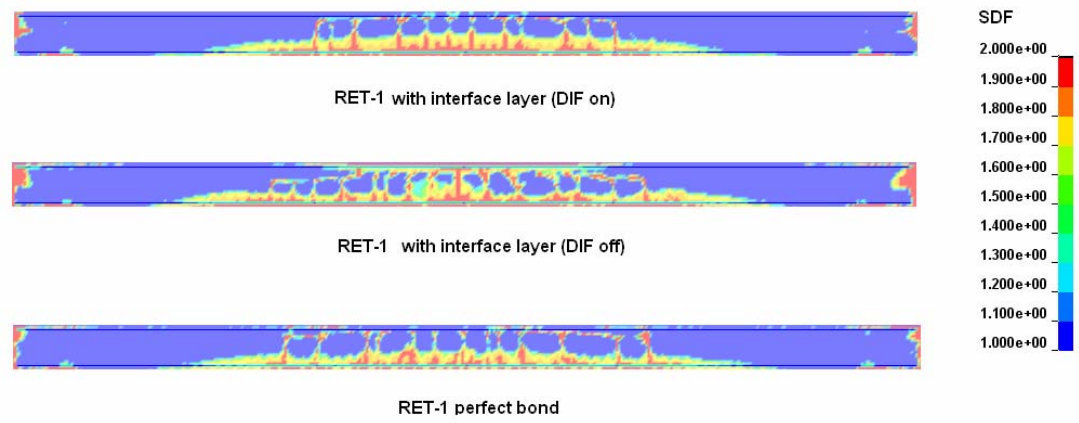

Figure 9-20 Damage contours at 9*ms* of the response in the three modelling cases

The comparison in Figure 9-19 clearly suggests that DIF for the FRP interface must be included into the model. Without considering this, the numerical maximum mid-span deflection is nearly twice of the test measurement. The interface elements fail at the very beginning of the process, 2 *ms* , when the interface DIF is not applied.

When the interface DIF for the dynamic bond-slip model is considered, the mid-span deflection time history matches well the test result. The maximum mid-span deflection reduces to 3.4 *mm* . No debonding is observed in the model with interface DIF applied.

In the model with a perfect bond condition without interface element, the initial part of the mid-span deflection time history is the same as the model with interface DIF. However the softening part is different. The permanent deflection for the perfect bond condition is larger than the model with interface element and using the dynamic bond-slip model. Inspection of the numerical damage progress indicates that failure happens in the layer of concrete elements adjacent to the FRP in the model with perfect bond, consequently the concrete slab is damaged more severely than the case with interface element because little damage occurs at the relevant concrete layer. Figure 9-22 shows the *SDF* time histories for a few concrete elements adjacent to FRP at mid-span, illustrated in Figure 9-18, for the two cases, namely with perfect bond condition and with interface element.

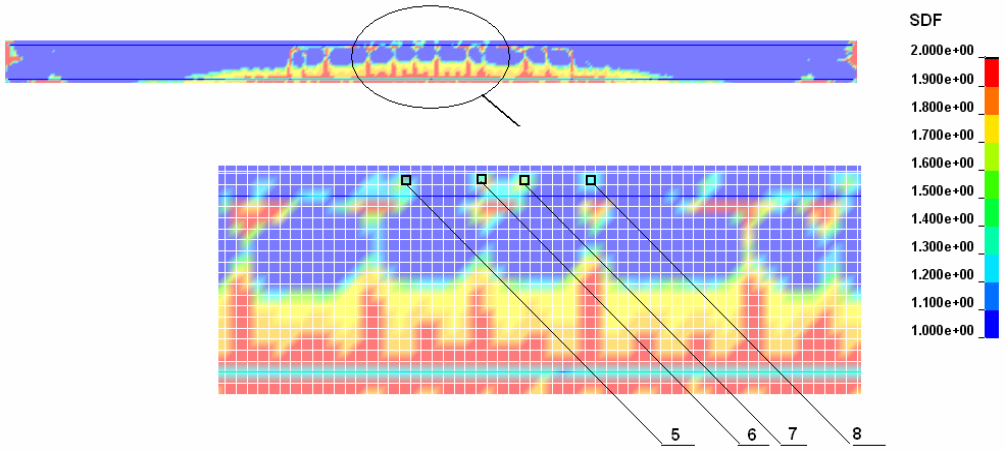

Figure 9-21 Picked elements for RET-1 at mid-span

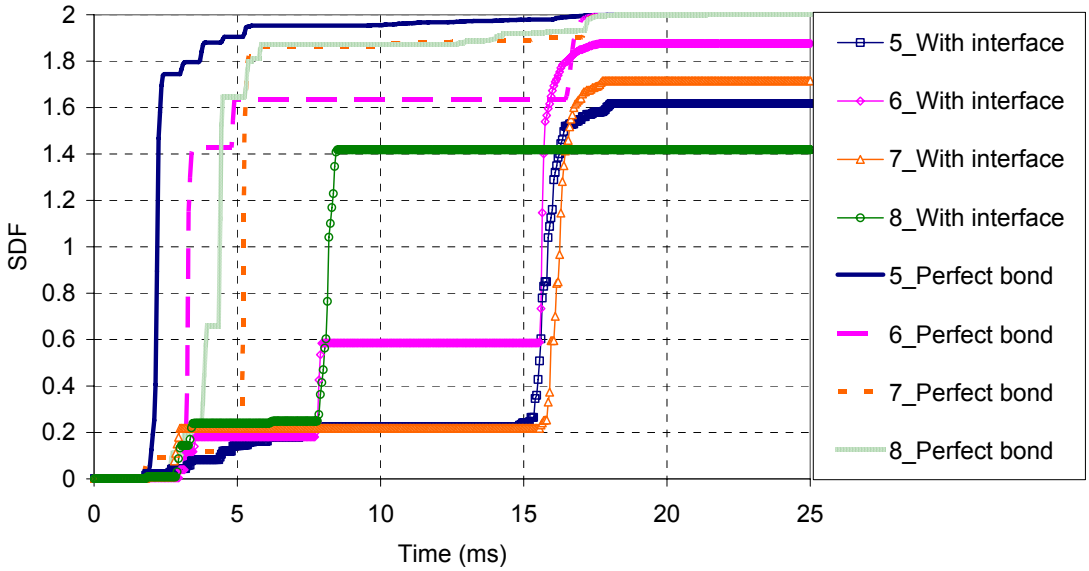

Figure 9-22 *SDF* for the concrete elements adjacent to FRP at mid-span

Clearly, with a perfect bond condition, the damage of the elements occurs before the maximum mid-span deflection is reached. On the contrary, for the model with interface element and dynamic bond-slip model, the damage of the same concrete elements happens after that. In fact, when the concrete elements in the model with interface start to incur damage, the same elements in the model with perfect bond have totally failed.

According to Wu et al. (2009a), debonding was never observed in the tests. So the modelling results with interface appear to be more reliable than those with a perfect bond condition, although the maximum mid-span deflections from these two models are the same.

9.5 Parametric study

9.5.1 Effects of Young's modulus

Based on the above evaluation of the modelling approach, a numerical parametric study on FRP for blast resistance strengthening is conducted. The test RET-1 is considered as the base model, which used FRP with a Young's modulus of 205 GPa and the thickness was 2.8 mm. The range of Young's modulus for CFRP is normally 120-250 GPa (Head 1996). Four more different values of FRP Young's modulus, namely 100 GPa, 150 GPa, 250 GPa and 300 GPa, are considered. All the other numerical settings are the same as the RET-1 model.

The *SDF* damage contours at the time when their respective maximum mid-span deflection is reached are shown in Figure 9-23. It can be seen that, with increasing the FRP Young's modulus, damage is gradually reduced, but the absolute reduction is not significant.

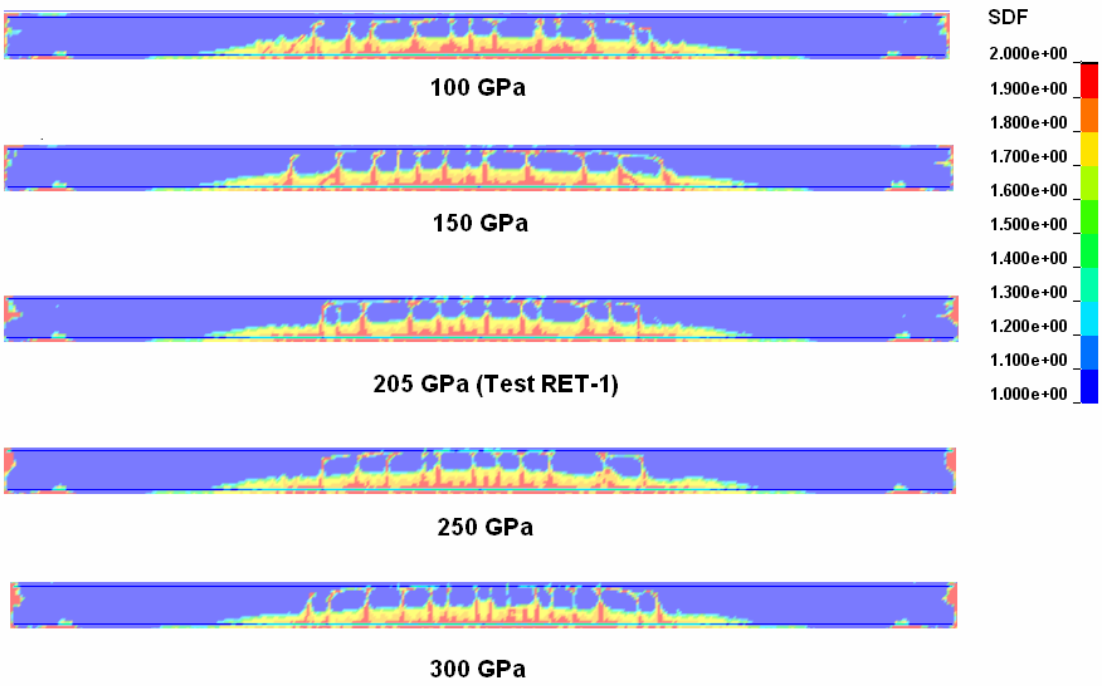

Figure 9-23 Effects of Young's modulus (SDF contour at maximum mid-span deflection under the same blast load)

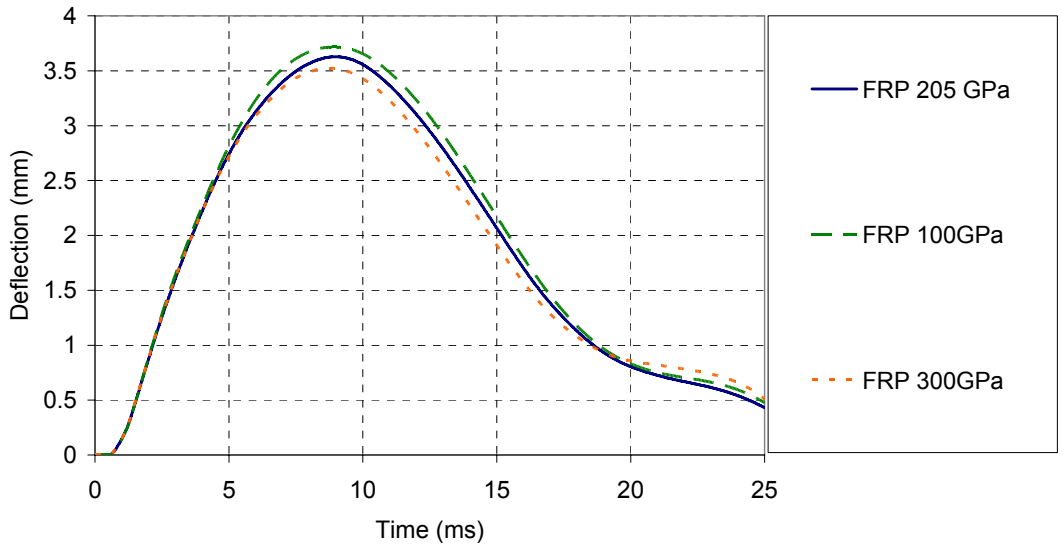

Figure 9-24 Effects of Young's modulus (mid-span deflection time histories under the same blast load)

The mid-span deflection time histories are compared in Figure 9-24. The comparison indicates that with reducing the FRP Young's modulus, the maximum mid-span deflection increases, and vice versa. However, the mount of increasing or decreasing is slight. The aim of compression retrofitting is for concrete protection, and its structural effect is less significant.

9.5.2 Effects of FRP thickness

For this evaluation, the FRP Young's modulus is kept as a constant of 205 GPa while the FRP thickness is varied. The original thickness is 2.8 mm with 2 layers of 1.4mm FRP plates retrofitting. Two more thicknesses 1.4 mm and 5.6 mm corresponding to 1 layer and 4 layers FRP plates, respectively, are modeled.

The damage contours of the above three thickness cases at the respective maximum mid-span deflections are compared in Figure 9-25. With increasing the FRP retrofitting layers, the damage of the specimen is reduced. A comparison of the maximum mid-span deflection time histories for different FRP thickness, shown in Figure 9-26, indicates that with reducing the FRP thickness, the maximum mid-span deflection is increased, and vice versa.

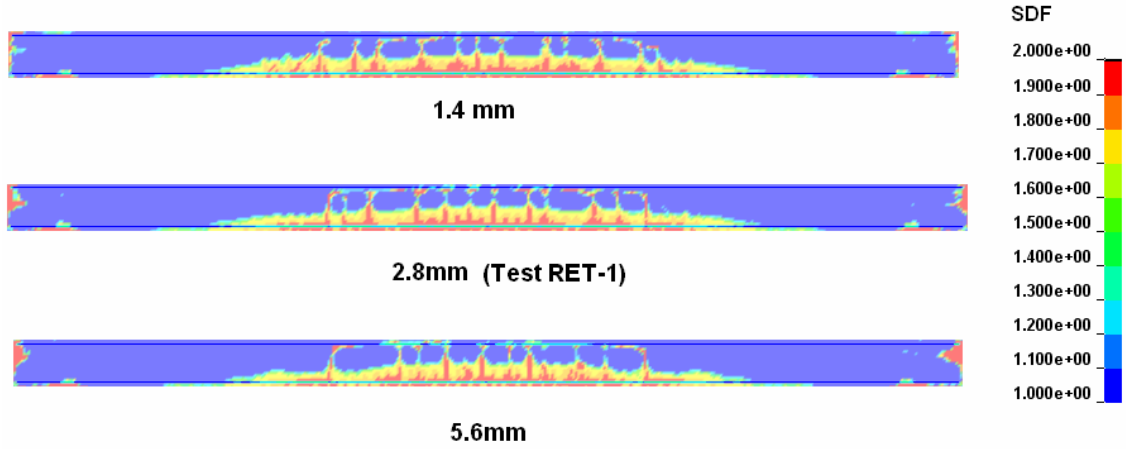

Figure 9-25 Effects of FRP thickness (SDF contour at maximum mid-span deflection under the same blast load)

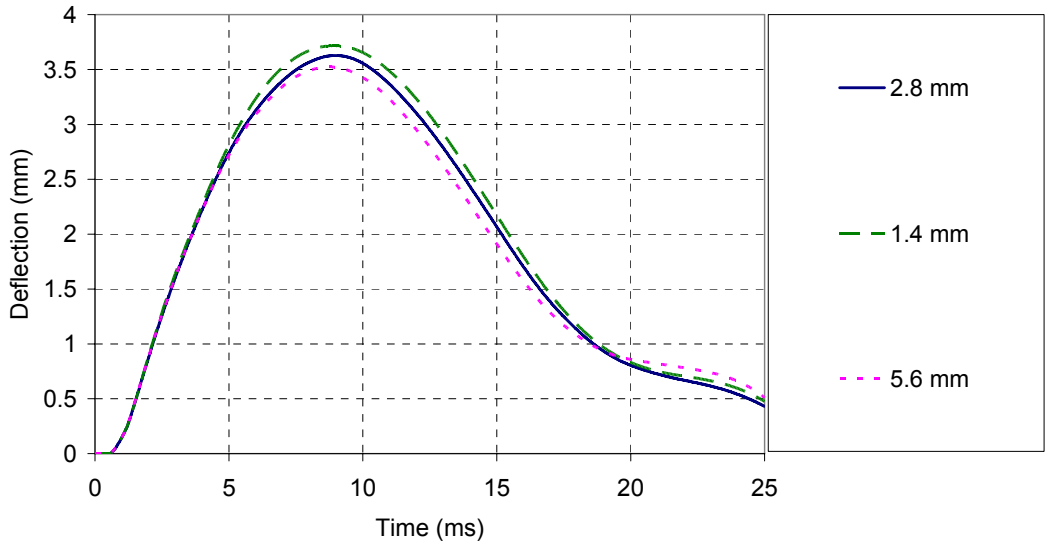

Figure 9-26 Effects of FRP thickness (mid-span deflection time histories under the same blast load)

9.5.3 Effects of strengthening method

So far the comparisons have been made with the FRP installed on the blast loading (compressive) side of the specimen, as it was done in the experiment. In this Section, the FRP is moved to the tensile face of the specimen and modeled. The damage

contours at the maximum mid-span deflection is shown in Figure 9-27. Figure 9-28 shows the mid-span deflection time histories.

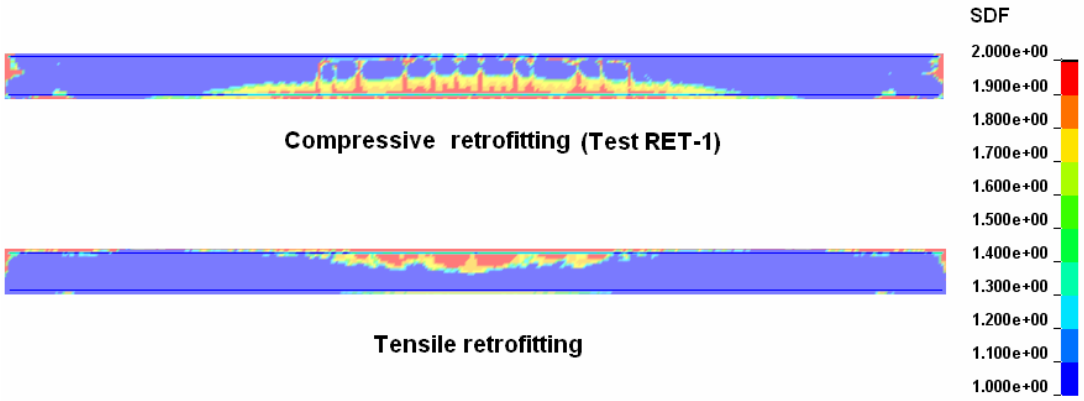

Figure 9-27 Effects of strengthening method (*SDF* contour at maximum mid-span deflection under the same blast load)

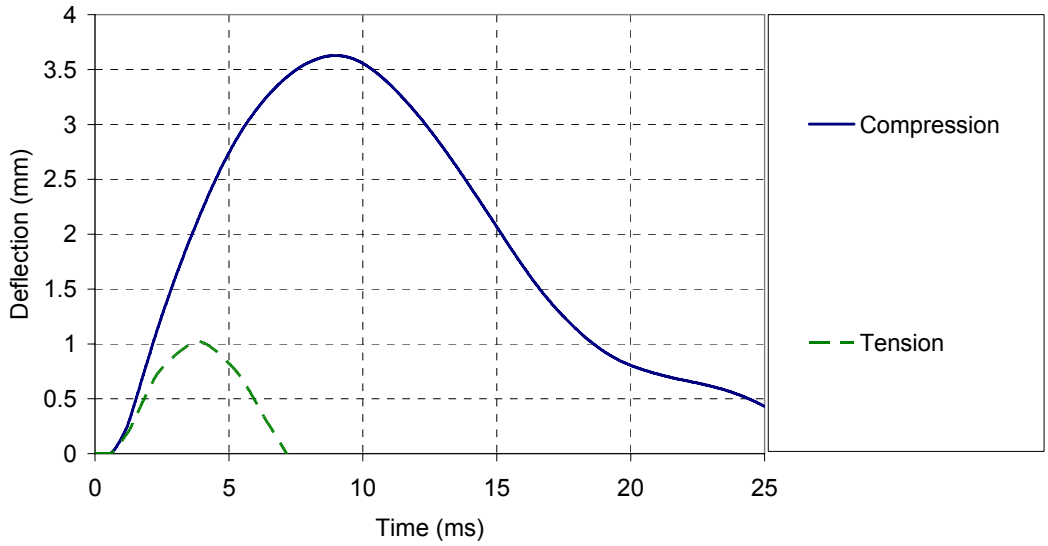

Figure 9-28 Effects of strengthening methods (mid-span deflection time histories under the same blast load)

The structure effects of retrofitting on the tension side are dramatic. The maximum mid-span deflection is reduced from about 3.5*mm* to 1*mm*. This is actually expected as applying FRP on the tension side is known to be most effective against bending.

However, local failure of the concrete on the compressive side occurs at about 4 *ms*, and this appears to reduce considerably the ductility of the specimen.

9.6 Conclusions

In this chapter, numerical simulations of RC slabs subjected to blast loading are carried out to demonstrate the application of the proposed concrete local DIF (Chapter 5) and dynamic bond slip model (Chapter 6) in a comprehensive blast response analysis scenario. The cases chosen were from actual experiments of RC slabs without and with FRP strengthening under blast (Wu et al. 2009a). The mesh convergence study demonstrates that the number of element layers through the thickness of the specimen must be sufficiently large in the numerical modelling of a bending-dominated response under blast load. Comparison with the test results suggests that the application of the proposed concrete DIF and the proposed dynamic bond-slip model leads to reasonable simulation results in both RC and FRP strengthened RC slabs. From the illustrative parametric study, it can be observed that increasing the Young's modulus and thickness of the FRP plate applied on the compressive face of the specimen will enhance the blast resistance, but to a limited extent. When the same FRP plate is applied on the tensile face of the specimen, the overall response tends to be significantly reduced, but the ductility of the specimen might be threatened due to the potential crushing failure of concrete on the compressive side. It is recommended that the tensile face strengthening of the specimen should be modelled, and the mount of FRP strengthening including FRP

Young's modulus and thickness need to be carefully justified to avoide concrete crushing failure on the compressive side before doing experiments.

9.7 References

American Society of Civil Engineers (ASCE) (1997), Design of Blast Resistant Buildings in Petrochemical Facilities, ASCE, USA.

Buchana, P.A. and Chen, J.F. (2007), "Blast resistance of FRP composites and polymer strengthened concrete and masonry structures – A state-of-the-art review", *Composites Part B: Engineering*, 38(5-6):509-522.

Camanho, P.P. and Davila, C.G. (2002), "Mixed-mode decohesion finite elements for the simulation of delamination in composite materials", *NASA Technical Paper*, 211737: 42.

Crawford J.E., Malvar L.J., Morrill K.B. and Ferritto J.M. (2001), Composite retrofits to increase the blast resistance of reinforced concrete buildings. *Proceedings of the tenth international symposium on interaction of the effects of munitions with structures*. San Diego, USA: 1–13.

Day, I., Glynn, C., Merrigan, M., and Spencer, A. (2006).Retrofitting Reinforced Concrete Members against Blast Loading Using Near Surface Mounted FRP, Final Year Undergraduate Research Thesis, School of Civil and Environmental Engineering, The University of Adelaide, Australia.

De Lorenzis L. and La Tegola A. (2005), "Bond of FRP laminates to concrete under impulse loading: a simple model", *Proceedings of the international symposium on bond behaviour of FRP in structures*: 495–500.

Dobrazt, B.M. and Crawford, P.C. (1985), Handbook of Explosives, UCRL-52997, Lawrence Livermore National Laboratory, Change 2: 8-21 to 8-23.

Head, P.R. (1996), "Advanced composites in civil engineering- a critical overview at the high interest, low usage stage of development", Advanced Composite Materials in Bridges and Structures, Proceedings of the Second International Conference, Quebec, Canada, edited by M.M.EI-Badry, pp.3-15, Canadian Society for Civil Engineering, Montreal, Canada.

Hyde, D.W. (1992), User's Guide for Microcomputer Program CONWEP, Application of TM5-855-1, Fundamental of Protective Design for Conventional Weapons, Instruction Report SL-88-1, Structures Laboratory, US Army Waterways Experiment Station, Vicksburg, Mississippi.

LSDYNA (1998), Theory Manual Version 971, Livermore Software Technology Corporation.

LSDYNA (2007), Keyword User's Manual Version 971, Livermore Software Technology Corporation.

Lu, Y., Wang, Z.Q. and Chong, K(2005), "A comparative study of buried structure in soil subjected to blast load using 2D and 3D numerical simulations", Soil Dynamics and Earthquake Engineering, 25(4):275-288.

Nam, J.W., Kim, H.J., Yi, N.Y., Kim, I.S., Kim, J.H.J. and Choi, H.J. (2009a), "Blast analysis of concrete arch structures for FRP retrofitting design", *Computers and Concrete*, 6(4): 305-18.

Nam, J.W., Kim, H.J., Kim, S.B., Kim, J.H.J. and Keun, J.B. (2009b), "Analytical study of finite element models for FRP retrofitted concrete structure under blast loads", *International Journal of Damage Mechanics*, 18(5): 461-490.

Nam, J.W., Kim, H.J., Kim, S.B., Yi, N.H. and Kim, J.H.J.(2010), "Numerical evaluation of the retrofit effectiveness for GFRP retrofitted concrete slab subjected to blast pressure", *Composite Structures*, 92(5):1212-1222.

Razaqpur, A.G., Tolba, A. and Contestabile, E. (2007), "Blast loading response of reinforced concrete panels reinforced with externally bonded GFRP laminates", *Composites: Part B 38*: 535–546.

Razaqpur, A.G., Contestabile, E. and Tolba, A. (2009), "Experimental study of the strength and deformations of carbon fibre reinforced polymer (CFRP) retrofitted reinforced concrete slabs under blast load", *Canadian Journal of Civil Engineering*, 36(8):1366-1377.

TM5-1300 (1990), Structures to Resist the Effect of Accidental Explosions, US Department of the Army, Navy and Air Force Technical Manual.

White, T., Soudki, K. and Erki, M. A. (2001), "Response of RC beams strengthened with CFRP laminates and subjected to a high rate of loading," *Journal of Composites for Construction*, ASCE, 5(3):153-162.

Wu, C., Oehlers, D.J., Rebentrost, M., Leach, J. and Whittaker, A.S. (2009a), "Blast testing of ultra-high performance fibre and FRP-retrofitted concrete slabs", *Engineering Structures*, 31(3): 2060-2069.

Wu, C., Oehlers, D.J and Day, I. (2009b), "Layered blast capacity analysis of FRP retrofitted RC member", *Advances in Structural Engineering*, 12(3): 435-49.

Zhou, X.Q. and Hao, H. (2007), "Prediction of air-blast loads on structures behind a protective barrier", *International Journal of Impact Engineering*, 35:363–375.

Chapter 10 Conclusions and future work

10.1 Summary

External bonding of fibre reinforced polymer (FRP) composites has been used worldwide for strengthening RC structures since early 1990s and more recently developed as an effective technique for retrofitting concrete structures for high energy events such as impact and blast. Debonding at the FRP-to-concrete interface is one of the predominant failure modes under both static (Chen and Teng 2001) and dynamic conditions (Buchana and Chen 2007; Bhatti et al. 2011). Comprehensive research has been conducted for the static bond behaviour (Chen and Teng 2001; Lu et al. 2004; Lu et al. 2005) but the bond mechanics under high strain rates is not well understood.

This thesis began with a systematic investigation of meso-scale modelling issues of the local concrete model and pull-off test under static condition. Concrete dynamic property and its application in local concrete model under high strain rate events were then explored. The inevitable mesh-dependency due to numerical localization and its implications on rate effects have been examined in detail. By introducing the concrete static and dynamic modelling issues into numerical experiment of the pull-

off test under different slip rates, a dynamic bond-slip model was then proposed. An impact test study was conducted with the strain time history of the FRP bonded to the concrete measured. The impact test and a higher energy blast test for concrete and FRP strengthened slabs are modelled. The close agreement between the tests and FE results validates the proposed concrete local DIF and dynamic bond-slip models.

10.2 Overall conclusions

This thesis has presented a systematic investigation on the meso-scale modelling of concrete and FRP-to concrete bonded joint. The following main conclusions can be drawn based on the studies presented:

1. In smeared meso-scale modelling of concrete under static condition, mesh objectivity can be achieved through the adoption of the crack band theory which keeps the fracture energy constant;

2. The dilation of concrete plays an important role in the FRP-to-concrete bond behaviour. A model has been proposed to relate the concrete shear dilation angle to the concrete strength based on a large number of FRP-to-concrete bonded joints tested under static condition;

3. Under high stain rates, mesh objectivity cannot be achieved in meso-scale FE models even when the crack band model is deplored if common fixed DIF of concrete is used. This differes from the static condition. This very important fact is identified for the first time in this study;

4. A mesh and strain rate dependent DIF model has been proposed in this study, which can achieve mesh objectivity in meso scale FE modelling of concrete when used in combination of the rack band model;

5. Based on a detailed meso-scale FE study of FRP-to-concrete bonded joint under high loading rate, a slip rate dependent bond-slip model has been developed for the first time;

6. A set of FRP-to-concrete bond tests has shown that the bond strength is enhanced under impact loading compared with static condtion;

7. The impact test together with a FRP plated slab under blast have been modelled including the proposed slip rate dependent bond-slip model. The predictions were in good agreement with the test results, validating the FE model and the rate-dependent bond-slip model.

10.3 Detailed conclusions

10.3.1 Issues of meso-scale modeling

Concrete is an important material in civil engineering and defence construction application. Because concrete material has very complicated non-linear behaviour it is difficult to be fully described for general stress conditions by a simple constitutive model. When concrete is subjected to extreme loading such as blast load and impact, the modelling can be further complicated due to rate effects, overloading and large

deformations. The K&C concrete damage was chosen as it has been demonstrated that this concrete model can properly structure global/local response in high energy events. The modelling of the tension dominated notched beam test and compressive localization issues with the local concrete damage model have been conducted in Chapter 3 indicating that the mesh sensitivity associated with material softening is a significant issue in finite element (FE) modelling with local concrete models for meso-scale numerical investigations.

Mesh-objectivity cannot be achieved without an appropriate consideration of the localization in the finite element model and its relationship to the fracture energy. For meso-scopic modelling where the element size is smaller than the standard concrete aggregate size, the localized width (or crack band) should be set as the element characteristic length. The results reported in this chapter prove that the uniaxial tension and compression stress strain curve in a single element is mesh dependent, but the overall behaviour becomes essentially mesh-independent if the tension and compression fracture energies are kept constants. An evaluation of the relationship between the commonly used damage indices, such as the *SDF* employed in LS-DYNA, and the consumed fracture energy enables a clear identification of the actual fracture zone from the damage contour plots.

10.3.2 Static pull-off test modeling

Chapter 4 develops a finite element model based on the K&C local damage concrete model in LS-DYNA for accurate prediction of debonding behaviour of the FRP-concrete bonded joint. Dilation is another important aspect of concrete modelling and

this was studied in Chapter 4 with a large number of static pull-off test modelling of which the failure mode was shear dominated. The model was first validated by a large number of specimens under static pull-off tests. It was then applied to simulate similar tests under high strain rate loadings exploring the effect of dynamic properties of the concrete. It has been shown that the model can simulate the static FRP-to-concrete bond behaviour, in terms of the load-carrying capacity, load-displacement behaviour and local bond-slip behaviour with reasonable accuracy and mesh objectivity subjected to both proper localization and dilation consideration with local concrete damage model. Proper guidelines were given to the selection of crack band width and shear dilatation factor. The static modelling forms the basis of dynamic modelling.

A preliminary finite element study on the effects of loading rate on the behaviour of FRP-to-concrete bonded pull-off tests is presented based on the mesh-independent load-slip curves. A good agreement with test data has been obtained for quasi-static loading. By considering the dynamic increase factor for concrete strength as a function of strain rate, the effects of loading rates on the load-slip curve, effective bond length, ultimate load and the damaged concrete area are elucidated. The developed numerical model is then further investigated under dynamic loadings in the following Chapters.

10.3.3 Dynamic increase factor (DIF) for concrete in tension

Concrete dynamic increasing factor (DIF) has been a subject of extensive investigation and debate for many years. It now tends to be generally accepted that

the compressive DIF as observed from standard sample tests is mainly attributable to the dynamic structural effect, whereas for concrete under tension the DIF is deemed to be governed by different mechanisms, probably more from the material and micro-fracture level. Chapter 5 presents a numerical study on the uniaxial tension DIF, with a particular focus on how the DIF, irrespective of its cause, should be included in an appropriate manner in the FE modelling with a local concrete model.

Based on the FE modelling studies presented in Chapter 5, the following conclusions are drawn:

1) The dynamic tensile strength increase (tension DIF) is demonstrated to be a genuine material property for concrete in tension. This observation is supported by a variety of tension-dominated modelling analyses, ranging from simplified direct tension, SHPB tension test, to three-point bend impact test. Without considering the DIF at the material property level, it is not possible to reproduce reasonable results compared with the experimental results.

2) However, the commonly adopted empirical global DIF models can not be directly applied in the FE analysis with a local concrete material model, due to strain localisation which leads to strain-rate localisation under dynamic loading. To rectify this problem and enable mesh convergence, a mesh-correction factor is proposed to be introduced in the local DIF input. Moreover, due to the complexity in the stress and strain distribution when the loading/strain rate is high, a rate correction factor is further incorporated. Thus, a "doubly-corrected" local DIF versus strain rate relationship is proposed for FE applications.

3) The appropriateness of the proposed doubly corrected local DIF is confirmed by various mesh convergence modelling studies and comparison of the computed results with experimental data. Although the specific correction parameters in the current study may be dependent upon to the concrete model employed (i.e., the K&C model), the approach is generally applicable and can be easily extended to other local material models.

10.3.4 Dynamic FRP to concrete bond-slip model

The first ever dynamic bond-slip model was developed in Chapter 6 through numerical experimentation. The K&C concrete model and the concrete local DIF discussed in Chapter 5 were introduced in the meso-scale modelling of the pull-off test. The DIF for the bond-slip relationship was then introduced to Lu et al's (2005) static bond-slip model forming a new dynamic bond-slip model.

The proposed slip rate dependent bond-slip model makes it possible for the first time to model the behaviour of FRP strengthened large structures with a proper consideration of the FRP-to-concrete bond behaviour under dynamic loads using reasonably large element size. Meso-scale modelling for practical structures is unrealistic because of computational cost. Proper application of the dynamic bond-slip model in FE modelling has also been briefly discussed.

10.3.5 FRP-to-concrete bond impact tests

The main characteristics of impact loads are high loading rates and very short duration that results in high material strain rates. The concrete strength is enhanced in high energy events due to the strain rate effect. The bond behaviour at high loading rates may be be quite different from the static state because the dynamic increasing effect under higher loading rate for concrete material as the debonding mostly occurs in concrete adjacent to the FRP unless the adhesive is very weak. A bending impact experiment was designed and tested in Chapter 7 to investigate the bond behaviour.

This chapter presented a set of FRP-to-concrete bond test under impact load. The measured strain time histories along the bond length of FRP can reflect the FRP-to-concrete bond behaviour under the impact load. An analysis indicated that the behavior of the bond is complex, with a combination of enhancement due to strain rate effects and weakening due to tensile stress wave indued by the impact. The test results showed that the enhancement was greater. The test data were used in the next chapter to validate the proposed dynamic bond-slip model in Chapter 6.

10.3.6 Modeling of impact test

Chapter 8 presented a study on the FE modelling of the impact tests. A typical specimen was first modelled using two options: 1) explicitly including the striker in the model and 2) without including the striker but use the measured impact load directly. It was concluded that explicitly modelling the striker does not produce satisfactory predictions because of the complex impact behaviour at the striker-

specimen interface. The measured impact load time history was therefore used in the modelling. A mesh convergence analysis was also conduced.

The FE predictions of test IT2 indicated possible errors in load measurements and improper surface treatment in the tests, resulting in that total debonding occurred in the test but not in the numerical simulations. However the FE predicted strain at SG1, where debonding occurred in both test and FE, was in good agreement with the test observation.

The predictions with and without concrete local DIF in the model with a striker showed that when the DIF is not considered, the strain-time history is far too low compared with the test. It has been concluded that only when concrete local DIF is considered, the predictions can give good match with the test results. If the DIF is not considered, the predictions are too low and the damage pattern does not match the test.

The dynamic bond-slip model was also implemented into the model and the mesh convergence was achieved at 10*mm*. The results are in reasonable good agreement in terms of both the slops of the curves and the peak values with test results at locations where debonding occur.

10.3.7 Modeling of FRP strengthened concrete slabs under blast

In Chapter 9, numerical simulations of RC slabs subjected to blast loading were carried out to demonstrate the application of the proposed concrete local DIF

(Chapter 5) and dynamic bond slip model (Chapter 6) in a blast response analysis scenario. The cases chosen were actual experiments of RC slabs with and without FRP strengthening under blast (Wu et al. 2009). The mesh convergence study demonstrates that the number of element layers through the thickness of the specimen must be sufficiently large in the numerical modelling of a bending-dominated response under blast load. Comparison with the test results suggests that the application of the proposed concrete DIF and the proposed dynamic bond-slip model leads to reasonable simulation results in both RC and FRP strengthened RC slabs. From the illustrative parametric study, it can be observed that increasing the Young's modulus and thickness of the FRP plate applied on the compressive face of the specimen enhance the blast resistance, but to a limited extent. When the same FRP plate is applied on the tensile face of the specimen, the overall response tends to be significantly reduced, but the ductility of the specimen might be compromised due to potential crushing failure of concrete on the compressive side.

10.4 Future research

The thesis represents an in-depth investigation on FRP-to-concrete bond behaviour under high strain events. Due to limitation of time and resources, many aspects of the research can be further studied. These may include at least the following:

1) Much of the work in this thesis is numerical and relies on the existing DIF model for concrete. However, most if not all the existing tests do not necessarily measure the actual material DIF, and therefore fundamental re-

design may be necessarily. For example, this research has shown that the strain rate in the concrete sample in the seemingly very simple SHPB test is clearly non-uniform so what is measured is the overall structural behaviour of the sample which can be significantly different from the local material behaviour. This implies that all existing tests and models need to be interpreted within this context and fundamental re-design of material tests may be necessarily.

2) The dynamic bond-slip relationship can be measured using properly designed tests as what presented in Chapter 7 with proposed improvements, such as an increased number of strain gauges so that local bond-slip relationship can be deduced. The preliminary test program presented in this thesis has shown that repeatability of such test is poor so a large number of specimens would be required.

3) Once the models developed in this thesis are further validated, they can be applied to model different structures strengthened with various strengthening schemes, leading to an in-depth understanding of the mechanics of these structures.

4) Further tests would be necessary to validate the above numerical predictions.

5) Based on the above, design guidelines for FRP retrofitting RC structures under high energy events can then be developed for practical engineering design.

10.5 References

Buchana, P.A. and Chen, J.F. (2007), “Blast resistance of FRP composites and polymer strengthened concrete and masonry structures – A state-of-the-art review”, *Composites Part B: Engineering*, 38(5-6):509-522.

Bhatti, A.Q., Kishi, N. and Tan, K.H. (2011), “Impact resistant behaviour of RC slab strengthened with FRP sheet”, *Materials and Structures/Materiaux et Constructions*, 1-10.

Chen, J.F., and Teng, J.G. (2001), "Anchorage strength models for FRP and steel plates bonded to concrete", *Journal of Structural Engineering, ASCE*, 127(7):784–791.

Lu, X.Z., Teng, J.G., Ye, L.P., and Jiang, J.J. (2005), "Bond–slip models for FRP sheets/plates bonded to concrete", *Engineering Structures*, 27: 920–937.

Lu, X.Z., Ye, L.P., Teng, J.G. and Jiang, J.J. (2004), "Mesco-scale finite element model for FRP sheets/plates bonded to concrete", *Engineering structures*, 27: 564-575.

Wu, C., Oehlers, D.J., Rebentrost, M., Leach, J. and Whittaker, A.S. (2009), “Blast testing of ultra-high performance fibre and FRP-retrofitted concrete slabs”, *Engineering Structures*, 31(3): 2060-2069.